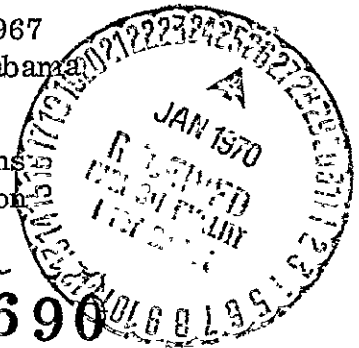




PROCEEDINGS OF THE  
THIRD SOUTHEASTERN SEMINAR  
ON THERMAL SCIENCES

May 8-9, 1967  
Huntsville, Alabama

H. L. Atkins  
R. I. Vachon



**N70-18686**  
(ACCESSION NUMBER)

**N70-18690**  
(THRU)

*236*  
(PAGES)

*1*  
(CODE)

*TMM-62639*  
(NASA CR OR TMX OR AD NUMBER)

*33*  
(CATEGORY)

NATIONAL AERONAUTICS AND SPACE ADMINISTRATION



Reproduced by  
NATIONAL TECHNICAL  
INFORMATION SERVICE  
Springfield, Va 22151

*33*

PROCEEDINGS OF THE  
THIRD SOUTHEASTERN SEMINAR  
ON THERMAL SCIENCES

May 8-9, 1967  
Huntsville, Alabama

H. L. Atkins  
R. I. Vachon



May 8, 1968

Sponsored by

George C. Marshall Space Flight Center  
Marshall Space Flight Center, Alabama 35812  
and  
Auburn University  
Auburn, Alabama

## TABLE OF CONTENTS

	Page
PREFACE . . . . .	1
RHEOLOGY . . . . .	3 ✓
REFERENCES . . . . .	38
LOW TEMPERATURE THERMODYNAMICS . . . . .	55 ✓
REFERENCES . . . . .	66
SOME ASPECTS OF AERODYNAMIC HEATING . . . . .	73 ✓
REFERENCES . . . . .	141
THERMOPHYSICS RESEARCH . . . . .	143 ✓
ABSTRACTS OF PROGRESS REPORTS . . . . .	192
BUOYANCY EFFECTS ON THERMAL BURNOUT IN VERTICAL CHANNELS . . . . .	193 ✓✓✓
ULTRAVIOLET RADIATION DAMAGE . . . . .	194
PROBLEM AREAS IN THE COMPOSITIONAL ANALYSIS OF THE LUMAN SURFACE BASED ON MEASUREMENTS OF FAR-INFRARED SPECTRAL EMISSION OBTAINED BY REMOTE SENSING . . . . .	195
THE EFFECT OF CRATERS ON LUNAR THERMAL RADIATION . . . . .	195
THERMALLY STRATIFIED SHEAR FLOWS . . . . .	196
FREE CONVECTION HEAT TRANSFER TO AIR BETWEEN NARROW VERTICAL CHANNELS . . . . .	197
THE LAMINAR BOUNDARY LAYER WITH HYDROGEN INJECTION INCLUDING DIFFUSION DUE TO THERMAL AND CONCENTRATION GRADIENTS . . . . .	197
TWO-PHASE FLOW DURING THE FORCED CONVECTION ELECTROLYSIS OF WATER . . . . .	198

## TABLE OF CONTENTS (Concluded)

	Page
DIRECTIONAL DIMENSIONAL ANALYSIS . . . . .	199
DETERMINATION OF THE MOON'S TEMPERATURE AND THERMAL PROPERTIES FROM MICROWAVE STUDIES . . . . .	199
THE EFFECT OF VIBRATION ON CONVECTIVE HEAT TRANSFER IN ENCLOSURES . . . . .	200
REPORT ON STUDIES OF TRANSIENTS IN COMPOSITE SYSTEMS WITH SURFACES OF CONTACT . . . . .	201
EXPERIMENTAL DETERMINATION OF THE CONSTANT IN THE CORRELATION FOR NATURAL CONVECTION FROM A HORIZONTAL FLAT PLATE . . . . .	202
BI-DIRECTIONAL THERMAL AND SPECTRAL INVESTIGATIONS OF POSTULATED LUNAR MATERIALS . . . . .	204
UNSTABLE NATURAL CONVECTION FLOW IN HORIZONTAL CYLINDRICAL ANNULI . . . . .	204
STUDIES OF SOLAR RADIATION . . . . .	205
ENERGY TRANSFER THROUGH EVACUATED NON-METALLIC MATERIALS . . . . .	206
APPENDIXES . . . . .	207
APPENDIX A ORGANIZING COMMITTEE . . . . .	208
APPENDIX B PROGRAM . . . . .	209
APPENDIX C BY-LAWS OF THE SOUTHEASTERN SEMINAR OF THERMAL SCIENCES . . . . .	213
APPENDIX D ATTENDEES . . . . .	218

## LIST OF ILLUSTRATIONS

Figure	Title	Page
1.	Steady Laminar Tube Flow, Experimental Arrangement . . . . .	7
2.	Steady Laminar Tube Flow, Experimental Results . . . . .	8
3.	Tangential Annular Flow . . . . .	12
4.	Cup-And-Bob System . . . . .	15
5.	Schematic Diagram Of Experimental Equipment . . . . .	59
6.	General Solutions At 140° K . . . . .	60
7.	Schematic Diagram Of Experimental Equipment . . . . .	61
8.	Isothermal Pressure-Composition Diagram . . . . .	62
9.	Isothermal Pressure-Composition Diagram Showing Liquid Region On Expanded Scale . . . . .	63
10.	Comparison Of The Two Systems At 20.4° K . . . . .	64
11.	Comparison Of The Two Systems At 31.5° K . . . . .	65
12.	Isothermal Pressure-Composition Diagram . . . . .	68
13.	Inversion Curve Of Barotropic Phenomenon . . . . .	69
14.	Schematic Diagram Of Experimental System . . . . .	70
15.	Pressure-Temperature Diagram For Bubble-Point Liquids . . . . .	71
16.	Pressure-Composition Diagram For Liquid And Vapor Phases On The Three-Phase Surface . . . . .	72
17.	Hemisphere-Cylinder Flow Geometry . . . . .	76

## LIST OF ILLUSTRATIONS (Continued)

Figure	Title	Page
18.	Density, Pressure, Ionization And Atom And Electron Variations Through The Shock . . . . .	85
19.	The Variation Of Temperatures And Degree Of Ionization In The Shock Detachment Region . . . . .	86
20.	Mole Fraction Versus Temperature For Hydrogen . . . . .	91
21.	Equilibrium To Frozen Flow Ratios Versus Temperature . . . . .	92
22.	Average Molecular Weight Versus Temperature . . . . .	93
23.	Equilibrium Ratios Of Specific Heats Versus Temperature—Hydrogen . . . . .	94
24.	Equilibrium Speed Of Sound Versus Temperature . . . . .	95
25.	Equilibrium Ratio Of Specific Heats Versus Temperature For Air . . . . .	96
26.	Pressure Distribution Over A Hemisphere-Cylinder. . . . .	97
27.	Equivalent Nozzle Concept . . . . .	98
28.	Results Of Nozzle Flow Analysis As Applied To Blunt Body . . . . .	99
29.	Flow Properties For Blunt Body Analysis . . . . .	100
30.	$\alpha_o$ Versus $A/A^*$ In A Hypersonic Nozzle . . . . .	101
31.	$T/T_d$ Versus $A/A^*$ In A Hypersonic Nozzle. . . . .	102
32.	$U/U_d$ Versus $\rho/A^*$ In A Hypersonic Nozzle . . . . .	103
33.	"Cold Gas" Analysis—Hypersonic Tunnel Design . . . . .	104

## LIST OF ILLUSTRATIONS (Continued)

Figure	Title	Page
34.	Geometry of the Shock Wave and the Body Surface .....	105
35.	Variation of $\alpha_0$ Along the Axial Streamline .....	106
36.	Variation of $\nu/u_\infty$ Along the Axial Streamline .....	107
37.	Variation of $T/T_\infty$ Along the Axial Streamline .....	108
38.	Variation of $\rho/\rho_\infty$ Along the Axial Streamline .....	109
39.	Variation Along the Body Surface .....	110
40.	Variation of $T/T_\infty$ Along Body Surface .....	111
41.	Variation of $P/\rho U_\infty^2$ Along the Body Surface .....	122
42.	Composite Plot Of Velocity Profiles With $T_w/T_\infty = 1/3$ For An Ionized Monatomic Gas .....	123
43.	Comparison Of Frozen And Equilibrium Temperature Profiles With $T_w/T_\infty = 1/3$ , $\epsilon_w = 0$ , $\epsilon_\infty = 0.997$ , and $M_\infty = 5$ For An Ionized Monatomic Gas .....	124
44.	Composite Plot Of Temperature Profiles With $T_w/T_\infty = 1/3$ For An Ionized Monatomic Gas .....	125
45.	Variation Of Boundary Layer Displacement Thickness With Mach Number For An Ionized Monatomic Gas .....	126
46.	Variation of $\epsilon$ With Respect To $u/V_\infty$ With $T_w/T_\infty = 1/3$ , $\epsilon_w = 0$ , $\epsilon_\infty = 0.600$ , And $M_\infty = 5$ For An Ionized Monatomic Gas .....	127

## LIST OF ILLUSTRATIONS (Continued)

Figure	Title	Page
47.	Ionization Profiles With $T_w/T_\infty = 1/3$ , $\epsilon_w = 0$ , $\epsilon_\infty = 0.600$ , And $M_\infty = 5$ For An Ionized Monatomic Gas . . . . .	128
48.	Effect Of Boundary-Layer Thickness On The Distribution Of $h/h_0$ Within 2 1/2 Inches Of The Flat-Plate Center Line For A 2.8-Inch-Diameter Right Circular Cylinder; $M = 3.51$ ; $R \approx 2.90 \times 10^6$ . . . . .	129
49.	Maximum Heating—Boundary Layer-Shock Wave Interaction . . . . .	130
50.	Shock Interaction With Turbulent Boundary Layer . . . . .	131
51.	Pressure Rise Versus Mach Number — Reynolds Number Product For Lambda-Footed Shock . . . . .	132
52.	Maximum Heating Rate As A Function Of $\chi_T$ . . . . .	133
53.	Flow Separation In Viscous Corner Flow . . . . .	134
54.	Pressure Distribution In Laminar And Turbulent Separated Flow . . . . .	135
55.	Spanwise Cross Section Of Flow Around Delta Wing At $\alpha = 17.6^\circ$ . . . . .	136
56.	Oblique Shock Pressure Ratio Including Real Gas Effects . . .	137
57.	Oblique Shock Temperature Ratio Including Real Gas Effects . . . . .	138
58.	Mach Number Behind An Oblique Shock Including Real Gas Effects . . . . .	139
59.	Oblique Shock Reynolds Number Ratio Including Real Gas Effects . . . . .	140

## LIST OF ILLUSTRATIONS (Continued)

Figure	Title	Page
60.	Conical Model Used In Thermal Similitude Tests . . . . .	150
61.	Configuration C - Transient Thermal Response Of Thermocouple No. 1 . . . . .	151
62.	Configuration C - Transient Thermal Response Of Thermocouple No. 3 . . . . .	152
63.	Geometrical Representation Of The Hapke Function . . . . .	153
64.	Angular Expressions Used In The Hapke Function . . . . .	155
65.	Lunar Brightness Temperature As Function Of The Angle Of Observation For Solar Incidence Of 30° . . . . .	156
66.	Brightness Temperature Versus Observer Elevation Angle . . . . .	157
67.	Distribution Of Planetary Heat Across The Disk Of The Full Moon . . . . .	158
68.	Calculated And Measured Temperatures For Surveyor I Site . . . . .	159
69.	Infrared Radiometer . . . . .	160
70.	Lunar IR Emission Data Acquisition Using An IR Radiometer On University Of Georgia 24" Cassegranian Telescope . . . . .	161
71.	Infrared Scan Across Entire Lunar Disk During Umbral Phase Of Eclipse . . . . .	162
72.	Michelson Interferometer . . . . .	163
73.	Completely Digitized Multi-Color Photometer . . . . .	164

## LIST OF ILLUSTRATIONS (Continued)

Figure	Title	Page
74.	Filter Spectral Band Pass And Letter Designation Of Johnson System . . . . .	165
75.	Comparison Of Light Curve Of $\beta$ Persei At Orange And IR Wavelength . . . . .	166
76.	Angular Device Used For Goniometric IR Studies . . . . .	167
77.	Heat Transfer Of Underdense Materials Versus Density . . . . .	168
78.	Thermal Contact Conductance Of Al As A Function Of The Contact Pressure . . . . .	169
79.	Vacuum Chamber Used In Studies Of Possible Lunar Materials . . . . .	170
80.	Bidirectional Spectroreflectometer . . . . .	171
81.	Reflectance Of MgO Versus Angle For Illumination Angle = 0 . . . . .	172
82.	Reflectance Of MgO Versus Angle For Illumination Angle = 30° . . . . .	173
83.	Reflectance Of MgO Versus Angle For Illumination Angle = 60° . . . . .	174
84.	Spectral Reflectance Studies Of ZnO Silicone Paint . . . . .	174
85.	Closeup Of Magnets Of Electron Spin Resonance Equipment	176
86.	Electron Spin Resonance Data Acquisition Equipment Of SSL . . . . .	177
87.	Electron Spin Resonance Curve . . . . .	178

## LIST OF ILLUSTRATIONS (Concluded)

Figure	Title	Page
88.	XUV Spectrum Of The Sun From 160 to 220 Å . . . . .	179
89.	Double Dispersion Spectrograph Of NRL . . . . .	179
90.	XUV Spectrograph, NRL ATM Experiment B . . . . .	180
91.	Schmidt Image Converter Stellar Spectrograph Of NRL . . . . .	181
92.	Flight Package Of Schmidt Spectrograph (NRL) . . . . .	182
93.	Rayleigh Scattering In The Earth's Atmosphere . . . . .	183
94.	Radiometer Used For Solar Albedo And Earth Radiation . . . .	184
95.	Solar Simulator At SSL . . . . .	185
96.	Pegasus Satellite . . . . .	186
97.	Thermal Environment Sensors Flown On Pegasus . . . . .	186
98.	Portable Solar Reflectometer . . . . .	188
99.	Flight Experiment For Measuring Heat Of Fusion . . . . .	189
100.	Lab Tests Of Temperature - Time Curves For Different Rates Of Heating Per Unit Area . . . . .	190
101.	AAP Flight Experiment T-005 - Apollo Crew Compartment . .	190
102.	AAP Flight Experiment T-005 - Observation Unit . . . . .	191

## LIST OF TABLES

Table	Title	Page
I.	Several Empirical Non-Newtonian Viscosity Expressions and Their Integrated Forms For Circular-Tube Flow . . . . .	10
II.	Ellis Model Parameters For Several Aqueous Polymer Solutions As Functions Of Temperature . . . . .	11
III.	Summary Of Definition Of Material Functions . . . . .	18
IV.	Normal Shock Analysis . . . . .	78
V.	Governing Equations For Molecular H <sub>2</sub> Undergoing Reaction Processes . . . . .	81
VI.	Nozzle-Flow Analysis . . . . .	89
VII.	Governing Equations For A Reacting Gas . . . . .	115
VIII.	C <sub>f</sub> And C <sub>f<sub>o</sub></sub> Analysis . . . . .	120
IX.	Thermophysics Division Work Areas . . . . .	146

## PREFACE

The idea for a regional seminar on heat transfer and related topics is credited to Professor J. Edward Sunderland, North Carolina State University, who had both the initiative and courage to organize the first meeting of the Southeastern Seminar on Thermal Sciences in April 1965 at Georgia Tech.

The stated objectives of the conference were; "to stimulate research, provide a formal means for presenting research, help research workers in the Southeast to become better acquainted with work, colleagues, and resources in the geographical area." Professor Sunderland felt that such a seminar with a limited number of formal lectures by prominent engineers and scientists, coupled with brief progress reports on current research by people in the southeastern area, would be of interest to the participants. The National Aeronautics and Space Administration agreed and fostered the first conference with Professor Sunderland.

Dr. Herbert W. Hoffman served as the general chairman of the Second Southeastern Seminar held in Oak Ridge, Tennessee, under the sponsorship of the Oak Ridge National Laboratory. Dr. Hoffman reinforced the firm foundation established by Professor Sunderland and enlarged the seminar to include topics in mass transfer, thermodynamics, fluid mechanics, and energy conversion in addition to heat transfer. It was at this second meeting that the official name was selected. The adoption of the title "Southeastern Seminar on Thermal Sciences" indicated the participants' enthusiasm for the idea originated by Professor Sunderland.

The Third Southeastern Seminar was organized by a committee consisting of the organizing committee for the second seminar, and Mr. H. L. Atkins of the Marshall Space Flight Center. Recognizing the significance of this undertaking, MSFC volunteered to sponsor the third seminar in Huntsville, May 8-9, 1967. The organizing committee decided to maintain the format of the first two seminars and to present a proposed set of by-laws. These by-laws were accepted by the participants, again indicating the continued interest in the seminar.

This volume contains the full text of the invited lecturers and abstracts of the progress reports. The group discussions have not been included since they were informal.

The organizing committee expresses its appreciation to those who participated in the 1967 seminar and to all those who helped in the preparation of this report.

PRECEDING PAGE BLANK NOT FILMED.  
RHEOLOGY

By

R. B. Bird

University of Wisconsin  
Madison, Wisconsin

N70 - 18687

Acknowledgment

The material in this chapter and the viewpoint adopted here are the result of research done under NSF grants G-11996 and GP-1875 and under an unrestricted research grant from the Petroleum Research Fund of the American Chemical Society. In addition generous thanks are due my graduate students, both past and present, many of whose ideas have been included in this review.

Definition Of Symbols

$a_m, b_m$  = constants in general linear viscoelastic model

$\mathcal{D}/\mathcal{D}t$  = Jaumann derivative in equation (29)

$\mathcal{F}_\epsilon$  = nonlinear operator defined in equation (28)

$G$  = shear modulus

$g$  = gravitational acceleration

$h$  = height of fluid surface

$i = \sqrt{-1}$

$L$  = length of tube

$m, n$  = parameters in power law

$p$  = pressure

- $Q$  = volume flow rate  
 $\mathcal{R}_*$  = real part of  
 $R$  = radius of tube; outer radius of annulus  
 $r$  = radial coordinate  
 $t$  = time  
 $t_c$  = characteristic time of viscoelastic fluid  
 $u_i$  = component of displacement  
 $\mathbf{v}$  = velocity vector  
 $x, y, z$  = Cartesian coordinates  
 $Z(\alpha)$  = Riemann zeta function  
 $\alpha$  = dimensionless rheological parameter in Ellis model and in Spriggs model  
 $\beta$  = secondary normal stress coefficient  
 $\gamma_0$  = parameter in several rheological models  
 $\gamma$  = velocity gradient  
 $\overline{\gamma}$  = elongational velocity gradient  
 $\gamma_{ij}$  = components of velocity gradient tensor  
 $\gamma_{ij}^0$  = complex velocity gradient amplitude  
 $\epsilon$  = parameter in viscoelastic models indicating deviations from the Weissenberg hypothesis  
 $\epsilon_{ij}$  = displacement gradient tensor

- $\Theta$  = primary normal stress coefficient  
 $\eta$  = non-Newtonian viscosity  
 $\eta_0$  = zero-shear viscosity  
 $\eta_C$  = cross viscosity  
 $\eta^*$  = complex viscosity =  $\eta' - i\eta''$   
 $\eta', \eta''$  = real and imaginary parts of the complex viscosity  
 $\overline{\eta}$  = elongational viscosity  
 $\kappa$  = radius ratio of an annulus  
 $\lambda_1, \lambda_2$  = time constants in Jeffreys and Oldroyd models  
 $\lambda_M$  = time constant in Maxwell model  
 $v_i$  = component of velocity  
 $\mu$  = Newtonian viscosity  
 $\rho$  = fluid density  
 $\tau$  = shear stress tensor  
 $\tau_{ij}$  = components of shear stress tensor  
 $\tau_R$  = shear stress at the wall of a circular tube  
 $\tau_{1/2}$  = Ellis model parameter  
 $\tau_{ij}^0$  = complex shear stress amplitude  
 $\Omega$  = angular velocity  
 $\omega$  = frequency  
 $\omega_{ij}$  = vorticity tensor components  
 $\dagger$  = transpose of a tensor or dyadic product

## Introduction

The engineer is familiar with the momentum flux tensor

$$\tau = -\mu (\nabla \vec{V} + (\nabla \vec{V})^T) + (2/3\mu - K) (\nabla \cdot \vec{V}) \delta$$

which describes the mechanical behavior of fluids which are "Newtonian." This expression is inappropriate for polymers, polymer solutions, and considerable effort has been expended in the past two decades to develop suitable substitutes for the above expression for these structurally complex materials. To date not enough has been done to provide a complete fluid dynamical description of polymers, but some of the recent results can now be put into a form suitable for industrial applications. The purpose of this presentation is to give a status report, emphasizing those facets of the subject which seem to have potential use by engineers. Additional material on theory and applications can be found in recent publications [1, 2, 3, 4].

We begin by discussing three experiments<sup>1</sup> that represent three classes of mechanical testing which have been performed to elucidate polymeric dynamical behavior. We see how each of these experiments has led to models capable of describing the fluid behavior in situations similar to the original experiment. Then we show how these experiments have gradually led to the evolution of three methods of attacking polymer-flow problems: (1) an empirical approach, based on the use of constants obtained from viscosity curves combined with some experimental data; (2) a model-building approach in which one attempts to generate models capable of describing a wide variety of dynamical responses, and (3) a model-building approach in which molecular-theory results are embedded in order to minimize the number of constants needed.

Throughout we shall restrict ourselves to incompressible fluids and isothermal conditions, so that the equations of change are:

$$\text{Continuity:} \quad 0 = (\nabla \cdot v) \quad (1)$$

$$\text{Motion:} \quad \frac{\partial}{\partial t} \rho \vec{v} = -[\nabla \cdot \rho \vec{v} \vec{v}] - \nabla \rho - [\nabla \cdot \tau] + \rho \vec{g} \quad (2)$$

---

1. Bird, R. B., Lightfoot, E. N., and Stewart, W. E., Selected Topics in Transport Phenomena (1965).

We shall have occasion also to refer to the Newtonian fluid, for which the momentum flux is given here, appropriately simplified for the incompressible fluid

$$\tau = -\mu [\nabla \vec{v} + (\nabla \vec{v})^{\dagger}] = -\mu \gamma \quad (3)$$

which serves to define the  $\gamma$  tensor as the symmetrized combination of velocity gradients. We shall also have occasion to refer to the incompressible Hookean solid, for which [5]

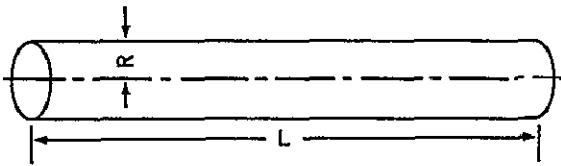
$$\tau = -G[\nabla \vec{u} + (\nabla \vec{u})^{\dagger}] = -G\epsilon \quad (4)^2$$

in which  $u$  is the displacement vector and  $\epsilon$  is the symmetrical combination of displacement gradients. Equations (1-4) summarize the starting equations for classical fluid dynamics and classical elasticity for materials which undergo no volume change on deformation.

## Experiment I: Steady Laminar Tube Flow

The first experiment we consider is an example of a viscometric experiment in which one considers shear stresses in steady flow.

We imagine a horizontal tube (Fig. 1) of length  $L$  and internal radius  $R$ .



One measures the volume rate of flow  $Q$  resulting from an impressed pressure difference  $\Delta p$ . For Newtonian fluids (N) a linear relationship is found experimentally between  $Q$  and  $\Delta p$ , but for polymer solutions (P) a distinctly nonlinear relation is found (Fig. 2).

FIGURE 1. STEADY LAMINAR TUBE FLOW, EXPERIMENTAL ARRANGEMENT

At low values of  $\Delta p$  the relation is linear and the fluid behaves as though it had a large viscosity. As  $\Delta p$  is increased, the volume rate of flow increases faster than would be anticipated for

---

2. valid only for small deformations

a Newtonian fluid—that is, the "viscosity" appears to be decreasing. Finally, at very high  $\Delta p$  there is some evidence that a linear relationship is again approached, but with a substantially lower viscosity; it should be remarked that this limiting linear behavior is extremely difficult to attain and that at such high flow rates viscous heating effects may obscure the phenomenon. An important point is that if one plots  $\log Q$  versus  $\log \Delta p$ , there is for many materials a large range (sometimes several decades) over which the plot is linear, with the lines for various materials having different slopes [6, 7].

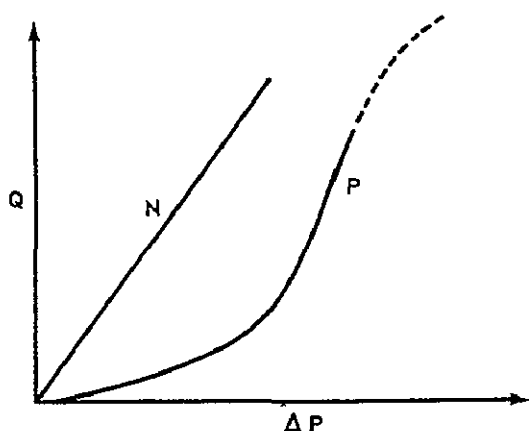


FIGURE 2. STEADY LAMINAR TUBE FLOW, EXPERIMENTAL RESULTS

It is quite clear that in this simple experiment Newtonian fluids and polymeric materials behave quite differently. We now ask how the Newtonian behavior can be described and whether or not some simple model can be evolved to describe the polymer behavior.

Newtonian Fluids. For any fluid, equation (2) may be integrated to give  $\tau_{rz} = \Delta p r / 2L$ , which shows that the

shear stress varies linearly with  $r$ . For Newtonian fluids one inserts into this expression the relation

$$\tau_{rz} = -\mu (dv_z/dr), \text{ which is just}$$

equation (3) written appropriately for the geometry under consideration. The resulting differential equation for  $v_z(r)$  can be integrated to obtain the usual parabolic velocity distribution, and this in turn may be integrated over the tube cross section to give the well-known result of Hagen and Poiseuille.

$$Q = \frac{\pi \Delta p R^4}{8 \mu L} \quad (5)$$

which has been adequately verified experimentally

Polymeric Materials. For polymers one has to try to guess a relation to take the place of  $\tau_{rz} = -\mu (dv_z/dr)$  which when substituted into

$\tau_{rz} = \Delta p r / 2L$  will yield a velocity profile that in turn will give a reasonable  $Q$  versus  $\Delta p$  curve. Of the many empirical relationships suggested, a few

that have been proposed for polymer solutions are given in Table I along with the corresponding  $Q$  versus  $\Delta p$  relationships for circular-tube flow.

To date, the most widely used model has been the power law, which describes the commonly observed linear  $\log Q$  versus  $\log \Delta p$  plots. Because of the ability of the model to describe this behavior and because of the simplicity of the model, it has been widely used, often quite successfully. Nonetheless, the model suffers from a number of defects which are worth noting. (1) Since  $n$  is usually less than unity, the power law predicts infinite viscosity at vanishingly small velocity gradients, (2) the parameter  $m$  has awkward dimensions which depend on  $n$ , (3) it is not possible to form a "characteristic time" with the model constants—a point that will be discussed in detail later—and (4) it has been demonstrated experimentally that if one determines  $m$  and  $n$  from a tube-flow experiment, one cannot use the same  $m$  and  $n$  for other geometries, such as an annulus [1], a packed column [8], etc.

Because of the linear  $\log Q$  versus  $\log \Delta p$  plots, it is natural to try to make minor improvements on the power law in order to preserve its good features and to remove its faults. Three such models have been listed in Table I—the truncated power law<sup>1</sup>, the Ellis model [6], and the Sisko model [9]. These three models represent different ways of combining the power law and Newton's law of viscosity. We also list the Eyring [10] model, inasmuch as this expression has been derived from a simple molecular picture. Numerous other models have been suggested, but we do not list them here [6, 8, 11, 12, 13]. Probably more information is available on the Ellis model than for any other three-constant model [14]. Some sample values of the Ellis model parameters are given in Table II [15].

The models in Table I have been written specifically for a flow situation with a velocity profile  $v_z = v_z(r)$ . For complicated flow patterns one can generalize these expressions by writing them all in the "generalized Newtonian model" form [16]:

$$\tau_{ij} = -\eta \gamma_{ij} \quad (6)$$

analogously to equation (3), in which  $\eta$  is a function of the  $\tau_{ij}$  or the  $\gamma_{ij}$ .

---

1. Spriggs, T. W., Private Communications

But since  $\eta$  is a scalar, it must depend on either of these two tensors in such a way that only certain combinations of tensor components appear which are scalars. Now we know that a scalar can be constructed from a vector  $v$  by forming the dot product of the vector with itself to get  $(v \cdot v) = v^2$ , which is a scalar.

TABLE I. SEVERAL EMPIRICAL NON-NEWTONIAN VISCOSITY EXPRESSIONS AND THEIR INTEGRATED FORMS FOR CIRCULAR-TUBE FLOW.

$$[\tau_R = \Delta p R / 2L = \text{Wall Shear Stress}]$$

Model	Shear-stress expression	Volume rate of flow	Characteristic time
Power law ( $m, n$ )	$\tau_{rz} = -m \left  \frac{dv_z}{dr} \right ^{n-1} \frac{dv_z}{dr}$	$Q = \frac{\pi R^3}{(1/n) + 3} \left( \frac{\tau_R}{m} \right)^{\frac{1}{n}}$	None
Truncated power law ( $\eta_0, \gamma_0, n$ )	$\tau_{rz} = -\eta_0 \frac{dv_z}{dr} \begin{pmatrix} \left  \frac{dv_z}{dr} \right  \leq \gamma_0 \\ \left  \frac{dv_z}{dr} \right  \geq \gamma_0 \end{pmatrix}$ $\tau_{rz} = -\eta_0 \left  \frac{dv_z}{dr} \right ^{n-1} \frac{dv_z}{dr} \begin{pmatrix} \left  \frac{dv_z}{dr} \right  \leq \gamma_0 \\ \left  \frac{dv_z}{dr} \right  \geq \gamma_0 \end{pmatrix}$	$Q = \frac{\pi R^3}{\left(\frac{1}{n}\right) + 3} \left( \frac{\tau_R}{\eta_0} \right) \left( \frac{R}{r_0} \right)^{\frac{1}{n} - 1} \left[ 1 + \frac{1}{4} \left( \frac{1}{n} - 1 \right) \left( \frac{r_0}{R} \right)^{\frac{1}{n} + 3} \right]$ where $r_0 = \eta_0 R \gamma_0 / \tau_R$	$\frac{1}{r_0}$
Sisko model ( $\eta_0, \gamma_0, n$ )	$\tau_{rz} = -\eta_0 \left( 1 + \left  \frac{1}{\gamma_0} \frac{dv_z}{dr} \right ^{n-1} \right) \frac{dv_z}{dr}$ where $dv_z/dr < \gamma_0$	$Q = \frac{\pi R^3 \eta_0 \gamma_0^4}{4 \tau_R^3} \left\{ 1 + 4 \left[ \frac{(n+2)}{(n+3)} \vee + \frac{(2n+1)}{(2n+2)} \vee^2 + \frac{(n)}{(3n+1)} \vee^3 \right] \right\}$ where $\vee = (\gamma_R / \gamma_0)^{n-1}$ and $\gamma_R$ is given by $\tau_R = \eta_0 \left( 1 + (\gamma_R / \gamma_0)^{n-1} \right) \gamma_R$	$\frac{1}{\gamma_0}$
Films model ( $\eta_0, \tau_1, \alpha$ )	$\frac{dv_z}{dr} = -\frac{1}{\eta_0} \left( 1 + \left  \frac{\tau_{rz}}{\tau_1} \right ^{\alpha-1} \right) \tau_{rz}$	$Q = \frac{\pi R^3 \tau_1}{4 \eta_0} \left[ 1 + \frac{4}{\alpha+3} \left( \frac{\tau_R}{\tau_1} \right)^{\alpha-1} \right]$	$\eta_0 / \tau_1$
Filling ( $\tau_0, t_0$ )	$\frac{dv_z}{dr} = -\frac{1}{t_0} \sinh \frac{\tau_{rz}}{\tau_0}$	$Q = \frac{2 \pi R^3}{t_0} \left( \frac{\tau_0}{\tau_R} \right) \left\{ \frac{1}{2} \cosh \left( \frac{\tau_R}{\tau_0} \right) - \left( \frac{\tau_0}{\tau_R} \right)^2 \vee \left[ \left( \frac{\tau_R}{\tau_0} \right) \sinh \left( \frac{\tau_R}{\tau_0} \right) - \cosh \left( \frac{\tau_R}{\tau_0} \right) + 1 \right] \right\}$	$t_0$

Similarly, one way to construct a scalar from the tensor  $\gamma$  is to form the double-dot product of the tensor with itself to get  $(\gamma : \gamma) = \sum_i \sum_j \gamma_{ij}^2$ , which is a scalar.

Hence one possible way to generalize models such as those in Table I is by writing, for example,

Power law:

$$\eta = m \left| \sqrt{\frac{1}{2} (\gamma : \gamma)} \right|^{n-1} \quad (7)$$

Ellis model:

$$\frac{1}{\eta} = \frac{1}{\eta_0} \left[ 1 + \frac{\sqrt{\frac{1}{2}(\tau : \tau)}^{\alpha-1}}{\tau_{\frac{1}{2}}} \right] \quad (8)$$

We thus ensure that  $\eta$  will be a scalar and that the models will behave properly under coordinate transformation. As only limited experimental tests of this mode of generalization have been made, however, it should be used with caution.

In conclusion, experiments such as laminar tube flow have led to the generalized Newtonian model in equation (6) and to the definition of a non-Newtonian viscosity  $\eta$ , which is a function of the shear stress or the shear rate. Actually, the tube-flow experiment has today generally been replaced by the cone-and-plate viscometer, which gives  $\tau_{ij}$  versus  $\gamma_{ij}$  directly, thereby removing the need for rather tedious data analysis. Finally, it should be emphasized that these non-Newtonian effects can be quite large, with the viscosity decreasing by a factor of  $10^2$  to  $10^3$  as the shear stress is increased.

TABLE II. ELLIS MODEL PARAMETERS FOR SEVERAL AQUEOUS POLYMER SOLUTIONS AS FUNCTIONS OF TEMPERATURE, [15]

Solution	Temperature, °C.	$\eta_0$ poise	$\tau_{\frac{1}{2}}$ dyne cm. <sup>-2</sup>	$\alpha$	Range of $\dot{\gamma}$ sec. <sup>-1</sup>	Deviation, %	
						Max.	Avg.
1.5% Poly- ethylene oxide	20	2.2	49.3	2.073	100-1700	1.6	0.6
	30	0.58	148	2.165	100-8000	7.8	1.7
	40	0.40	165	2.268	200-3000	5.1	1.0
	50	0.235	214	2.306	200-6000	6.8	1.7
	60	0.180	200	2.206	400-7000	7.3	1.9
2.0% Hy- droxyethyl- cellulose	20	198.5	1140	4.454	10-900	8.5	2.9
	30	142.0	936	4.068	10-1000	10.5	3.3
	40	104.0	846	3.920	10-1500	10.3	3.6
	50	71.0	760	3.662	10-1000	10.6	4.8
	60	39.3	833	3.699	20, 1000	6.8	2.2
0.5% Hy- droxyethyl- cellulose	20	81.1	30.3	2.438	10-3000	10.2	3.3
	30	50.0	38.0	2.442	15-5000	8.7	1.5
	40	33.0	32.8	2.350	15-5000	9.7	2.0
	50	21.5	41.6	2.486	30-1000	5.8	2.1
	60	12.3	47.5	2.408	30-2000	5.8	1.4

## Experiment II: Shape Of Free Surface In Tangential Annular Flow

The next experiment we consider is observing the shape of the surface of a liquid contained in the annular space between two cylinders, of which the inner is rotating with a constant velocity (Fig. 3). The Newtonian fluid tends to pile up at the outer (stationary) wall because of the centrifugal force. The polymeric materials, on the other hand, do just the reverse—they tend to move toward the inner (rotating) shaft and to climb up it; this is called the Weissenberg effect [5, 17]. Here again is a striking difference between the behavior of Newtonian and polymeric materials. As in the previous experiment, we show how the Newtonian behavior can be explained; then we try to understand what modifications in the equations are suggested by the strange behavior of the polymeric substances.

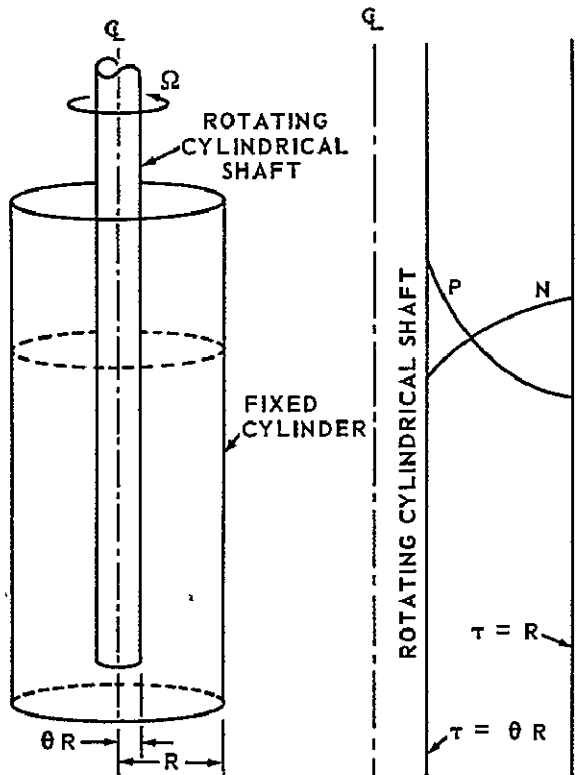


FIGURE 3. TANGENTIAL ANNULAR  
FLOW

Newtonian Fluids. In the system under consideration the following postulates seem reasonable:  $v_\theta = v_\theta(r)$ ,  $v_r = 0$ ,  $v_z = 0$ ,  $p = p(r, z)$ . Then the equations of motion for the Newtonian fluid [equations (1, 2, 3)] become in curvilinear coordinates

$$\rho \frac{v_\theta^2}{r} = \frac{\partial p}{\partial r} \quad (9)$$

$$0 = \mu \frac{d}{dr} \left[ \frac{1}{r} \frac{d}{dr} (rv_\theta) \right] \quad (10)$$

$$0 = -\frac{\partial p}{\partial z} - \rho g \quad (11)$$

These equations can be solved for the velocity and pressure distributions. The shape of the free surface is just the locus of all points  $r, z$  for which  $p(r, z) = p_0$ , the atmospheric pressure.

This shape is given by

$$h(R) - h(r) = \frac{1}{2g} \left( \frac{\kappa^2 R \Omega}{1 - \kappa^2} \right)^2 \left[ \left( \frac{R}{r} \right)^2 - \left( \frac{r}{R} \right)^2 - 4 \ln \frac{R}{r} \right] \quad (12)$$

in which  $h$  is the height of the surface and  $\Omega$  is the angular velocity of rotation of the rotating shaft.

Polymeric Materials. The Weissenberg effect for polymeric materials cannot be explained by the generalized Newtonian models described earlier. It seems to be generally agreed now that the origin of the effect is in the "normal stresses"  $\tau_{tt}$ ,  $\tau_{\theta\theta}$ ,  $\tau_{zz}$ . These stresses are zero for the Newtonian fluid and they do not appear anywhere in the equations of motion above. If we now postulate that for some reason these normal stresses do not vanish for structurally complicated fluids, then the equations of motion contain a few extra terms and the result of the final expression for the shape of the fluid surface which is only approximate is

$$h(R) - h(r) = \frac{1}{g} \int_r^R \frac{v_\theta^2}{r} dr - \frac{1}{\rho g} \int_r^R \left( \frac{\tau_{rr} - \tau_{\theta\theta}}{r} \right) dr -$$

$$\frac{1}{\rho g} [\tau_{rr}(R) - \tau_{rr}(r)] \quad (13)$$

The dotted underlined terms, which did not appear in equation (12), do indeed contribute to the shape of the surface.

This analysis suggests that equation (6) should be generalized in some way so as to cause  $\tau_{rr}$ ,  $\tau_{\theta\theta}$ , and  $\tau_{zz}$  to be nonzero. About fifteen years ago the following suggestion was made almost simultaneously by several investigators:

$$\tau_{ij} = -\eta \gamma_{ij} - \frac{1}{2} \eta_c \left[ \sum_k \gamma_{ik} \gamma_{kj} - \frac{1}{3} \left( \sum_k \sum_l \gamma_{kl} \gamma_{lk} \right) \delta_{ij} \right] \quad (14)$$

which is the Reiner-Rivlin-Prager equation [18, 19, 20]; here  $\eta$  is the non-Newtonian viscosity and  $\eta_c$  is the cross viscosity, and both are shear-dependent. (Actually they are functions of the invariants of the  $\gamma$ -tensor.)

When one uses this equation to compute the normal stresses in equation (13), he finds that  $\tau_{rr} = \tau_{\theta\theta}$  and furthermore that  $\tau_{rr}(R) - \tau_{rr}(r)$  is positive if  $\eta_c$  is positive. This is in agreement with the fact that the fluid tends to climb up the rotating shaft.

This apparent success of the model gave considerable impetus to its further study. It appeared, however, that in rotating-annulus systems of this type,  $\tau_{rr} \neq \tau_{\theta\theta}$  but that perhaps  $\tau_{rr} = \tau_{zz}$  (the Weissenberg hypothesis) or at least approximately so [21].

It is possible to modify the Reiner-Rivlin-Prager model in order to avoid the above objection. One very tentative suggestion is the Bird-Williams-Spriggs equation [22]:<sup>1</sup>

$$\begin{aligned} \tau_{ij} = & -\eta\gamma_{ij} - \frac{1}{2}(\Theta + 2\beta) \times [\sum_k \gamma_{ik} \gamma_{kj} - \frac{1}{3}(\sum_k \sum_l \gamma_{kl} \gamma_{lk}) \delta_{ij}] \\ & + \frac{1}{2} \Theta (\mathcal{D} \gamma_{ij} / \mathcal{D} t) \end{aligned} \quad (15)$$

Here  $\mathcal{D}/\mathcal{D}t$  is the Jaumann derivative [23] defined in equation (29). It represents a time derivative in a coordinate system moving with the fluid and rotating with it. In equation (15) there are two shear-dependent normal stress functions  $\Theta$  and  $\beta$ ; setting  $\beta = 0$  corresponds to the Weissenberg hypothesis that in simple shear flow the normal stresses perpendicular to the direction of flow are equal.

The experiment described above was one of the first normal stress experiments performed and illustrates strikingly the need for formulating rheological equations to describe normal stresses properly. It is not, however, a suitable experiment for measuring  $\Theta$ . The current methods of precise measurement of these normal stress phenomena have been described elsewhere [5, 22, 24].<sup>2</sup>

- 
1. Apparently suggested earlier by Ericksen, J. L., in *Viscoelasticity*, Academic Press, 1960, (see eq. 2.12). This gives the same results for viscometric flow as the simple fluid model (see 2).
  2. Coleman, B., Markovitz, H., and Noll, W., *Viscometric Flows of Non-Newtonian Fluids*, Springer, 1960

## Experiment III: Transient Response in a Cup-Bob System

We now consider the system in Figure 4. A fluid is placed in a cup, in the middle of which a solid cylindrical bob is suspended by a torsion wire. The block diagram (Fig. 4) shows the experimental arrangement with input oscillation to cup. The curve (Fig. 4) shows the amplitude ratio for Newtonian fluids (N) and polymeric materials (P). One causes the cup to oscillate with an amplitude  $A_c$  (about 1 degree) and a

frequency  $\omega$ . After the initial transients have been damped out, one can measure the amplitude of oscillation of the bob  $A_b$  and the phase difference  $\phi$  between the input and output oscillations, both as functions of the frequency. Here we consider just the behavior of the amplitude ratio  $A_b/A_c$ .

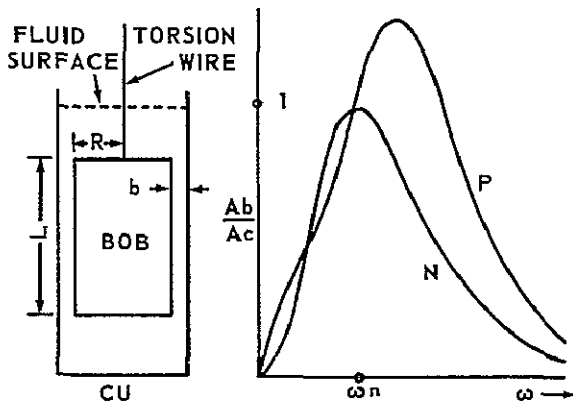


FIGURE 4 CUP-AND-BOB SYSTEM

For Newtonian fluid  $A_b/A_c$  is zero at  $\omega = 0$  and  $\omega = \infty$  and goes through a maximum at the natural frequency  $\omega_n$  of the torsion pendulum.

For polymeric materials, on the other hand, the maximum—greater than unity—occurs at frequencies higher than the natural frequency of the torsion pendulum. Here again we have an example of a striking difference in the dynamical behavior of Newtonian and polymeric materials. Let us now see how these two kinds of behavior can be described analytically.

Newtonian Fluids. The response curve for the Newtonian fluid [25] can be derived from the set of coupled equations describing the motion of the pendulum and the motion of the fluid. We do not go through the details here but only state the final result for the special case that the clearance  $b$  between the torsion pendulum and the cup is small:

$$\frac{A_c}{A_b} = \sqrt{\left\{ 1 + \frac{1}{M^2} \left[ -\frac{\omega^2}{24} + \frac{(1-\omega^2)}{6A} \right] \right\}^2 + \left\{ \frac{1}{M} \left[ \frac{\omega}{2} - \frac{(1-\omega^2)}{A\omega} \right] \right\}^2} \quad (16)$$

where  $M = (\nu/b^2) \sqrt{I/k}$  and  $A = 2\pi R^3 L \rho b/I$ . Here  $\nu$  is the kinematic viscosity,  $I$  the moment of inertia of the bob,  $k$  the torsional spring constant of the wire,  $R$  the radius of the bob, and  $L$  its length.

Polymeric Materials. For polymers [25, 26, 27] the explanation of the large amplitude ratio is sought in the elastic behavior of the fluid. The simplest possible suggestion is to combine Newton's law of viscosity with Hooke's law of elasticity. If one multiplies Hooke's law in equation (4) by  $\mu/G$  and differentiates with respect to time, then adds the result to Newton's law of viscosity, he obtains (using  $\partial \epsilon_{ij}/\partial t = \gamma_{ij}$ )

$$\tau_{ij} + \lambda_M \frac{\partial \tau_{ij}}{\partial t} = -\eta_0 \gamma_{ij} \quad (17)$$

in which  $\lambda_M = \mu/G$  and  $\eta_0 = 2\mu$ . This simple superposition is called the Maxwell model [5]. Further differentiation and combining gives

$$\tau_{ij} + \lambda_1 \frac{\partial \tau_{ij}}{\partial t} = -\eta_0 \left( \gamma_{ij} + \lambda_2 \frac{\partial \gamma_{ij}}{\partial t} \right) \quad (18)$$

which is called the Jeffreys model. Clearly the process can be continued, and one obtains finally

$$\left( 1 + \sum_{m=1}^{\infty} a_m \frac{\partial^m}{\partial t^m} \right) \tau_{ij} = \eta_0 \left( 1 + \sum_{m=1}^{\infty} b_m \frac{\partial^m}{\partial t^m} \right) \gamma_{ij} \quad (19)$$

which is called the general linear viscoelastic model.

Since equation (3) is limited to very small displacements, equation (4) must be similarly restricted. If we confine our interest to sinusoidal disturbances—as in the experiment under consideration—we can postulate that the shear stress and the velocity gradient will be undergoing sinusoidal oscillations:

$$\tau_{ij} = \mathcal{R}_e \{ \tau_{ij}^0 e^{i\omega t} \} \quad (20)$$

$$\gamma_{ij} = \mathcal{R}_e \{ \gamma_{ij}^0 e^{i\omega t} \} \quad (21)$$

in which  $\tau_{ij}^0$  and  $\gamma_{ij}^0$  are complex amplitudes. Substitution of these expressions into equation (19) gives

$$\tau_{ij}^0 = -\eta^* \gamma_{ij}^0 \quad (22)$$

where

$$\eta^* = \eta' - i\eta'' = \eta_0 \left[ \frac{1 + b_1(i\omega) + b_2(i\omega)^2 + \dots}{1 + a_1(i\omega) + a_2(i\omega)^2 + \dots} \right] \quad (23)$$

is the complex viscosity. Clearly the real and imaginary parts  $\eta'$  and  $\eta''$  are functions of  $\omega$ . The quantity  $\eta'$  contains information about the viscous response, whereas  $\eta''$  contains information about the elastic response.

One can now go back to the equations of motion and insert equation (19) [or one of its special cases such as equation (18) or (17)]. These equations can be solved and do indeed predict the kind of behavior which polymeric systems indicate in Figure 4 [25]. It is further possible to analyze the amplitude ratio and phase-shift data to get a tabulation of  $\eta'$  and  $\eta''$  for a polymeric material. A wide variety of experimental arrangements have been used by the polymer physicists, and these have been described extensively in Ferry's treatise [28].

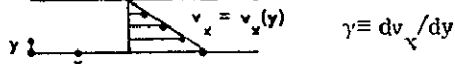
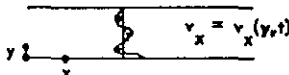
## Summary Of The Experiments—The Material Functions

We have seen how the above-described three experiments [29, 30, 31, 32] have led to the definition of various measurable material functions. The tube-flow experiment suggests the definition of a non-Newtonian viscosity  $\eta(\dot{\gamma})$ . The study of the Weissenberg effects has led to the definition of a primary normal stress coefficient  $\Theta(\dot{\gamma})$  and a secondary normal stress coefficient  $\beta(\dot{\gamma})$ . The oscillatory flow experiments have suggested the definition of the complex viscosity  $\eta^*$ , with its real and imaginary contributions  $\eta'(\omega)$  and  $\eta''(\omega)$ . A further experiment, which we have not described here, deals with

the study of the normal stresses in oscillatory small amplitude motion; this leads to the definition of still more material functions [32].<sup>1</sup>

Since all the experiments we have discussed have involved rather complicated geometrical arrangements and curvilinear coordinates, it is perhaps advisable to summarize the definition of these material functions at this point in terms of flow between two infinite flat plates. Such a summary is given in Table III [31, 33].

TABLE III. SUMMARY OF DEFINITION OF MATERIAL FUNCTIONS

<p>1. Steady shear flow</p>  <p><math>\gamma \equiv dv_x/dy</math></p> <p>a Viscosity</p> $\tau_{yx} = \eta \dot{\gamma}$ <p>b Normal stress functions</p> $\tau_{xx} - \tau_{yy} = -\Theta \dot{\gamma}^2$ $\tau_{yy} - \tau_{zz} = -\beta \dot{\gamma}^2$	<p>2. Small amplitude sinusoidal oscillations</p>  $\gamma = \Re \{ \dot{\gamma}^0 e^{i\omega t} \}$ $\tau_{yx} = \Re \{ \tau_{yx}^0 e^{i\omega t} \}$ $\tau_{ii} = \Re \{ d_i^0 + \tau_{ii}^0 e^{2i\omega t} \}$ <p>a Complex viscosity</p> $\tau_{yx}^0 = -\eta^* \dot{\gamma}^0, \quad \eta^* = \eta' - i\eta'' \quad i = x, y, z$ <p>b Complex normal stress coefficients</p> $\tau_{xx}^0 - \tau_{yy}^0 = -\Theta^* (\dot{\gamma}^0)^2, \quad \Theta^* = \Theta' - i\Theta''$ $\tau_{yy}^0 - \tau_{zz}^0 = -\beta^* (\dot{\gamma}^0)^2, \quad \beta^* = \beta' - i\beta''$ <p>c. Normal stress displacement functions</p> $\Re \{ d_x - d_z \} = -\Theta^d  \dot{\gamma}^0 ^2$ $\Re \{ d_y - d_z \} = -\beta^d  \dot{\gamma}^0 ^2$
<p>Note For Newtonian fluids <math>\eta = \mu</math>, <math>\eta' = \mu</math>, and all others are zero.</p>	

This summary does not exhaust the possible definitions of material functions. These are, however, all the material functions needed for any viscometric flow—that is, flows in which there is only one non-zero velocity component (in, say, the  $i$  direction) which depends on one coordinate only (but not the  $i$  coordinate). Consider, as an example of a nonviscometric flow, steady elongational flow in which  $v_z = \dot{\gamma}z$ ,  $v_r = -(\frac{1}{2})\dot{\gamma}r$ ,  $v_\theta = 0$ ; this is the kind of flow which might be approximated in fiber spinning. One then defines an

1. For superposition of steady and oscillatory motions, see MacDonald, I. F., and Bird, R. B., Journal Physical Chemistry, 70, 2068-2069, 1966.

elongational viscosity by

$$p + \tau_{zz} = \bar{\eta} \bar{\gamma} \quad (24)$$

where  $\bar{\eta}$  is known to be dependent upon the elongation rate  $\bar{\gamma} = dv_z/dz$ . For a Newtonian fluid  $\bar{\eta} = 3\mu$ , sometimes called the Trouton viscosity.

Thus it is possible to measure all kinds of material functions. Many measurements of  $\eta$  are available for many materials, since all one needs is a viscometer and since this property has been recognized as useful for predicting flow in pipe lines, etc. Frequently  $\eta^*$  has been measured, since this measurement is a basic one used for some time in the analysis of polymer structure. The primary normal stress coefficient  $\Theta$  has been measured in a few laboratories, but equipment for trustworthy measurements is limited. Only several isolated attempts have been made to measure the secondary normal stress coefficient  $\beta$ , very careful experiments have to be run, and the data have to be analyzed with caution [35]. To date no experimental curves of  $\Theta^*$ ,  $\beta^*$ ,  $\Theta^d$ ,  $\beta^d$  have been presented in the literature. Also, surprisingly, it seems to be well nigh impossible to find trustworthy data on  $\bar{\eta}$  in the technical literature.

What would be highly desirable are experimental data on quite a few of these material functions for a number of polymeric systems. Such data could be useful in testing and improving the methods discussed in the next three sections.

## Method I: Use Of Non-Newtonian Viscosity Parameters

In order to describe the mechanical behavior of polymeric materials we need some relation for  $\tau$  to use in place of equation (3) for Newtonian fluids or in place of equation (4) for Hookean solids [36]. We do not know what this relation is, but perhaps we can make some statements concerning what it should contain:

a. Experimental data on  $\eta$  indicate that in the limit of zero velocity gradient  $\eta$  tends toward a limiting value  $\eta_0$ . Data on  $\eta'$  also indicate that as the frequency tends to zero,  $\eta'$  approaches the same limiting value. Hence it seems reasonable to suggest that the expression for  $\tau$  ought to contain a zero-shear viscosity  $\eta_0$ .

b. Experimental observations on polymeric materials indicate that relaxation phenomena are important. If one suddenly stops the motion of a viscoelastic material, there is a relaxation of the stresses in the system and this relaxation process can be characterized by a time. We note also that the simplest viscoelastic model—that due to Maxwell in equation (17)—contains a characteristic time. In addition, the Eyring rate theory of viscosity gives an expression for  $\eta$  which contains a characteristic time (Table I). Hence the expression for  $\tau$  ought to contain some kind of characteristic time  $t_c$ .

c. Experimental observations on  $\log Q$  versus  $\log \Delta p$  for polymer flow in tubes give straight lines over a wide range of variables. The slopes of these lines are dimensionless quantities which cannot be formed from a viscosity and a time. Hence one might conclude that  $\tau$  ought to contain at least one additional dimensionless parameter  $\alpha$ .

The above arguments lead to the conclusion that

$$\tau = \tau(\gamma; \eta_0, t_c, \alpha) \quad (25)$$

where  $\tau$  is a function that we do not know. All we suspect is that it ought to contain certain parameters.

Now if the function  $\tau$  were known, then we could presumably calculate the various material functions with it to get

$$\eta = \eta(\gamma; \eta_0, t_c, \alpha) \quad (26)$$

$$\Theta = \Theta(\gamma; \eta_0, t_c, \alpha)$$

If we were to fit, say, data on  $\eta(\gamma)$  with a curve containing a zero-shear viscosity, a characteristic time, and some other parameter  $\alpha$ , we should then have a set of three parameters to describe the fluid. These parameters, although obtained from the measurement of just one material function, should nonetheless contain information which is also contained in the  $\tau$  equation. - Once these parameters have been obtained, they can be used in several ways:

1. They can be used in the function  $\eta(\gamma)$  to describe viscometric flows [1, 2, 37].<sup>1</sup>

2. They can be used for dimensional analysis of complex flow systems [12, 15, 38, 39, 40]

3. The characteristic time can be used to delineate various regions of behavior, by comparing it with the characteristic times of the macroscopic system [41].

4. The zero shear viscosity can be used for getting asymptotic solutions for flow problems analytically to tie in with the correlations in step 2 [12].

5. Attempts might be made to correlate  $\eta_0$ ,  $t_c$ , and  $\alpha$  with concentration, molecular weight, chain length, etc., in an effort to interconnect the mechanical and physicochemical properties.

We see thus that the empirical  $\eta(\gamma)$  functions discussed earlier may in fact have considerably wider utility than might at first be expected—at least those three parameter functions which have a characteristic time and a lower limiting viscosity.

A rather complete summary of results obtained by this method is given elsewhere [36]. We just mention the experiments which have been performed and the models which were used in the analysis:

a. Correlation of drag coefficients for flow around spheres—Ellis model [40].

b. Correlation of friction factors for turbulent flow in tubes—meter model, Ellis model [38].

c. Interrelation of tube flow and annular flow data—Ellis model [1, 37].<sup>1</sup>

d. Correlation of wall corrections for falling sphere viscometer—Ellis model [15].

e. Correlation of friction factors for packed bed flows—Ellis model [39].

---

1. Ashare, E., and R. B. Bird, to be published.

f. Correlation of pressure drops through converging sections—Sutterby model [12].

g. Simulation of unsteady state flow in a manometer—Sisko model [41].

The last experiment demonstrated that it is probably possible to describe some unsteady state motions using only information on  $\eta(\dot{\gamma})$ , provided that the characteristic time of the fluid is considerably less than the characteristic time of the system (in this case, the time for one manometer oscillation).

## Method II: Use Of Viscoelastic Models

A second approach to polymer fluid dynamics [31,42] is to try to guess the unknown function in equation (25). Trying to guess a complicated functional relation which will give the proper limiting behavior for all the experimentally known material functions is no easy task. We will make no attempt to reproduce all the arguments which have led to the kinds of functions which are now regarded as useful viscoelastic functions. The discussion here is influenced primarily by the trail-blazing papers of Oldroyd [43,44]. We discuss a special case of one of his models—a four-constant Oldroyd model which has considerable instructional value, since it displays all of the effects we have discussed.

Let us begin with equation (18)—the Jeffreys linear viscoelastic model—which is known to describe certain low-frequency oscillatory behavior of some polymers fairly well. In order to describe nonlinear behavior, we replace the linear time operator  $\partial/\partial t$  by a nonlinear operator  $\mathcal{F}_\epsilon$ :

$$\tau_{ij} + \lambda_1 \mathcal{F}_\epsilon \tau_{ij} = -\eta_0 (\dot{\gamma}_{ij} + \lambda_2 \mathcal{F}_\epsilon \dot{\gamma}_{ij}) \quad (27)$$

in which  $1 > (\lambda_2/\lambda_1) > \frac{1}{9}$ , and the operator  $\mathcal{F}_\epsilon$  is given by reference [33]

$$\mathfrak{F}_\epsilon \tau_{ij} = \frac{\mathcal{D}}{\mathcal{D}t} \tau_{ij} - (1 + \epsilon) \left[ \frac{1}{2} (\sum_k \tau_{ik} \gamma_{kj} + \sum \tau_{jk} \gamma_{ki}) - \frac{1}{3} \left( \sum_m \sum_n \tau_{mn} \gamma_{nm} \right) \delta_{ij} \right] \quad (28)^1$$

Here the Jaumann derivative (P3) is .

$$\frac{\mathcal{D}}{\mathcal{D}t} \tau_{ij} = \frac{\partial}{\partial t} \tau_{ij} + \sum_k \nu_k \frac{\partial}{\partial x_k} \tau_{ij} + \frac{1}{2} (\sum_k \omega_{ik} \tau_{kj} - \sum_k \tau_{ik} \omega_{kj}) \quad (29)$$

The tensor  $\omega_{ij} = (\partial \nu_j / \partial x_i - \partial \nu_i / \partial x_j)$  is the vorticity tensor and is a measure of the local rate of rotation of the fluid. The Jaumann derivative,  $\mathcal{D}/\mathcal{D}t$ , describes the change in  $\tau_{ij}$  as the observer floats along with the fluid and rotates

with it. Hence, to get equation (27), one first replaces  $\partial/\partial t$  by  $\mathcal{D}/\mathcal{D}t$  in the Jeffreys model in order that the latter describe the viscoelastic behavior locally, with the rotation and translation separated off. Then one adds some nonlinear terms reminiscent of those in the Reiner-Rivlin-Prager model—such as  $\sum \gamma_{ik} \gamma_{kj}$  and  $\sum \tau_{ik} \gamma_{kj}$ . Finally, two other nonlinear terms are included

$(\frac{1}{3} \sum \sum \tau_{mn} \gamma_{nm} \delta_{ij})$  and  $(\frac{1}{3} \sum \sum \gamma_{mn} \gamma_{nm} \delta_{ij})$  in order to make  $\tau_{ij}$  traceless.

This results in equation (27), which has been constructed so as to incorporate deviations from the Weissenberg hypothesis (that  $\beta = 0$ ) by inclusion of the small parameter  $\epsilon$ .

---

1. The models discussed earlier assume that the stress tensor  $\tau$  is symmetric. One may allow for deviations from symmetry by introducing an additional term on the right side of equation (28) of the form

$$- \xi \left[ \sum_k \gamma_{ik} \tau_{kj} - \left( \frac{1}{3} \sum_m \sum_n \tau_{mn} \gamma_{nm} \right) \delta_{ij} \right]$$

in which  $\xi$  is an additional constant which indicates the extent to which  $\tau$  is nonsymmetrical. Introduction of this extra term contributes to deviations from the Weissenberg hypothesis; furthermore, it produces deviations from the "analogies" [see equations (31, 32, 34, 35) and the concomitant discussion] between the steady shear-flow and oscillatory shear-flow properties. To date no experiments have been performed to determine whether or not  $\tau$  is symmetrical.

To show how equation (27) is used to obtain explicit expressions for the material functions in Table III, we consider first steady shear flow and calculate  $\eta$ ,  $\Theta$ , and  $\beta$ ; then we consider oscillatory motion and get  $\eta'$  and  $\eta''$ .

Steady Shear Flow With  $v_x(y)$ ,  $v_y = 0$ ,  $v_z = 0$ ;  $\gamma \equiv dv_x/dy$ . For this

situation it is desired to compute the six components of  $\tau_{ij}$  from equation (27).

These are found to be

$$\begin{aligned}
 \tau_{xx} - \left(\frac{4 + \epsilon}{3}\right) \lambda_1 \tau_{xy} \gamma &= + \left(\frac{4 + \epsilon}{3}\right) \eta_0 \lambda_2 \gamma^2 \\
 \tau_{yy} + \left(\frac{2 - \epsilon}{3}\right) \lambda_1 \tau_{xy} \gamma &= - \left(\frac{2 - \epsilon}{3}\right) \eta_0 \lambda_2 \gamma^2 \\
 \tau_{zz} + \left(\frac{2 + 2\epsilon}{3}\right) \lambda_1 \tau_{xy} \gamma &= - \left(\frac{2 + 2\epsilon}{3}\right) \eta_0 \lambda_2 \gamma^2 \\
 \tau_{xy} - \left(\frac{2 + \epsilon}{2}\right) \lambda_1 \tau_{yy} \gamma - \left(\frac{\epsilon}{2}\right) \lambda_1 \tau_{xx} \gamma &= - \eta_0 \gamma \\
 \tau_{xz} = 0 \quad \tau_{yz} = 0
 \end{aligned} \tag{30}$$

These equations may be solved simultaneously to give the expressions for the individual components of the  $\tau$  tensor. Then from the definitions in Table III one can find the following expressions for the material functions  $\eta$ ,  $\Theta$ , and  $\beta$ :

$$\frac{\eta}{\eta_0} = \frac{1 + (\lambda_2/\lambda_1) (c\lambda_1\gamma)^2}{1 + (c\lambda_1\gamma)^2} \tag{31}$$

$$\left(\frac{c}{2}\right) \frac{\Theta\gamma}{\eta_0} = \frac{[(1 - (\lambda_2/\lambda_1))] (c\lambda_1\gamma)}{1 + (c\lambda_1\gamma)^2} = \left(\frac{c}{\epsilon}\right) \frac{\beta\gamma}{\eta_0} \tag{32}$$

in which  $c = \sqrt{\frac{2}{3} \left(1 - \epsilon - \frac{1}{2} \epsilon^2\right)}$  is called the shift factor for reasons which will be apparent later. These results show how the various material functions depend upon the zero-shear viscosity, the characteristic time  $\lambda_1$ , and two dimensionless parameters  $\lambda_2/\lambda_1$  and  $\epsilon$ , when  $\epsilon = 0$ , the function  $\beta$  is zero. Note that this model predicts that the secondary normal stress coefficient is

just a constant multiplied by the primary normal stress coefficient; there are probably not enough reliable data to verify or contradict this at the present time [45]

Oscillatory Small-Amplitude Motion With  $v_x(y, t)$ ,  $v_y = 0$ ,  $v_z = 0$ . For small-amplitude oscillatory motion, equation (27) reverts to the Jeffreys model in equation (18). When the postulates in equations (20, 21) are made for the Jeffreys model, one obtains a simplified form of equation (23) namely,

$$\frac{\eta^*}{\eta_0} = \frac{1 + i\lambda_2\omega}{1 + i\lambda_1\omega} \quad (33)$$

When  $\eta^* = \eta' - i\eta''$  is broken up into real and imaginary parts, one gets

$$\frac{\eta'}{\eta_0} = \frac{1 + (\lambda_2/\lambda_1) (\lambda_1\omega)^2}{1 + (\lambda_1\omega)^2} \quad (34)$$

$$\frac{\eta''}{\eta_0} = \frac{[1 - (\lambda_2/\lambda_1)] (\lambda_1\omega)}{1 + (\lambda_1\omega)^2} \quad (35)$$

The expressions for  $\Theta'$ ,  $\Theta''$ , and  $\Theta^d$  have been derived in detail elsewhere [32] for the special case that  $\epsilon = 0$ .

The general shapes of the functions in equations (31, 32, 34, 35) are correct, but it is not possible to get quantitative fits of the experimental data. It is possible to make order-of-magnitude calculations, however, and these have proved useful. In addition, it appears from equations (31, 34) that  $\eta/\eta_0$  versus  $c\gamma$  ought to be the same as  $\eta'/\eta_0$  versus  $\omega$ . Experimentally analogies of this type have been found and experimental values of the shift factor  $c$  are of the order of magnitude one expects from this model. Experimental values of  $c$  have ranged from about 0.25 to 0.7 [21, 24, 38, 46, 47, 48], and the model gives  $c < \sqrt{2/3}$  or about 0.8. Furthermore, comparison of equations (32, 35) shows a similar analogy between  $(c/2)\Theta\gamma/\eta_0$  and  $\eta''/\eta_0$ . Analogies of this type have also been reported, but they do not seem to be quite so good as the first one mentioned. In any case we see here the possibility of interrelating various material functions by means of a model.

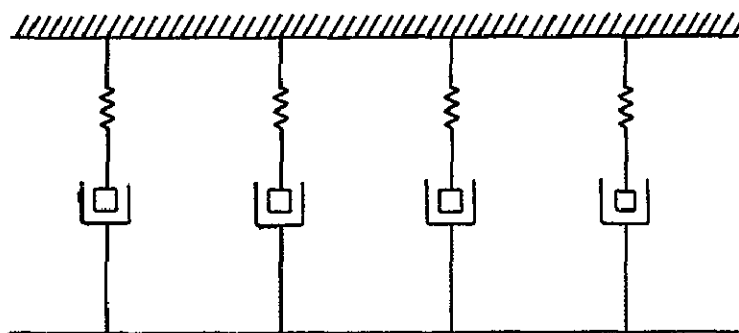
## Method III: Incorporation Of Molecular Theory Results Into Viscoelastic Models

The limited success of the Oldroyd models suggested that better results might be obtained by working with the nonlinear analogs of viscoelastic models of order higher than that of the Jeffreys model. It is possible, for example, to generalize equation (19) in exactly the same way that we generalized equation (18) in the preceding section. The model that results has too many constants to be of any value. Hence the Rouse molecular theory of linear viscoelasticity [49] was used to evaluate the parameters  $a_m$  and  $b_m$  in terms of a single time constant  $\lambda$ . In that way the two-constant Spriggs-Bird model was obtained [50].

In an effort to improve on the latter, Spriggs [33] reformulated and extended the two-constant equation just mentioned, and it is his results that we choose to summarize here, since they tend to tie together many of the ideas in this chapter. The starting point for the discussion is equation (19), which we wish to generalize to handle nonlinear problems. First equation (19) can be written in an alternate form as a sum of Maxwell models:

$$\tau = \sum_{p=1}^{\infty} \tau^{(p)} \quad (36)$$

$$\tau^{(p)} + \lambda_p \frac{\partial}{\partial t} \tau^{(p)} = -\eta_0 \left( \lambda_p / \sum_{p=1}^{\infty} \lambda_p \right) \dot{\gamma} \quad (37)$$



SPRING-DASHPOT REPRESENTATION

and the constants  $a_m$  and  $b_m$  can be related to the time constants  $\lambda_p$  used here. If one now puts in  $\lambda_p = \lambda/p^2$ , one gets a good approximation to the results of the Rouse molecular theory

Spriggs suggested that the Rouse model thus formulated be extended in the following way: (1) replace  $\partial/\partial t$  everywhere by  $\mathcal{F}_\epsilon$  (equation 28), (2) set  $\lambda_p = \lambda/p^\alpha$ . In this way one obtains a model containing four constants:<sup>1</sup>

- $\eta_0$  = zero-shear viscosity
- $\lambda$  = characteristic time (Rouse's longest relaxation time if  $\alpha = 2$ )
- $\epsilon$  = a dimensionless parameter which is small and accounts for deviations from the Weissenberg hypothesis
- $\alpha$  = a dimensionless parameter which governs the slope of the  $\log \eta$  versus  $\log \gamma$  line in the "power-law" region, usually between 2 and 4.

This model has been extensively studied by Spriggs who has derived expressions for the material functions and given limiting forms which are computationally easy to use. It seems to give material functions for  $\eta$ ,  $\eta'$ , and  $\eta''$  which are capable of fitting the experimental data quite well; the  $\Theta$  data do not seem to be described as well as the other properties.

The model also predicts exactly the same analogies as are predicted by the four-constant Oldroyd model with exactly the same shift factor  $c$ . Hence all the material functions ( $\eta$ ,  $\eta'$ ,  $\eta''$ ,  $\Theta$ ,  $\beta$ ) can be obtained from Spriggs's results for  $\eta'$  and  $\eta''$ :

$$\frac{\eta'(\omega)}{\eta_0} = 1 - \frac{(\lambda\omega)^2}{Z(\alpha)} \sum_{p=1}^{\infty} \frac{1}{p^\alpha (p^{2\alpha} + (\lambda\omega)^2)} \quad \frac{1}{\lambda\omega} \frac{\eta''(\omega)}{\eta_0} = \frac{Z(2\alpha)}{Z(\alpha)} - \quad (38)$$

$$\frac{(\lambda\omega)^2}{Z(\alpha)} \sum_{p=1}^{\infty} \frac{1}{p^{2\alpha} (p^{2\alpha} + (\lambda\omega)^2)} \quad (39)$$

in which  $Z(\alpha) = \sum_{n=1}^{\infty} n^{-\alpha}$  is the Riemann zeta function.

---

1. Another nonlinear extension of the general linear viscoelastic model was made independently by Roscoe [58], he did not, however, incorporate any molecular theory results into his model.

Spriggs has also shown how to relate his four-constant model to the Ellis model discussed, by noting that both models exhibit linear log  $\eta$  versus log  $\gamma$  behavior beyond about  $\lambda c \gamma = 1$ . For large  $\gamma$  the asymptotic forms of the two models are

$$\text{Ellis: } \tau_{yx} \rightarrow \eta_0 \left( \frac{\eta_0}{\tau_{\frac{1}{2}}} \right)^{\frac{1-\alpha}{\alpha}} \gamma^{\frac{1}{\alpha}} \quad (40)$$

$$\text{Spriggs: } \tau_{yx} \rightarrow \eta_0 \left[ \frac{\pi}{Z(\alpha) 2\alpha \sin\left(\frac{\alpha+1}{2\alpha} \pi\right)} \right] \times (c\lambda)^{\frac{1-\alpha}{\alpha}} \gamma^{\frac{1}{\alpha}} \quad (41)$$

From this it is evident that  $\alpha$  has the same meaning in both models and furthermore that

$$c\lambda = \left( \frac{\eta_0}{\tau_{\frac{1}{2}}} \right) \left[ \frac{\pi}{Z(\alpha) 2\alpha \sin\left(\frac{\alpha+1}{2\alpha} \pi\right)} \right]^{\frac{\alpha}{\alpha-1}} \quad (42)$$

This gives a means of estimating  $\lambda$  from Ellis model parameters, or vice versa. For  $\alpha = 2$  and  $\epsilon = 0$ , the time constants are related by  $\lambda = 0.56(\eta_0/\tau_{\frac{1}{2}})$ . Hence the characteristic time of the Ellis fluid is of the same order of magnitude as the largest relaxation time of the Rouse theory. Since some work has been done on the temperature dependence of the Ellis parameters [15], this information can be transferred to the Spriggs parameters by means of equation (42).

## Summary Of Analytical Methods

The preceding methods must be regarded as tentative, since as more data accumulate and various new models are devised and tested, undoubtedly better procedures can be established. In any case considerably more is known about viscoelastic models today than was known twenty years ago, and the three methods summarized here show some promise.

The kind of rheological models that are to be used in any given problem depends on the variety of phenomena which must be interrelated, on the viscometric data available for the fluid, and on the degree of complexity of the flow configuration.

For polymer structure studies, small amplitude oscillatory responses are measured; this kind of "mechanical spectroscopy" is well described by Ferry [28]. For the interpretation and design of those experiments, the general linear viscoelastic model is quite adequate. Furthermore, considerable progress has been made in understanding these problems from a molecular point of view [51, 52].

For engineering problems involving steady flow in closed channels, the simple generalized-Newtonian models are probably sufficient. Even some unsteady problems can probably be worked, with only viscometric data, provided that the time constants for the macroscopic system are larger than the characteristic time of the fluid. For heat transfer problems in steady state flow, probably viscometric  $\eta$  data will be sufficient. It will, however, be required to have information concerning the temperature dependence of the viscometric parameters; this information is known for the power-law model and the Ellis model for a few fluids [15]. Most of the existing analytic solutions for heat transfer problems have just assumed that the rheological parameters are insensitive to temperature [53, 54, 55, 56, 57]. A notable exception is Turian's recent study of viscous heating in a cone-and-plate viscometer [15].

For systems involving viscoelastic recoil phenomena, large amplitude oscillatory flows, spinning operations, and normal stress phenomena, nonlinear viscoelastic models are required [3]. It would be helpful to be able to describe these highly nonlinear phenomena by equations which contain only three or four constants at the most and to be able to determine these constants in one or two well-defined experiments. For that reason, the discussion here has been restricted entirely to models containing small numbers of constants rather than functions. Such models show more promise for use by the engineer. (For a comparative summary of rheological models see; Spriggs, T. W., Huppler, J. D., and Bird, R. B., *Trans. Soc. Rheol.*, 10:1, 191-213, 1966. This paper includes both "differential models" and integral models.)

## Illustrative Examples

### Laminar Flow of an Ellis Fluid in a Thin Slit.

Problem: Derive an expression for the flow rate of an Ellis fluid in a slit of width  $W$ , thickness  $2B$ , and length  $L$ . Let the  $z$  axis go down the middle of the channel so that the side walls of the slit are located at  $x = \pm B$  and

$$y = \pm \frac{1}{2} W.$$

Solution: The equation of motion for any fluid in a slit is

$$0 = - \frac{dp}{dz} - \frac{d\tau_{xz}}{dx}$$

We may integrate this using the boundary condition that  $\tau_{xz} = 0$  at  $x = 0$ ;

$$\tau_{xz} = (\Delta p/L)x$$

Introduction of the Ellis model into this result gives

$$\frac{dv_z}{dx} = - \frac{1}{\eta_0} \left[ 1 + \left( \frac{\Delta px}{L\tau_{\frac{1}{2}}} \right)^{\alpha-1} \right] \left( \frac{\Delta px}{L} \right)$$

which can be integrated with the boundary condition that  $v_z = 0$  at  $x = \pm B$  to give

$$\frac{v_z}{B\tau_{\frac{1}{2}}/\eta_0} = \left( \frac{1}{2} \right) \Pi (1 - \xi^2) + \frac{1}{\alpha+1} \Pi^\alpha (1 - \xi^{\alpha+1})$$

where  $\xi = x/B$  and  $\Pi = \Delta pB/L\tau_{\frac{1}{2}}$ . Then integration over the flow cross section gives

$$Q = 2WB \int_0^1 v_z d\xi$$

or

$$Q = \frac{2WB^2\tau_{\frac{1}{2}}}{\eta_0} \left( \frac{1}{3} \Pi + \frac{1}{\alpha+2} \Pi^\alpha \right)$$

for flow in a plane slit.

We may adopt this result to flow in an annulus formed by two tubes of radii  $\kappa R$  and  $R$ , provided that  $\kappa > 0.6$ . We are then dealing with a slit for which  $2B = (1 - \kappa)R$  and  $W = 2\pi R [1 - \frac{1}{2}(1 - \kappa)]$ . We can in addition multiply the final result by the function  $\left[ 1 + \frac{1}{60} (1 - \kappa)^2 + \dots \right]$  by which the analogous Newtonian slit formula is "corrected for curvature" in order to describe annular flow. The final result is

$$Q = \frac{\pi R^3 (1 - \kappa)^2 \left[ 1 - \frac{1}{2} (1 - \kappa) \right] \left[ 1 + \frac{1}{60} (1 - \kappa)^2 + \dots \right] \tau_{\frac{1}{2}}}{\eta_0} \times \left[ \frac{1}{3} \Pi + \frac{1}{\alpha + 2} \Pi^\alpha \right]$$

where  $\Pi = (1 - \kappa) R \Delta p / 2L \tau_{\frac{1}{2}}$ .

Laminar Flow of a Polymer Solution in an Annulus.

Problem: For an aqueous 3.5% CMC-70-medium-solution Ellis parameters were determined from Fredrickson's [1] tube flow data to be

$$\begin{aligned} \eta_0 &= 22.7 \text{ poise} \\ \tau_{\frac{1}{2}} &= 1,520 \text{ dyne cm.}^{-2} \\ \alpha &= 3.0 \end{aligned}$$

Find the flow rate (expressed as  $4Q/\pi R^3$ ) of this fluid in an annulus with radius ratio  $\kappa = 0.624$ , when  $\Delta p R / 2L = 5 \times 10^3 \text{ dyne cm.}^{-2}$

Solution: Use the result of illustrative Example 1 with  $1 - \kappa = 0.376$ ,  $1 - \frac{1}{2} (1 - \kappa) = 0.812$ , and

$$\Pi = (0.376) (5 \times 10^3) / (1,520) = 1.24.$$

Then

$$\begin{aligned} \frac{4Q}{\pi R^3} &= \frac{4(0.376)^2(0.812)(1.002)(1,520)}{(22.7)} \times \left[ \frac{1}{3} (1.24) + \frac{1}{5} (1.24)^3 \right] \\ &= 24.3 \text{ sec.}^{-1} \end{aligned}$$

This result agrees very closely with the experimental value obtained by Fredrickson [1].

## Stretching of a Viscoelastic Fiber.

Problem: A polymeric material [34] is being drawn out as a fiber. A relation of the form of equation (24) is desired in order to relate the tension,  $p + \tau_{zz}$ , to the rate of elongation of the fiber,  $\bar{\gamma} = d\bar{\nu}/dz$ ; that is, we wish to know the elongational viscosity. Further, we want to relate this quantity to the shear viscosity (non-Newtonian viscosity), which is normally measured with a viscometer, such as a cone-and-plate instrument.

Solution: We consider a coordinate system oriented so that the central axis of the fiber is the  $z$  axis, and we assume that the flow is steady, elongational flow with  $\nu_z = \bar{\gamma}z$ ,  $\nu_r = -\frac{1}{2}\bar{\gamma}r$ ,  $\nu_\theta = 0$ . This assumed velocity distribution satisfies the equation of continuity exactly. It is further assumed that the stretching is sufficiently slow that the term  $[\nabla \cdot \rho \mathbf{v} \mathbf{v}]$  is not important in the equation of motion; also external forces are neglected. These assumptions lead to the fact that the shear stresses are independent of position, a point we shall use subsequently. The first thing we have to do is to summarize the input information for equation (27, 28, 29) for the assumed flow pattern. Because the problem involves cylindrical coordinates  $(r, \theta, z)$  we have to know various operations—specifically  $\nabla \mathbf{v}$  and  $\{\mathbf{v} \cdot \nabla \tau\}$  in cylindrical coordinates. These have been tabulated by Williams and Bird [32], and we use those results here. We find that

$$\nabla \mathbf{v} = (\nabla \mathbf{v})^\dagger = \begin{bmatrix} -\frac{1}{2} & 0 & 0 \\ 0 & -\frac{1}{2} & 0 \\ 0 & 0 & +1 \end{bmatrix} \bar{\gamma}$$

$$\gamma = \nabla \mathbf{v} + (\nabla \mathbf{v})^\dagger = \begin{bmatrix} -1 & 0 & 0 \\ 0 & -1 & 0 \\ 0 & 0 & +2 \end{bmatrix} \bar{\gamma}$$

$$\omega = \nabla \mathbf{v} - (\nabla \mathbf{v})^\dagger = 0$$

$$\tau = \begin{bmatrix} \tau_{rr} & 0 & 0 \\ 0 & \tau_{\theta\theta} & 0 \\ 0 & 0 & \tau_{zz} \end{bmatrix} ; \quad \{\mathbf{v} \cdot \nabla \tau\} = 0$$

$$\{\tau \cdot \gamma\} = \begin{bmatrix} -\tau_{rr} & 0 & 0 \\ 0 & -\tau_{\theta\theta} & 0 \\ 0 & 0 & +2\tau_{zz} \end{bmatrix} \quad \bar{\gamma}; \quad \{\gamma \cdot \gamma\} = \begin{bmatrix} 1 & 0 & 0 \\ 0 & 1 & 0 \\ 0 & 0 & 4 \end{bmatrix} \bar{\gamma}^2$$

When this information is put into equation (27), the three nonzero components of that equation become

$$\begin{aligned} \tau_{rr} - \lambda_1(1 + \epsilon) \left[ -\tau_{rr} \bar{\gamma} - \frac{1}{3} (-\tau_{rr} - \tau_{\theta\theta} + 2\tau_{zz}) \bar{\gamma} \right] \\ = -\eta_0 \left\{ -\bar{\gamma} - \lambda_2(1 + \epsilon) \left[ \bar{\gamma}^2 - \frac{1}{3} (6\bar{\gamma}^2) \right] \right\} \end{aligned}$$

$$\begin{aligned} \tau_{\theta\theta} - \lambda_1(1 + \epsilon) \left[ -\tau_{\theta\theta} \bar{\gamma} - \frac{1}{3} (-\tau_{rr} - \tau_{\theta\theta} + 2\tau_{zz}) \bar{\gamma} \right] \\ = -\eta_0 \left\{ -\bar{\gamma} - \lambda_2(1 + \epsilon) \left[ \bar{\gamma}^2 - \frac{1}{3} (6\bar{\gamma}^2) \right] \right\} \end{aligned}$$

$$\begin{aligned} \tau_{zz} - \lambda_1(1 + \epsilon) \left[ +2\tau_{zz} \bar{\gamma} - \frac{1}{3} (-\tau_{rr} - \tau_{\theta\theta} + 2\tau_{zz}) \bar{\gamma} \right] \\ = -\eta_0 \left\{ +2\bar{\gamma} - \lambda_2(1 + \epsilon) \left[ 4\bar{\gamma}^2 - \frac{1}{3} (6\bar{\gamma}^2) \right] \right\} \end{aligned}$$

Solving for  $\tau_{zz}$  and  $\tau_{rr}$  gives

$$2\tau_{rr} = \tau_{zz} = -2\eta_0 \bar{\gamma} \left[ \frac{1 - \lambda_2(1 + \epsilon) \bar{\gamma}}{1 - \lambda_1(1 + \epsilon) \bar{\gamma}} \right]$$

At the outer edge of the fiber there should be no normal forces, so that

$$p + \tau_{rr} = 0, \text{ whence } p = -\tau_{rr} = +\frac{1}{2} \tau_{zz}. \text{ Hence}$$

$$p + \tau_{zz} = \frac{3}{2} \tau_{zz} = -3\eta_0 \bar{\gamma} \left[ \frac{1 - \lambda_2(1 + \epsilon)\bar{\gamma}}{1 - \lambda_1(1 + \epsilon)\bar{\gamma}} \right]$$

Comparison of this with equation (24) gives

$$\bar{\eta} = 3\eta_0 \left[ \frac{1 - \lambda_2(1 + \epsilon)\bar{\gamma}}{1 - \lambda_1(1 + \epsilon)\bar{\gamma}} \right]$$

Since  $\lambda_1 > \lambda_2$ , this predicts that  $\bar{\eta}$  will increase with the rate of elongation. Note that  $\eta$  decreases with  $\gamma$  for the same viscoelastic model. For Newtonian fluids  $\lambda_1 = \lambda_2 = 0$ , and we get the classical result that  $\bar{\eta} = 3\mu$ .

We can now try to interrelate  $\bar{\eta}$  and  $\eta$  by using this result and that in equation (31). We define two functions S and T thus

$$S(\bar{\gamma}) = 1 - \left( \frac{\eta}{\eta_0} \right) \Big|_{\gamma=\bar{\gamma}} \quad \text{and} \quad T(\bar{\gamma}) = -\frac{\gamma}{2} \frac{d}{d\gamma} \left( \frac{\eta}{\eta_0} \right) \Big|_{\gamma=\bar{\gamma}}$$

These functions can be tabulated when non-Newtonian viscosity data are available. These functions can also be calculated from equation (31). Then if we set  $\epsilon = 0$  and eliminate  $\lambda_1$  and  $\lambda_2$  among the expressions for  $\bar{\eta}$ , S, and T, we get

$$\frac{\bar{\eta}}{3\eta_0} = \frac{1 - \left[ \frac{S(1-S) - T}{S-T} \right] \sqrt{\frac{3}{2} \frac{S-T}{T}}}{1 - \sqrt{\frac{3}{2} \frac{S-T}{T}}}$$

which gives an estimate of  $\bar{\eta}$  from viscosity data. There do not seem to be data available to test this relation.

### Tube Flow of an Oldroyd Fluid.

Problem: Obtain the volume rate of flow for the model given in equation (27) (the four-constant Oldroyd fluid) [42].

Solution: As pointed out earlier, the equation of motion gives for tube flow

$$\tau_{rz} = \Delta p r / 2L.$$

From equation (31) we find that

$$\tau_{rz} = -\eta_0 \left[ \frac{1 + n(c\lambda_1\gamma)^2}{1 + (c\lambda_1\gamma)^2} \right] \gamma$$

where  $n = \lambda_2/\lambda_1$ . Combining these we get

$$r = \frac{2\eta_0 L}{\Delta p} \left[ \frac{1 + n(c\lambda_1\gamma)^2}{1 + (c\lambda_1\gamma)^2} \right] \gamma$$

This could be integrated again to get the velocity profile, but we want only  $Q$  versus  $\Delta p$ . Hence we write the volume rate of flow  $Q$  in this way by two integrations by parts:

$$Q = 2\pi \int_0^R \nu_z r dr = \frac{\pi}{3} \left( R^3 \gamma_R - \int_0^{\gamma_R} r^3 d\gamma \right)$$

where  $\gamma_R = -dv_z/dr|_{r=R}$ ;  $\gamma_R$  is related to the pressure drop  $\Delta p$  by

$$\frac{c\lambda_1}{\eta_0} \left( \frac{\Delta p R}{2L} \right) = \left( \frac{1 + nX_R}{1 + X_R} \right) \sqrt{X_R}$$

where  $X_R = (c\lambda_1\gamma_R)^2$ . When the integral in  $Q$  is evaluated, we get

$$\frac{3c\lambda_1 Q}{\pi R^3} = \left[ 1 - \frac{1}{2X_R^2} \left( \frac{1 + X_R}{1 + nX_R} \right)^3 f_R(n; X_R) \right] \sqrt{X_R}$$

where

$$f_R(n; X_R) = \frac{1}{2} n^3 X_R^2 - 3n^2(n-1)X_R + 3n(n-1)(2n-1) \\ \times \ln(1 + X_R) - \frac{1}{2} X_R \left( \frac{n-1}{1 + X_R} \right)^2 [6n + (7n-1)X_R]$$

From the above equations for  $\Delta p$  and  $Q$  the quantity  $X_R$  has to be eliminated to get the  $Q$  versus  $\Delta p$  relation. This can be done numerically, and dimensionless plots are available both for circular tubes and for plane slits. The results have been compared with experimental data for carboxymethyl-cellulose, sodium polymethacrylate, and cholesterylbutyrate [42].

Relative Magnitude of Normal and Shear Stresses.

Problem: In simple shear flow what is the maximum value of  $|\tau_{yy}|/|\tau_{yx}|$  for the Oldroyd model in equation (27) when  $\epsilon = 0$ ? This gives some idea as to the relative magnitudes of the normal and shear forces.

Solution: Let  $R$  be the desired ratio. Then from the definitions in Table III and the results in equations (31, 32)

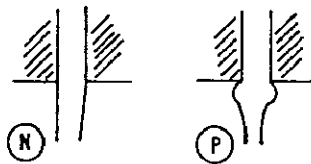
$$R = \frac{|\tau_{yy}|}{|\tau_{yx}|} = \frac{\frac{1}{3}\theta\gamma^2}{\eta\gamma} = \frac{(\lambda_1 - \lambda_2)\gamma}{1 + \frac{2}{3}\lambda_1\lambda_2\gamma^2}$$

Setting  $dR/d\gamma = 0$  gives  $\gamma^2 = 1/(\frac{2}{3}\lambda_1\lambda_2)$ , and so

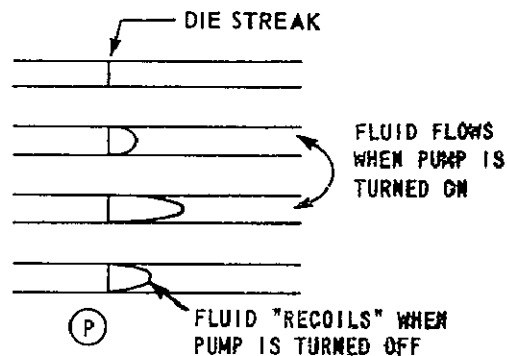
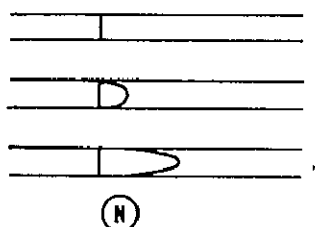
$$R_{\max} = \frac{(\lambda_1 - \lambda_2)}{2\sqrt{\frac{2}{3}\lambda_1\lambda_2}}$$

As  $\lambda_2/\lambda_1$  goes from 1 to 1/9,  $R_{\max}$  goes from zero to  $\sqrt{8/3}$ .

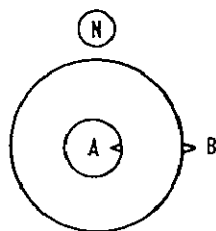
DIE SWELL



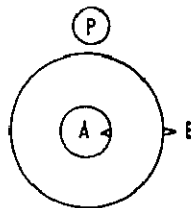
RECOIL



AXIAL ANNULAR FLOW

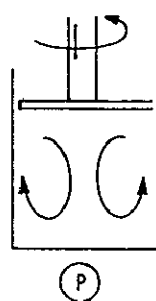
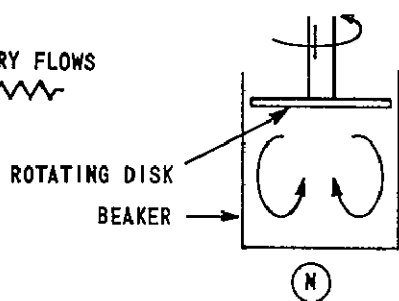


PRESSURE-SENSING DEVICES READ SAME AT A AND B



PRESSURE-SENSING DEVICES READ DIFFERENTLY AT A AND B

SECONDARY FLOWS



[SEE C.T. HILL, J.D. HUPPLER, AND R.B. BIRD, CHEM. ENGR.SCI., (1966)]

### COMPARATIVE RESULTS OF NEWTONIAN AND POLYMERIC FLUIDS

## REFERENCES

1. Fredrickson, A. G., Ph.D. thesis, Univ. of Wisconsin, Madison, Wisconsin (1959).
2. McKelvey, J. M., "Polymer Processing," Wiley, New York (1962).
3. Lodge, A. S., "Elastic Liquids," Academic Press, New York (1964).
4. Pearson, J. R. A., Mechanical Principles of Polymer Melt Processing, Pergamon Press, Oxford (1966).
5. Landau, L. D., and E. M. Lifshitz, "Theory of Elasticity," Addison-Wesley, Reading, Massachusetts (1959).
6. Reiner, M., "Deformation, Strain, and Flow," Interscience, New York (1960).
7. Metzner, A. B., chapter in "Advances in Chemical Engineering," vol. I, pp. 77-153, Academic Press, New York (1956).
8. Seely, G. R., A.I.Ch.E. Journal, 10, 56-60 (1964).
9. Sisko, A. W., Ind. Eng. Chem., 50, 1789-1792 (1958).
10. Eyring, H., J. Chem. Phys., 4, 283 (1936).
11. Meter, D. M., and Bird, R. B., A.I.Ch.E. Journal, 10, 878 (1964).
12. Sutterby, J. L., Ph.D. thesis, Univ. of Wisconsin, Madison, Wisconsin (1964); Trans. Soc. Rheology, 10(1966).
13. Philippoff, W., "Viskosität der Kolloide," Steinkopff (1942).
14. Matsuhisa, S., and R. B. Bird, A.I.Ch.E. Journal, 11, No. 4 (1965).
15. Turian, R. M., Ph.D. thesis, Univ. of Wisconsin, Madison, Wisconsin (1964).
16. Hohenemser, K., and W. Prager, Z. Angew. Math. Mech., 12, 216-226 (1932).

## REFERENCES (Continued)

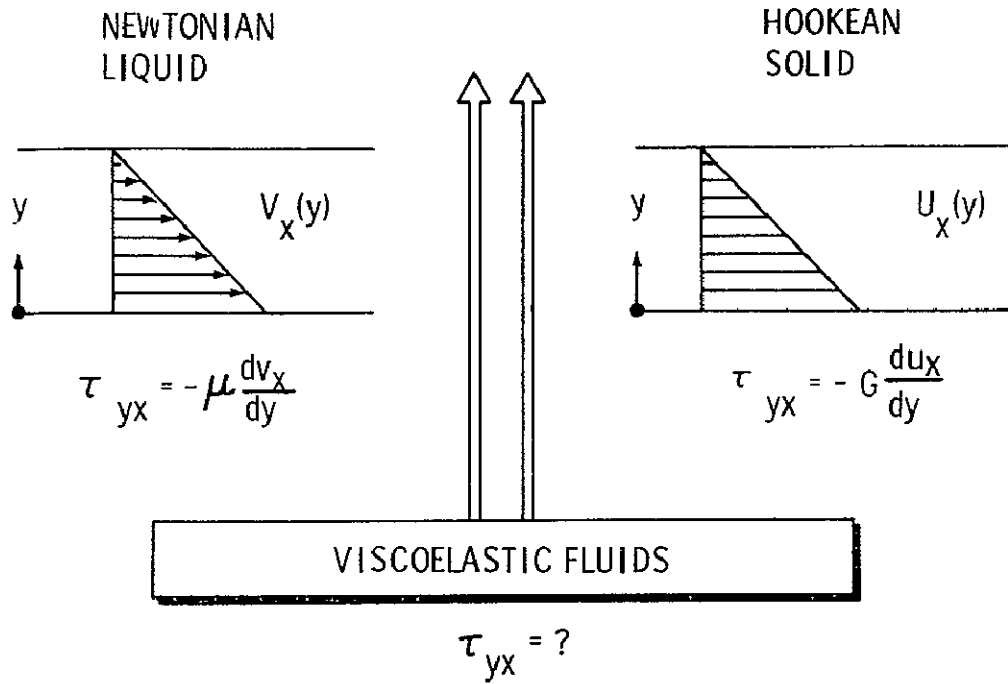
17. Weissenberg, K., *Nature*, 159, 310 (1947).
18. Reiner, M., *Am. J. Math.*, 67, 350 (1945).
19. Rivlin, R. S., *Proc. Roy. Soc. (London)*, A193, 260 (1948); *Proc. Cambridge Philos. Soc.*, 45, 88 (1949).
20. Prager, W., *J. Appl. Phys.*, 16, 837 (1945).
21. Markovitz, H., *Trans. Soc. Rheol.*, 1, 33-52 (1957).
22. Williams, M. C., Ph.D. thesis, Univ. of Wisconsin, Madison, Wisconsin (1964).
23. Prager, W., "Introduction to Mechanics of Continua," Ginn, Chicago, Illinois (1961).
24. Markovitz, H., and R. B. Williamson, *ibid.*, 25.
25. Toms, B. A., Chapter 12 in Vol. II of "Rheology," F. R. Eirich, ed., Academic Press, New York (1958); see particularly pp. 496-500.
26. Markovitz, H., *J. Appl. Phys.*, 23, 1070-1077 (1952).
27. Oka, S., Chapter 2 in vol. III, "Rheology," F. R. Eirich, ed., Academic Press, New York (1958).
28. Ferry, J. D., "Viscoelastic Properties of Polymers," Wiley, New York (1961).
29. Coleman, B., and W. Noll, *Rev. Mod. Phys.*, 33, 239 (1961).
30. Coleman, B., *Ann. N. Y. Acad. Sci.*, 89, 672-699 (1961).
31. Weissenberg, K., *Phys. Fluids*, 5, 1126 (1962).
32. Weissenberg, K., *Ind. Eng. Chem. Fundamentals*, 3, 42-49 (1964).
33. Spriggs, T. W., *Chem. Eng. Sci.*, 20, 931-940 (1965).

## REFERENCES (Continued)

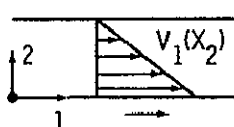
34. Bird, R. B., and T. W. Spriggs, *Phys. Fluids*, 8 (1965).
35. Huppler, J. D., Paper presented at Soc. of Rheology, Santa Barbara, California (January, 1965). —also *Trans. Soc. Rheol.*, 9:2, 273-286, 1966.
36. Bird, R. B., *Can. J. Chem. Engr.*, 43, 161 (1965).
37. McEachern, D. W., Paper presented at A.I.Ch.E. Meeting, Houston, Texas (1965).
38. Meter, D. M., Ph.D. thesis, Univ. of Wisconsin, Madison, Wisconsin (1963); also *A.I.Ch.E. Journal*, 10, 881 (1964).
39. Sadowski, T. J., Ph.D. thesis, Univ. of Wisconsin, Madison, Wisconsin (1963); Sadowski, T. J., and R. B. Bird, *Trans. Soc. Rheology*, 10 (1966); Sadowski, T. J., *ibid.*
40. Slattery, J. C., Ph.D. thesis, Univ. of Wisconsin, Madison, Wisconsin (1959); J. C. Slattery and R. B. Bird, *Chem. Eng. Sci.*, 16, 231-241 (1961).
41. Biery, J. C., *A.I.Ch.E. Journal*, 10, 551-557 (1964).
42. Williams, M. C., and R. B. Bird, *A.I.Ch.E. Journal*, 8, 378-382 (1962).
43. Oldroyd, J. G., *Proc. Roy. Soc. (London)*, A200, 523 (1950).
44. Oldroyd, J. G., *ibid.*, A245, 291 (1958).
45. Huppler, J. D., *Trans. Soc. Rheol.*, 9:2, 273-286, 1966.
46. Arai, T., *Kōbunshi Kagaku*, 18, 292 (1961).
47. DeWitt, T. W., H. Markovitz, F. J. Padden, and J. Zapas, *J. Colloid Sci.*, 10, 174 (1955).

## REFERENCES (Concluded)

48. Philippoff, W., J. Appl. Phys., 25, 1102 (1954).
49. Rouse, P. E., J. Chem. Phys., 21, 1272 (1953).
50. Spriggs, T. W., and R. B. Bird, Ind. Eng. Chem. Fundamentals, 4, 182-186 (1965).
51. Zimm, B. H., J. Chem. Phys., 24, 269 (1956).
52. Zimm, B. H., G. M. Roe, and L. F. Epstein, *ibid.*, 279 (1956).
53. Beek, W. J., and R. Eggink, Ingenieur, 74, Ch81-Ch89 (1962).
54. Bird, R. B., Chem. Ing. Tech., 31, 569-572 (1959).
55. Fredrickson, A. G., "Principles and Applications of Rheology, Prentice-Hall, Englewood Cliffs, New Jersey (1964).
56. Lyche, B. C., and R. B. Bird, Chem. Eng. Sci., 6, 35-41 (1956).
57. Ziegenhagen, A. J., Ph. D. thesis, Univ. of Wisconsin, Madison, Wisconsin (1962).
58. Roscoe, R., British J. Appl. Phys., 15, 1095-1101 (1964).

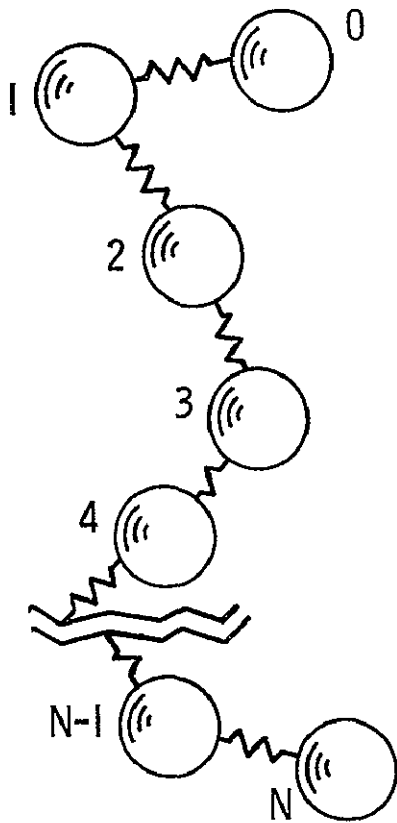


**SUMMARY OF NOTATION**

STEADY SHEAR FLOW	OSCILLATORY SHEAR FLOW
 $\gamma = \frac{dv_1}{dx_2}$	 $\gamma = \text{Re} \left\{ \gamma^0 e^{i\omega t} \right\}$ $\tau_{12} = \text{Re} \left\{ \tau_{12}^0 e^{i\omega t} \right\}$ $\tau_{22} = \text{Re} \left\{ \tau_{22}^0 e^{2i\omega t} \right\} + d_2$
$\tau_{12} = -\eta \gamma$	$\tau_{12}^0 = -\eta^* \gamma^0 \quad \eta^* = \eta' - i\eta''$
$\tau_{11} - \tau_{22} = -\theta \gamma^2$	$\left\{ \begin{array}{l} \tau_{11}^0 - \tau_{22}^0 = -\theta^* \gamma^{02} \quad \theta^* = \theta' - i\theta'' \\ d_1 - d_2 = -\theta^d  \gamma^0 ^2 \end{array} \right.$
$\tau_{11} - \tau_{33} = -\zeta \gamma^2$	
$\tau_{22} - \tau_{33} = -\beta \gamma^2$	
<p>&amp; SIMILARLY FOR <math>\zeta^*, \zeta^d, \beta^*, \beta^d</math></p>	

## FOUR TYPES OF MOLECULAR THEORIES

- |    |  |          |
|----|--|----------|
| 1. | SUSPENDED PARTICLES<br>(ANNALEN DER PHYSIK 1906, 1911) | EINSTEIN |
| 2. | PEARL NECKLACES<br>(JOURNAL OF CHEMICAL PHYSICS, 1956) | ZIMM     |
| 3. | ACTIVATED STATE<br>(JOURNAL OF CHEMICAL PHYSICS, 1936) | EYRING   |
| 4. | NETWORK<br>(TRANS. FARADAY SOCIETY, 1956)              | LODGE    |



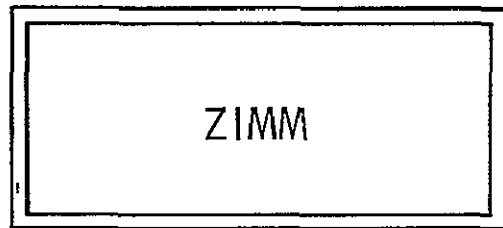
### BEAD-SPRING MODEL

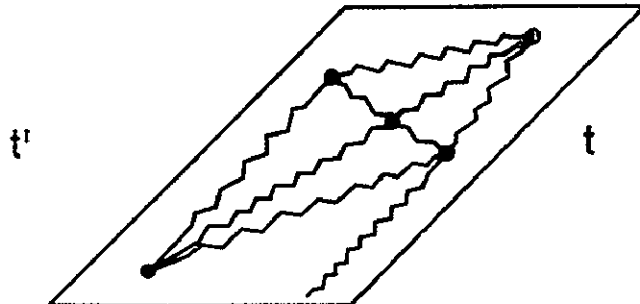
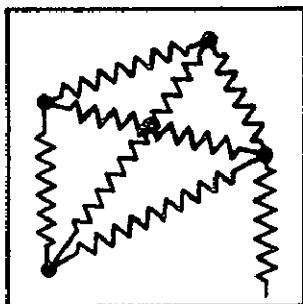
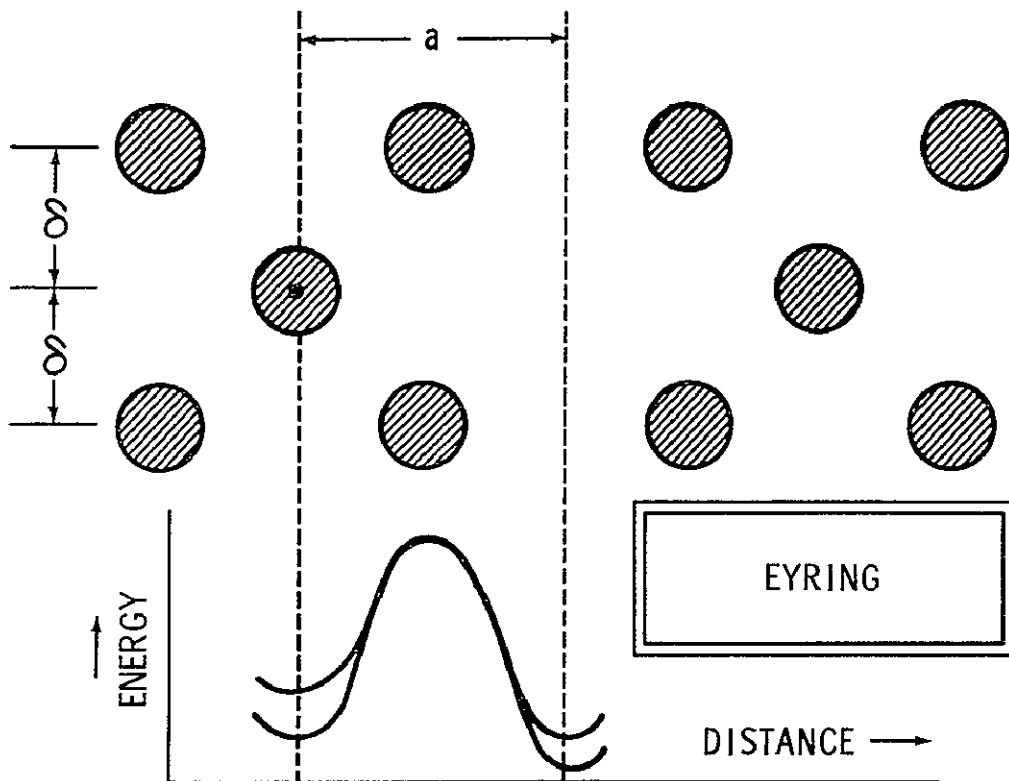
FLEXIBLE JOINTS

SPRINGS ARE "GAUSSIAN  
CHAINS"

SPRING CONST. =  $\frac{3kT}{b^2}$

$b^2$  = MEAN SQUARE END-  
TO-END DISTANCE





JUNCTIONS DON'T FLUCTUATE; HAVE FINITE LIFETIMES  
 CHAINS ARE GAUSSIAN; FORM COHERENT NETWORK  
 AFFINE DEFORMATIONS  
 NO POLYMER-SOLVENT  
 INTERACTION  
 USE RUBBER THEORY RESULTS

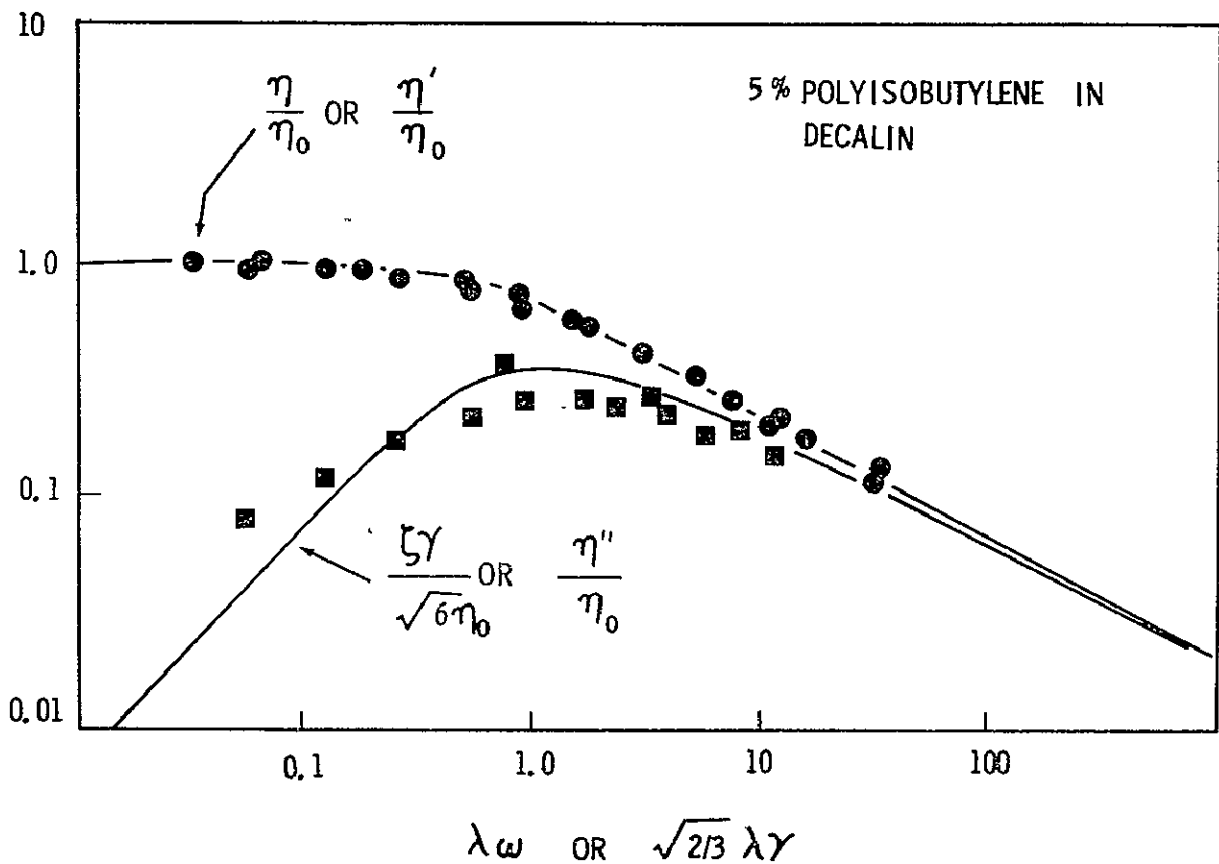
LODGE

## ELLIS MODEL (3 CONSTANTS)

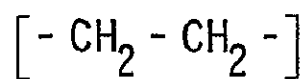
$$\frac{1}{\eta} = \frac{1}{\eta_0} \left[ 1 + \left| \frac{\tau}{\tau_{1/2}} \right|^{\alpha-1} \right]$$

1. ZERO-SHEAR VISCOSITY  $\eta_0$
2. CHARACTERISTIC TIME  $\eta_0 / \tau_{1/2}$
3. CONSTS. HAVE SIMPLE DIMENSIONS
4. SIMPLE, YET USEFUL

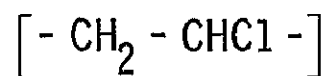
## SPRIGGS - BIRD MODEL ( $\alpha=2, \epsilon=0$ )



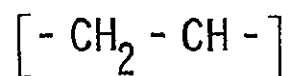
POLY-



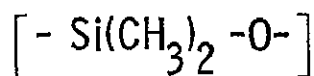
ETHYLENE



VINYL-CHLORIDE



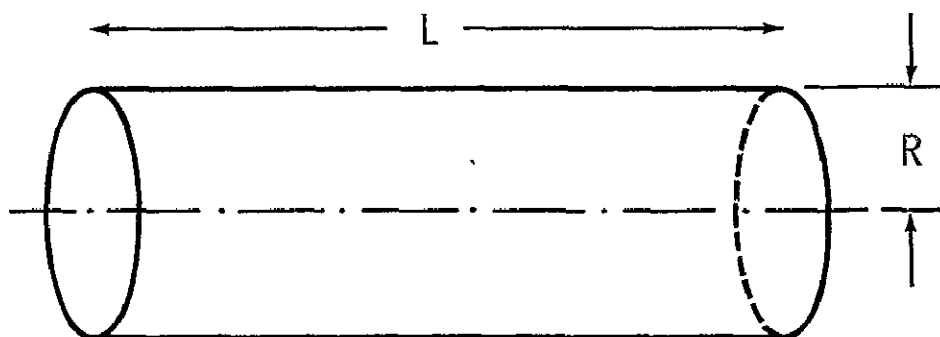
STYRENE



DIMETHYLSILOXANE

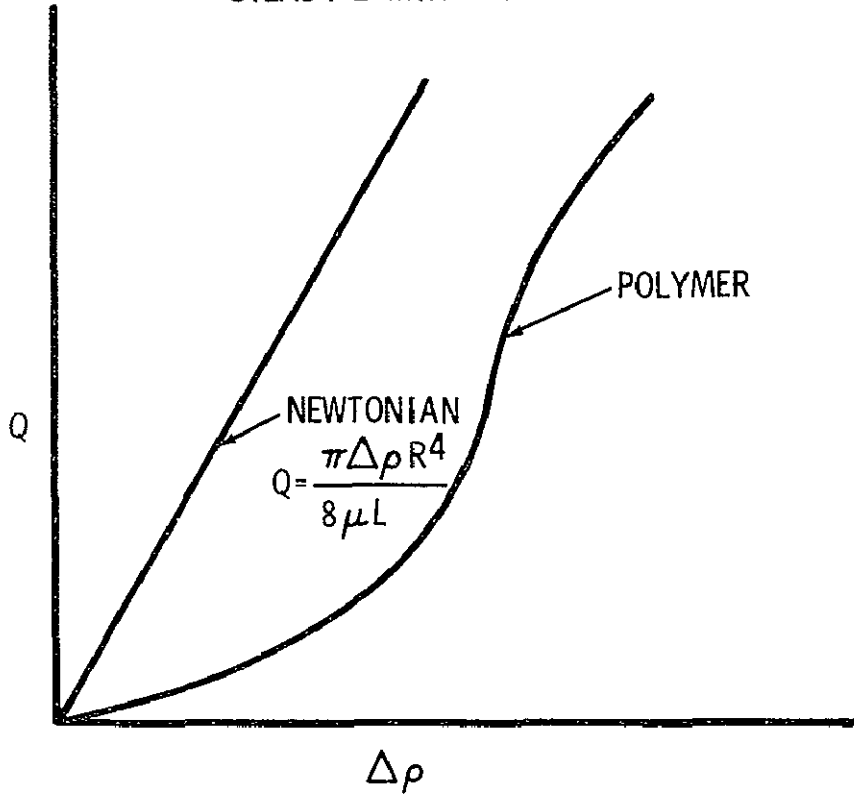
管内の層流

STEADY LAMINAR TUBE FLOW

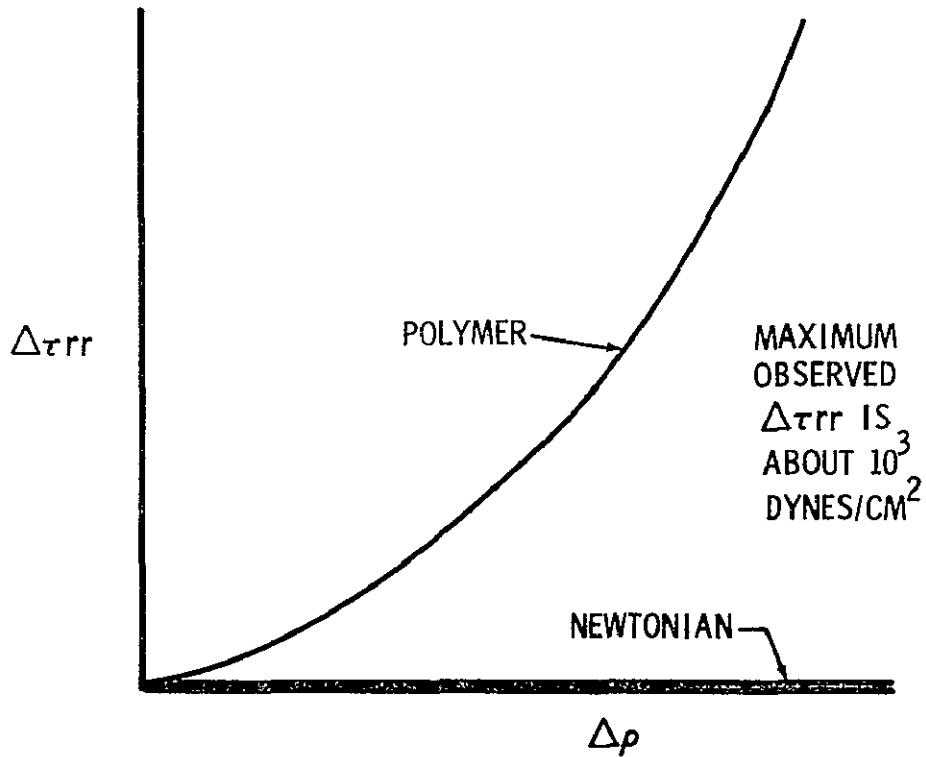


MEASURE : VOLUME RATE OF FLOW  
Q, AS A FUNCTION OF PRESSURE  
DROP  $\Delta P$

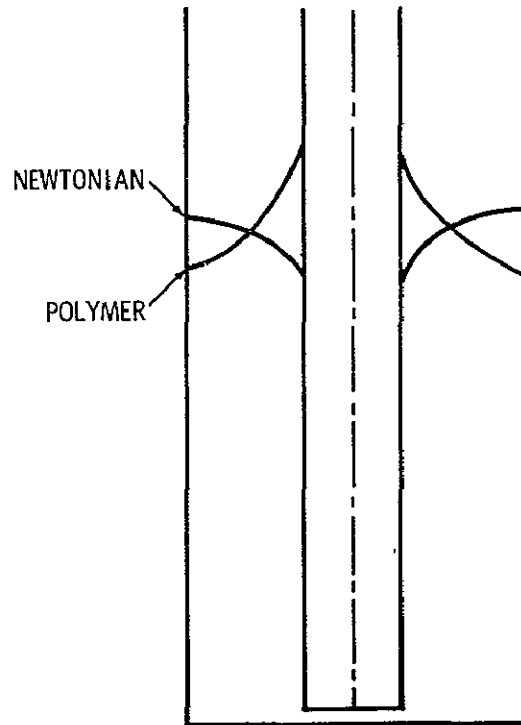
### STEADY LAMINAR TUBE FLOW



### AXIAL ANNULAR FLOW

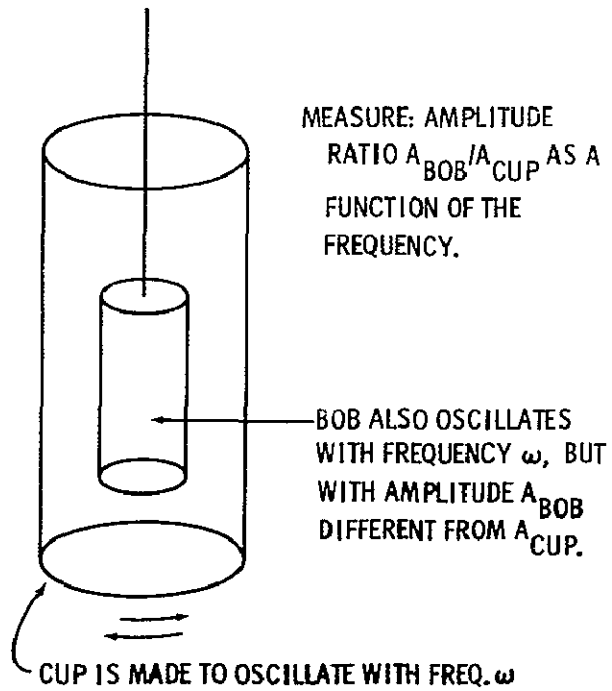


TANGENTIAL ANNULAR FLOW

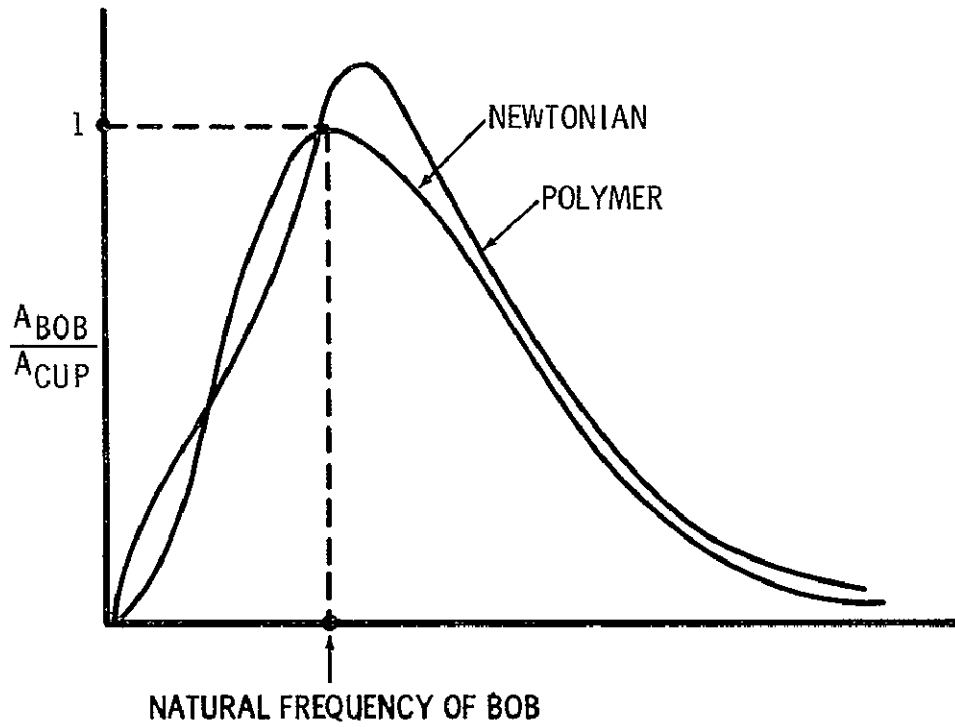


振  
動  
粘  
度  
計

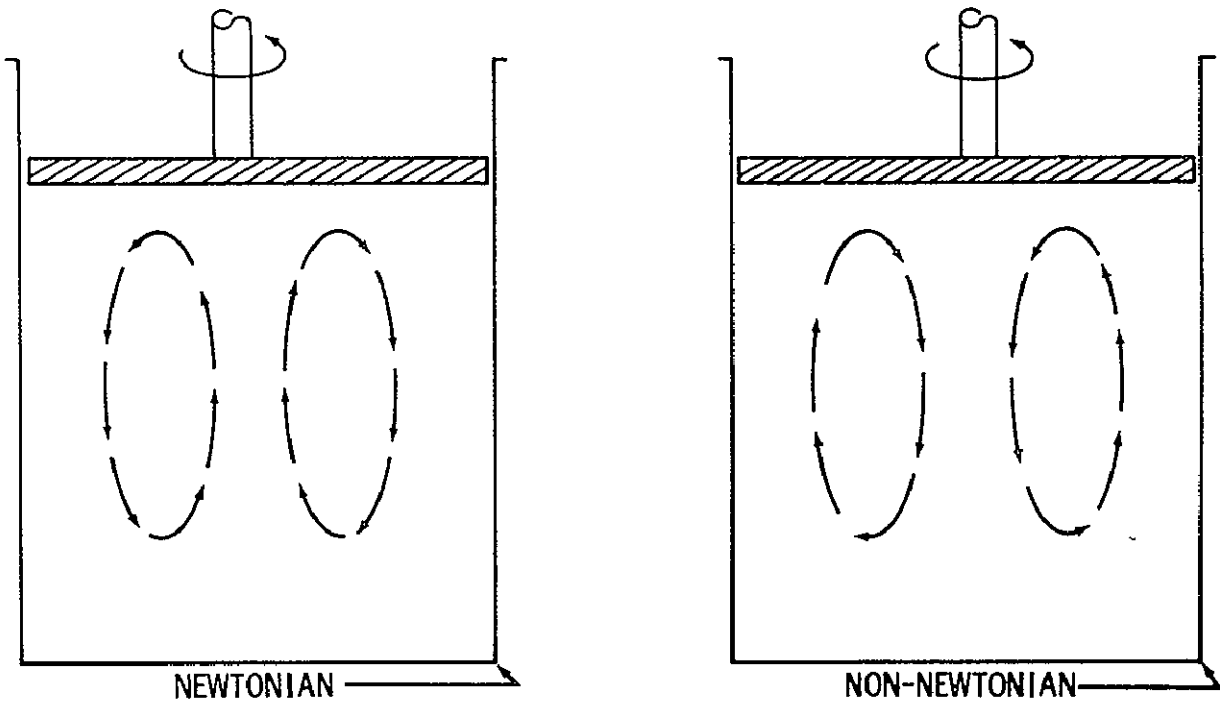
OSCILLATOR VISCOMETER



### OSCILLATORY VISCOMETER



### DISK IN CYLINDER EXPERIMENT



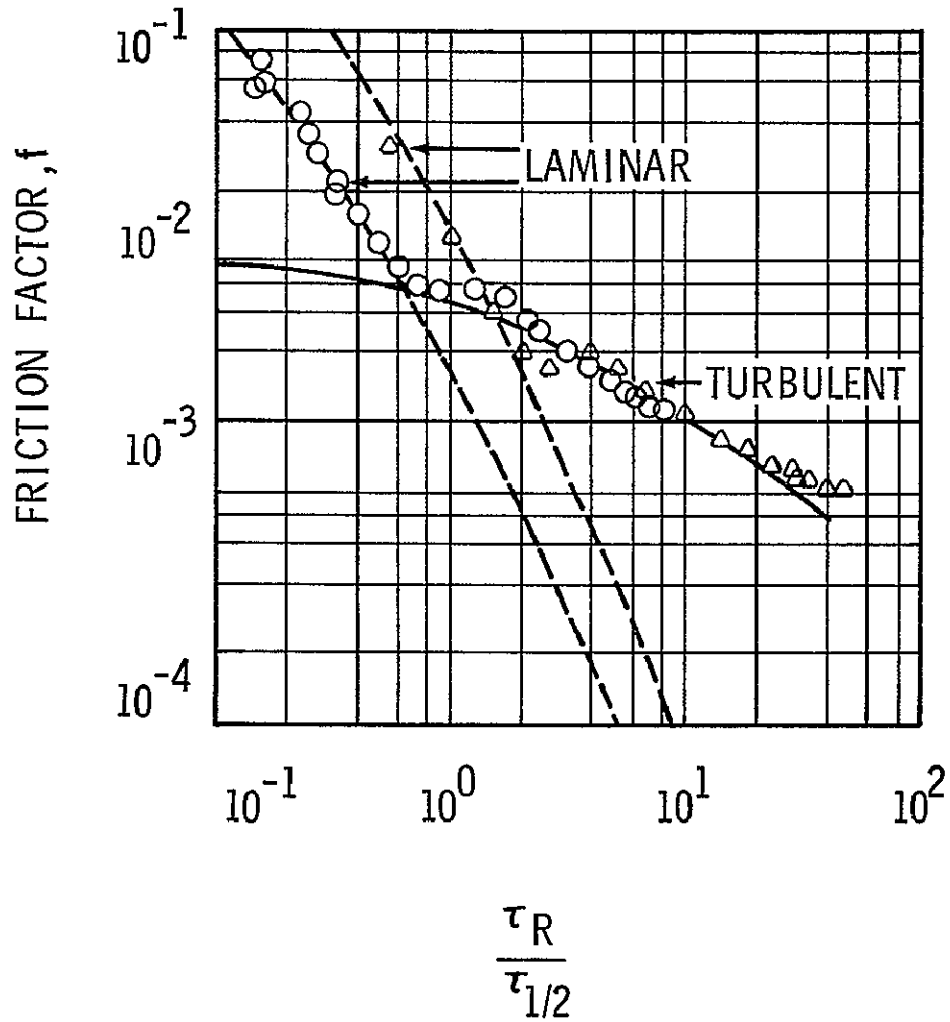
## RANDALL STREET RHEOLOGICAL SOCIETY

A. G. FREDRICKSON	M. C. WILLIAMS
J. C. SLATTERY	J. L. SUTTERBY
A. J. ZIEGENHAGEN	R. M. TURAIN
J. C. BIERY	J. D. HUPPLER
D. W. McEACHERN	T. W. SPRIGGS
T. J. SADOWSKI	S. MATSUHISA (松久)
D. M. METER	E. ASHARE

### 7 EXPERIMENTS TO TEST MODELS CONTAINING $\eta_0$ AND A CHARACTERISTIC TIME

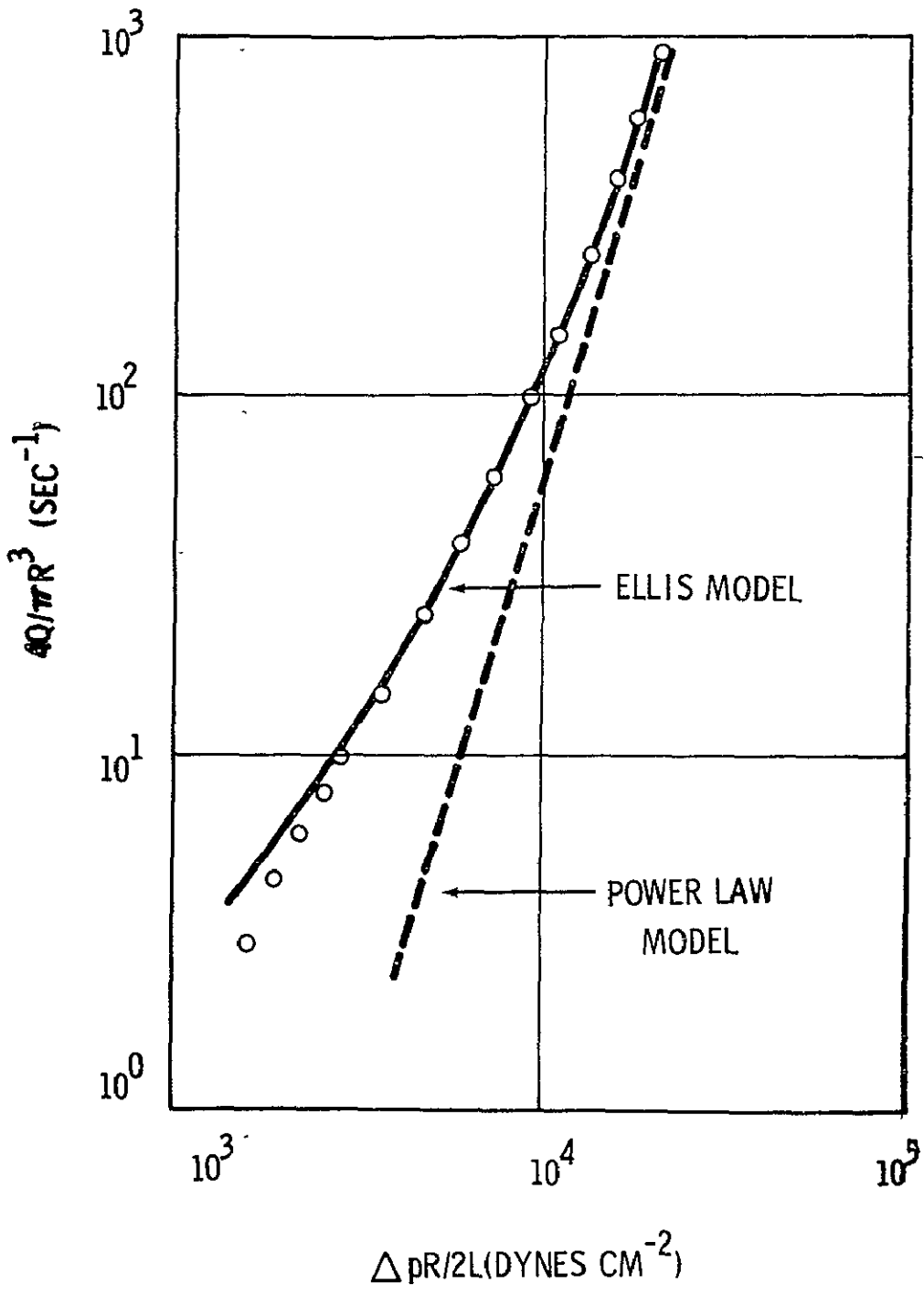
- |                                 |                                  |
|---------------------------------|----------------------------------|
| 1. TURBULENT TUBE FLOW          | (METER)                          |
| 2. LAMINAR ANNULAR FLOW (AXIAL) | { (FREDRICKSON)<br>{ (McEACHERN) |
| 3. FLOW IN A CONVERGING CHANNEL | (SUTTERBY)                       |
| 4. FLOW IN A PACKED COLUMN      | (SADOWSKI)                       |
| 5. DRAG COEFFICIENTS OF SPHERES | (SLATTERY)                       |
| 6. SPHERES FALLING IN CYLINDERS | (TURIAN)                         |
| 7. OSCILLATING MANOMETERS       | (BIERY)                          |

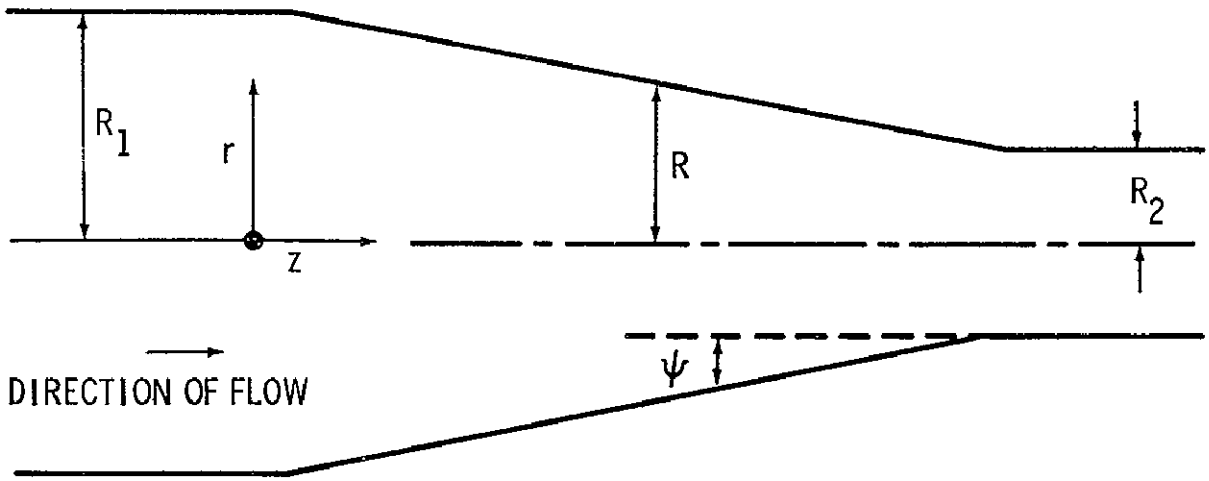
# METER'S FRICTION FACTOR CORRELATION



0.3% HYDROXYETHYLCELLULOSE

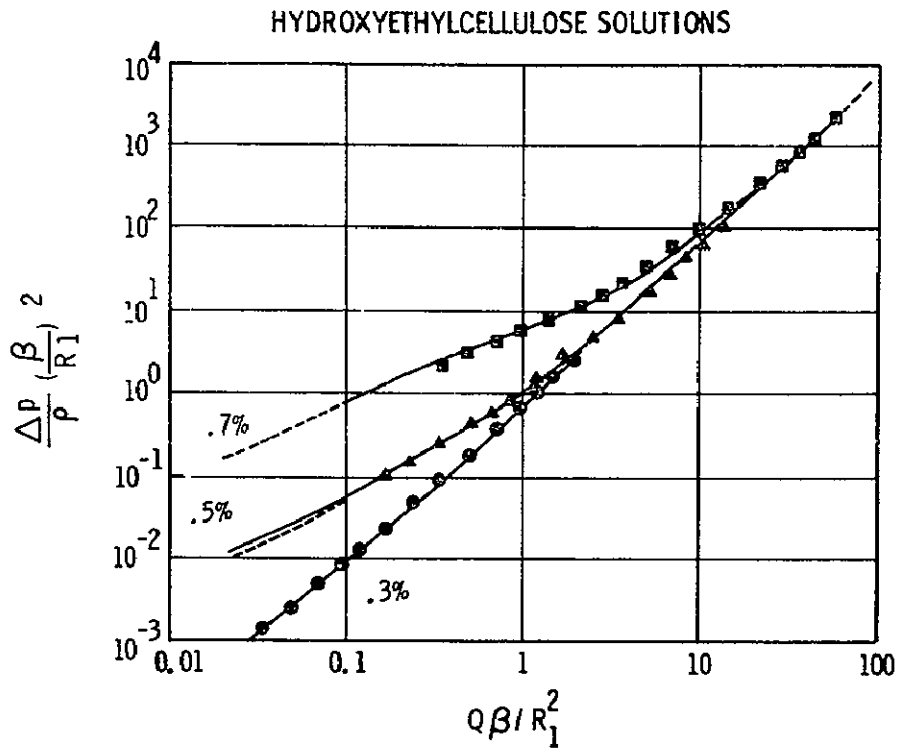
FREDRICKSON'S ANNULAR FLOW DATA  
FOR CMC



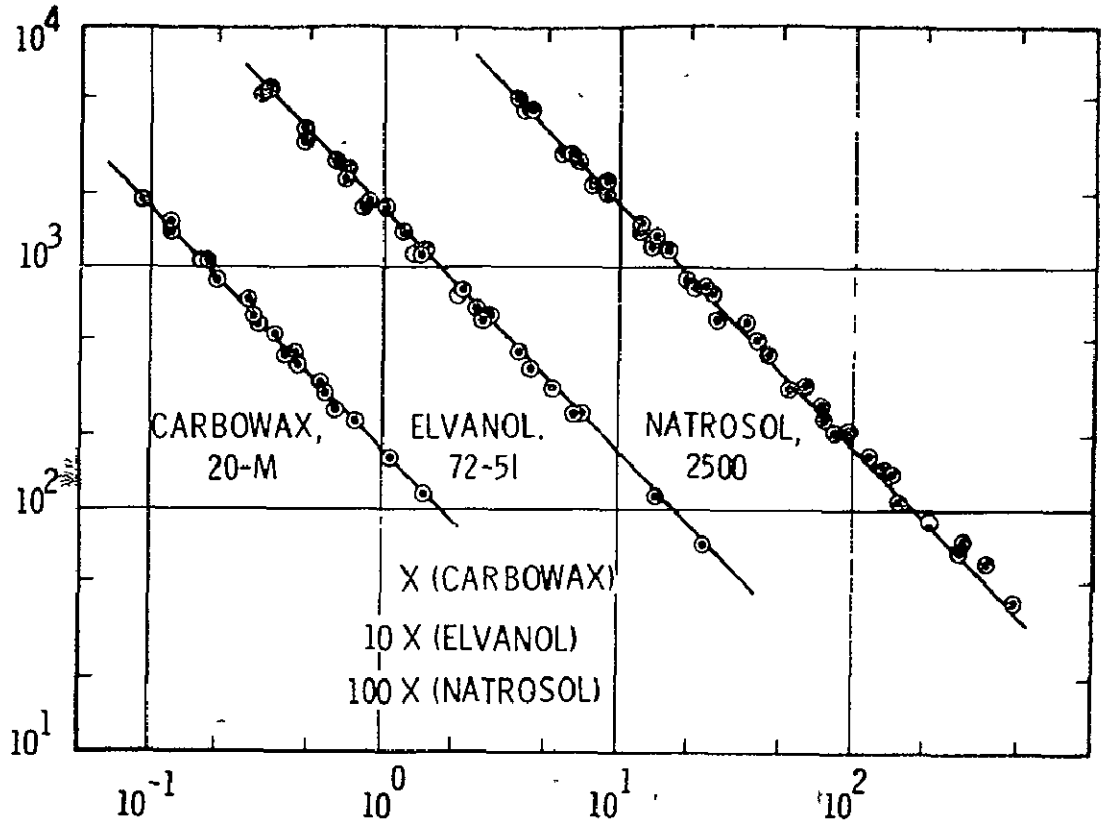


CONVERGING FLOW SECTION

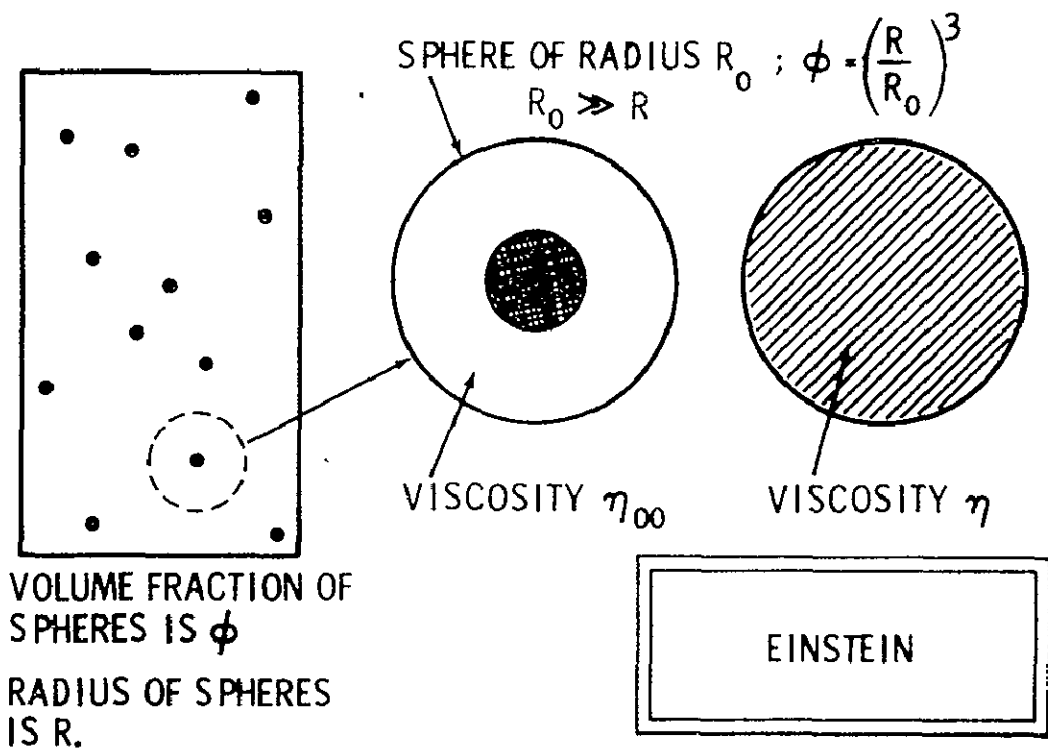
$$\Psi = 7^{\circ}5'50''$$



SUTTERBY'S CONVERGING FLOW DATA AND THEORETICAL RESULTS



SADOWSKI'S PACKED BED DATA AND CALCULATED CURVES BASED ON ELLIS MODEL



# LOW TEMPERATURE THERMODYNAMICS

By

Richard E. Sonntag  
University of Michigan  
Ann Arbor, Michigan

Introduction

N70 - 18688

Thermal analysis of processes involving simple substances and their mixtures at near-ambient conditions has not commonly presented any unusual problems, because in this range the behavior of such systems can be predicted or correlated by simple and familiar models. In recent years, however, it has become necessary to consider the thermodynamic behavior of these substances at extreme conditions of both temperature and pressure, each extreme having its own class of problems that does not lend itself to as simple an analysis.

The purpose of this discussion is to consider the low temperature region, in which problems of thermodynamic phase behavior become of fundamental interest and importance. Two classes of processes in which phase equilibrium problems arise will be discussed, with particular emphasis on the low temperature system hydrogen-helium.

## Condensation Problem

To illustrate this problem, let us begin by considering the simple process of cooling a pure gas (for example, nitrogen or oxygen) in a heat exchanger. The thermodynamic properties and various phase boundaries of most pure substances in the cryogenic region are reasonably well known at low and moderate densities, and for a few substances at high density. Thus, the gas behavior during cooling and the conditions at which various phase changes will occur can be predicted with a high degree of confidence. Of course, heat transfer and flow considerations are vitally important to such an analysis, but not to the purpose of this discussion.

This condensation process becomes much more complex if a mixture instead of a pure gas is being cooled, and is much less capable of being satisfactorily analyzed at the present time. Knowledge of the thermodynamic behavior of the gas mixture (enthalpy, for example), requires experimental measurements, calorimetric or P - V - T - Y. Except for the low density region, these have been almost non-existent in the low temperature range until the past few years. Consequently, analytical correlations of this type are not well developed. The phase equilibria can, in principle, be predicted from pure component phase behavior and P - V - T - Y behavior of the individual phases, but again, experimental data for the latter are very sparse at present and efforts in predictions of this type have not been generally successful.

Certain special problems can be correlated by analytical techniques, however, and help to give an insight into the more general problem. As an example of such a simplified phase equilibrium problem, consider the selective freezing of component "A" from a binary gas mixture of "A" and "B" being cooled to a low temperature. This process may be used in the purification of gas "B," or the situation may simply arise in cooling the gas to low temperature for liquefaction. In either case, it is important to know the amount of "A" being solidified from the mixture onto the heat exchanger tubes.

This situation can be classified as a binary solid vapor phase equilibrium problem, and commonly the condensed phase can be assumed to be pure "A." It is not the purpose of this presentation to develop an analysis of this problem. Nevertheless, a brief discussion of a set of assumptions commonly made in developing a simplified model will help to point out the regime in which such a model is or is not reasonable. The requirement for the equilibrium of "A" between the two phase at a given T, P can be expressed in terms of the fugacities as

$$f_A^{\text{SOL}} = f_A^{\text{GAS}} \quad (1)$$

The solid phase fugacity at T, P is given in terms of the fugacity of saturated "A" at the same temperature T and saturation (sublimation) pressure

$$P_A^{\text{SAT}} \text{ as } \ln \left( \frac{f_A^{\text{SOL}}}{f_A^{\text{SAT}}} \right) = \frac{1}{RT} \int_{P_A^{\text{SAT}}}^P V_A^{\text{SOL}} dP \quad (2)$$

The fugacity of component "A" in the gas mixture can be expressed in terms of the P - V - T - Y behavior of the mixture. Thus, the problem can, in principle, be evaluated for the composition of the gas mixture at equilibrium.

Let us now make a set of three assumptions regarding this phase equilibrium:

1. The right-hand side of equation 2 is negligibly small; i. e. ,  

$$f_A^{\text{SOL}} = f_A^{\text{SAT}}$$
2. Pure saturated vapor "A" at T,  $P_A^{\text{SAT}}$  behaves as an ideal gas; i. e. ,  

$$f_A^{\text{SAT}} = P_A^{\text{SAT}}$$
3. The gas mixture at T, P behaves as an ideal gas mixture;  
i. e. , 
$$\bar{f}_A^{\text{GAS}} = Y_{A_0} P$$

Substituting, equation (1) becomes

$$P_A^{\text{SAT}} = Y_{A_0} P \quad (3)$$

which is the equilibrium equation commonly used in analyzing familiar thermodynamic problems of this type (e.g., saturated air-water vapor mixtures at near ambient conditions). Of the assumptions made in developing this simplified model, the third assumption is generally the most serious. Careful consideration must be given to the regions in which equation (3) is used to predict equilibrium composition, because it may be in error by unexpectedly large amounts. A convenient parameter for evaluating the system departure from ideal behavior is the ratio of the actual mole fraction  $Y_A$  to that given by equation (3),  $Y_{A_0}$ , or

$$\epsilon = \frac{Y_A}{Y_{A_0}} = \frac{Y_A P}{P_A^{\text{SAT}}} \quad (4)$$

A number of solid-vapor systems have been studied experimentally in recent years, and compared with analyses that include the corrections and

utilize accurate equations of state to predict the mixture P - V - T behavior. An example of this type of investigation is the CO<sub>2</sub> - N<sub>2</sub> system [1], with CO<sub>2</sub> solidifying from gas mixtures of the two components. The apparatus required for experimental measurements of this type is shown schematically in Figure 5, and a set of results, experimental and analytical, in Figure 6. It is seen that the departure from ideal behavior becomes extremely large, with the gas-phase concentration of CO<sub>2</sub> being 250 times that predicted by equation (3) at the highest pressure studied.

It is also seen that the various analytical equations used in the more general analysis give very good predictions of the composition within the range of validity of the equations themselves. The analytical solution is involved and tedious, even for a simple phase problem as posed here. For more complex equilibria, predictions become even more difficult, and in all cases rely very heavily on the accuracy with which the P - V - T - Y behavior of the phases can be represented.

## Tank Pressurization Problem

The storage or transfer of a cryogenic liquid by pressurizing with an "inert" gas, commonly helium, leads to another consideration of binary phase equilibria in the low-temperature region; this is a liquid-vapor equilibrium problem. Under most conditions, there will be only a small amount of helium in the liquid, and the vapor will be mostly helium. Knowledge of the phase compositions at different temperatures and pressures is a necessary prerequisite to analysis of a transfer process.

The general lack of present ability to predict even this problem has led to a number of experimental studies of liquid-vapor equilibria in binary systems. The hydrogen-helium system is one of particular interest in the field of cryogenics, and has been investigated over a fairly extensive range of temperature and pressure during the past several years. The majority of this work [2] was done using normal hydrogen for convenience, and comparisons made using parahydrogen [3].

A schematic diagram of the vapor-recirculation apparatus used in this research is shown in Figure 7, and a portion of the results in Figures 8 - 11. Of particular interest in this study were the solubilities of helium in the liquid phase as a function of T and P, given in Figure 9.

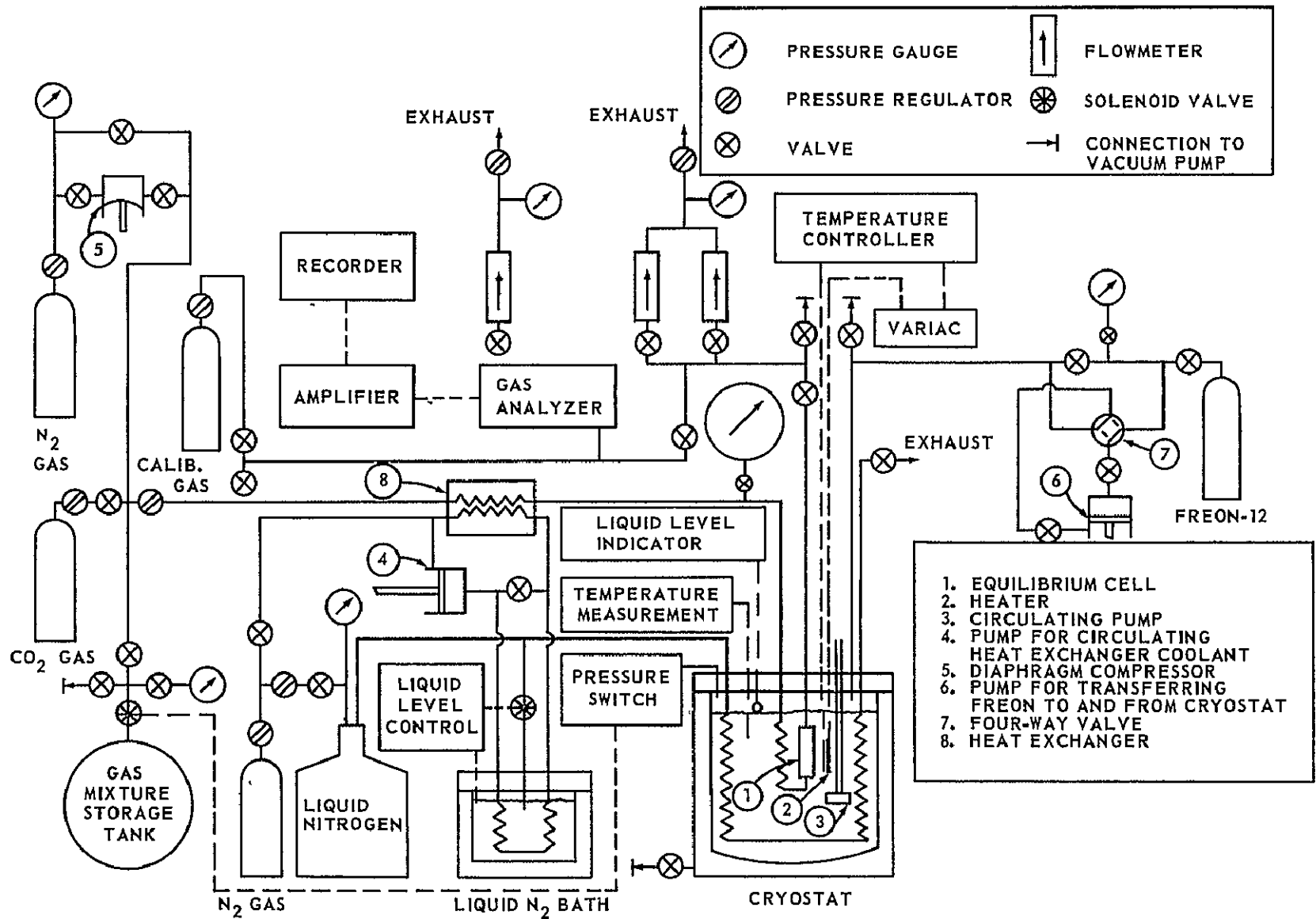


FIGURE 5. SCHEMATIC DIAGRAM OF EXPERIMENTAL EQUIPMENT

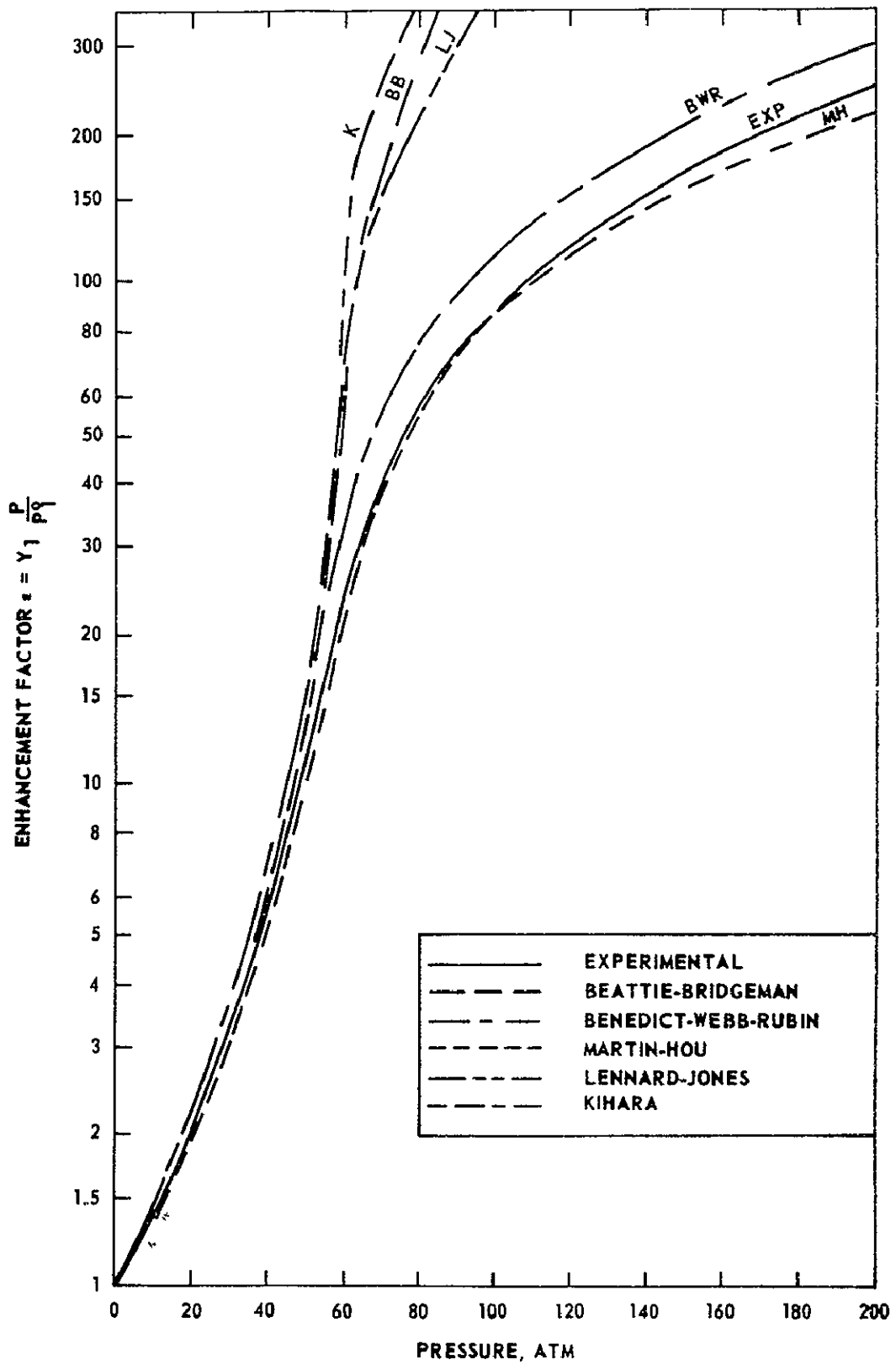


FIGURE 6. GENERAL SOLUTIONS AT 140°K

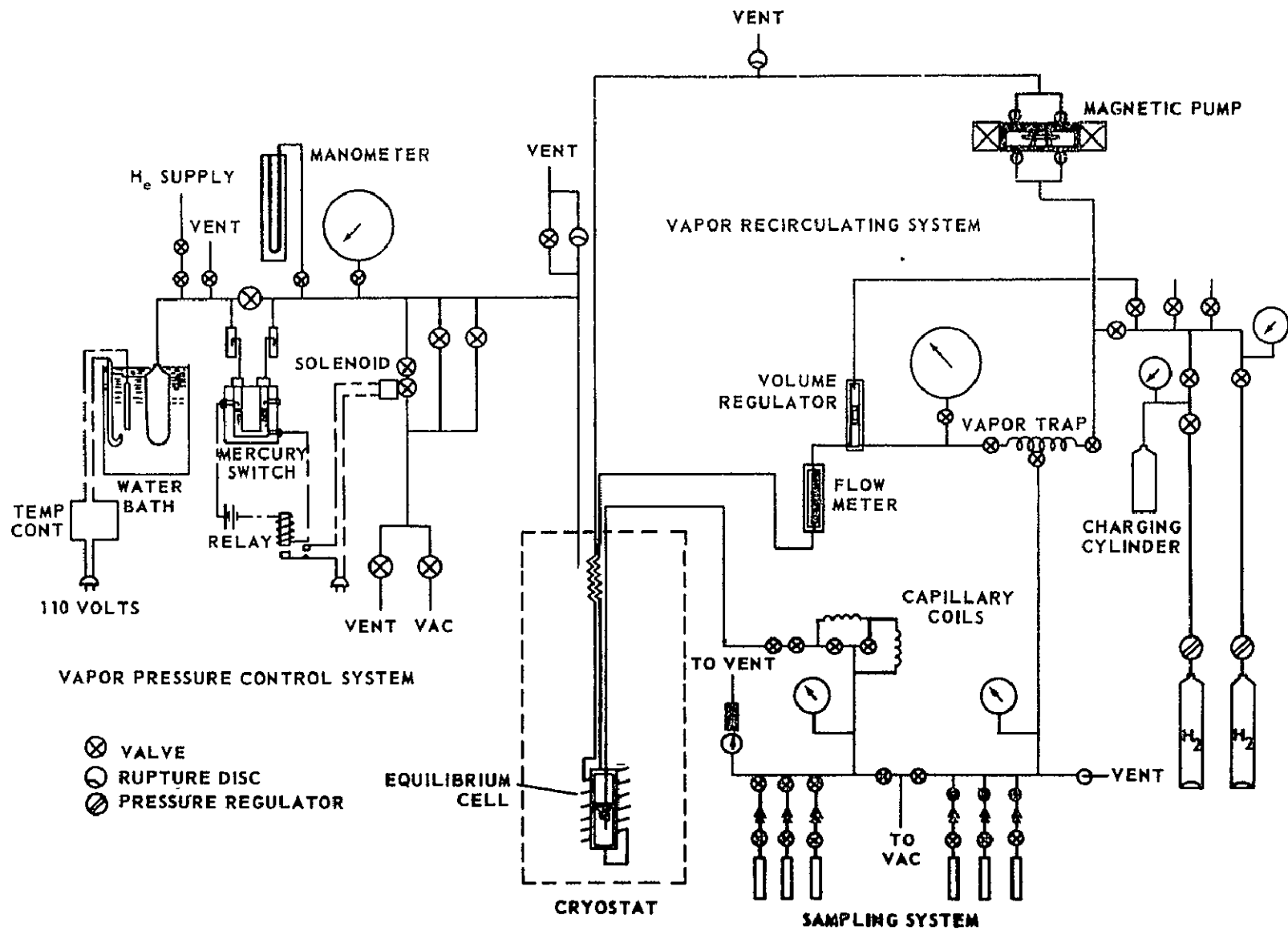


FIGURE 7. SCHEMATIC DIAGRAM OF EXPERIMENTAL EQUIPMENT

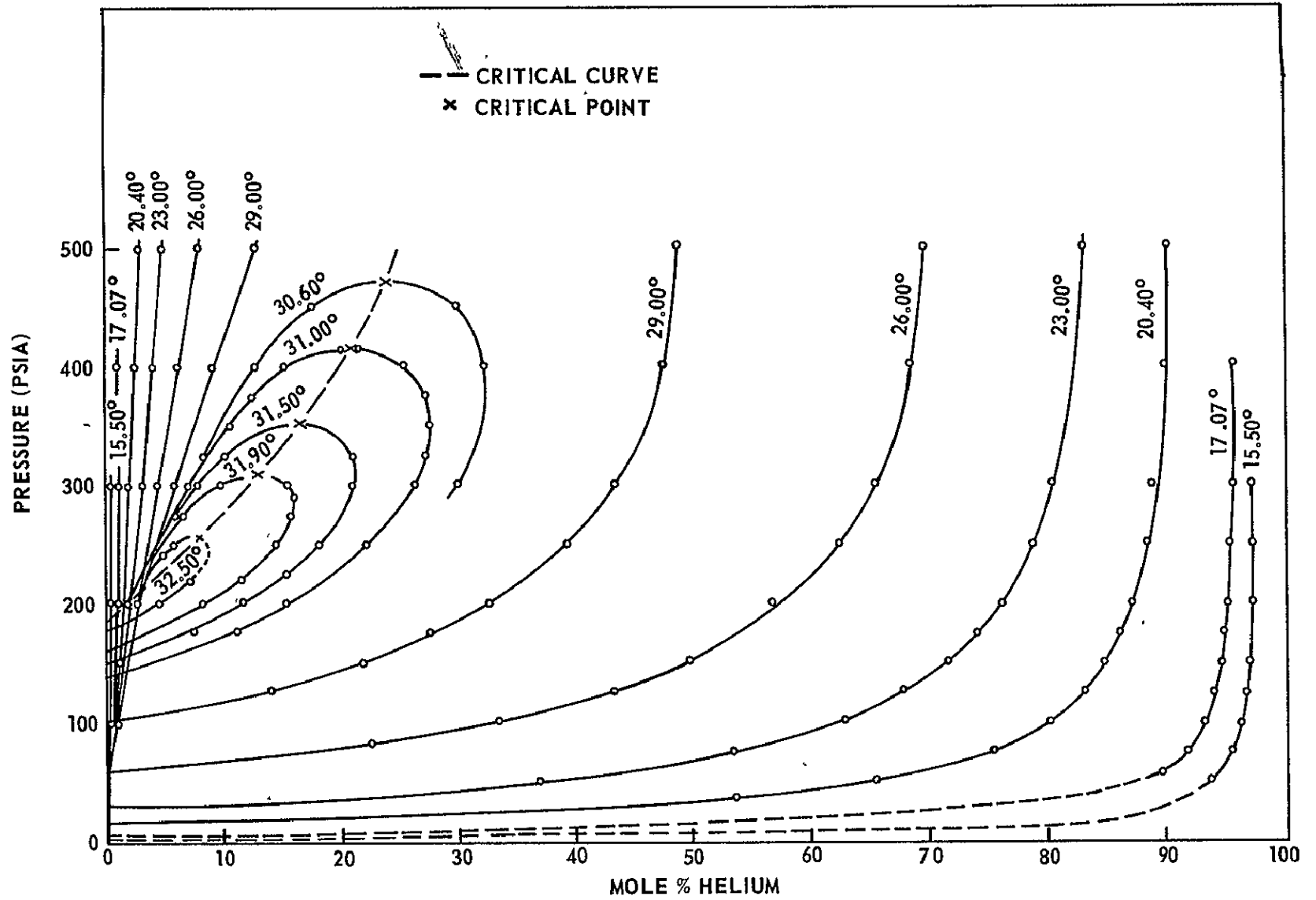


FIGURE 8. ISOTHERMAL PRESSURE-COMPOSITION DIAGRAM

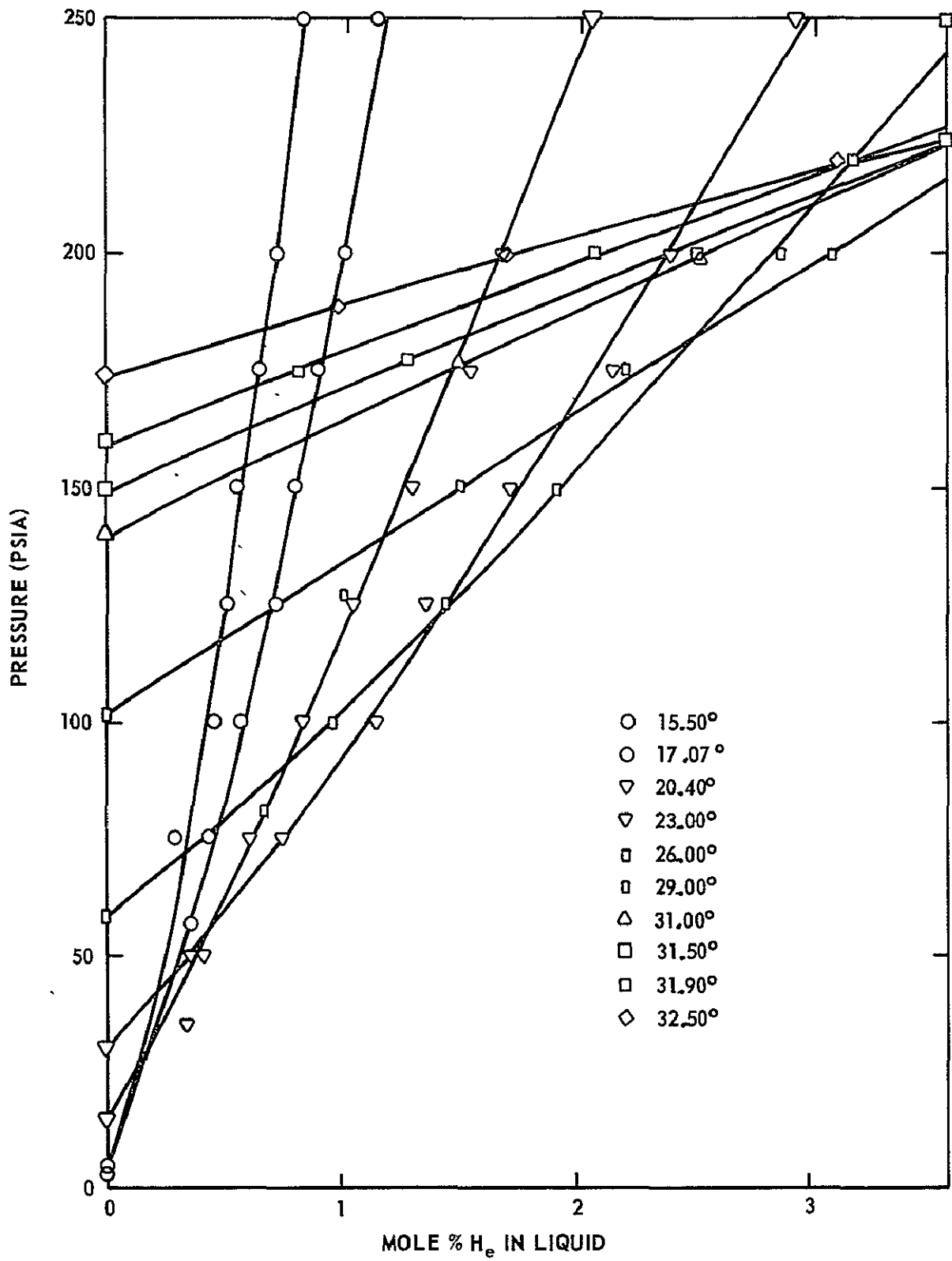


FIGURE 9. ISOTHERMAL PRESSURE-COMPOSITION DIAGRAM SHOWING LIQUID REGION ON EXPANDED SCALE

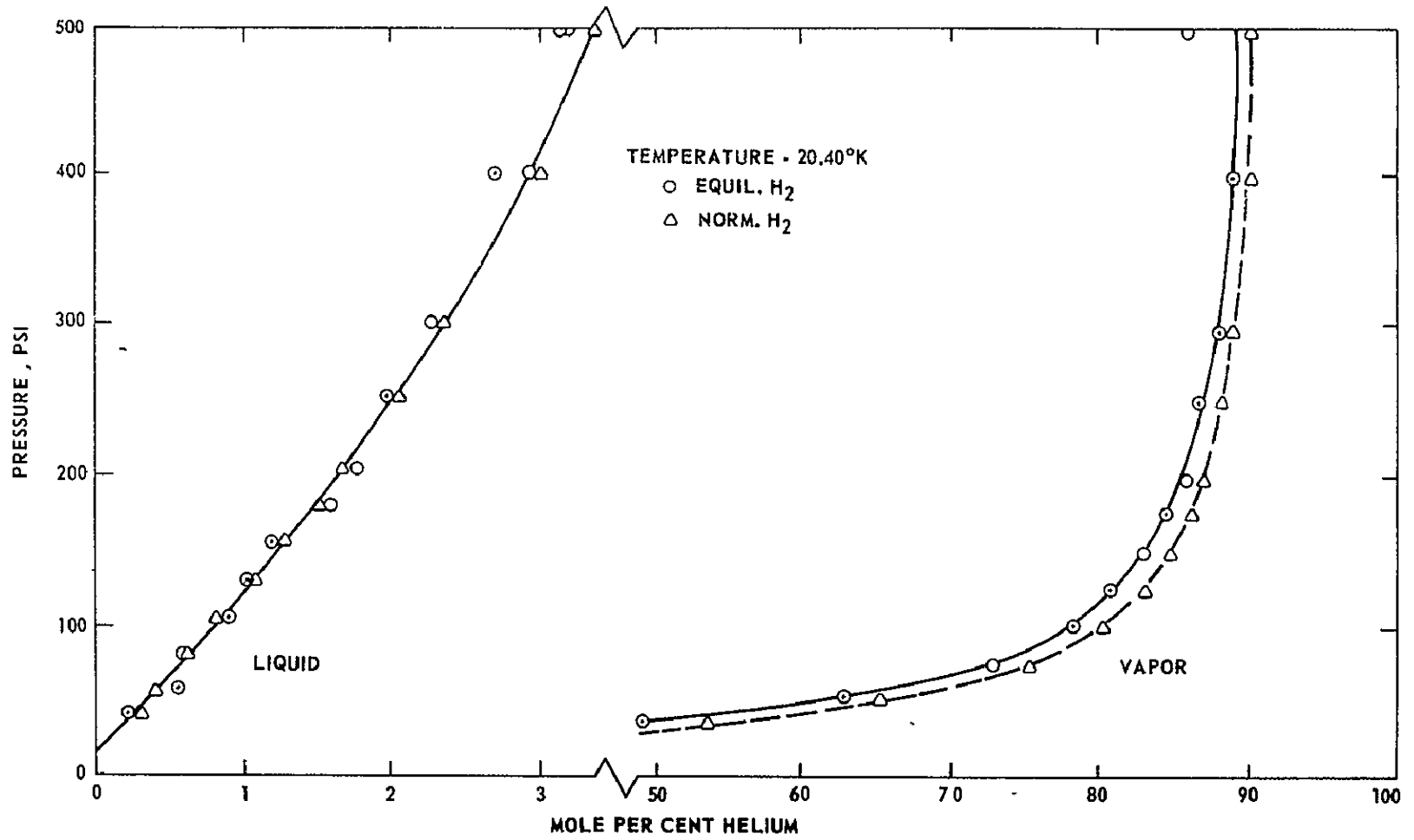


FIGURE 10. COMPARISON OF THE TWO SYSTEMS AT 20.4°K

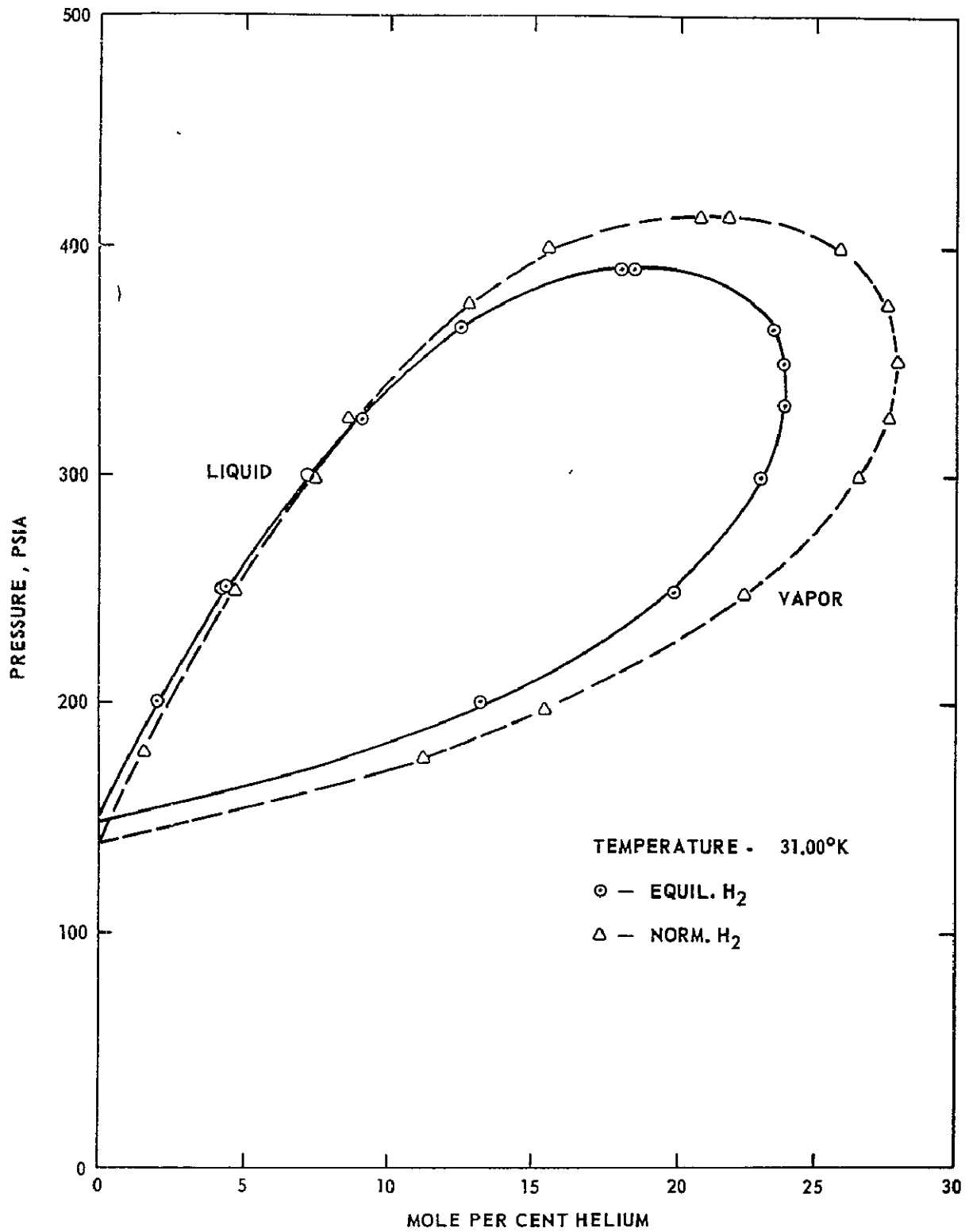


FIGURE 11. COMPARISON OF THE TWO SYSTEMS AT 31.5°K

Measurements of liquid and vapor compositions in this system have more recently been extended to higher pressures [4], using the same type of technique. The results shown on the plot of Figure 12 have a shape in the vicinity of 28°K that is characteristic of a system exhibiting a high - pressure phenomenon commonly termed gas-gas equilibria. This occurs where the system critical locus changes to a positive slope on a P - T projection, and is believed to exist for the hydrogen-helium system, although not directly confirmed.

Another phenomenon studied in this research was the phase-density inversion locus, that condition under which the vapor (helium rich) phase becomes more dense than the liquid (hydrogen rich) phase, and settles to the bottom of the containing vessel. This locus is shown in Figure 13.

In connection with the problem of liquid hydrogen storage, it has been proposed to store cryogenic hydrogen in a slush form, mixtures of the solid and liquid phases. The technique appears promising at present, and has two significant advantages over liquid storage: higher density, with resulting decrease in storage volume; and decreased storage losses, resulting from the heat of fusion of the solid and heat capacity of the subcooled liquid.

Consequently, a study to evaluate the lower-temperature liquid-vapor and solid-liquid-vapor equilibria in the hydrogen-helium system was undertaken, and has recently been completed [5]. A glass dew-bubble point apparatus, Figure 14, was used to determine the various phase boundaries in this region. Results of particular interest are the liquid-phase compositions in the liquid-vapor region, Figure 15, and the liquid and vapor compositions on the three-phase surface, shown in Figure 16. Research on this type of system is being extended at the present time to evaluate the effects of ambient and other heating on the storage of slush mixtures.

## References

1. Smith, G. E., Sonntag, R. E., and Van Wylen, G. J.: Advan. Cryog. Engr., v. 9, 197, 1964.
2. Streett, W. B., Sonntag, R. E., and Van Wylen, G. J.: J. Chem. Phys., v. 40, 1390, 1964.
3. Sonntag, R. E., Van Wylen, G. J., and Crain, R. W., Jr.: J. Chem. Phys., v. 41, 2399, 1964.

4. Sneed, C. M.: Ph.D. dissertation, University of Michigan, 1966.
5. Greene, N. E.: Ph.D. dissertation, University of Michigan; 1966.

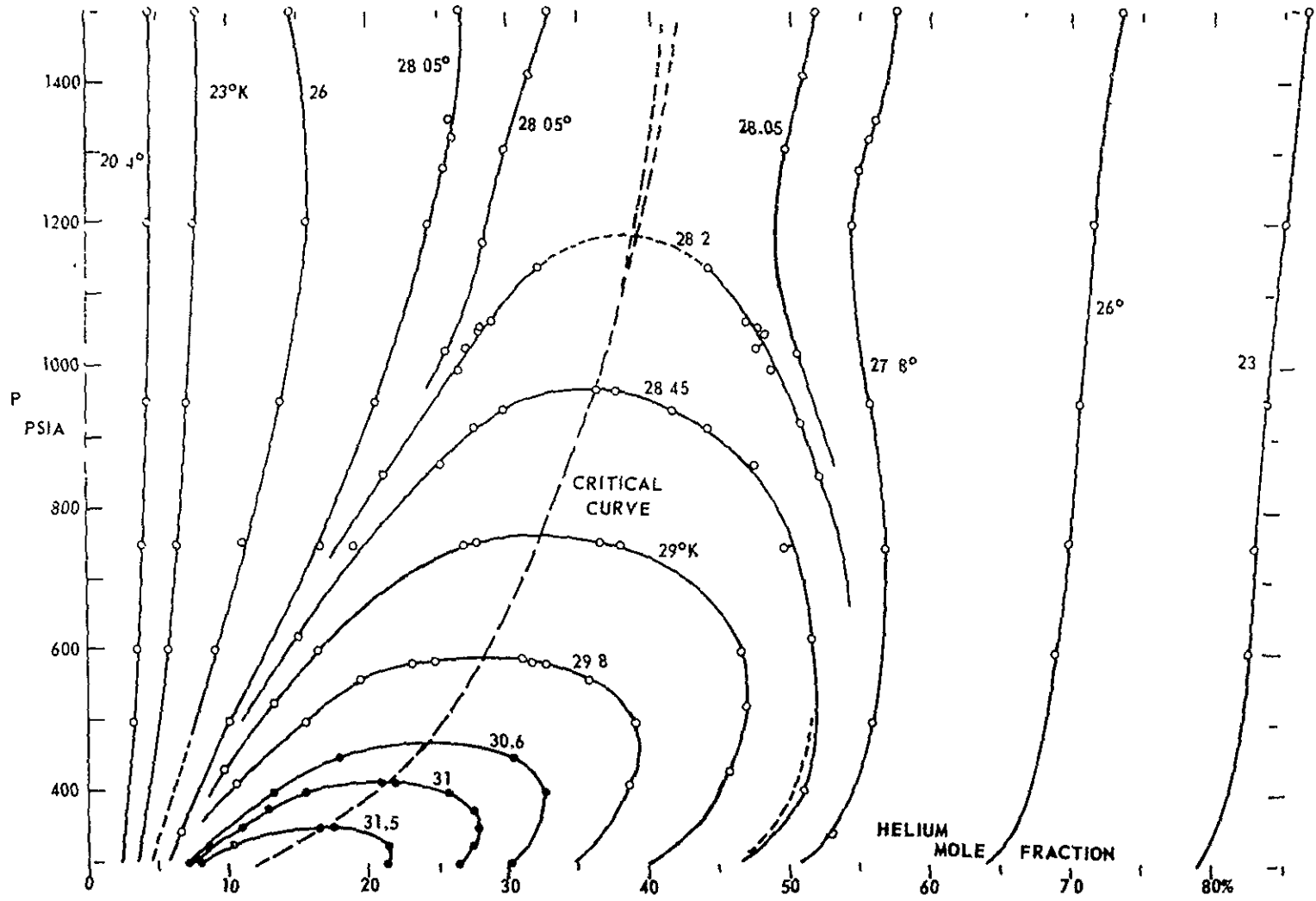


FIGURE 12. ISOTHERMAL PRESSURE-COMPOSITION DIAGRAM

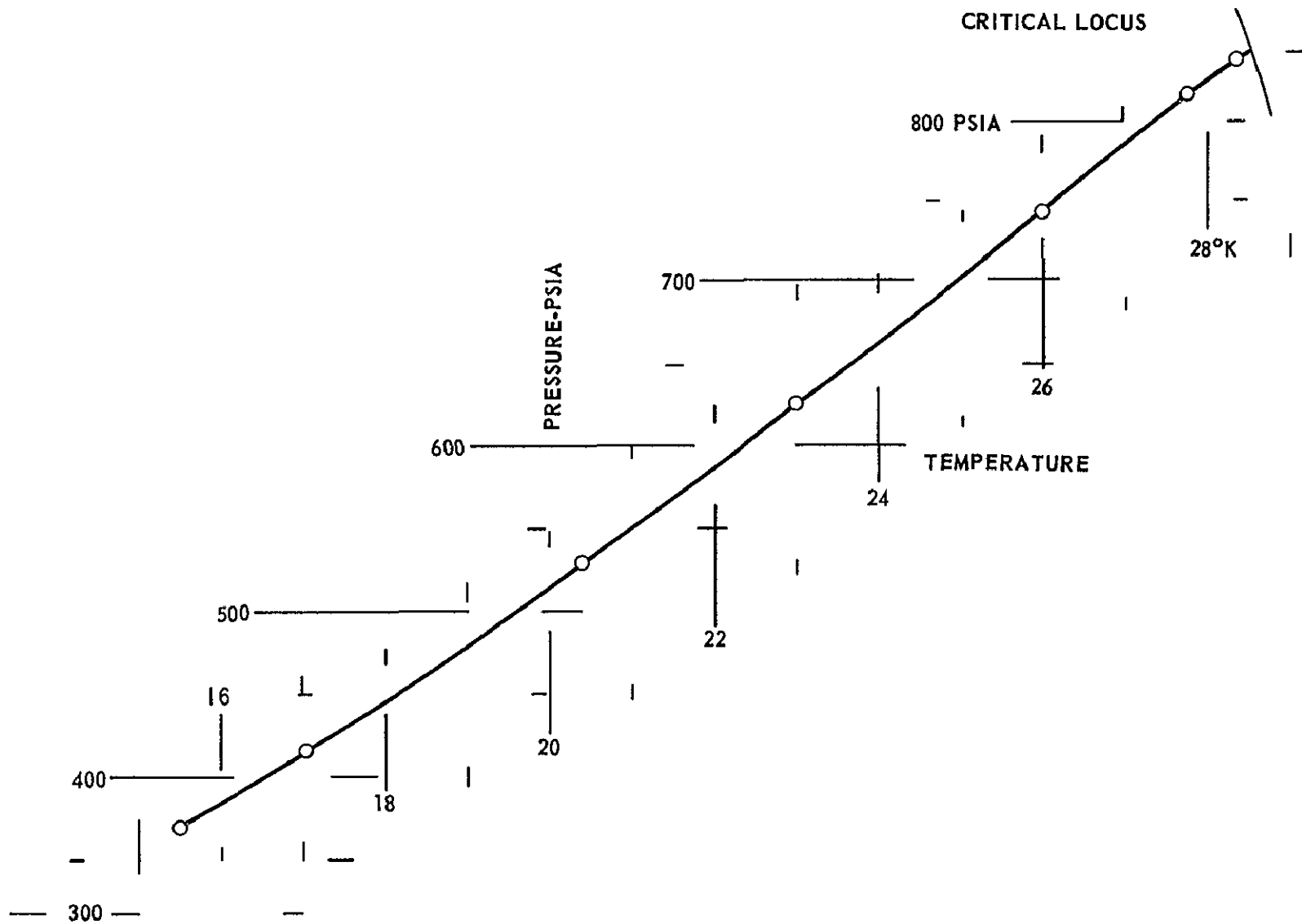


FIGURE 13. INVERSION CURVE OF BAROTROPIC PHENOMENON

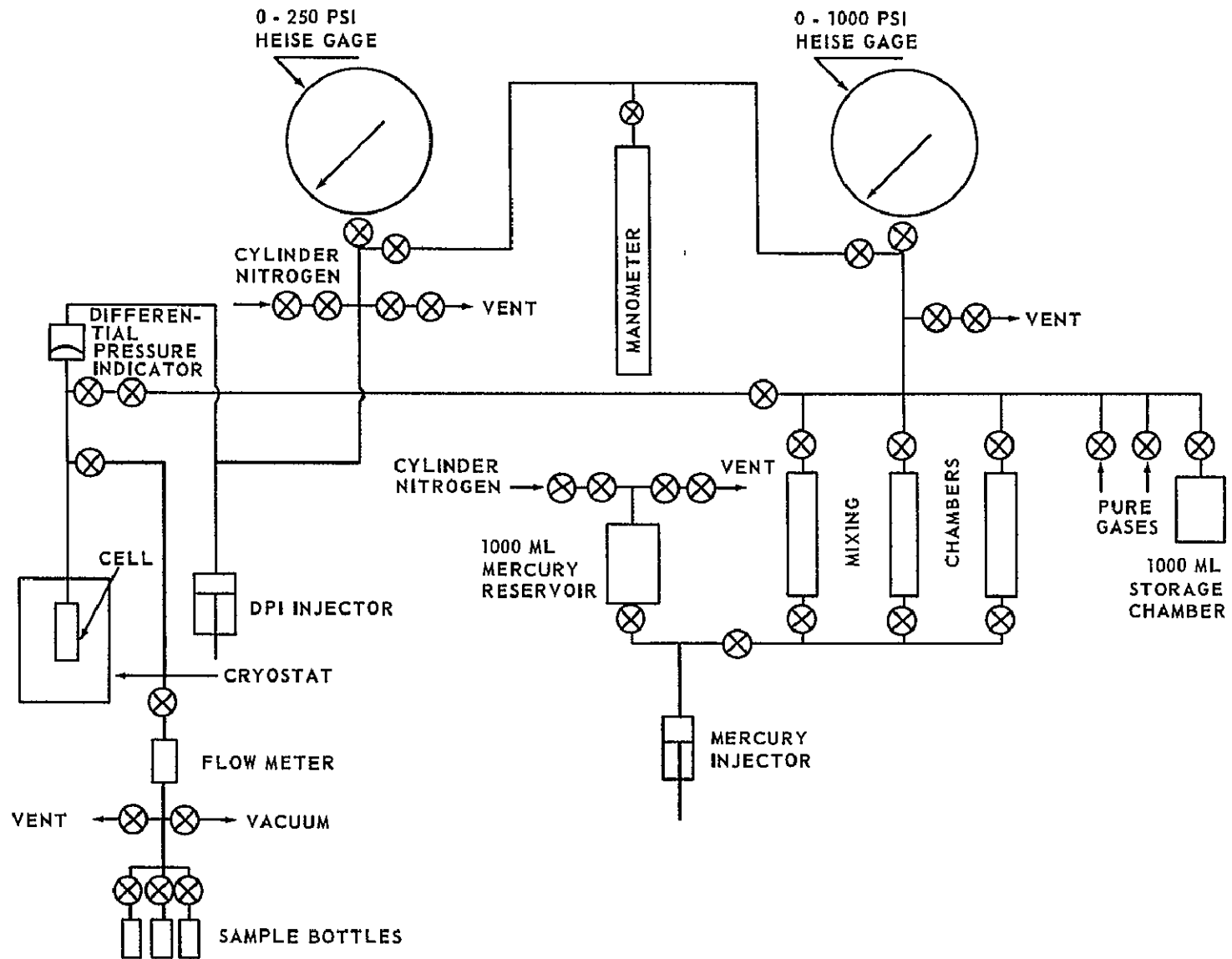


FIGURE 14. SCHEMATIC DIAGRAM OF EXPERIMENTAL SYSTEM

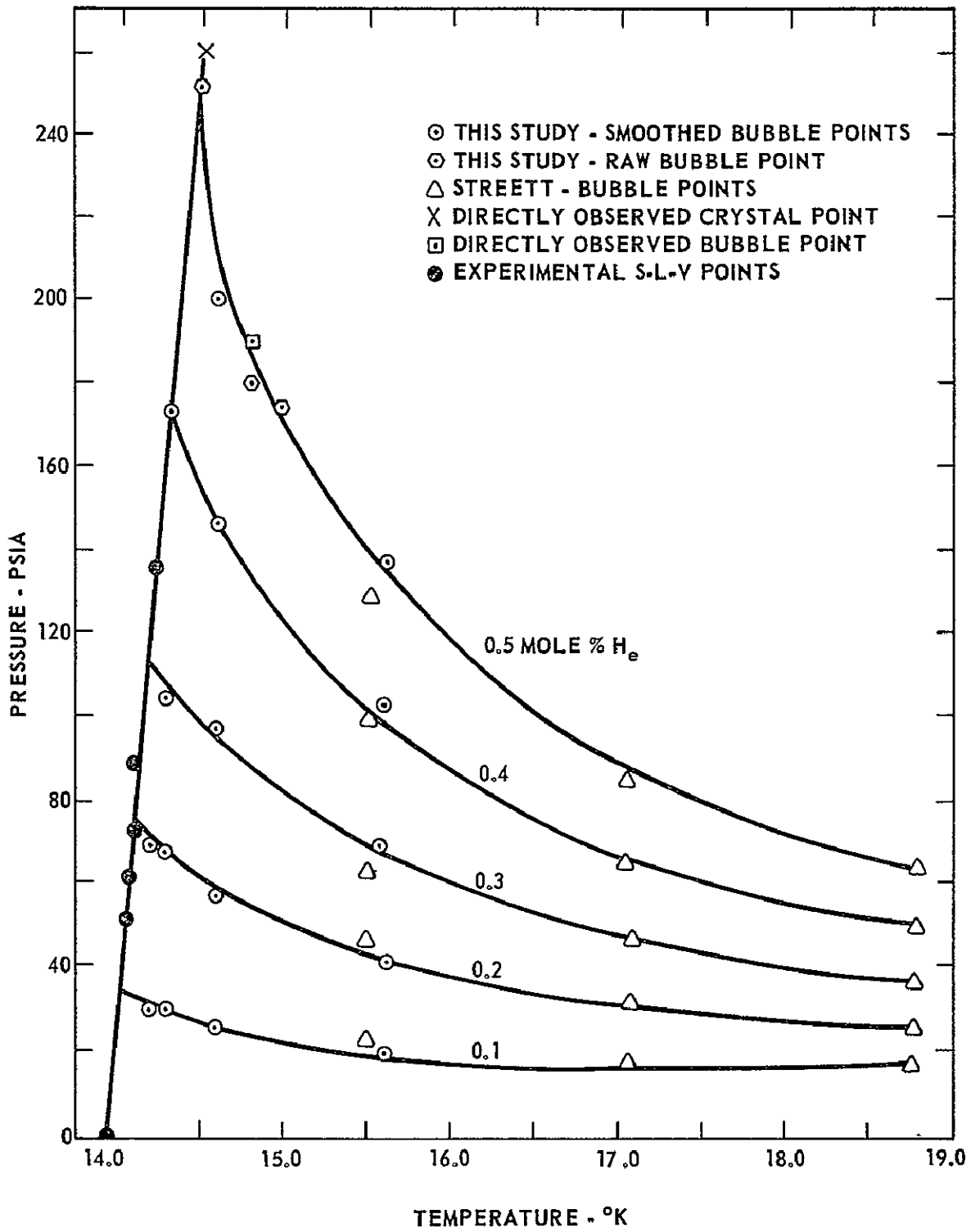


FIGURE 15. PRESSURE-TEMPERATURE DIAGRAM FOR BUBBLE-POINT LIQUIDS

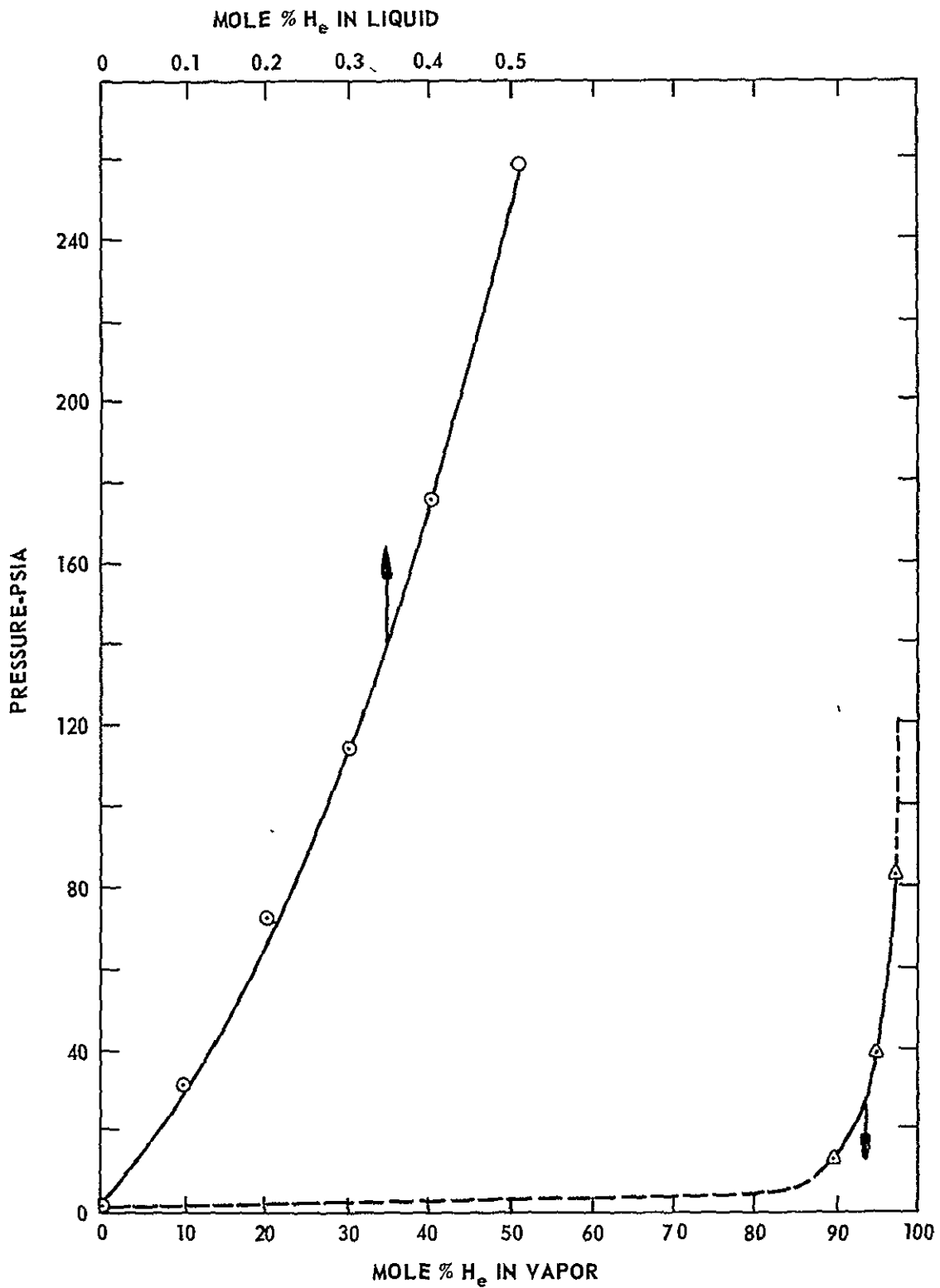


FIGURE 16. PRESSURE-COMPOSITION DIAGRAM FOR LIQUID AND VAPOR PHASES ON THE THREE-PHASE SURFACE

# SOME ASPECTS OF AERODYNAMIC HEATING

By

R. W. Truitt  
North Carolina State University  
Raleigh, North Carolina

Introduction

N70 - 18689

The problem of continuum aerodynamic heating on a body involves the solution of the boundary layer over the body. Generally speaking, the solution of the boundary layer over a body depends on first, determining the local inviscid (or aerodynamic) flow over the body. The simplest body is, of course, that of an infinitely thin flat plate at zero angle of attack and, as a first approximation, it becomes a trivial aerodynamic problem since one may assume with good approximation that the pressure gradient is zero in all directions. On the other hand, for certain combinations of Mach numbers and Reynolds numbers, the boundary layer thickness on the flat plate may cause the flow to "feel" a body of finite thickness such that the assumption of zero pressure gradient is no longer valid. The solution to the "flat plate" boundary layer then becomes considerably more complex and the classical boundary-layer-shock-wave interaction phenomenon must be considered as a dominant factor in the aerodynamic heating problem. If the boundary layer flow over a simple or complex body shape, either two-dimensional or axisymmetric, is to be calculated, the local inviscid flow field must be found. In the cases in which aerodynamic heating is involved, this means that one is confronted with the rather formidable task of determining the local inviscid flow field where the local pressure, density, temperature, etc., are varying from point to point over the body. Unfortunately, the flow and thermophysical properties of the fluid are strong functions of the altitude, speed of flight, the kind of gas, and the attitude and shape of the body. Numerical techniques of varying complexity and accuracy are available, not only for solving the inviscid flow field but for the local boundary layer as well. No completely satisfactory solutions for either the inviscid flow field or the boundary layer have been found that consider the actual non-equilibrium flow over a typical blunt-nosed flight vehicle at hypersonic speeds. However, some real progress has been made that allows the approximate solutions for some important limiting cases.

It is the purpose of this paper to review the factors involved in the calculation of the aerodynamic heating over a typical blunt-nosed body at hypersonic speeds, with particular attention to the problem of determining the local inviscid flow field under the most realistic flow condition, i. e. , non-equilibrium flow. It should be emphasized that this is undoubtedly the most important factor in the aerodynamic heating problem, since the local freestream conditions of pressure, temperature, density, degree of dissociation and ionization must be known before any attempt can be made to solve the corresponding boundary layer problem.

Once the local conditions have been determined, the general governing equations of the boundary layer must be cast in a form that considers the viscous non-equilibrium flow of a reacting gas under gradients in the flow direction of pressure, temperature, density, dissociation, ionization, etc., and for wall conditions that must involve the chemical character of the wall (material, surface condition, catalysis, etc.). At the present time, some rather sophisticated numerical solutions for the non-equilibrium hypersonic laminar boundary in air have been calculated for flat plates under special wall conditions. The results found are valuable, but in no way represent what could be classified as satisfactory for practical aerodynamic bodies. No satisfactory solutions for separated, transitional, or turbulent boundary layers have been found for non-equilibrium hypersonic flows.

Perhaps the classical case that embodies all of the various conditions of flow regimes and thermophysical conditions is that of the flow over a blunt-nosed body at hypersonic speeds ( Fig. 17) . Here one sees the characteristic bow shock wave standing off from the body a certain distance,  $d$ . The formation of the shock represents the mechanism of heating the gas as it flows from the relatively cold freestream, experiencing an abrupt rise in pressure, temperature and density, a decrease in velocity and a decrease in Mach number. Generally speaking, the abrupt rise in pressure, density, temperature, etc. is accompanied by abrupt changes in the character of the gas. That is, before the gas passes through the shock and indeed as it passes through the shock and experiences the abrupt rise in pressure, temperature, etc., in one to two mean free paths, the gas is said to have certain "active" and "inert" degrees of freedom. For a monatomic gas, the active degrees of freedom are those in translation, i. e. there are 3 active degrees of freedom, and the ratio of specific heats  $\frac{c_p}{c_v} = \gamma = 1 + \frac{2}{z}$ , where  $z$  is the number of (classic) degrees of freedom. Thus for a monatomic gas under, say, room temperature,

$\gamma = 1 + \frac{2}{3} = 1.667+$ . For a diatomic gas at room temperature, there are 3 degrees of freedom in translation, and 2 in rotation that are "active" degrees of freedom and thus  $\gamma = 1 + \frac{2}{5} = 1.4$ . Now the inert degrees of freedom for the diatomic gas are those in vibration, dissociation, ionization, etc., in which energy is taken from the gas in order to cause these "excitations." For a monatomic gas there is no vibration or dissociation mode, but the gas may undergo excitation of the planetary electrons and experience high excited states, single ionization, double ionization, etc. Counting each excitation as a degree of freedom, it is clear that  $\gamma \rightarrow 1$  for very high temperatures.

When the cold gas passes through the shock, the active degrees of freedom are those in translation (for a diatomic gas, the 2 rotational degrees of freedom). The high temperatures generated then begin to activate the "inert" degrees of freedom. Now, whereas the active degrees of freedom are adjusted in one or two, or a few collisions (mean free paths), i. e., are adjusted "instantaneously," the inert degrees of freedom require several or many collisions to come to so-called equilibrium conditions. Since the gas is moving and time is involved in bringing the gas to equilibrium in the vibrational, dissociation or ionization mode, it is clear that there is a distance over which the gas is in a non-equilibrium state. The extent of the non-equilibrium regime downstream of the shock is one of the classical problems in the hypersonic flow over a blunt body and the nature and extent of the non-equilibrium flow determines, to a large extent, the character of the inviscid flow over the body, i. e., the local inviscid flow, which in turn determines the condition and nature of the local boundary layer.

The inviscid flow over the body may be thought of as the flow through a certain convergent-divergent nozzle (or streamtube) from a fictitious reservoir represented by conditions in the stagnation region of the blunt body. Clearly, then, the character of the flow, i. e., frozen, equilibrium or non-equilibrium, along the convergent-divergent streamtube, is a sole function of the initial conditions at the stagnation point. The initial conditions at the stagnation point are, of course, a function of the altitude and Mach number and, perhaps to some extent, the shape of the body. At any rate, for true hypersonic speeds one would anticipate the gas, if diatomic, to be either partially or fully dissociated and partially or fully dissociated and partly ionized; if a monatomic gas, it would be electronically excited and probably ionized. For either gas, the rate equations for the various reactions will require a certain time (or distance) to reach equilibrium and the problem is to determine if the flow has had time (or enough distance) to reach equilibrium

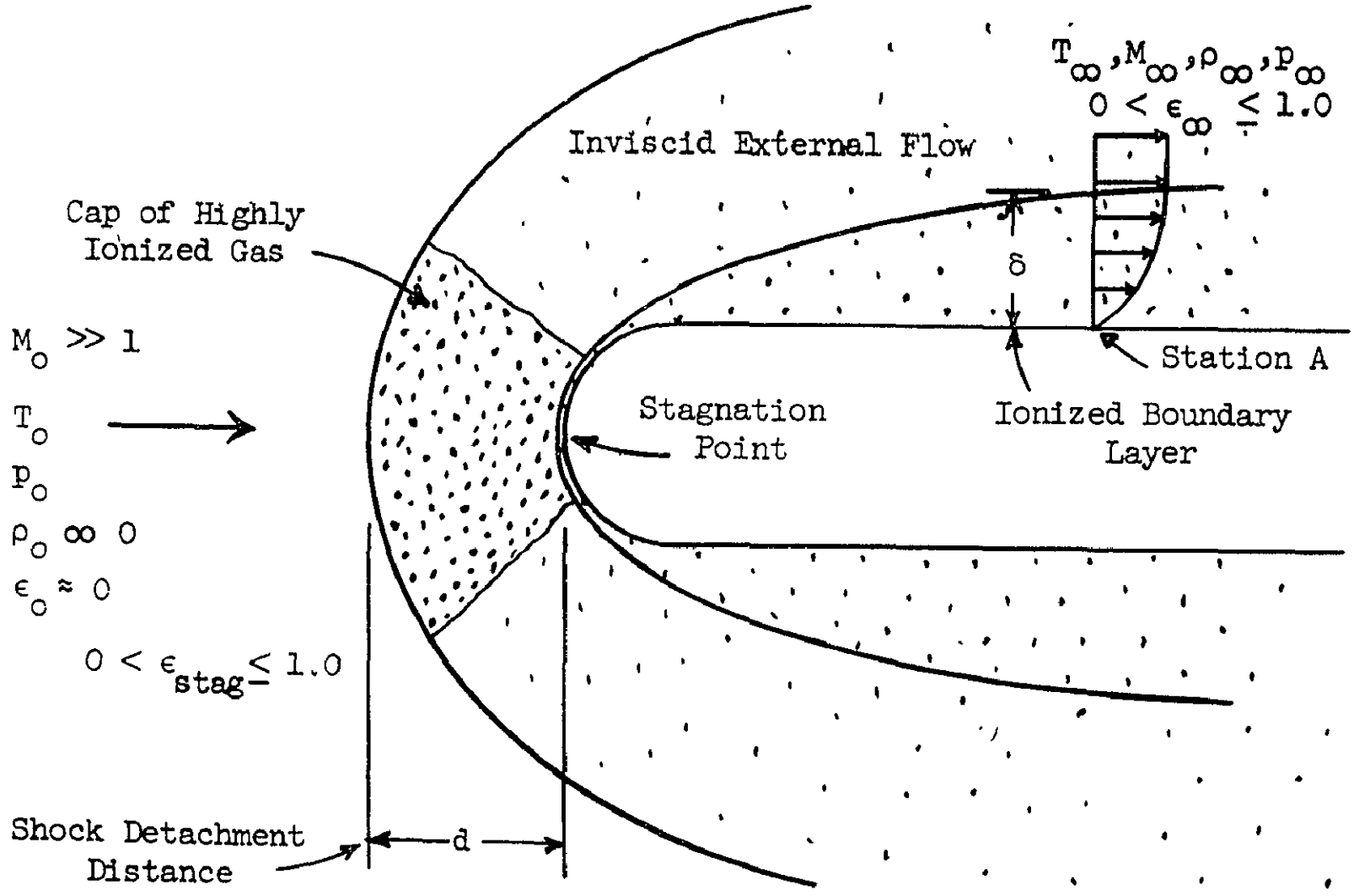


FIGURE 17. HEMISPHERE-CYLINDER FLOW GEOMETRY

at the stagnation point and, if it has, or has not, to determine what the conditions are at the stagnation point, i. e., the degree of dissociation, ionization, etc.

In the following, it will be of interest to examine briefly the various real gas problems in the hypersonic flow over a blunt body that are necessary to determine the local inviscid flow from which the boundary layer is determined and thus the skin friction and heat transfer, i. e. the aerodynamic heating. The first to be considered is the non-equilibrium flow downstream of the normal portion of the bow shock. This allows the determination of the conditions in the "reservoir" or stagnation region. Then the classical "equilibrium" nozzle flow is summarized for a reacting gas and some of its characteristics are discussed. A more general analysis of the equilibrium and frozen thermophysical properties are discussed in which both dissociation and ionization are considered. The frozen and equilibrium cases are important, since they represent the "bounds" of the actual gas state. That is, the actual gas flow is generally in the non-equilibrium condition which lies somewhere between the two extreme states of frozen (zero reaction rate) and equilibrium (infinite reaction rate). This will be carried out for the simplest possible gas, hydrogen, and then results for the so-called "air-like" ideal dissociating gas will be indicated, both for nozzle flow and the blunt body problem. The implications of these results in the calculation of the boundary layer skin friction and aerodynamic heating will be indicated. Finally, a review of the boundary-layer-shock-wave interaction problem will be given and its effect on aerodynamic heating will be discussed.

## Normal Shock Analysis

In order to treat the boundary layer over a blunt body (which is shown to an exaggerated scale in Figure 17) it is first necessary to determine the flow conditions through the bow shock wave. Since the external inviscid flow just outside the boundary layer represents the local "freestream" conditions needed for the calculation of the local boundary layer, the flow conditions along the stagnation streamline must be determined. For given freestream conditions, the solution for the flow through the normal portion of the bow shock gives the first step in determining the flow properties along the stagnation streamline.

An example of a normal shock analysis is outlined in Table IV. Details of this analysis are given in Reference 1. This analysis is carried out for argon and considers atom-atom and atom-electron collisions and takes into

TABLE IV. NORMAL SHOCK ANALYSIS

$$\begin{aligned} A + A &\neq A + A^+ + e \\ A + e &\neq A^+ + e + e \end{aligned} \quad (1)$$

$$\text{Mass:} \quad \rho u = \rho_0 U \quad (2)$$

$$\text{Momentum:} \quad p + \rho u^2 = \rho_0 U^2 \quad (3)$$

$$\text{Energy:} \quad i + u^2/2 = U^2/2 \quad (4)$$

where the enthalpy,  $i$ , of the gas is

$$i = (5/2) (k/m) [T_a + \epsilon T_e] + (k/m) T_{ion} \epsilon \quad (5)$$

$$p/\rho = (k/\pi) [T_a + \epsilon T_e] \quad (6)$$

$$T_a^* = (\lambda/2) \left\{ (5/8) [1 - (4/5)^2 (\lambda - \epsilon)/\lambda]^{1/2} + (3/8) - (\epsilon/\lambda) \right\} - \epsilon T_e^* \quad (7)$$

$$\rho^* = (\rho_0/\rho_{ion}) / \left\{ 1 - (2/\lambda) [T_a^* + \epsilon T_e^*] - (\epsilon/\lambda) \right\} \quad (8)$$

$$\lambda = mU^2/2 k T_{ion} \quad (9)$$

$$T_a^* = T_a/T_{ion} \quad T_e^* = T_e/T_{ion} \quad \rho^* = \rho/\rho_{ion} \quad (10)$$

TABLE IV. NORMAL SHOCK ANALYSIS (Concluded)

$$u (d\epsilon/dx) = (\rho/m) \{ (1 - \epsilon) A_1 T_a^{3/2} [(T_{exc}/T_a) + 2] \exp(-T_{exc}/T_a) \times \\ \{ (1 - \epsilon) - (\epsilon A_3 \exp(1/T_a^*)) / T_a^{3/2} \} + \\ \epsilon A_2 T_e^{3/2} [(T_{exc}/T_e) + 2] \exp(-T_{exc}/T_e) \{ (1 - \epsilon) - \\ (\epsilon A_3 \exp(1/T_e^*)) / T_e^{3/2} \} \} \quad (11)$$

in which, for argon,  $A_1 = 0.1488 \times 10^{-17}$ ,  $A_2 = 0.3759 \times 10^{-15}$ , and  $A_3 = 0.3451 \times 10^{-16}$  and  $T_{exc}$  is the energy of the first excited state

$$[(3/2)T_e^* + 1] \{ (1 - \epsilon) T_a^{*3/2} [(T_{exc}/T_a) + 2] \exp(-T_{exc}/T_a) \{ (1 - \epsilon) \times \\ T_{ion}^{3/2} - (\epsilon A_3 \exp(1/T_a^*)) / T_a^{*3/2} \} + \epsilon A_2 T_e^{*3/2} [(T_{exc}/T_e) + 2] \times \\ \exp(-T_{exc}/T_e) \{ (1 - \epsilon) T_{ion}^{3/2} - (\epsilon A_3 \exp(1/T_e^*)) / T_e^{*3/2} \} \} = A_8 \epsilon \sqrt{T_e} \times \\ \{ (\epsilon A_4 / T_e^*) \log_e [A_5 T_e^{3/2} / \sqrt{\epsilon \rho}] + (1 - \epsilon) [A_6 + A_7 (T_e^* - 0.016)^2] \} \times \\ (T_a^* - T_e^*) \quad (12)$$

where, for argon,  $A_4 = 0.1004 \times 10^{-4}$ ,  $A_5 = 0.7064 \times 10^{-8}$ ,  $A_6 = 0.1600 \times 10^{-16}$ ,  $A_7 = 0.5015 \times 10^{-13}$ ,  $A_8 = 0.1510 \times 10^2$

$$x = A_9 \int_{\epsilon_0}^{\epsilon_{eq}} \{ [1 - (2/\lambda) (T_a^* + \epsilon T_e^*) - (\epsilon/\lambda)]^2 / [F(T_a^*, \epsilon) + G(T_e^*, \epsilon)] \} d\epsilon$$

where  $A_9 = 0.2230 \times 10^{-11}$ . (13)

$$\lambda_D = k T_e / n^{1/3} e^2 \gg 5 \quad (14)$$

account the difference between the atom and electron temperatures during this non-equilibrium flow process. The integration of equation (13) (Table IV) allows the determination of the flow properties through the shock wave. Figure 18 shows the variation of the pressure,  $p$ , density,  $\rho$ , degree of ionization,  $\epsilon$ , the atom temperature,  $T$ , and the electron temperature,  $T_e$ ,

through the shock in the form of dimensionless parameters. The example shown is for a Mach number of approximately 27 and reveals that the shock thickness is 0.19 cm (0.075 in.). The shock thickness is defined here as the distance required for the flow to reach equilibrium conditions and is of key importance in determining the flow conditions at the stagnation point on the body. The relation of the shock flow to the blunt body stagnation point can perhaps be better understood by referring to the schematic curves in Figure 19. This is essentially the same character of the solution shown in Figure 18 but depicts the critical relations between the shock detachment distance, the shock thickness (shown as the relaxation distance) and the stagnation point. The equilibrium flow region is actually an isentropic deceleration of the flow from just downstream of the shock to the stagnation point. The conditions at the stagnation point are strong functions of the freestream conditions, the kind of gas, the shock detachment distance and the relaxation distance. It is entirely possible, under certain conditions, that the relaxation distance is greater than the shock detachment distance. It is obviously important to know when and if this situation occurs, since the entire flow from the stagnation point downstream along the body depends on the initial "reservoir," or stagnation point, conditions

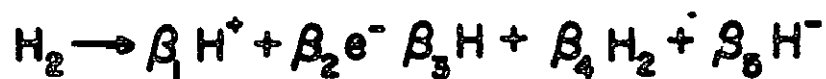
## Stagnation Point Conditions

3

Once the stagnation conditions are known, then the thermophysical properties of the gas can be calculated to get the "starting" conditions of the gas state in the stagnation region. Table V gives the governing equations for determining the properties of molecular hydrogen,  $H_2$ , undergoing the various reaction processes of dissociation, ionization, and electron attachment. Molecular hydrogen is chosen here, since it is the simplest diatomic gas that still retains the essential physical and chemical features of an air-like gas. For given thermodynamic conditions one can thus determine the mole fraction of the various species (ions,  $H^+$ , electrons,  $e^-$ , atoms,  $H$ , molecules,  $H_2$ , and atoms with an electron attached,  $H^-$ ). Other important parameters can be found, namely, the equilibrium speed of sound,  $a_e$ , the frozen speed of sound,  $a_f$ , the frozen ratio of specific heats,  $\gamma_f$ , the equilibrium ratio of

TABLE V. GOVERNING EQUATIONS FOR MOLECULAR H<sub>2</sub> UNDERGOING REACTION PROCESSES

BASIC EQUATIONS



CONSERVATION OF H NUCLEI (PROTONS):

$$2 = \beta_1 + \beta_3 + 2\beta_4 + \beta_5$$

CONSERVATION OF ELECTRICAL CHARGE:

$$0 = \beta_1 - \beta_2 - \beta_5$$

$$\text{H}_2 \rightleftharpoons 2\text{H}: \quad K_{\text{H}_2}(T) = \frac{\beta_3 \sum \beta_i}{\beta_2^2 p}$$

$$\text{H} \rightleftharpoons \text{H}^+ + \text{e}^- : \quad K_{\text{H}}(T) = \frac{\beta_3 \sum \beta_i}{\beta_1 \beta_2 p}$$

$$\text{H}^- \rightleftharpoons \text{H} + \text{e}^- : \quad K_{\text{H}^-} = \frac{\beta_3 \sum \beta_i}{\beta_2 \beta_5 p}$$

$$\text{MOLE FRACTION: } y_1 = \frac{\beta_1}{\sum \beta_i}$$

$$\ln K_{\text{H}} = \frac{-(\Delta E_0)_{\text{H}}}{RT} - \left[ \frac{F^\circ - E_0^\circ}{RT} \right]_{\text{H}} + \left[ \frac{F^\circ - E_0^\circ}{RT} \right]_{\text{H}^+} + \left[ \frac{F^\circ - E_0^\circ}{RT} \right]_{\text{e}^-}$$

TABLE V. GOVERNING EQUATIONS FOR MOLECULAR H<sub>2</sub> UNDERGOING REACTION PROCESSES (Continued)

$$-\left[\frac{F^\circ - E_0^\circ}{R}\right] = \frac{5}{2} \ln T - 3.6645 + \frac{3}{2} \ln m + \ln Q$$

$$Q = Q_{\text{TRAN}} Q_{\text{ROT}} Q_{\text{VIB}} Q_{\text{EL}}$$

$$\frac{1}{K_H} = 6.58 \times 10^{-7} T^{5/2} G e^{-I(H)/T} \text{ ATM.}$$

$$G = \frac{Q_{H^+}}{Q_H}$$

$$K_H = \frac{1 - \alpha^2}{\alpha^2 p}$$

$$K_{H_2} = \frac{1 - \alpha}{\alpha^2 p}$$

$$\alpha^2 = \left[\frac{\partial p}{\partial \rho}\right]_{S, \Delta F=0} = \left[\frac{\partial p}{\partial \rho}\right]_{S, \beta_i} + \sum_{i=1}^n \left[\frac{\partial p}{\partial \beta_i}\right]_{P, S, \Delta F=0} \cdot \left[\frac{\partial \beta_i}{\partial \rho}\right]_{S, \Delta F=0}$$

$$\alpha_i^2 = \left[\frac{\partial p}{\partial \rho}\right]_{S, \beta_i} = \frac{\gamma_i RT}{m}$$

$$\gamma_i = \frac{\sum y_i C_{p_i}}{\sum y_i (C_{p_i} - R)}$$

$$m = \frac{\sum \beta_i m_i}{\sum \beta_i} = \sum y_i m_i$$

TABLE V. GOVERNING EQUATIONS FOR MOLECULAR H<sub>2</sub> UNDERGOING REACTION PROCESSES (Continued)

$$\text{GIBBS-HELMHOLTZ : } E = -T^2 \frac{\partial}{\partial T} \left[ \frac{F}{T} \right]_V$$

$$F = -kT \ln [Q^N / N!]$$

$$E = NkT^2 \frac{\partial}{\partial T} \left[ \ln Q_{\text{TRAN}} + \ln Q_{\text{ROT}} + \ln Q_{\text{VIB}} + \ln Q_{\text{EL}} \right]$$

$$Q_{\text{TRAN}} = \left[ \frac{2\pi(m_A + m_B)kT}{h^2} \right]^{3/2} V$$

$$Q_{\text{ROT}} = \sum_{j=0}^{\infty} (2j+1) e^{-j(j+1)\theta_r/T} \quad \theta_r = \frac{h^2}{8\pi^2 A k}$$

$$Q_{\text{VIB}} = \frac{e^{-\theta_v/2T}}{1 - e^{-\theta_v/T}} \quad \theta_v = \frac{h\nu}{k}$$

$$Q_{\text{EL}} = \omega_1 + \omega_2 e^{-\epsilon_1/kT} + \dots$$

$$C_V = \left[ \frac{\partial E}{\partial T} \right]_V \quad C_p = C_V + R, \text{ per mole}$$

$$\gamma = C_p / C_V$$

TABLE V. GOVERNING EQUATIONS FOR MOLECULAR H<sub>2</sub> UNDERGOING REACTION PROCESSES (Concluded)

DISSOCIATION RANGE.

$$\delta\beta_3 + 2\delta\beta_4 = 0$$

$$\frac{\delta T}{T} + \frac{RT\delta\rho}{mp} - \frac{\delta m}{m} - \frac{\delta p}{p} = 0$$

$$\sum\beta_i \delta m + \sum(m - m_i) \delta\beta_i = 0$$

$$\frac{\delta\beta_4}{\beta_4} + \frac{\sum\delta\beta_i}{\sum\beta_i} - \frac{2\delta\beta_3}{\beta_3} - \frac{\delta p}{p} - \frac{\Delta H_{H_2}^\circ}{RT^2} \delta T = 0$$

$$\Delta H_{H_2}^\circ \delta\beta_4 + \sum\beta_i c_{p_i} \delta T - \frac{RT}{p} \delta p = 0$$

$$\frac{\delta p}{\delta\rho} = \left[ \frac{\partial p}{\partial\rho} \right]_{S, \Delta F=0} = a_0^2$$

$$\gamma_0 = \frac{a_0^2 m}{RT}$$

$$\frac{C_{p_0}}{R} = \frac{\gamma_0}{\gamma_0 - 1}$$

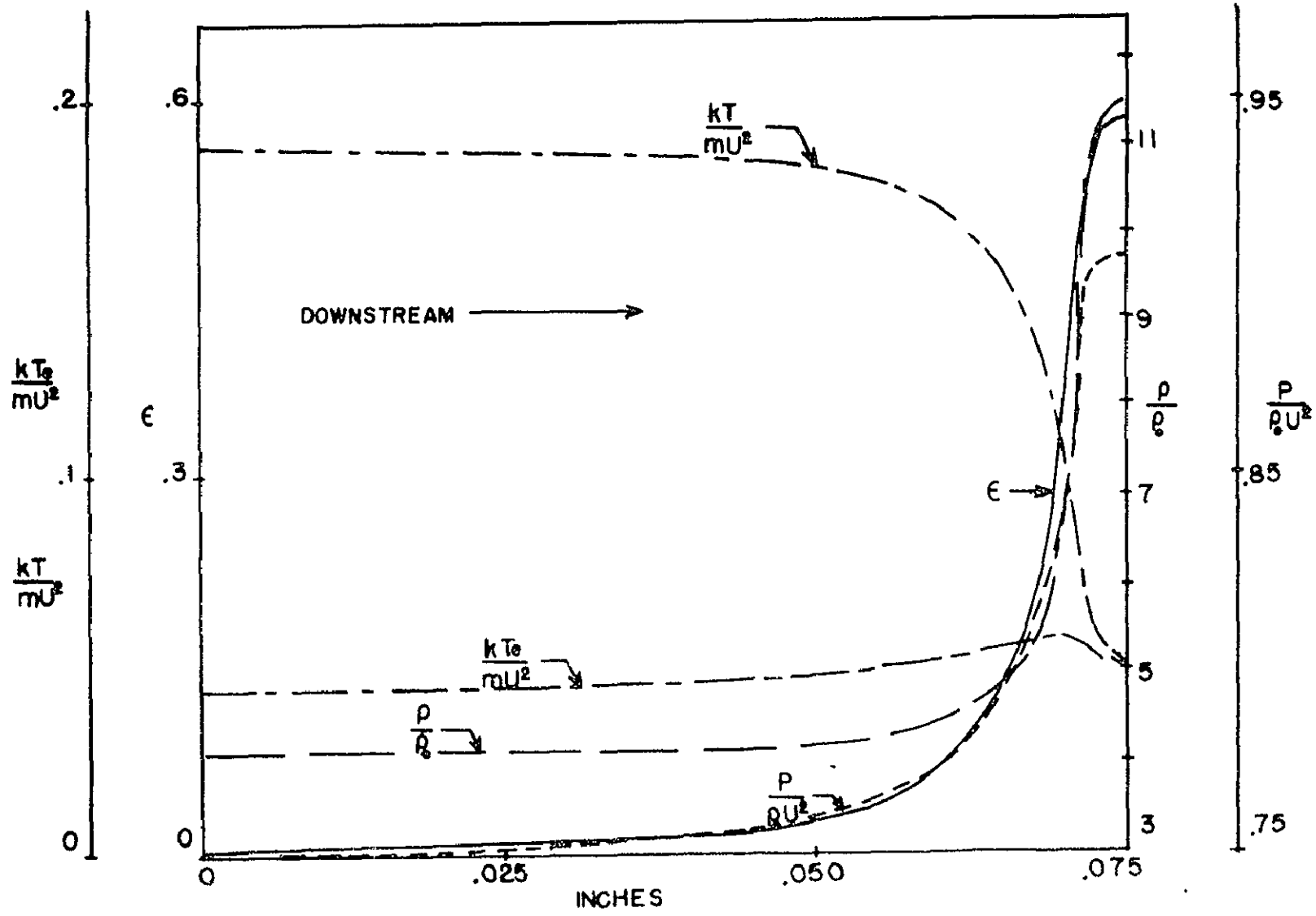


FIGURE 18. DENSITY, PRESSURE, IONIZATION AND ATOM AND ELECTRON VARIATIONS THROUGH THE SHOCK

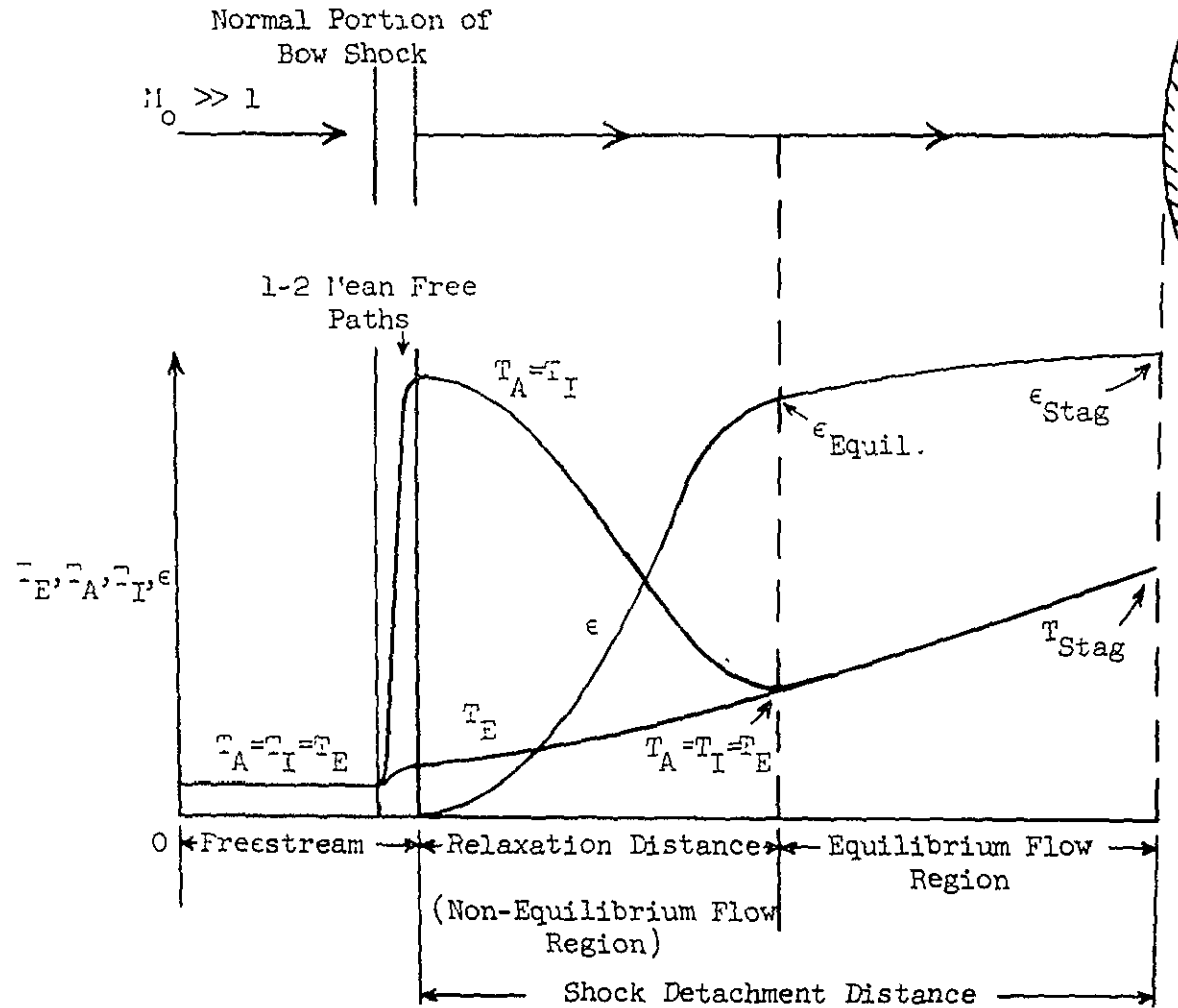


FIGURE 19. THE VARIATION OF TEMPERATURES AND DEGREE OF IONIZATION IN THE SHOCK DETACHMENT REGION (not to scale)

specific heats,  $\gamma_e$ , etc. Since dissociation is essentially complete before ionization begins, it is possible to treat the governing equations in "steps" as for the dissociation range.

Typical results for hydrogen are shown in Figures 20 through 24. Figure 20 verifies that the process of dissociation is essentially complete before ionization begins. Figure 21 shows the variation with temperature of the ratio of the equilibrium and frozen values of the speeds of sound, the ratios of specific heats and the specific heats at a constant pressure, for a pressure of one atmosphere. Figure 22 shows the average molecular weight of the gas as the temperature is increased from  $10^3$  to  $10^5$  °K, for one atmosphere. At the lowest temperature the gas is a diatomic one and as the temperature increases the "plateau" represents the attainment of complete dissociation to a monatomic gas. Further increase in temperature results in the attainment of complete ionization of the hydrogen gas. Figure 23 shows that, for a given pressure, an increase of temperature yields oscillatory-type variations in the equilibrium ratio of specific heats that finally approaches the classical monatomic value of 1.667, as the temperature is increased to large values. The effect of decreasing the pressure is to "squeeze" the curve. It is interesting to note that the envelope of the curves approaches  $\gamma_e = 1$ , at high temperatures. Figure 24 shows the equilibrium speed of sound as a function of temperature and the attainment of complete dissociation and ionization are evident as "plateaus" in the curve. Figure 25 shows typical results for  $\gamma_e$  for air and it is clear that the character of this curve is quite similar to that found for hydrogen (Fig. 23).

The foregoing discussion summarizes the type of analysis required to determine the thermophysical properties of a typical air-like (diatomic) gas under either equilibrium or frozen conditions in the stagnation region. Although tedious, the calculations are quite straightforward but require a detailed knowledge of the quantum mechanical properties of the gas which can be obtained from the NBS Tables or other similar sources.

## Inviscid Blunt-Body Real-Gas Flow

For simplicity, it is usually assumed that the flow at the stagnation point is under equilibrium conditions. As the flow accelerates from the stagnation point around the blunt body, the flow will probably depart from equilibrium as

the gas begins to expand and cool. Whether or not the gas species recombine to form atoms and molecules (and thus release heat), or "freeze" at some fixed composition, must be determined by a detailed numerical analysis.

In order to calculate this flow over the body it is advantageous to know, if possible, the pressure distribution along the body surface (stagnation streamline). Fortunately, the pressure distribution over a blunt-nosed body can be determined by a combination of Newtonian Impact Theory, Prandtl-Meyer flow and Blast Wave Theory [2]. It is particularly important to note that this pressure distribution (shown schematically in Figure 26) is essentially insensitive to whether the flow is frozen, equilibrium or non-equilibrium. On the other hand, the flow properties along the body are very strong functions of the flow conditions (frozen, equilibrium or non-equilibrium) as well as the stagnation conditions.

As noted previously, it is helpful to consider the flow along the body surface as analogous to the flow through an equivalent convergent-divergent nozzle (Fig. 17). With this conceptual model, it is simple to identify the stagnation point on the body as a fictitious reservoir, the sonic point (SP) on the body which corresponds to the "throat" of the equivalent nozzle, and a downstream station, A, as a supersonic station of the nozzle. Since the pressure distribution is known from hypersonic theory, an isentropic analysis in terms of pressure ratio will yield the area ratio,  $A/A^*$ , similar to that depicted in Figure 27. Using this approximation for the area ratio of the body surface streamtube, it now remains to calculate the real-gas flow through this fictitious nozzle, the results of which should approximate closely the inviscid flow properties along the body surface.

Table VI outlines a nozzle-flow analysis for a triply-ionized monatomic gas under equilibrium stagnation conditions. This analysis is one of the simplest examples of a reacting gas flow that still retains the essential physical features of a typical reacting monatomic gas. Details of this analysis are given in Reference 3. Interpreted as a blunt-body problem as described above, the stagnation conditions are such that the argon gas is 50 percent triply ionized (Fig. 28). As the flow accelerates from the stagnation point and expands (to larger values of  $A/A^*$ ) the gas recombines first to a fully (100 percent) doubly ionized gas (first transition region). As the flow continues to expand downstream, the gas continues to recombine to a fully (100 percent) singly ionized gas (second transition region).

Figure 29 gives the complete solution for the flow properties for the given stagnation conditions including the variation of the pressure,  $p$ , the

TABLE VI. NOZZLE-FLOW ANALYSIS

The governing equations for the isentropic, equilibrium flow of a triply-ionized monatomic gas in a convergent-divergent nozzle are:

Law of Mass Action

$$n_r n_e / n_{r-1} = 2(2\pi m_e kT/h^2)^{3/2} [Q_e(A_r)/Q_e(A_{r-1})] \exp[-(I_r - I_{r-1})/kT], r=1,2,3 \quad (15)$$

Conservation of Electric Charge

$$\sum_{r=1}^3 r n_r = n_e \quad (16)$$

Conservation of Nuclei

$$\sum_{r=0}^3 n_r = n_t \quad (17)$$

Equation of State

$$P = kT(n_e + \sum_{r=0}^3 n_r) \quad (18)$$

Conservation of Energy

$$i_0 = V^2/2 + E + P/\rho \quad (19)$$

Specific Entropy

$$S = E/T + k\phi/\rho = \text{constant} \quad (20)$$

Specific Internal Energy

$$E = (kT^2/\rho) \partial\phi/\partial T \quad (21)$$

Conservation of Mass

$$\rho AV = \rho_t A_t V_t \quad (22)$$

where

$$\begin{aligned} \phi = & \sum_{r=0}^3 n_r \{ \ln[ (2\pi m_A kT/h^2)^{3/2} Q_e(A_r)/n_r ] + 1 - I_r/kT \} \\ & + n_e \{ \ln[ 2(2\pi m_e kT/h^2)^{3/2} / n_e ] + 1 \} \end{aligned} \quad (23)$$

$$Q_e(A_r) = g_0(A_r) + g_1(A_r) \exp(-\frac{I_1}{kT}) \quad (24)$$

density,  $\rho$ , the velocity,  $v$ , and the temperature,  $T$ , along the body (equivalent nozzle). An interesting property of the flow, which is typical of the flow of any reacting gas over a blunt body, is the sudden drop in temperature along the body corresponding to the location of the transition regions (Fig. 28). Although the density is not influenced by these sudden drops of temperature, the pressure is influenced considerably as noted by the large pressure drops in these transition regions.

It is important to note that these pressure drops may have important implications in the boundary layer development along the body. The large pressure drops may tend to thin out the boundary layer in the transition region but the less favorable pressure gradient downstream of this region may create a situation that is destabilizing and may cause the boundary layer to tend to separate

The preceding equilibrium solution for a triply-ionized gas flow in a nozzle is typical of that for any reacting gas, in which only one reaction is occurring under given thermodynamic conditions. This is best demonstrated by examining the results of a nozzle flow analysis for an ideal dissociating gas. Figures 30 through 33 represent the solution for the flow of Lighthill's ideal dissociating gas (IDG) [4] in a typical hypersonic nozzle. The curves denoted with the letter "E" represent the equilibrium solution similar to that outlined for the ionizing gas, except that only one reaction, the dissociation, is considered for the IDG, whereas three reactions, separated by transition regions, had to be considered for the triply-ionized case. In addition to the equilibrium solution, the solutions for the hypersonic nozzle flow for the frozen (denoted by "F") and the non-equilibrium (denoted by "N") cases are given in Figures 30 through 33. The frozen solution is actually the well-known "cold gas" analysis (i.e., a non-reacting nozzle flow, with the same reservoir conditions as the other two cases:  $T = 5900$  °K,  $p = 1.15 \times 10^2$  atm.) The non-equilibrium solution was first discussed by Bray [5] and uses Freeman's [6] rate equation in conjunction with the Lighthill ideal dissociating gas.

An examination of the three solutions given in Figures 30 through 33 show a large difference in the values of the degree of dissociation,  $\alpha_0$ , the local temperature parameter,  $T/T_d$ , the local velocity parameter,  $u/u_d$ , and the local Mach number,  $M$ , for given values of nozzle station,  $A/A^*$ . The dotted line shown in Figures 30 through 32 is Bray's simplified approximate solution to the non-equilibrium case.

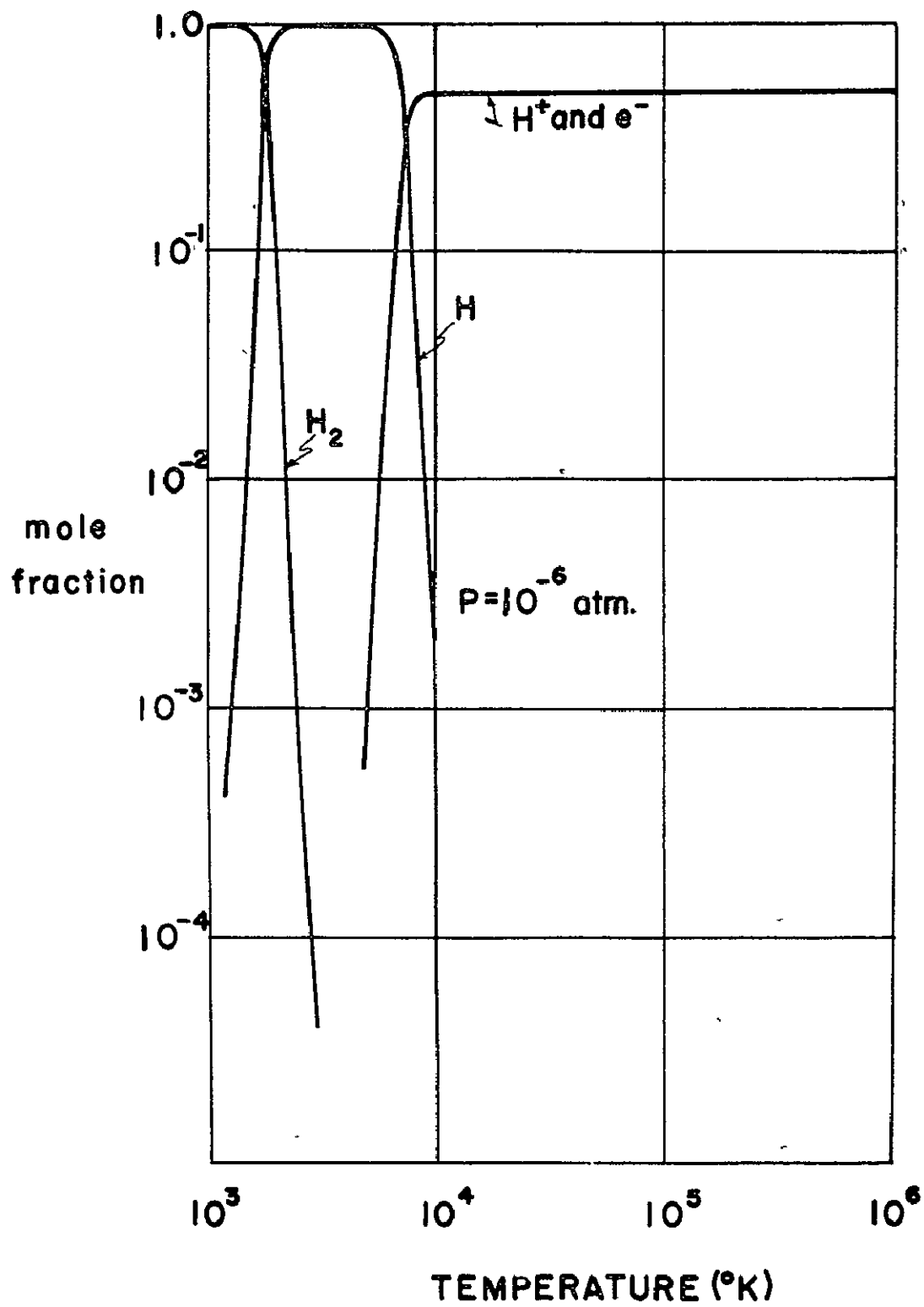


FIGURE 20. MOLE FRACTION VERSUS TEMPERATURE FOR HYDROGEN

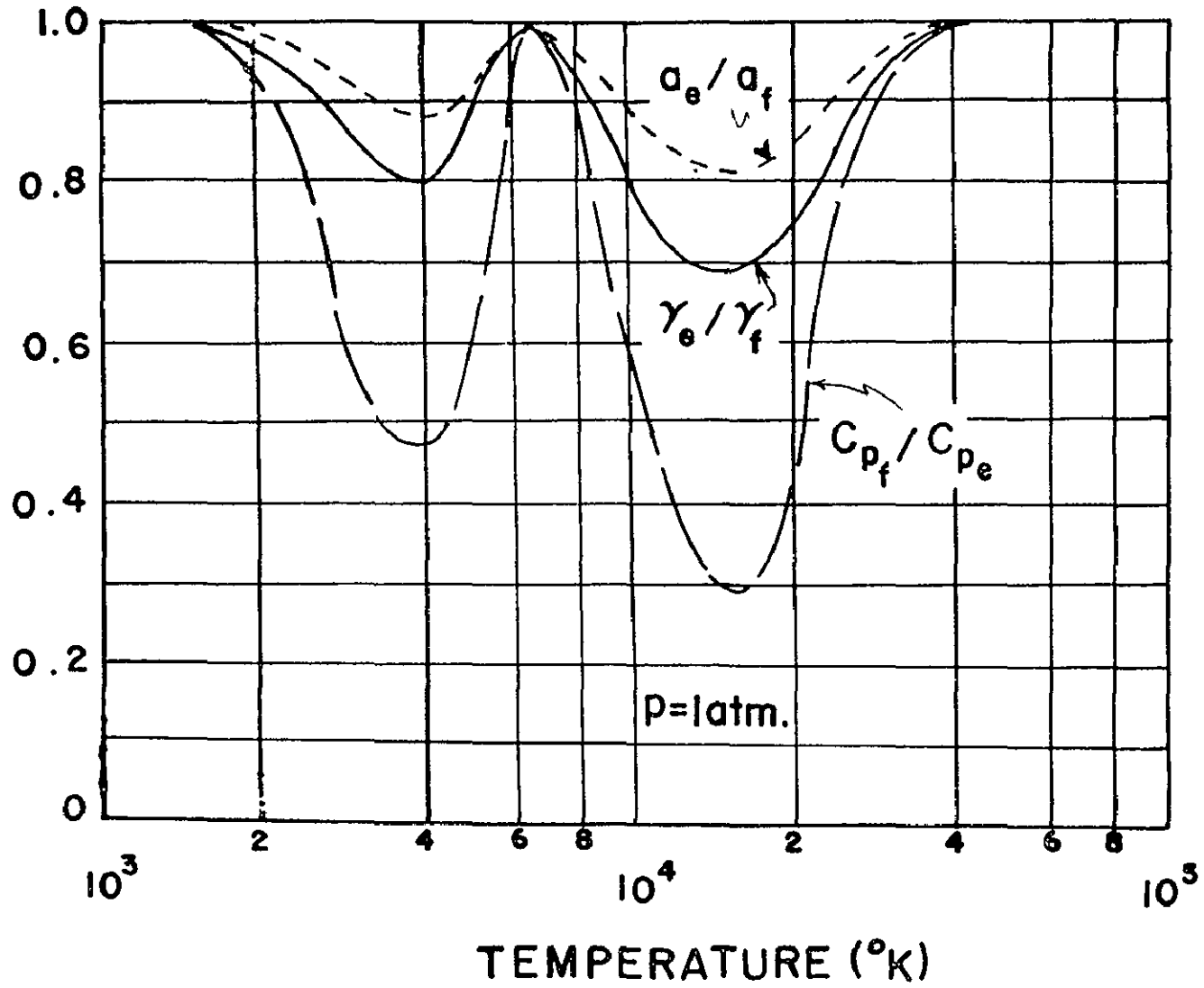


FIGURE 21. EQUILIBRIUM TO FROZEN FLOW RATIOS VERSUS TEMPERATURE

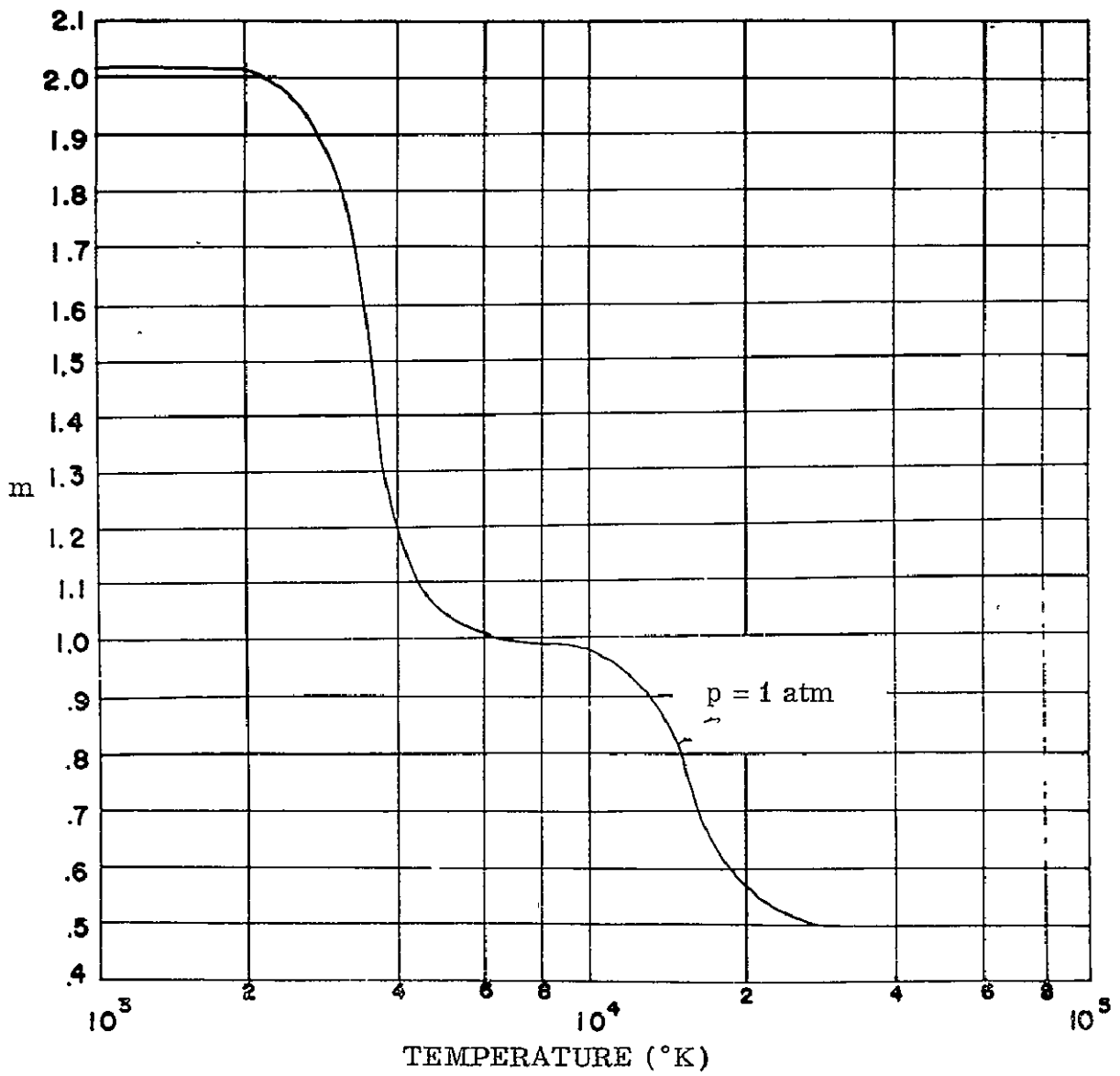


FIGURE 22. AVERAGE MOLECULAR WEIGHT VERSUS TEMPERATURE

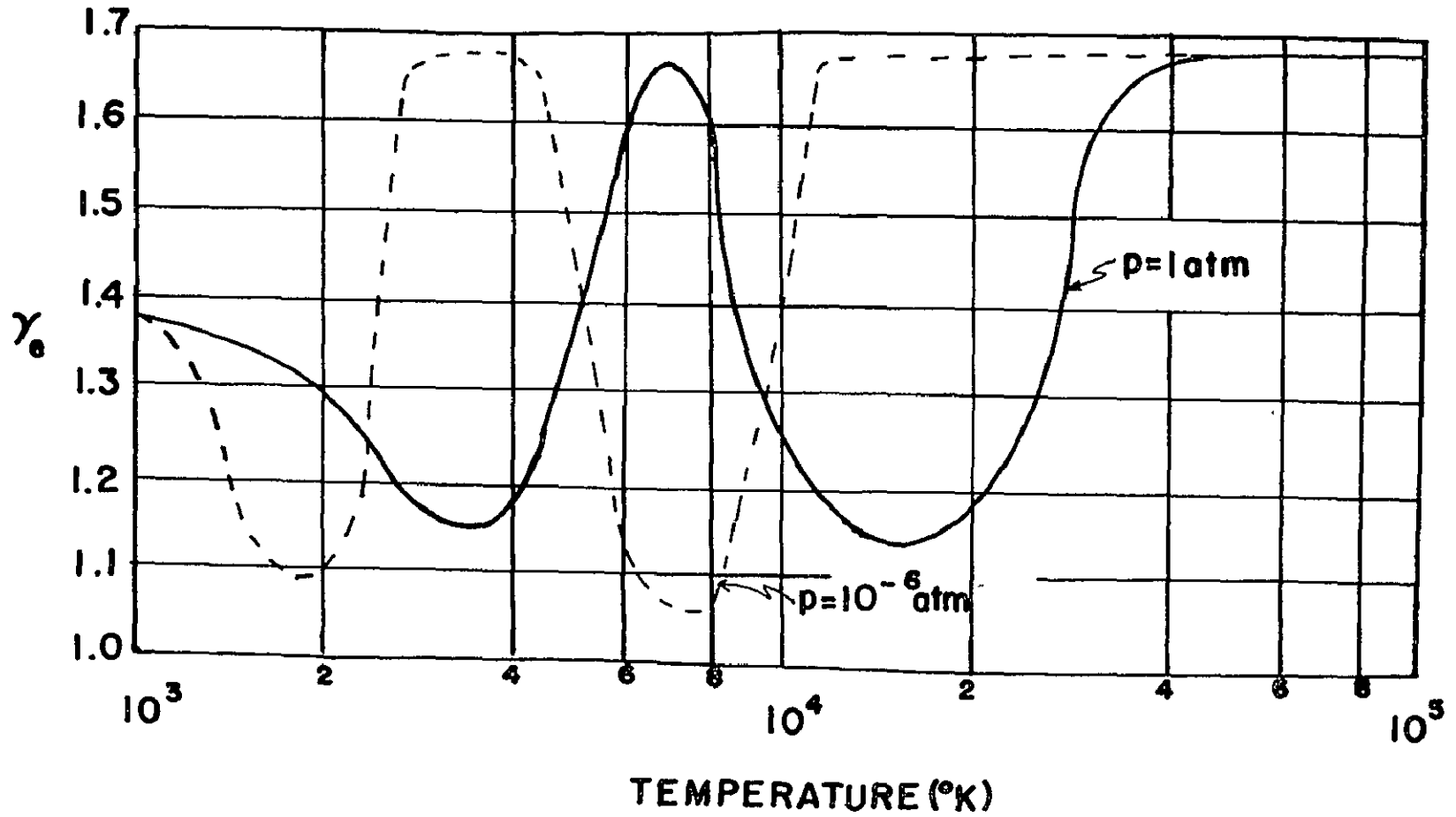


FIGURE 23. EQUILIBRIUM RATIOS OF SPECIFIC HEATS VERSUS TEMPERATURE-HYDROGEN

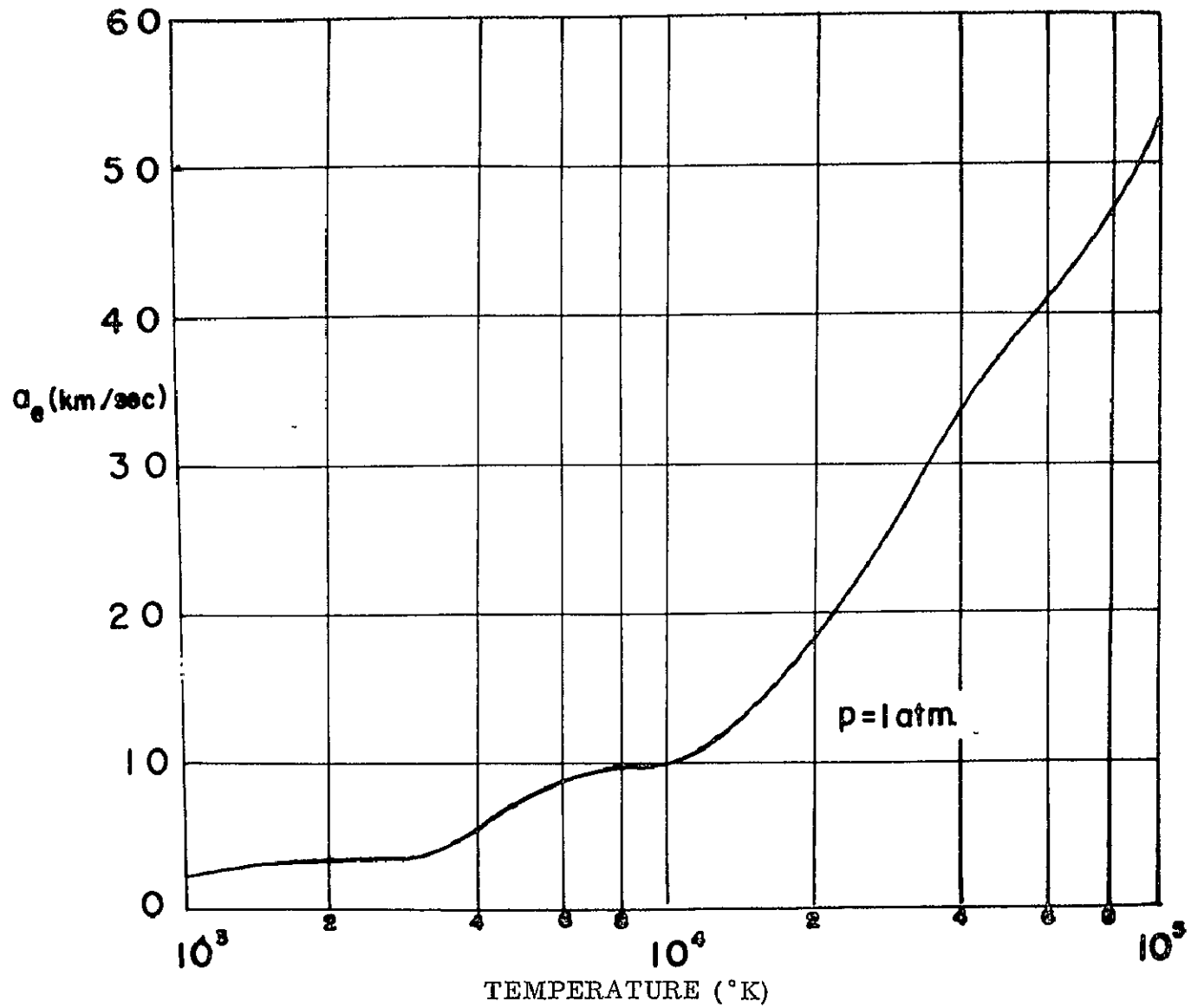


FIGURE 24. EQUILIBRIUM SPEED OF SOUND VERSUS TEMPERATURE

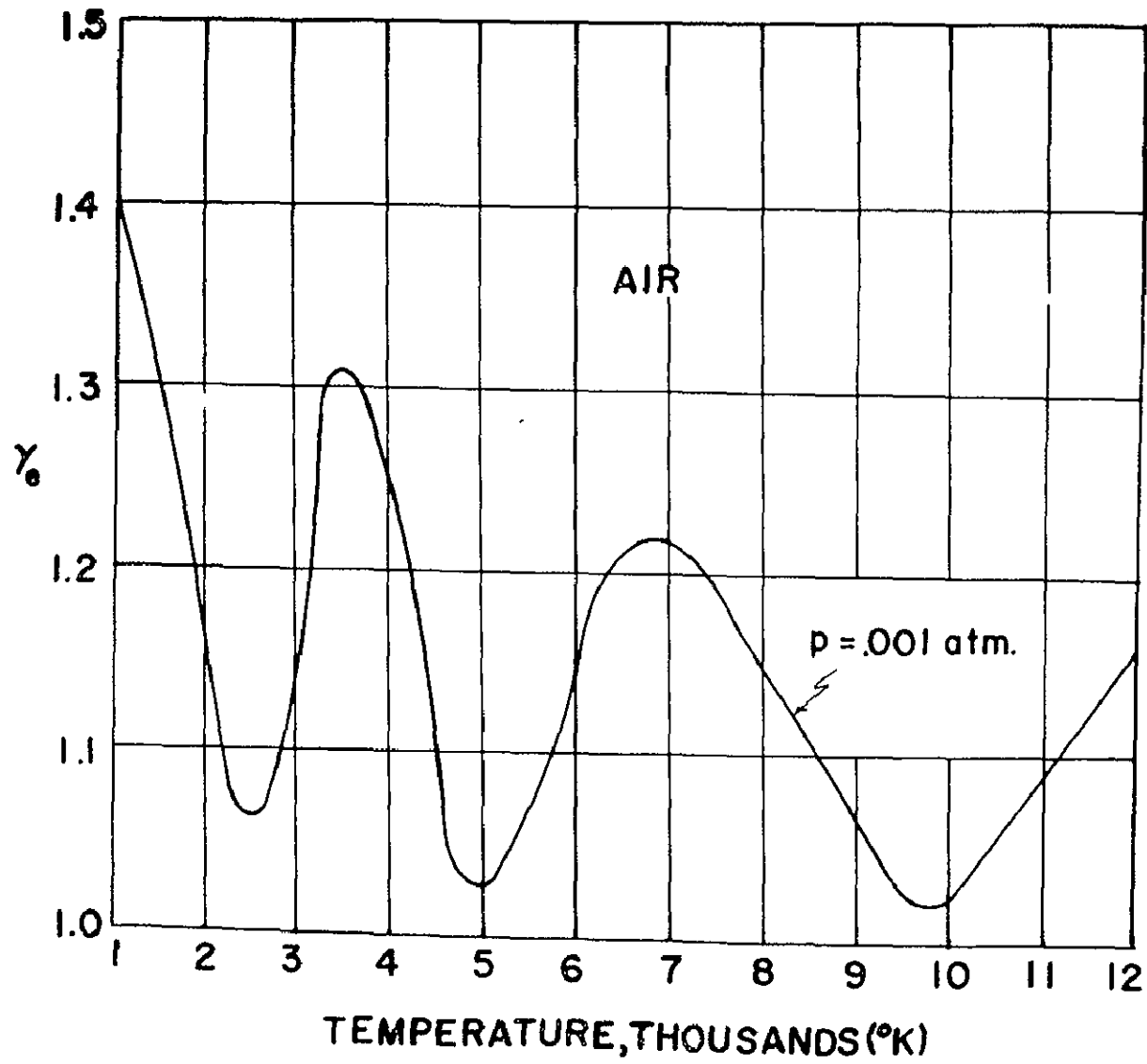


FIGURE 25. EQUILIBRIUM RATIO OF SPECIFIC HEATS VERSUS TEMPERATURE FOR AIR

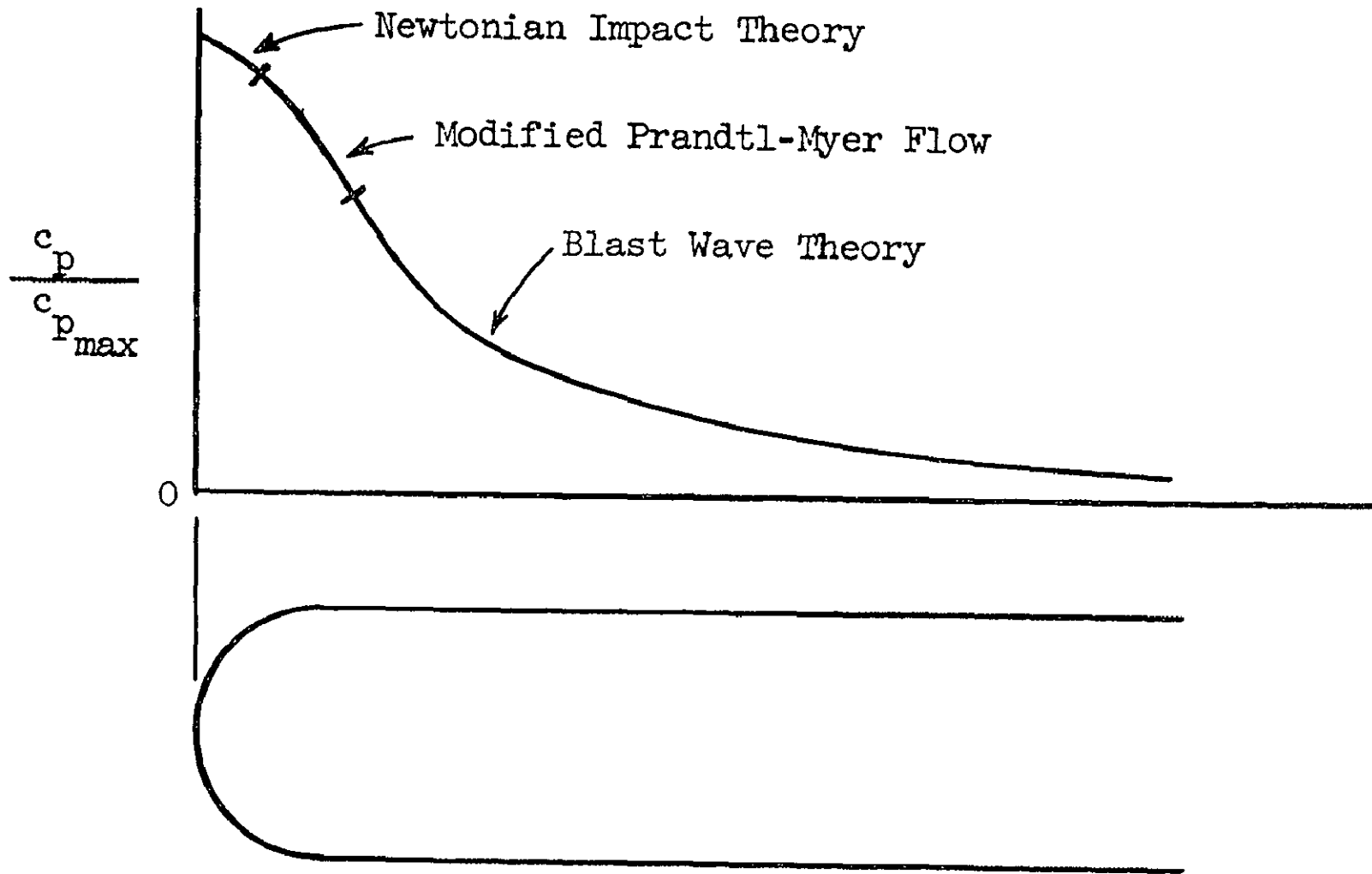


FIGURE 26. PRESSURE DISTRIBUTION OVER A HEMISPHERE-CYLINDER (Schematic)

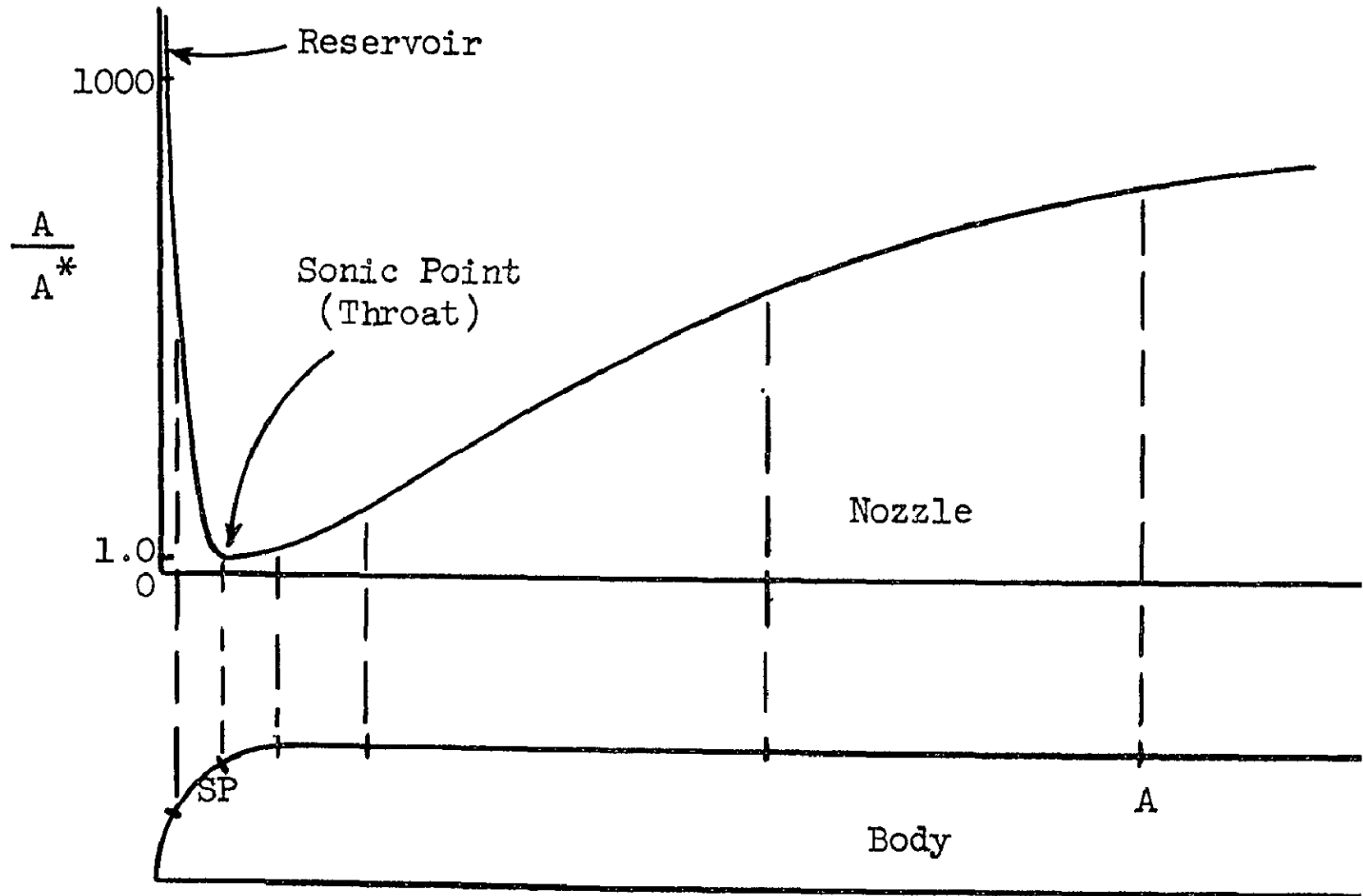


FIGURE 27. EQUIVALENT NOZZLE CONCEPT

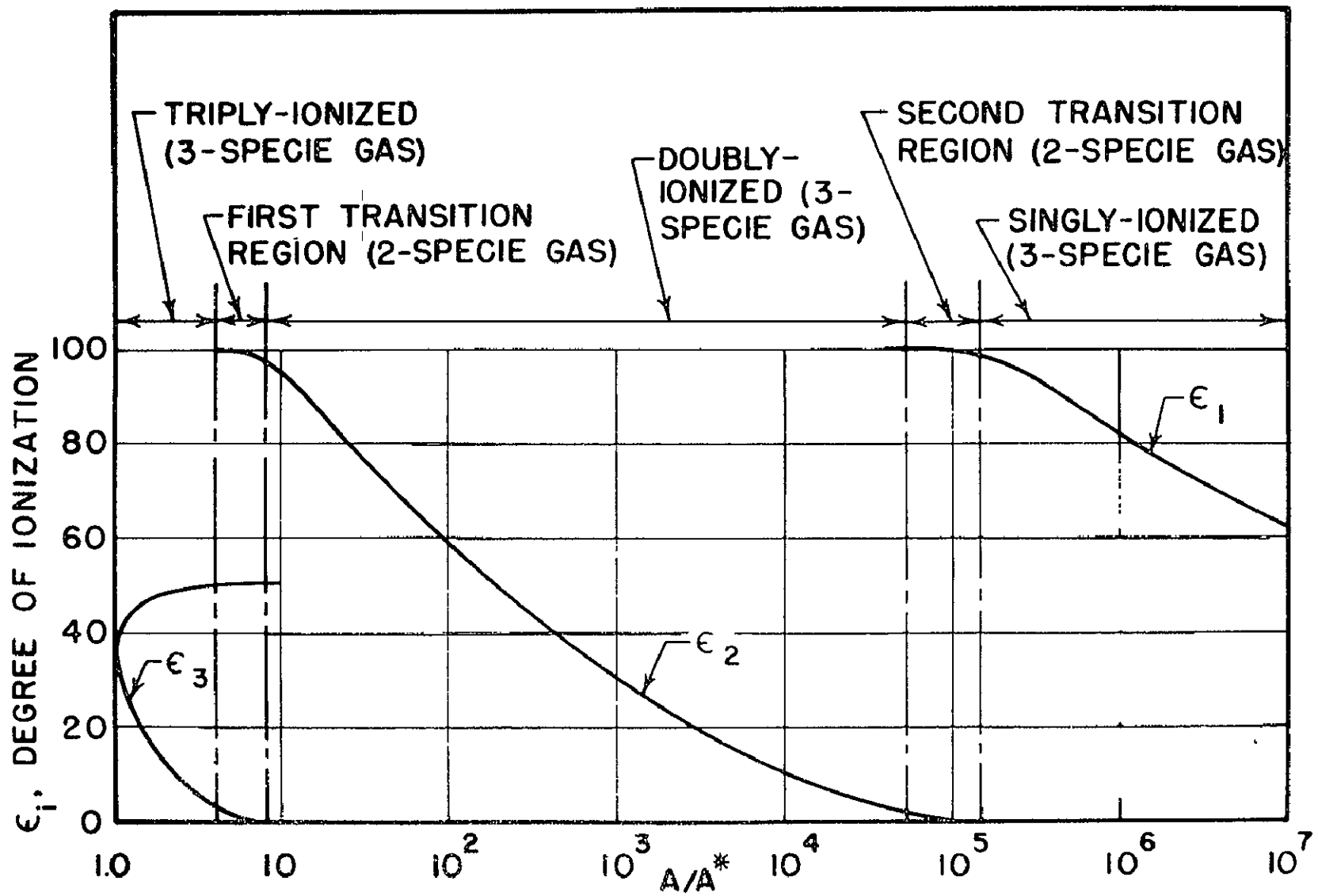


FIGURE 28. RESULTS OF NOZZLE FLOW ANALYSIS AS APPLIED TO BLUNT BODY

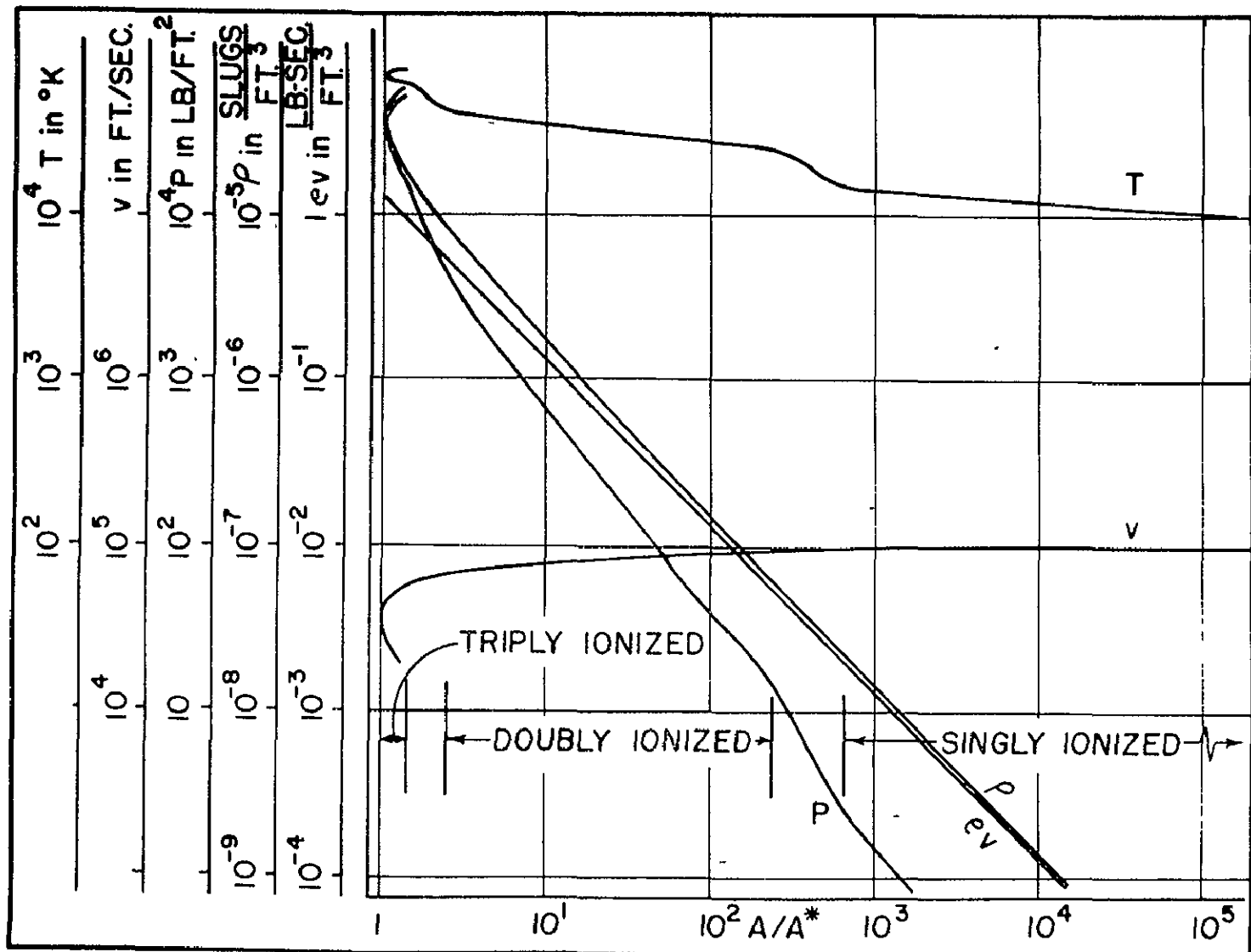


FIGURE 29 FLOW PROPERTIES FOR BLUNT BODY ANALYSIS

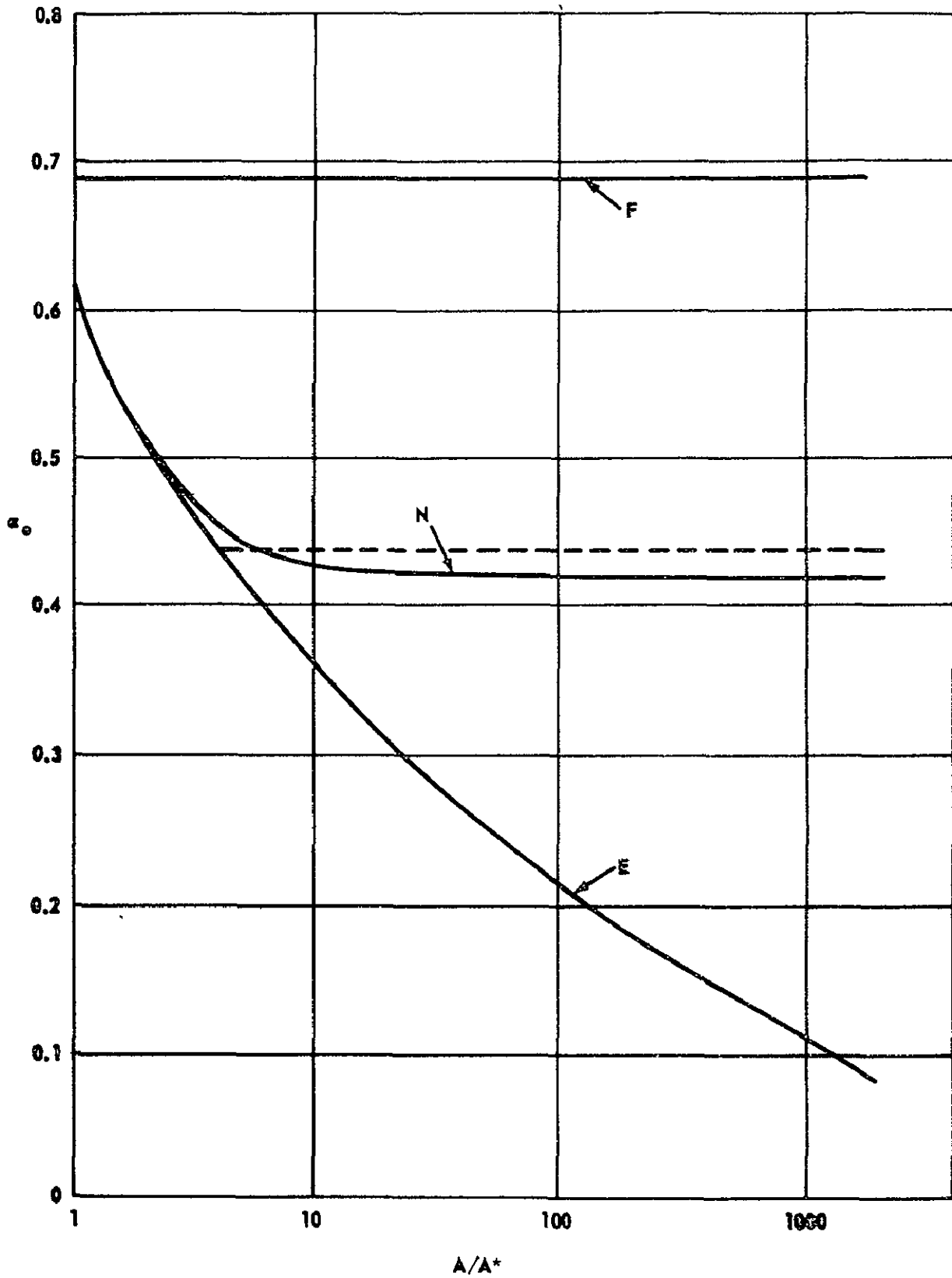


FIGURE 30.  $\alpha_0$  VERSUS  $A/A^*$  IN A HYPERSONIC NOZZLE  
 (Stagnation conditions:  $T_0 = 5900 \text{ }^\circ\text{K}$   $p = 1.15 \times 10^2 \text{ atm}$ )

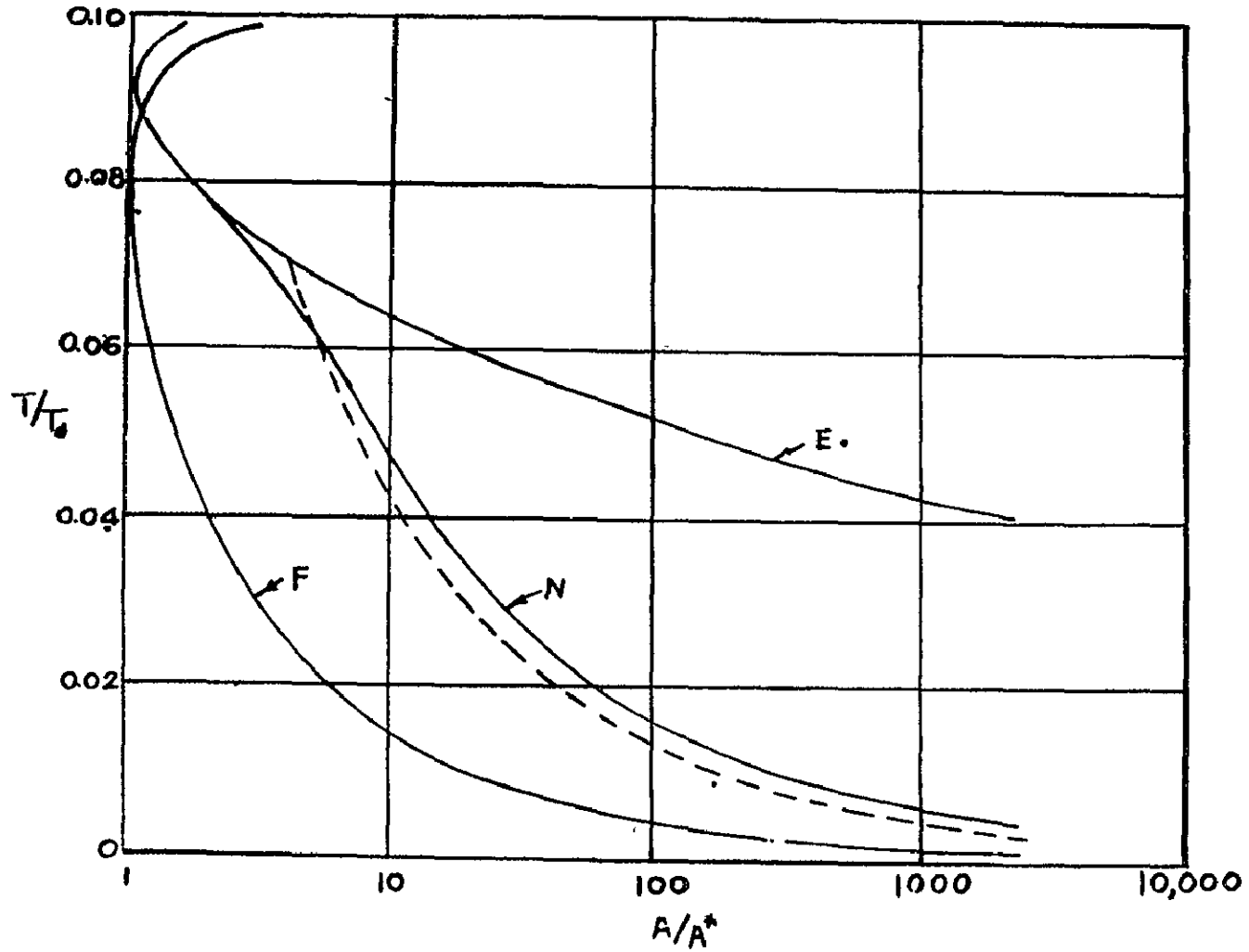


FIGURE 31.  $T/T_0$  VERSUS  $A/A^*$  IN A HYPERSONIC NOZZLE  
 (Stagnation conditions:  $T_0 = 5900^\circ\text{K}$   $p_0 = 1.15 \times 10^2 \text{ atm}$ )  
 (Solid lines = "exact" solution, Dotted line = "approximate" solution)

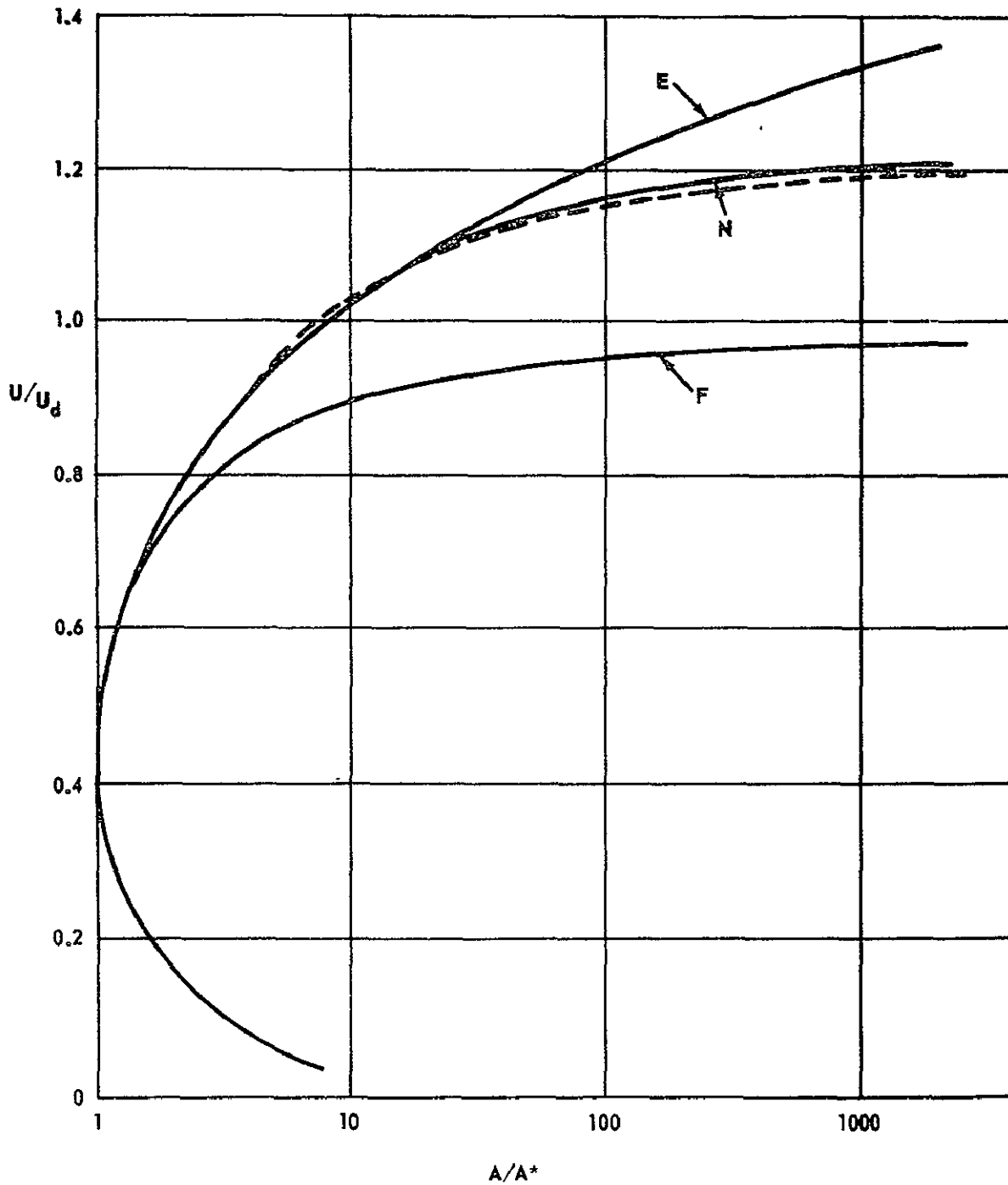


FIGURE 32.  $U/U_d$  VERSUS  $\rho/A^*$  IN A HYPERSONIC NOZZLE  
 (Stagnation conditions:  $T_o = 5900 \text{ }^\circ\text{K}$   $p_o = 1.15 \times 10^2 \text{ atm}$ )

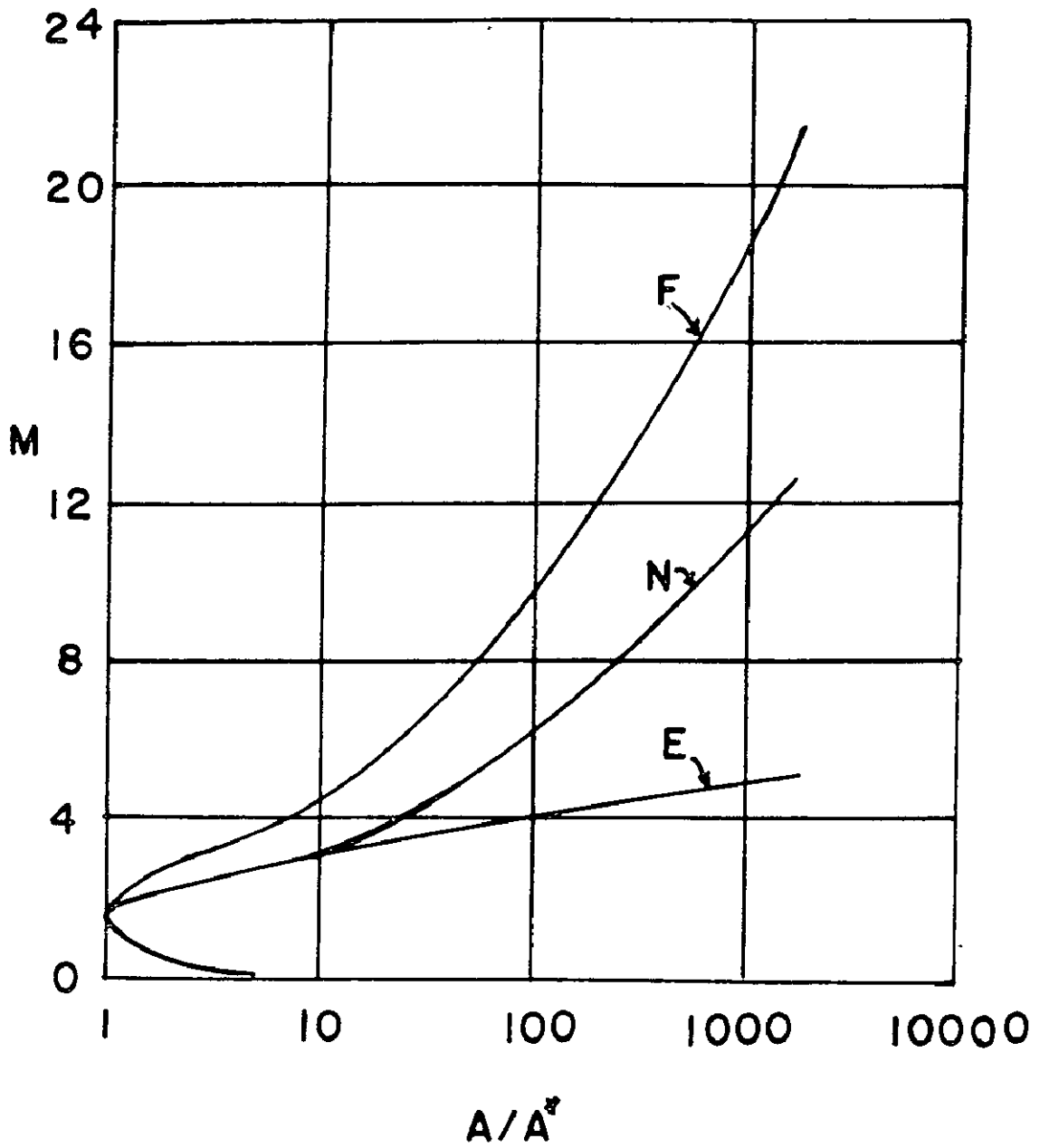


FIGURE 33. "COLD GAS" ANALYSIS-HYPERSONIC TUNNEL DESIGN

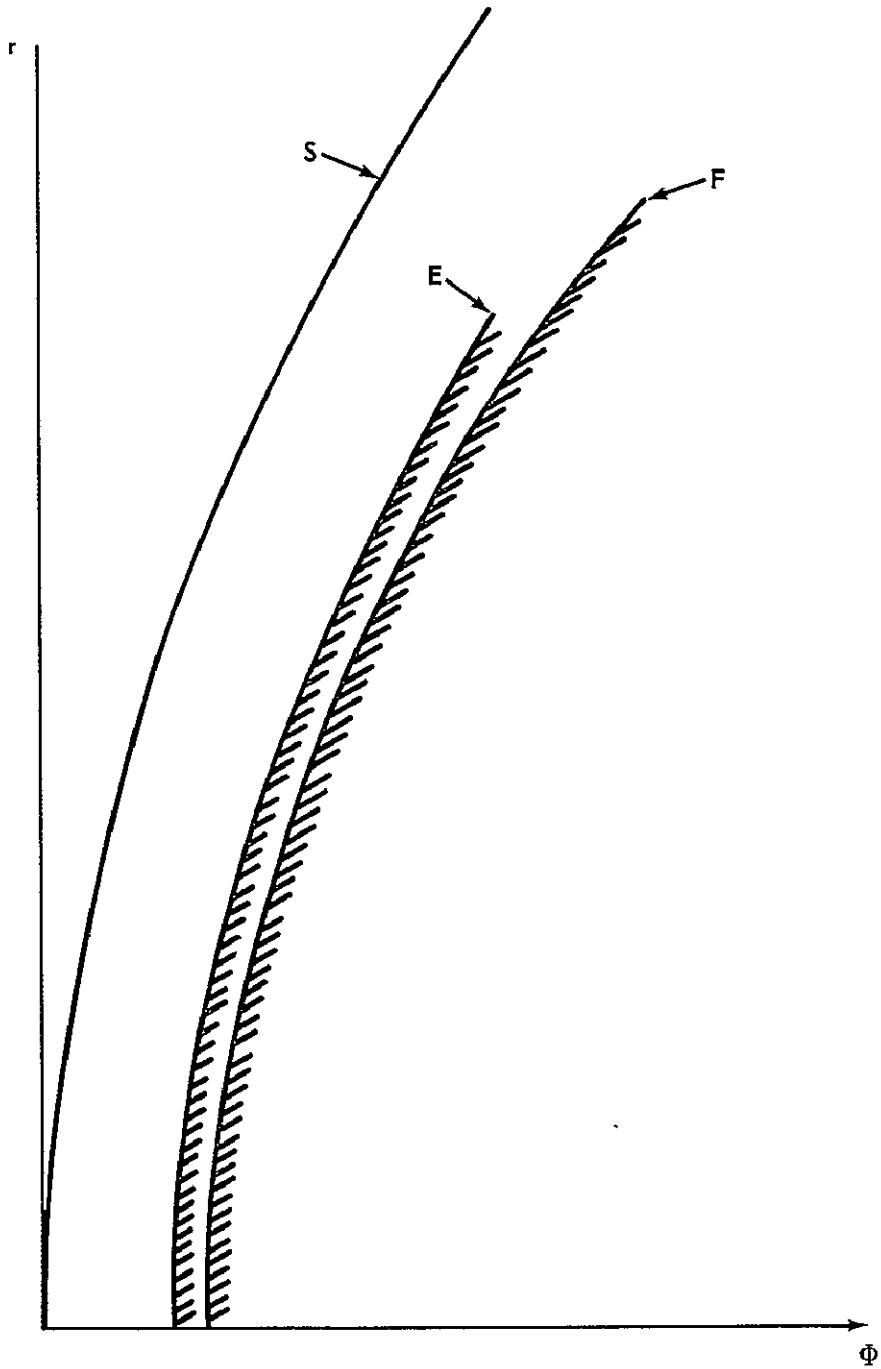


FIGURE 34. GEOMETRY OF THE SHOCK WAVE AND THE BODY SURFACE  
(S = Shock Wave)

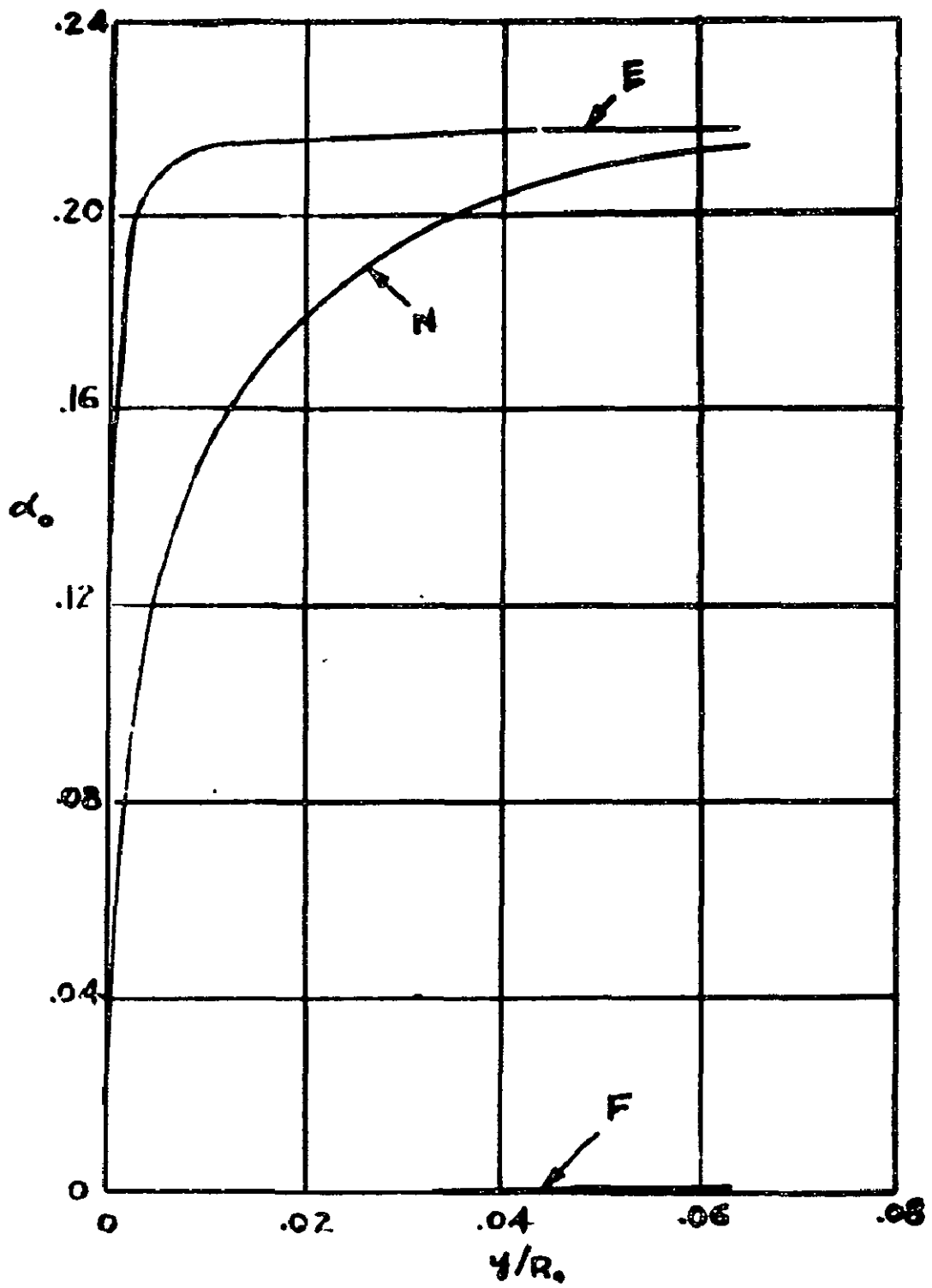


FIGURE 35. VARIATION OF  $\alpha_0$  ALONG THE AXIAL STREAMLINE

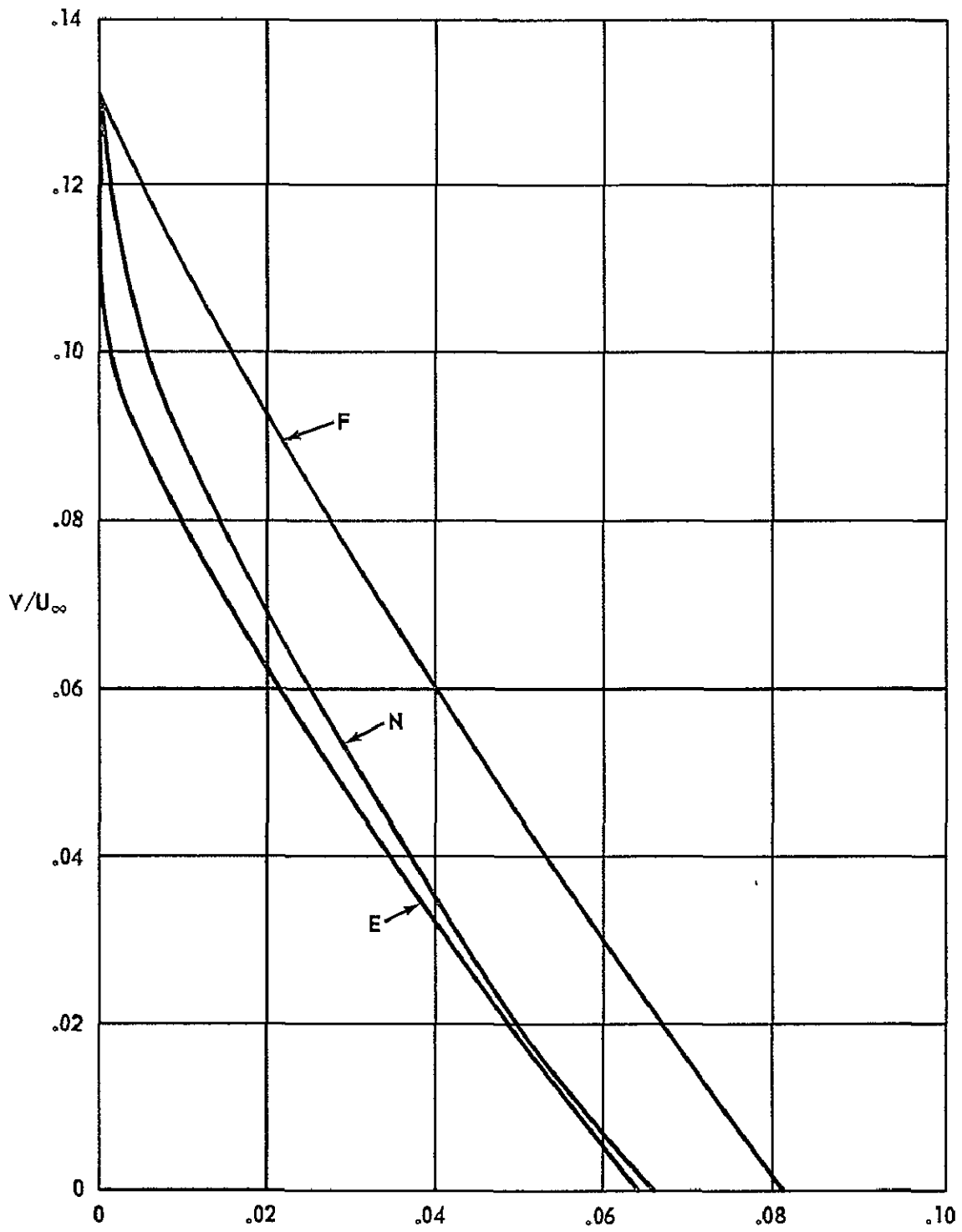


FIGURE 36. VARIATION OF  $\nu/U_\infty$  ALONG THE AXIAL STREAMLINE

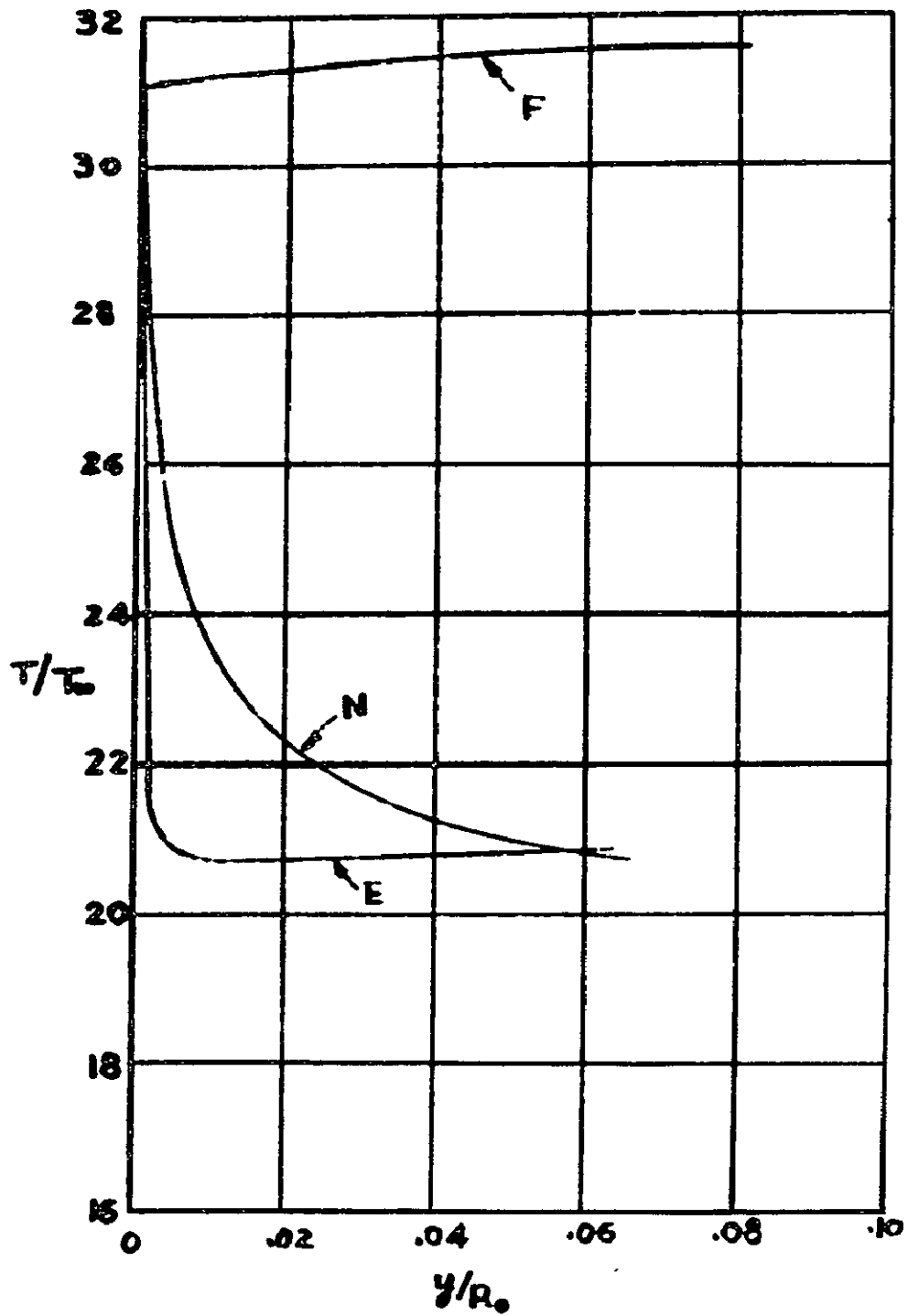


FIGURE 37. VARIATION OF  $T/T_\infty$  ALONG THE AXIAL STREAMLINE

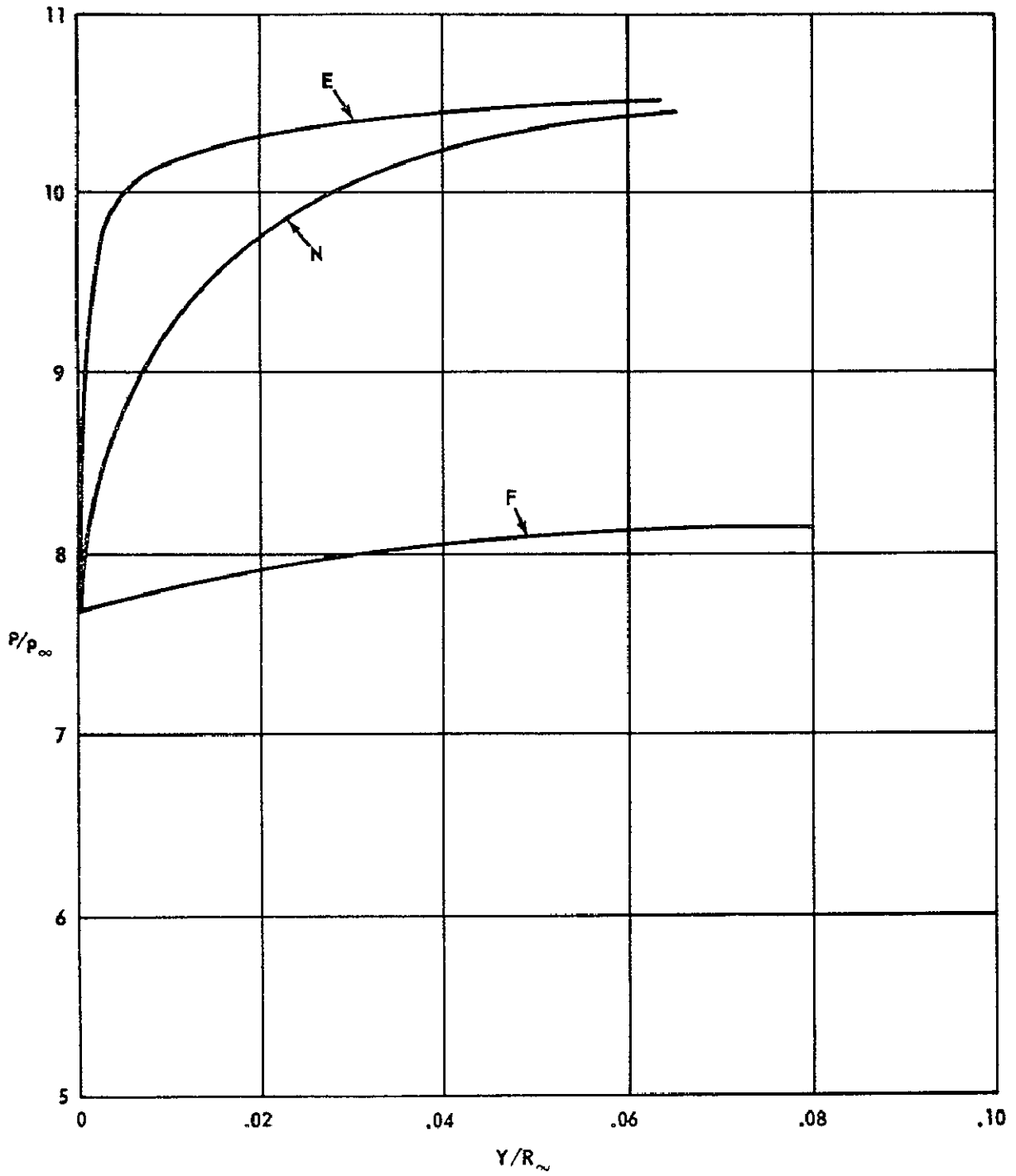


FIGURE 38. VARIATION OF  $\rho/\rho_\infty$  ALONG THE AXIAL STREAMLINE

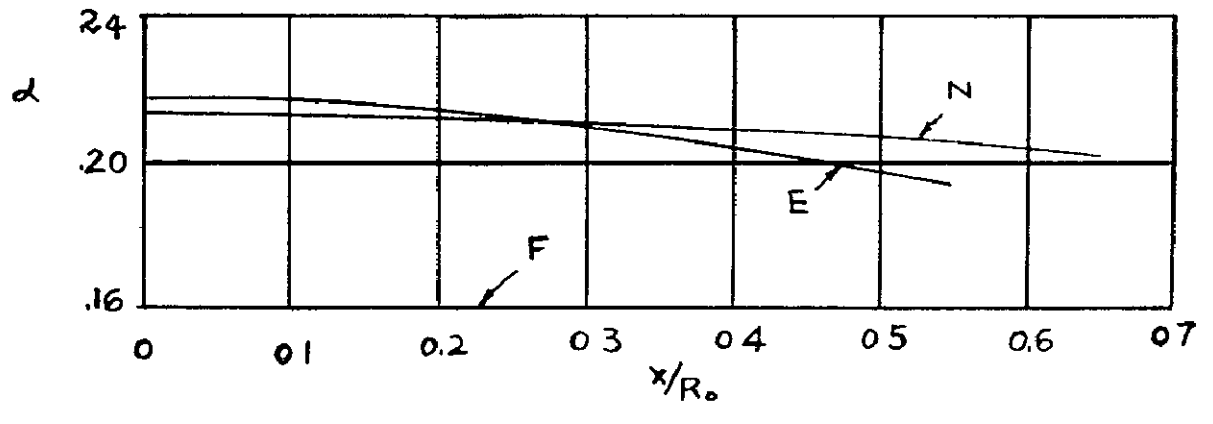
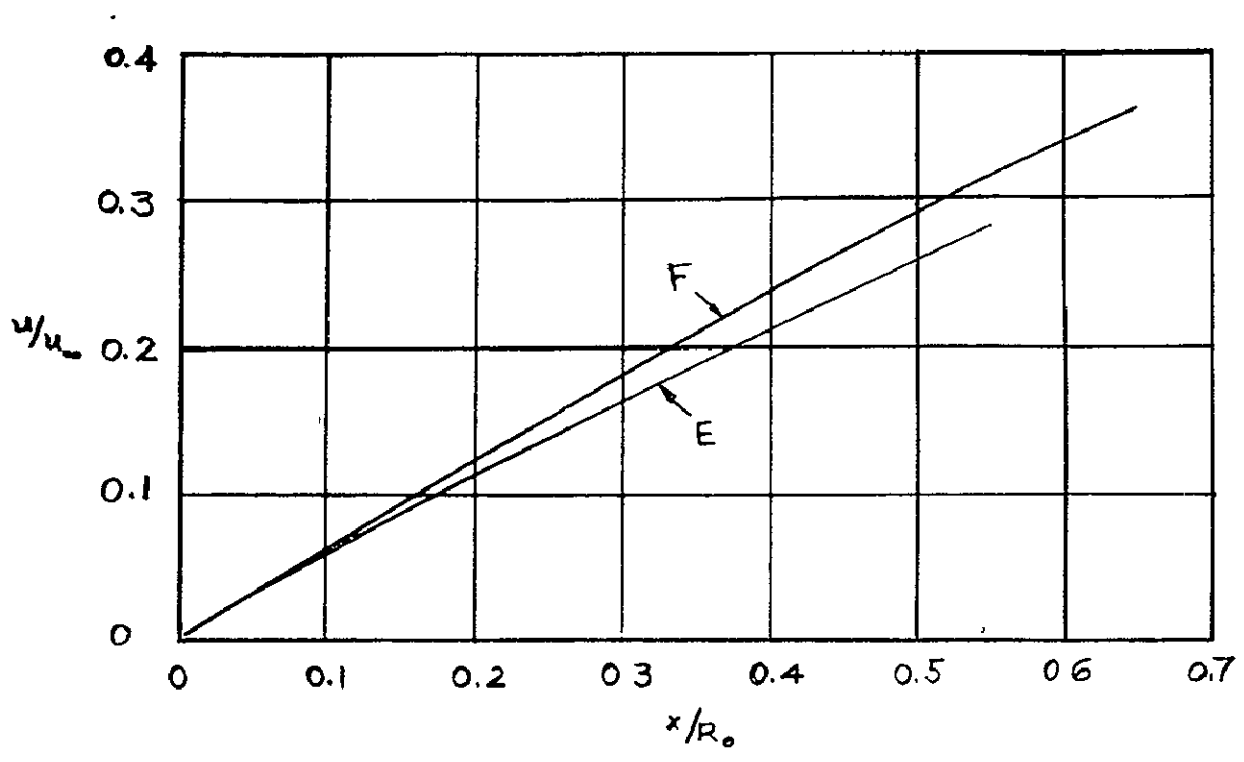


FIGURE 39. VARIATION ALONG THE BODY SURFACE

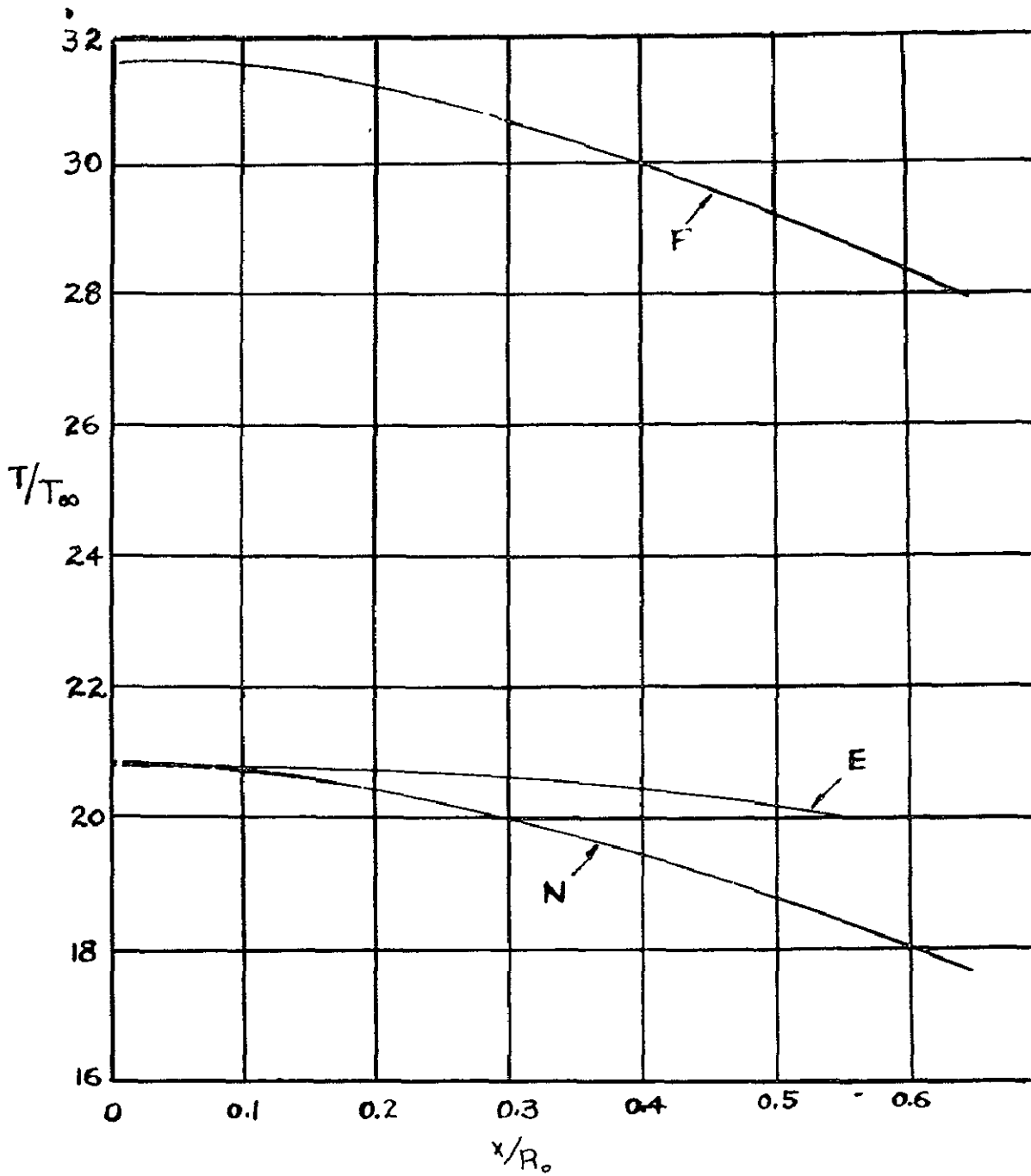


FIGURE 40. VARIATION OF  $T/T_\infty$  ALONG THE BODY SURFACE

As might be expected, the non-equilibrium solution, which is essentially an exact solution, is the most difficult case requiring a numerical solution. In all cases shown, the non-equilibrium solution lies somewhere between the two "bounds" (i.e., the frozen and equilibrium cases). It is important to note that the reservoir conditions are assumed to be under equilibrium conditions as "starting values" for the three cases treated. Under these assumptions, it is clear that, if one interprets  $A/A^*$  as the location along the blunt body surface, the local temperature, degree of dissociation, velocity, local Mach number, etc., are strong functions of the character of the flow (frozen, equilibrium, non-equilibrium). The fact that these values represent the local inviscid conditions that would be used to calculate the boundary layer, indicate the importance of determining the most realistic inviscid flow conditions. Taking the non-equilibrium solution as exact, it is apparent that the incorrect assumption of either frozen or equilibrium flow could introduce large errors in the corresponding boundary layer solution.

If one interprets these results in the design of a hypersonic wind tunnel, Figure 33 shows that the conventional "cold gas" analysis (frozen case) would predict, say, a Mach number 20 for a given  $A/A^*$ , whereas the actual flow (non-equilibrium with no boundary layer correction) would produce a Mach number of only 10. A detailed study of these results will convince even the most skeptical of the importance of obtaining the non-equilibrium solution for reacting flows at hypersonic speeds.

## Non-Equilibrium Flow

As already indicated, the inviscid real gas flow over a blunt body at hypersonic speeds is a strong function of the shock detachment distance and the starting or "reservoir" conditions (i.e., whether the flow is frozen, equilibrium or non-equilibrium at the stagnation point). It was shown that the attainment of equilibrium flow in the stagnation region is not always guaranteed, although the nozzle solutions discussed did assume equilibrium conditions in the reservoir (or at the equivalent body stagnation point). It is clear from the foregoing that the non-equilibrium condition in the stagnation region makes the flow over the blunt body considerably more difficult to calculate than for the frozen or equilibrium cases. The flow over a blunt-nosed body was calculated for the frozen, equilibrium and non-equilibrium cases but for the same freestream hypersonic conditions [7]. The model gas was essentially the Lighthill IDG where the Freeman rate equation was used for the non-equilibrium case.

The inverse method was employed wherein the shock shape is assumed and the shape of the corresponding blunt body is determined together with the solution of the inviscid flow along the stagnation streamline. The results are shown in Figures 34 through 41. Figure 34 shows that, for given freestream conditions and given shock shape, the shock detachment distance is largest for the frozen flow case and smallest for equilibrium conditions. Figures 35 through 38 show the variation of the flow parameters along the stagnation streamline from the station just downstream of the normal portion of the shock ( $g/R_0 = 0$ , where  $R_0$  is the radius of curvature of the blunt body) to the body stagnation point. Note that in all these figures the frozen flow case terminates at the stagnation point corresponding to the shock detachment distance,  $\delta = y/R_0 \approx 0.08$ , whereas the equilibrium flow solution terminates at  $\delta \approx 0.063$ . The non-equilibrium solution shows the shock detachment distance to be less than that for the equilibrium solution. Figure 35 shows that the degree of dissociation at the stagnation point for non-equilibrium flow is less than that for the equilibrium case. The corresponding values of the velocity parameter,  $v/u_\infty$ , are plotted in Figure 36 for the three flow conditions. Figure 37 reveals rather large difference in the local temperatures, although the equilibrium and non-equilibrium stagnation values are nearly identical and are much lower than the temperatures for the frozen flow case. The local density ratios plotted in Figure 38 show that the equilibrium and non-equilibrium values are nearly the same at the stagnation point and are considerably larger than the corresponding values for the frozen flow.

Starting with these values of the parameters in the stagnation region, the local flow along the blunt body was calculated for the three cases and the results plotted in Figures 39 through 41. Figure 39 shows the variation of the velocity ratio,  $u/u_\infty$ , for the frozen and equilibrium cases; the non-equilibrium solution coincides with the equilibrium solution. The variation of the degree of dissociation,  $\alpha_0$ , is shown in the lower curve of Figure 39. The local body temperatures are seen (Fig 40) to be the lowest for the non-equilibrium solution and highest for frozen flow. The reason that the equilibrium solution yields higher temperatures farther along the body, as compared to the non-equilibrium case, is due to the large number of atoms recombining and consequently releasing more heat. Figure 41 depicts the pressure distribution for the three cases. The curve denoted as  $E_N$  is the Newtonian (impact) pressure distribution which is plotted for comparison. The pressure distributions are quite similar in character with only slight differences in the magnitudes of the pressure ratios. This is convincing evidence of the fact,

as indicated earlier, that the pressure distribution is relatively insensitive to real gas effects. It is clear from this example that the local values of Reynolds number, Mach number, temperature, etc., are strong functions of the flow conditions (frozen, equilibrium or non-equilibrium) and would therefore result in significantly different values of boundary layer skin friction and heat transfer for the three cases.

## Laminar Boundary Layer In Hypersonic Real Gas Flow

The calculation of the boundary layer over a blunt body in hypersonic flow depends on an accurate knowledge of the local inviscid flow properties just outside the boundary layer. An inviscid flow analysis similar to that outlined above will yield these required local flow properties. The analysis of the boundary layer for the flow of a reacting gas over a blunt body is quite complex and, as yet, no satisfactory solution has been found. In the discussion to follow, a relatively simple solution of a laminar boundary layer for a reacting gas will be described. In particular, the results of an analysis for the frozen and equilibrium laminar boundary layer flow of a singly-ionized monatomic gas over a flat plate will be discussed. The results of this simple solution should nevertheless reveal the essential features of the laminar boundary layer of a reacting gas flow.

The governing two-dimensional, laminar boundary layer equations for a reacting gas are summarized in Table VII, namely, the equation of state, the conservation of species, the continuity equation, the x- and y- momentum equations and the energy equation. The details of the derivation of these equations are given in Reference 8. A modified Karman-Tsien-Lees solution is found [8] for the frozen and equilibrium flow over a flat plate for both an ideal ionizing monatomic gas and an ideal dissociating gas. Typical results are shown in Figures 42 through 47 for the ionized monatomic gas. It is important to note that the frozen and equilibrium solutions represent the upper and lower "bounds" so that the more realistic non-equilibrium solution lies somewhere between these two limits.

Figure 42 gives the velocity profiles for Mach numbers 5 and 10 for three local "freestream" values of degree of ionization, namely,  $\epsilon_\infty = 0.6$ , 0.933, and 0.997. The Blasius solution ( $M_\infty = 0$ ) is plotted for comparison. The results presented are for the "cold wall" case since the degree of ionization at the wall,  $\epsilon_w = 0$ . The important features to be noted in Figure 42 are

TABLE VII. GOVERNING EQUATIONS FOR A REACTING GAS

$$p = \sum_i p_i = \sum_i \rho_i \frac{k}{m_i} T = \sum_i \rho_i R_i T = \rho \bar{R} T$$

$$\rho u \frac{\partial c_i}{\partial x} + \rho v \frac{\partial c_i}{\partial y} = \frac{\partial}{\partial y} \left( \rho D_{12} \frac{\partial c_i}{\partial y} \right) + \dot{w}_i$$

$$\frac{\partial(\rho u)}{\partial x} + \frac{\partial(\rho v)}{\partial y} = 0$$

$$\rho u \frac{\partial u}{\partial x} + \rho v \frac{\partial u}{\partial y} = - \frac{\partial p}{\partial x} + \frac{\partial}{\partial y} \left( \mu \frac{\partial u}{\partial y} \right)$$

$$\frac{\partial p}{\partial y} = 0$$

TABLE VII. GOVERNING EQUATIONS FOR A REACTING GAS (Concluded)

$$\rho u \frac{\partial h}{\partial x} + \rho v \frac{\partial h}{\partial y} = \frac{\partial}{\partial y} \left[ \frac{\mu}{Pr} \frac{\partial h}{\partial y} \right] + \frac{\partial}{\partial y} \left[ \frac{\lambda}{c_p p_f} (Le - 1) \sum_i h_i \frac{\partial c_i}{\partial y} \right] + \mu \left( \frac{\partial u}{\partial y} \right)^2$$

$$\rho u \frac{\partial I}{\partial x} + \rho v \frac{\partial I}{\partial y} = \frac{\partial}{\partial y} \left[ \frac{\mu}{Pr} \frac{\partial I}{\partial y} \right] + \frac{\partial}{\partial y} \left[ \mu \left( 1 - \frac{1}{Pr} \right) \frac{1}{2} \frac{\partial u^2}{\partial y} \right] \\ + \frac{\partial}{\partial y} \left[ (Le - 1) \frac{\lambda}{c_p p_f} \sum_i h_i \frac{\partial c_i}{\partial y} \right]$$

$$\rho u \frac{\partial h}{\partial x} + \rho v \frac{\partial h}{\partial y} = \frac{\partial}{\partial y} \left[ \mu \frac{\partial h}{\partial y} \right] + \mu \left( \frac{\partial u}{\partial y} \right)^2$$

$$\rho u \frac{\partial I}{\partial x} + \rho v \frac{\partial I}{\partial y} = \frac{\partial}{\partial y} \left[ \mu \frac{\partial I}{\partial y} \right]$$

the large growth of the boundary layer with increase in Mach number, the influence of the local inviscid degree of ionization on the velocity profile, and the nearly linear character of the velocity profile at Mach number 10. Figure 43 shows the differences in the temperature profiles for the frozen and equilibrium solutions for a moderate hypersonic Mach number. Note that the frozen case predicts much higher temperatures near the wall than for the equilibrium case. Figure 44 gives a composite plot of the frozen temperature profiles for Mach numbers 0, 5, and 10 for different values of freestream ionization. For a given Mach number the main differences in temperature occur in the outer region of the boundary layer.

One of the most important parameters in hypersonic boundary layer flow is the boundary layer displacement thickness. That is, the effective body shape is found by adding the local boundary layer displacement thickness to the corresponding geometrical ordinate of the body. Thus, the present flat plate has an effective "parabolic" shape that will experience a corresponding hypersonic pressure distribution. Figure 45 shows the very marked growth of the boundary layer with increase in Mach number. It is also clear that increasing the degree of ionization in the local inviscid flow tends to "thin out" the boundary layer. Finally, Figures 46 and 47 show the differences in the character of the ionization profiles for frozen and equilibrium flows for Mach number 5 for  $\epsilon_\infty = 0.60$ . Of particular interest is the "knee" in the equilibrium curve and the absence of one for the frozen case which corresponds to a "hot spot" in the boundary layer for the frozen flow (Fig. 43).

## Boundary Layer-Shock Wave Interaction

At hypersonic Mach numbers the character of the laminar boundary layer flow over a flat plate results in high skin friction and heat transfer rates. Even higher aerodynamic heating rates occur for a turbulent boundary layer. Details of the theory of laminar and turbulent boundary layers and the techniques for calculating the aerodynamic heating over bodies are given in Reference 9, including a full discussion of the maximum aerodynamic heating condition at the body stagnation point. Another critical aerodynamic heating situation that may rival or exceed the stagnation point heating rate is when a shock wave in hypersonic flow interacts with a turbulent boundary layer. This problem has been treated for the case of protuberances in Reference 10 and will be discussed briefly in the following.

Figure 48 shows a plot of the ratio of the local heating rate,  $h$ , (due to boundary layer-shock interaction) to the flat-plate heating rate,  $h_0$ , (with no interaction) for the case of a cylindrical protuberance mounted on a flat plate at Mach number 3.51. It is clear that the detached bow wave which "wraps" itself around the cylinder interacts with the turbulent boundary layer creating a maximum heating region on the plate near the normal portion of the bow shock (Fig. 49). A side view schematic of the flow situation is shown in Figure 50 where the shock wave interacts with the turbulent boundary layer (on centerline) giving rise to an abrupt thickening of the boundary layer and the formation of a lambda-footed shock. This abrupt thickening of the boundary layer acts as an equivalent wedge angle,  $\theta$ , with an attached shock wave and creates a pressure jump and a corresponding increase in aerodynamic heating in this region. A detailed mathematical analysis of the flow model is given in Reference 10 and the results are plotted in Figures 51 and 52. The pressure rise predicted by the theory is plotted in Figure 51 along with experiment as a function of the product of Mach number,  $M_0$ , and Reynolds number,  $Re_0$ . It is clear that the agreement between theory and experiment is excellent. Figure 52 shows a parametric plot of the maximum heating rate,  $h_{max}$ , as a function of the new hypersonic turbulent boundary layer parameter,  $\chi_t$ . The correlation with experiment is considered satisfactory. The important and rather surprising point is that, under these interaction conditions, an extreme "hot spot" is generated ahead of the protuberance that can be many times greater than that of the simple undisturbed turbulent boundary layer for the same flow conditions. For example, Figure 48 shows the maximum local "hot spot" to be more than 7 times hotter than the heat transfer rate for the undisturbed turbulent boundary layer for a moderate Mach number of 3.51. It is to be noted that the heating rate for the undisturbed turbulent flat plate boundary layer at hypersonic speeds can be of such intensity that the ablation of steel can easily occur. For true hypersonic flow the "hot spot" can approach values of  $h/h_0$  much greater than 10, so it is easy to see that this represents one of the most critical design conditions for hypersonic vehicles.

## Flow Separation

Another severe aerodynamic heating problem occurs when the supersonic flow separates upstream of a geometrical flow deflection and reattaches downstream (Fig. 53). It is clear that the separation region as well as the

reattachment region can both be treated by an analysis similar to that of Reference 10. It is interesting to note the differences between the separated flows for laminar and turbulent boundary layers (Fig. 54). The pressure rise can be predicted by the model used in Reference 10 by using the skin friction and boundary layer displacement thickness expressions for laminar and turbulent flows.

Boundary layer separation on delta wings has been studied [11]. The separation phenomena is shown in Figure 55 and can be treated by a method similar to that of Reference 10 as regards the formation of the lambda-footed shock and the calculation of the pressure rise and heat transfer. Note that a vortex has formed downstream of the point of separation. This additional flow parameter complicates the flow pattern considerably and, as yet, has not been treated analytically.

## Real Gas Effects In Shock Interaction

The analysis used in Reference 10 can be modified to take into account the real gas effects. This can be accomplished by taking into account the real gas effects across the oblique shock portion of the lambda-footed shock (Fig. 50). Figures 56 through 59 give the pressure, temperature, Mach number and Reynolds number as a function of the angle of incidence,  $\alpha$ , which corresponds to the angle  $\theta$  of Reference 10 (Fig. 50). These figures show clearly the difference between the assumption of a perfect gas (frozen flow) and an equilibrium flow. These results are based on the analysis of References 11 and 12. To use these results in the analysis of Reference 10, it is necessary to derive an expression for the ratio of the skin friction coefficient due to interaction,  $c_{f_i}$ , to the skin friction coefficient without interaction,  $c_{f_0}$ , as a function of the corresponding ratios of temperature,  $T/T_0$ , Mach number,  $M/M_0$ , and pressure,  $p/p_0$ . The desired analysis is outlined in Table VIII using the notation of Reference 10. Note, in this analysis, that the assumption that the velocity ratio,  $V/V_0 \simeq 1$ , which was made in Reference 10, is not made here. The last expression for  $c_{f_i}/c_{f_0}$  in Table VIII can be used in conjunction with Figures 56 through 58 to calculate  $c_{f_i}/c_{f_0}$  for the frozen and equilibrium cases, provided one knows  $\alpha$ , the boundary layer displacement thickness (referred to as  $\theta$  in Reference 10). It is clear from the results shown in

TABLE VIII.  $C_f$  AND  $C_{f_0}$  ANALYSIS

$$C_{f_w} = C(Rey_w)^m$$

$$C_{f_w} = c_f (V_0/V)^2 (\rho_0/\rho_w)$$

$$c_f = C(V/V_0)^2 (\rho_w/\rho_0)(Rey_w)^m$$

$$\frac{Rey_w}{Rey_0} = \left(\frac{\rho_w}{\rho_0}\right) \left(\frac{\mu_0}{\mu_w}\right) \left(\frac{V}{V_0}\right) = \left(\frac{p}{p_0}\right) \left(\frac{T_0}{T_w}\right)^{1+n} \left(\frac{V}{V_0}\right)$$

$$c_f = C(p/p_0)^{1+m} (T_0/T_w)^{1+m(1+n)} (V/V_0)^{2+m} (Rey_0)^m$$

$$C_{f_0} = C(1/\xi_0^{1+m(1+n)}) (Rey_0)^m$$

$$\xi_0 = T_w/T_0 = 1 + Pr^a(\gamma - 1)/2M_0^2$$

$$c_f/c_{f_0} = (p/p_0)^{1+m} \left( (T_0/T_w) \xi_0 \right)^{1+m(1+n)} (V/V_0)^{2+m}$$

$$(T_0/T_w) \xi_0 = \frac{T_0(1 + Pr^a(\gamma - 1)/2M_0^2)}{T(1 + Pr^a(\gamma - 1)/2M^2)} \approx (T_0/T)(M_0/M)^2$$

$$(V/V_0) = (M/M_0)(T/T_0)^{1/2}$$

$$\frac{c_f}{C_{f_0}} = (T/T_0)^{\frac{2+m}{2} - [1+m(1+n)]} (M/M_0)^{2+m - \{2[1+m(1+n)]\}} (p/p_0)^{1+m}$$

$$c_f/c_{f_0} = (T/T_0)^A (M/M_0)^B (p/p_0)^C$$

Figure 45, and the analysis of Reference 8, that the boundary layer displacement thickness can be determined by a real gas analysis and thus the problem is tractable. In order to get numerical results, the Reynolds number,  $Re_{\infty}$ , and the Mach number,  $M_{\infty}$ , shown in Figure 45 must be recognized as those corresponding to the unsubscripted parameters  $M$ ,  $p$ ,  $T$ , etc. in the analysis of Table VIII (i. e., the local values downstream of the oblique shock). Therefore, the solution will, of necessity, be an iterative one similar to that described in the boundary layer-shock interaction analysis of Reference 2. It is clear from Figures 56 through 59 that this refinement in the shock wave interaction problem is essential if accurate aerodynamic heating rates are to be calculated. The correlation of pressure rise and aerodynamic heating can still be obtained in the form shown in Figures 51 and 52.

## Conclusion

From this discussion in which the various factors involved in the determination of the aerodynamic heating of bodies traveling at hypersonic speeds are presented, it should be evident that even the "simple" mathematical analyses and physical models required to get an approximate solution are quite complex and can only be found by numerical techniques. Although more accurate analyses and physical models can be used at each step in the calculation (inviscid real gas solution, the boundary layer analysis, and the real gas interaction problem, etc.) the questions of computer capacity and cost versus the desired engineering accuracy must be considered.

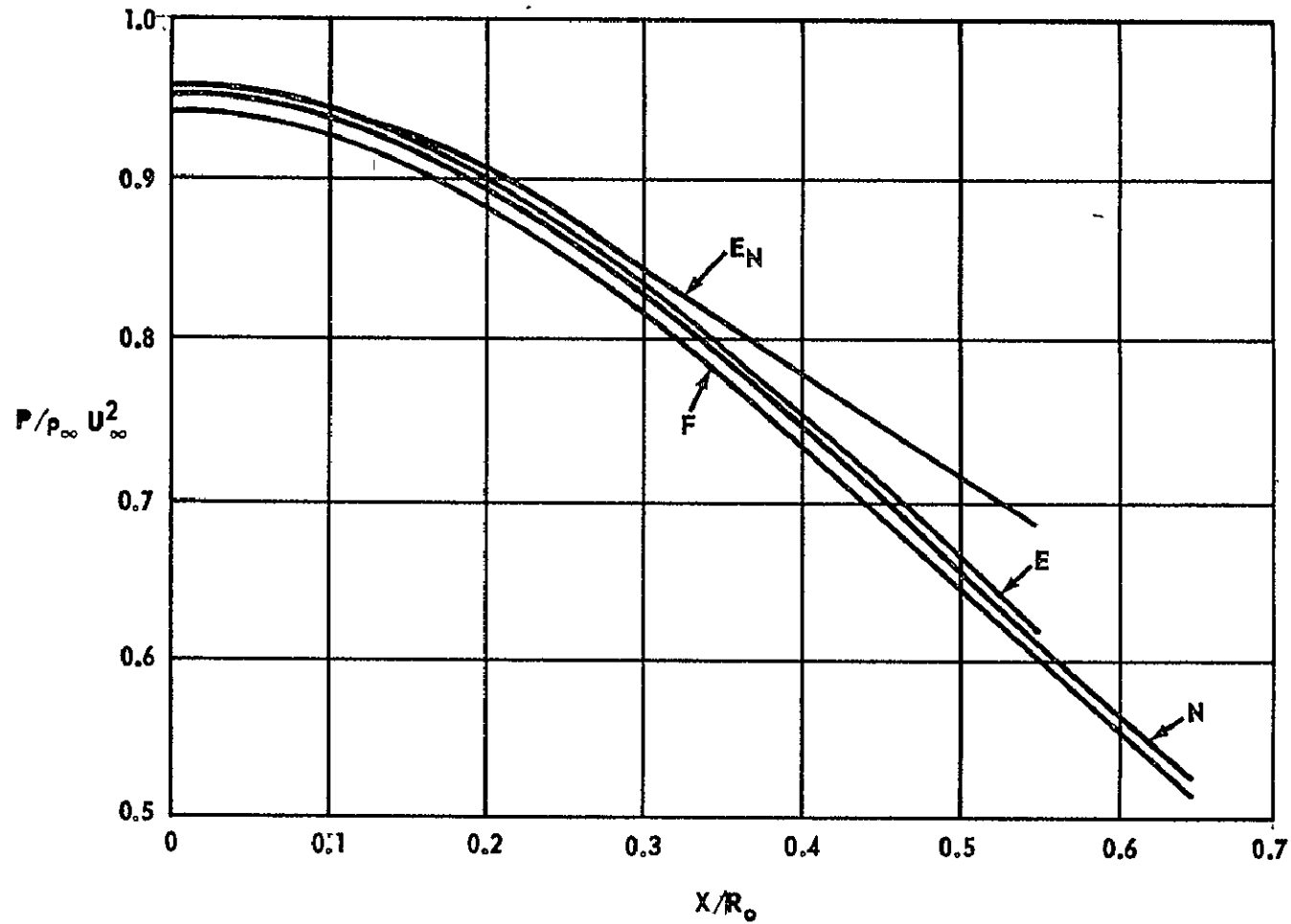


FIGURE 41. VARIATION OF  $P/\rho_\infty U_\infty^2$  ALONG THE BODY SURFACE

( $E_N$  = Newtonian Pressure Law)

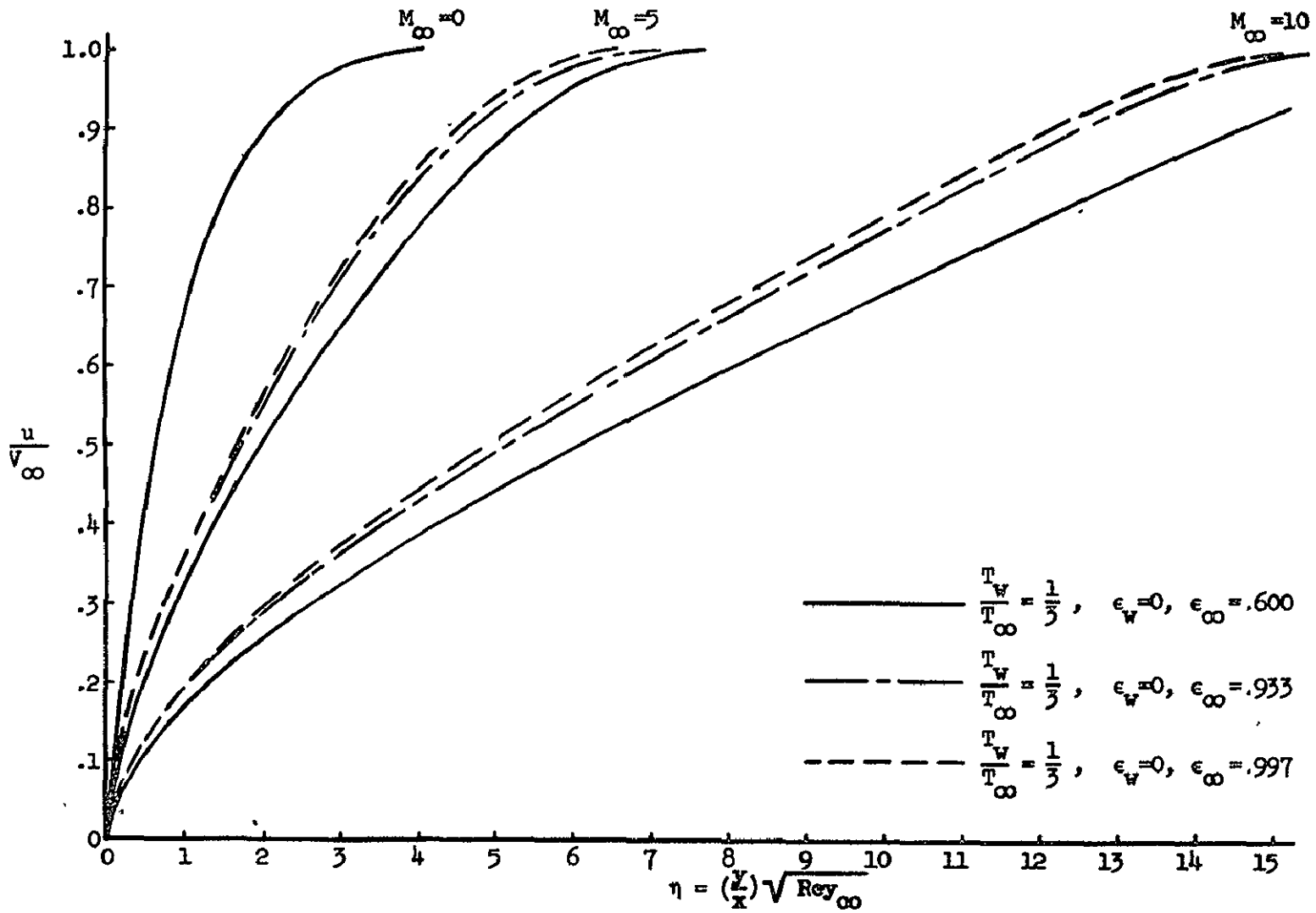


FIGURE 42. COMPOSITE PLOT OF VELOCITY PROFILES WITH  $T_w/T_{\infty} = 1/3$  FOR AN IONIZED MONATOMIC GAS

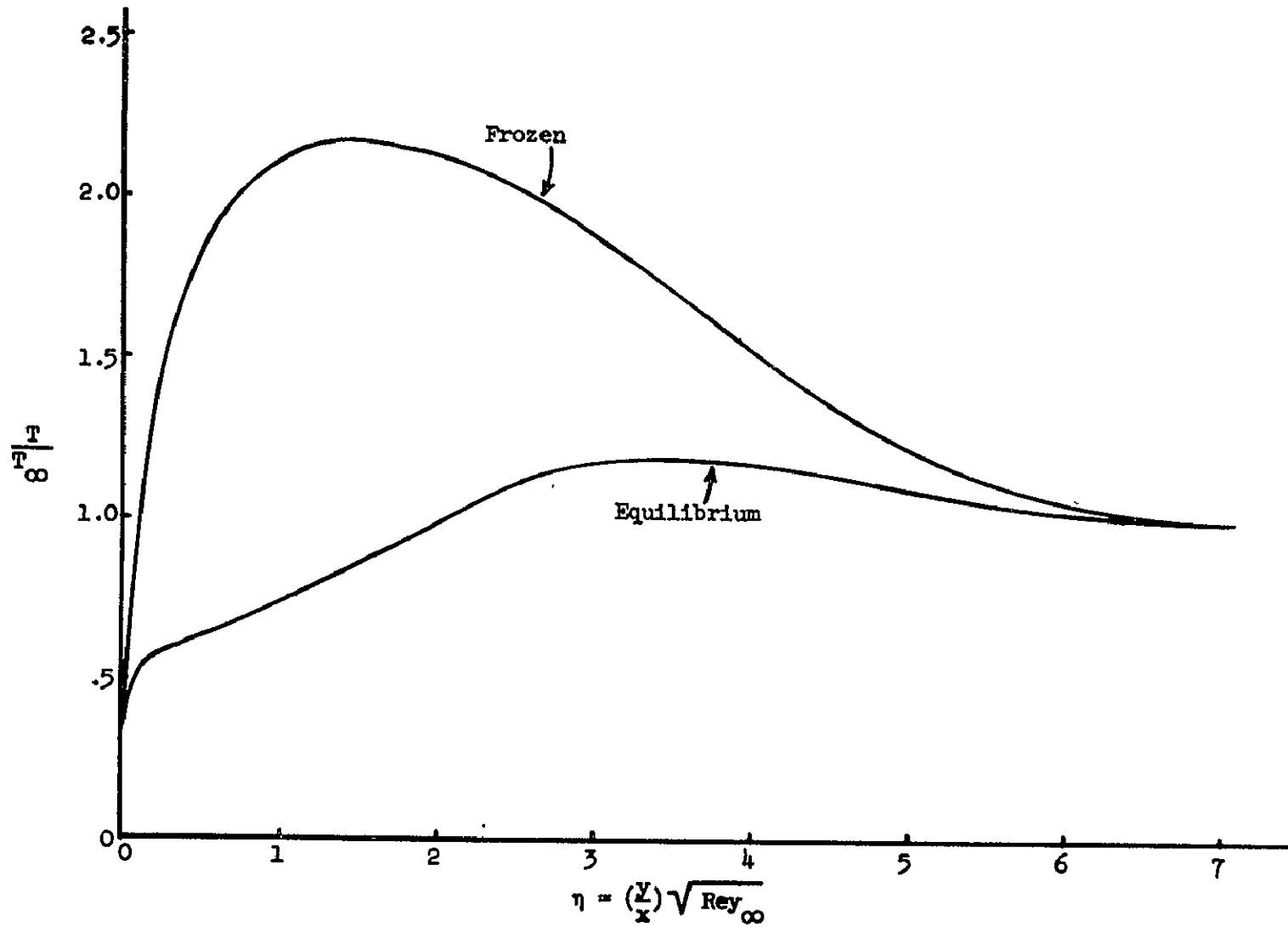


FIGURE 43. COMPARISON OF FROZEN AND EQUILIBRIUM TEMPERATURE PROFILES WITH  $T_w/T_\infty = 1/3$ ,  $\epsilon_w = 0$ ,  $\epsilon_\infty = 0.997$ , and  $M_\infty = 5$  FOR AN IONIZED MONATOMIC GAS

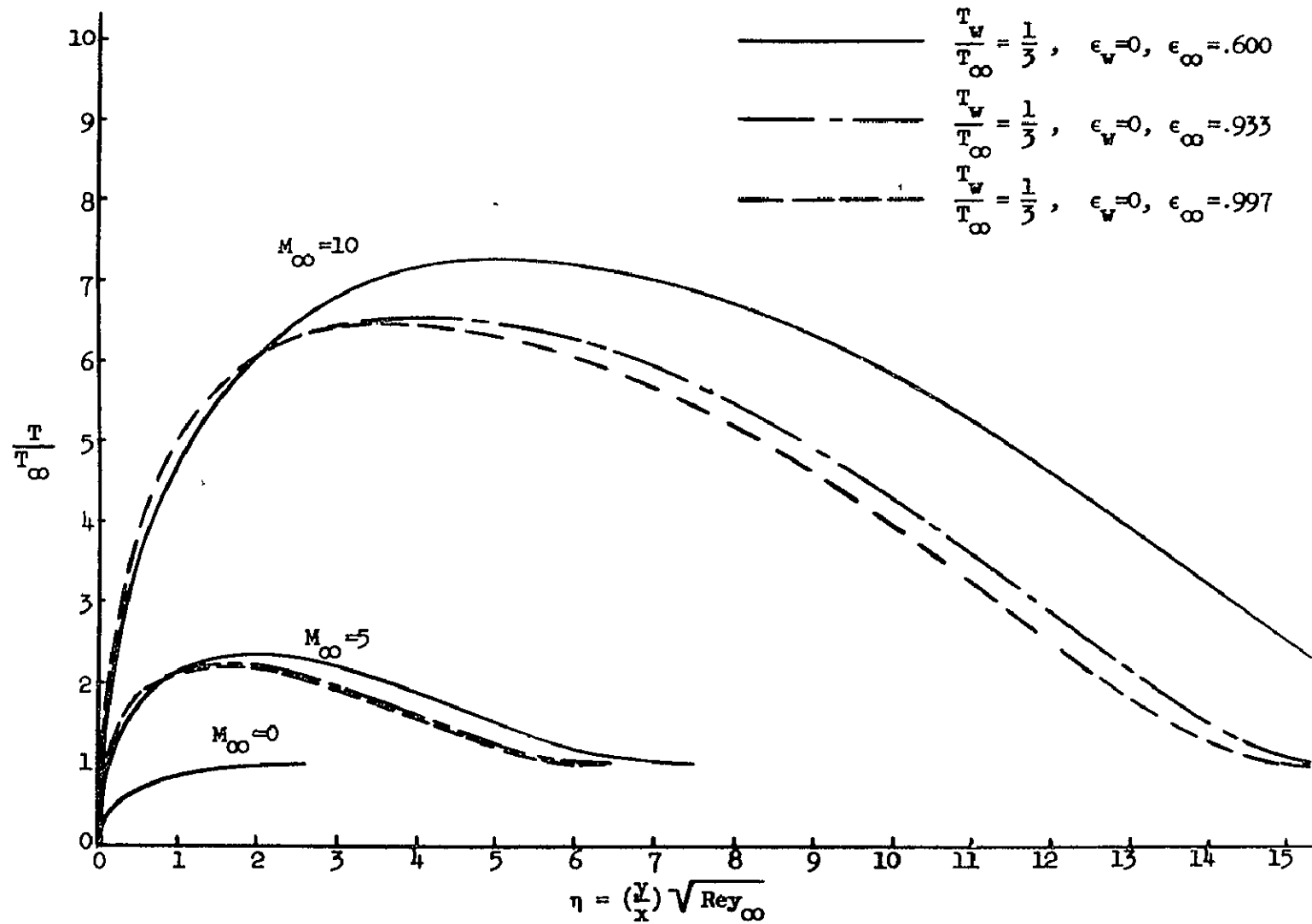


FIGURE 44. COMPOSITE PLOT OF TEMPERATURE PROFILES WITH  $T_w/T_\infty = 1/3$  FOR AN IONIZED MONATOMIC GAS (Frozen Flow)

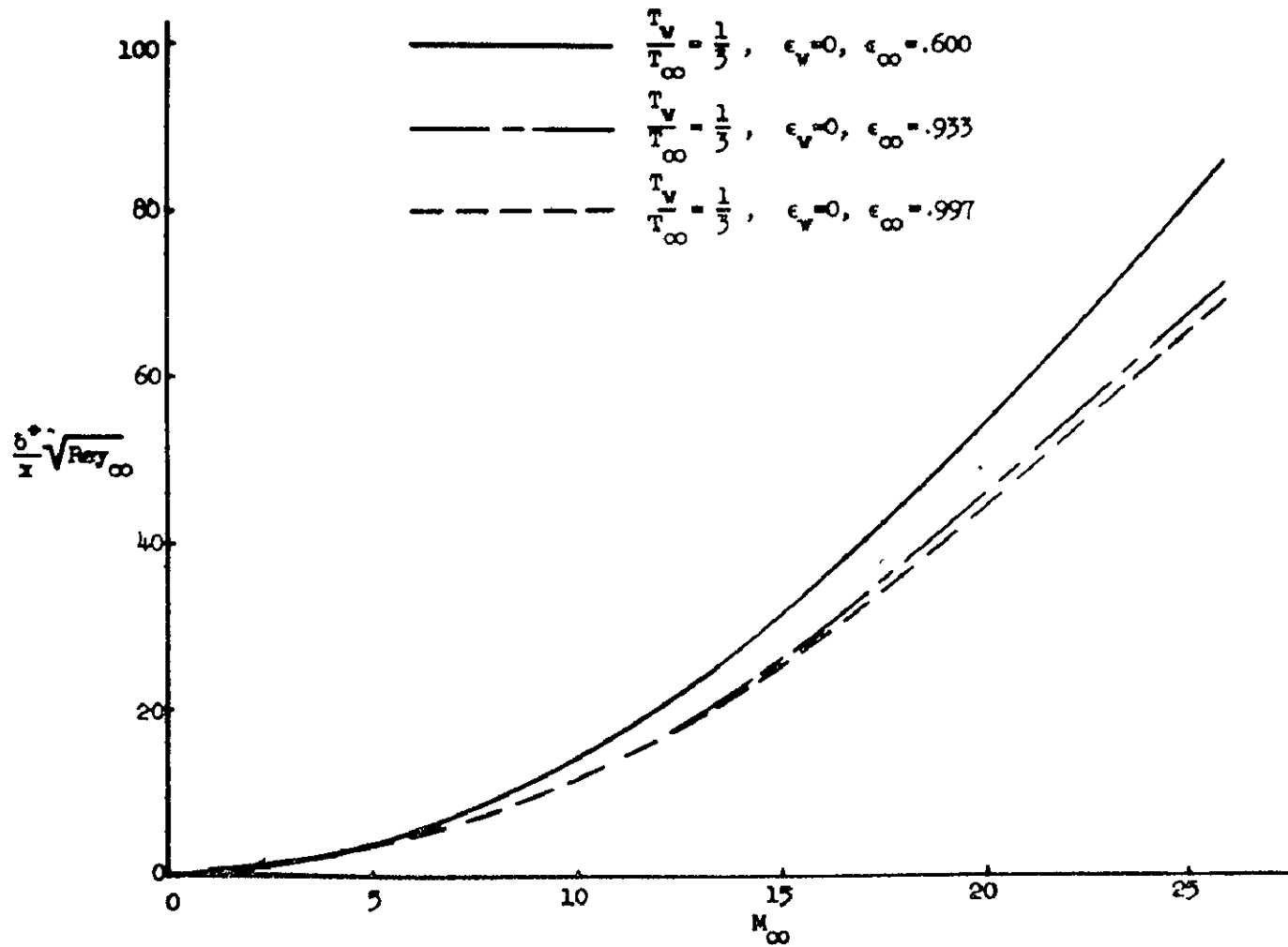


FIGURE 45. VARIATION OF BOUNDARY LAYER DISPLACEMENT THICKNESS WITH MACH NUMBER FOR AN IONIZED MONATOMIC GAS

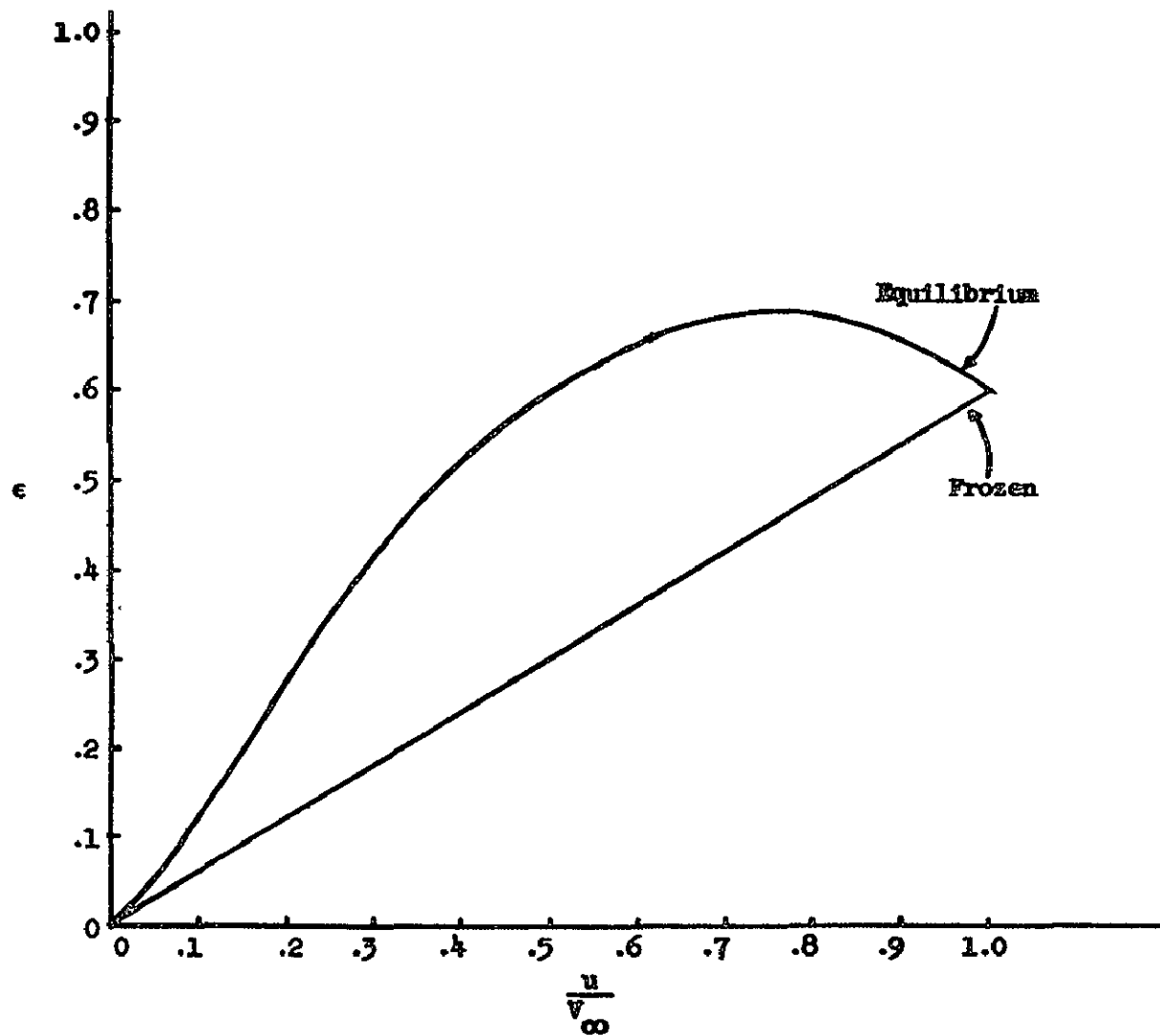


FIGURE 46. VARIATION OF  $\epsilon$  WITH RESPECT TO  $u/V_\infty$  WITH  $T_w/T_\infty = 1/3$ ,  
 $\epsilon_w = 0$ ,  $\epsilon_\infty = 0.600$ , AND  $M_\infty = 5$  FOR AN IONIZED MONATOMIC GAS

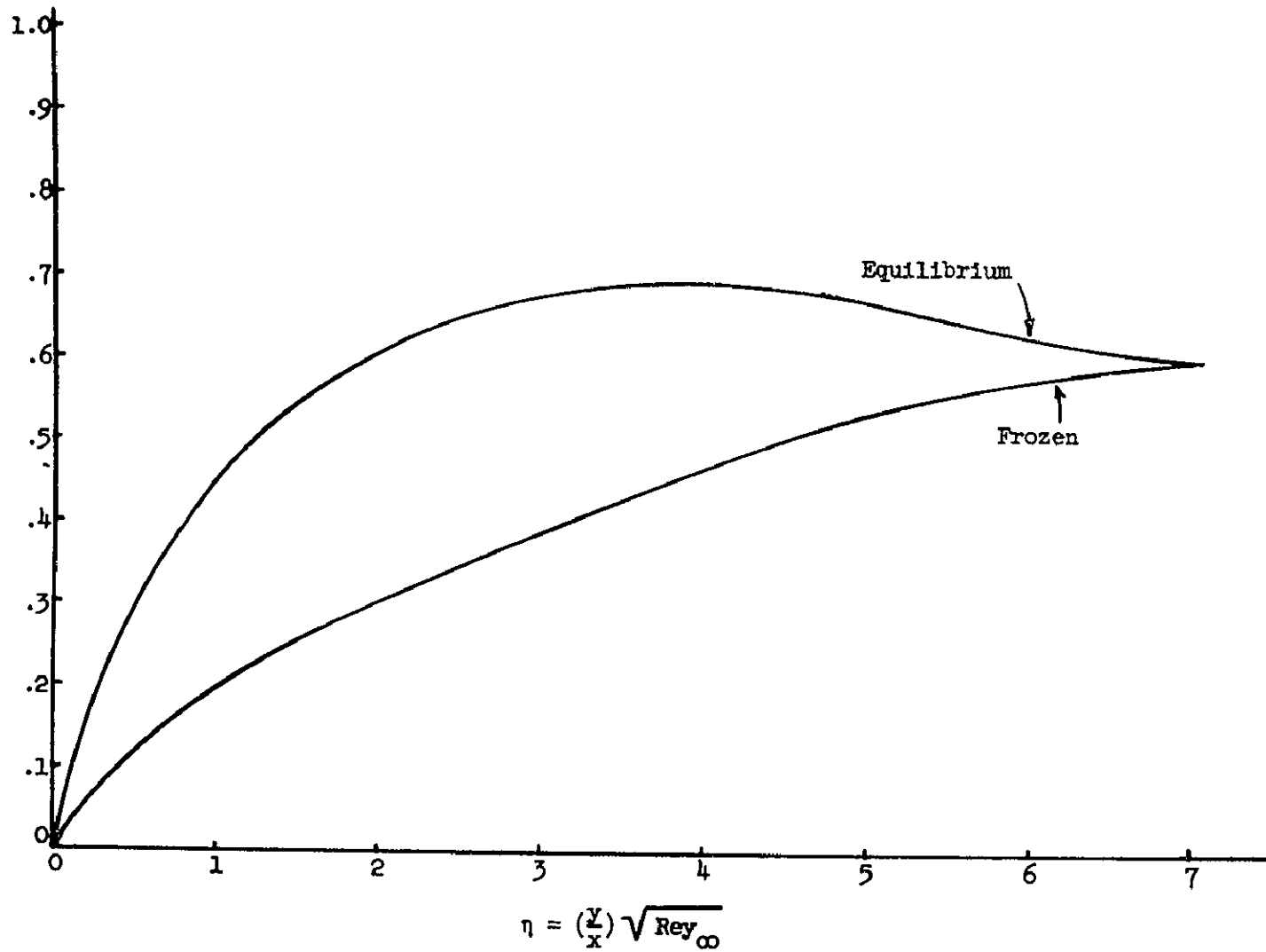


FIGURE 47 IONIZATION PROFILES WITH  $T_w/T_{\infty} = 1/3$ ,  $\epsilon_w = 0$ ,  $\epsilon_{\infty} = 0.600$ , AND  $M_{\infty} = 5$   
FOR AN IONIZED MONATOMIC GAS

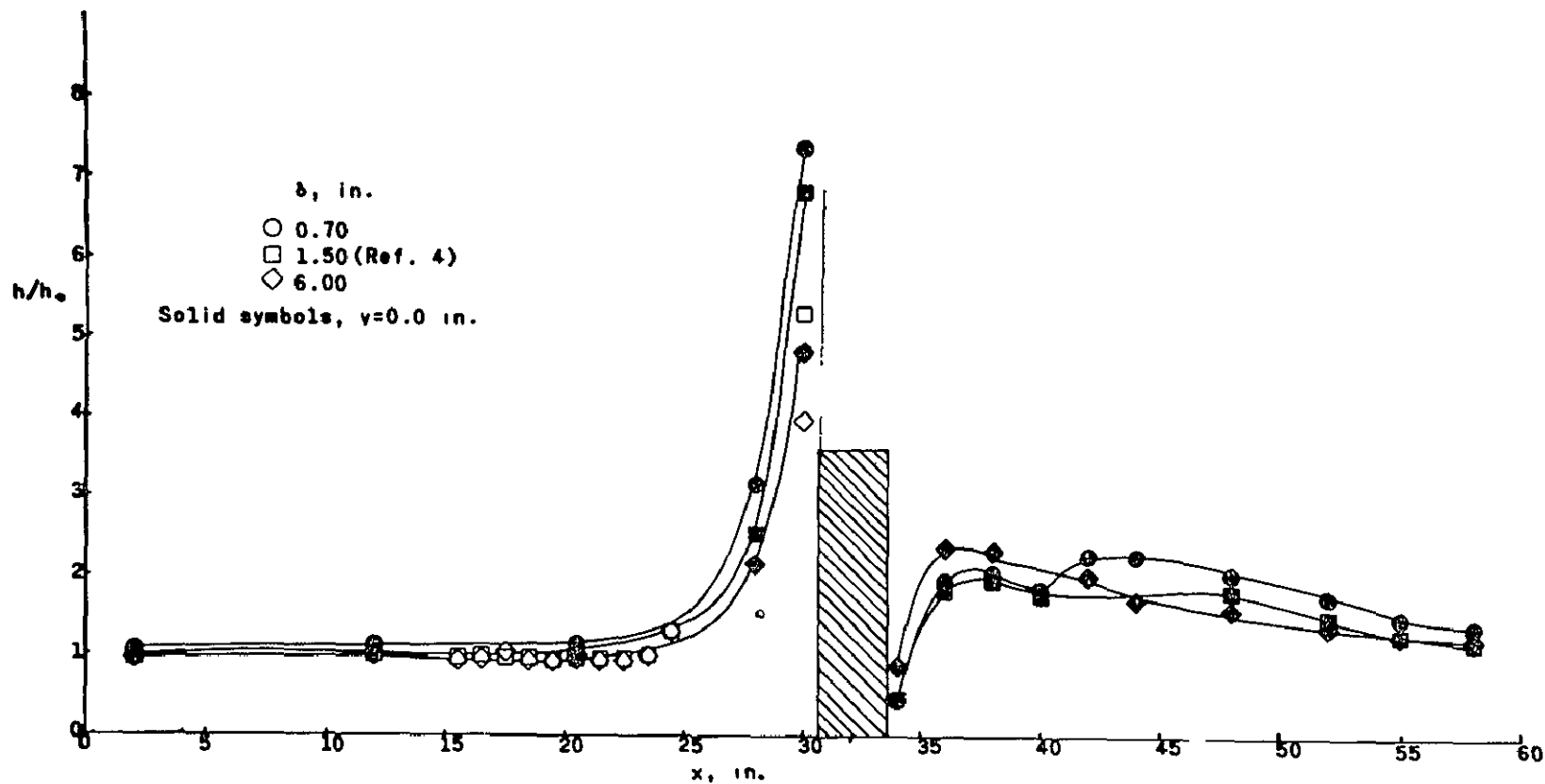


FIGURE 48. EFFECT OF BOUNDARY-LAYER THICKNESS ON THE DISTRIBUTION OF  $h/h_0$  WITHIN 2 1/2 INCHES OF THE FLAT-PLATE CENTER LINE FOR A 2.8-INCH-DIAMETER RIGHT CIRCULAR CYLINDER;  $M = 3.51$ ;  $R \approx 2.90 \times 10^6$ .

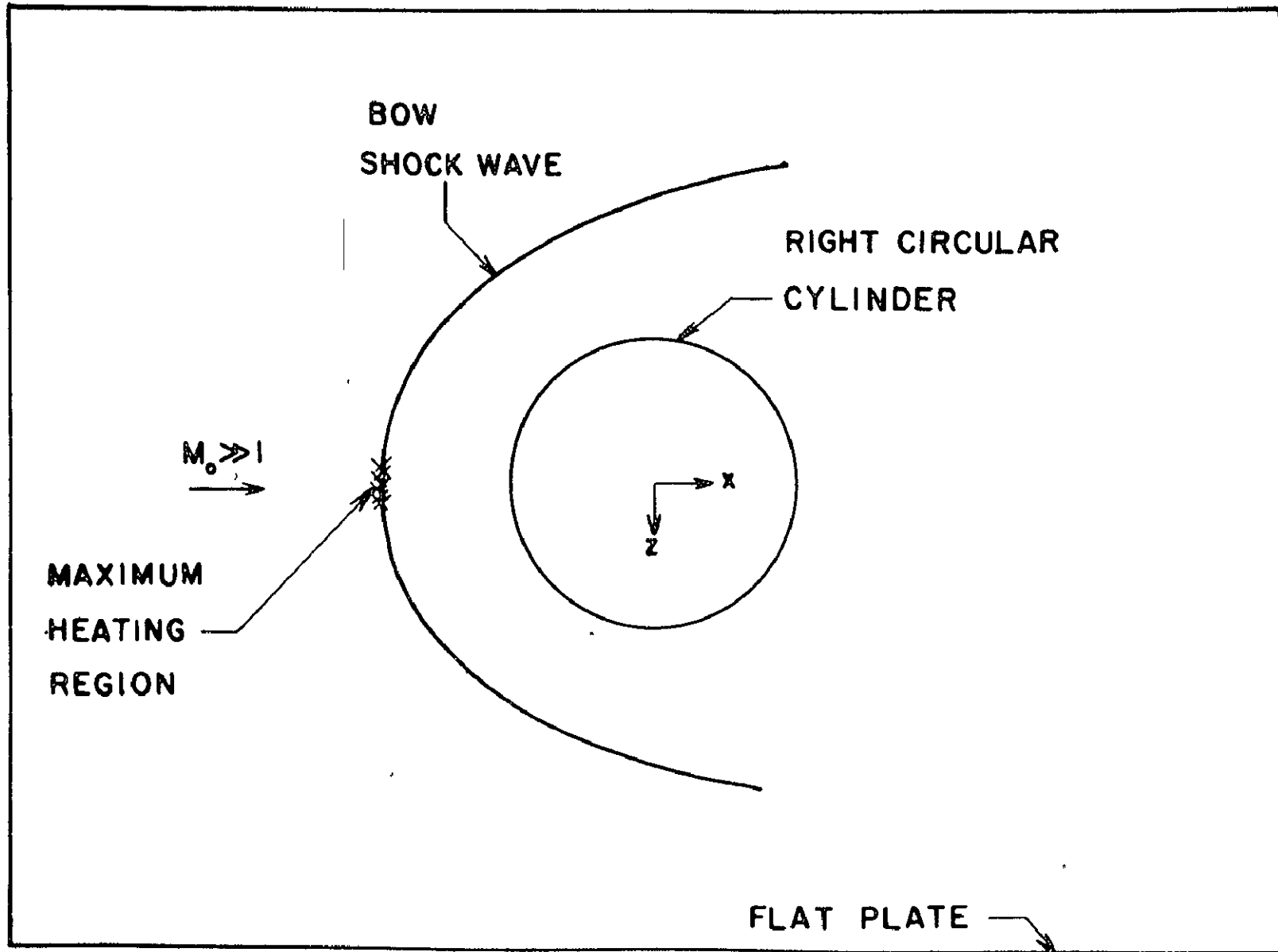


FIGURE 49. MAXIMUM HEATING — BOUNDARY LAYER-SHOCK WAVE INTERACTION

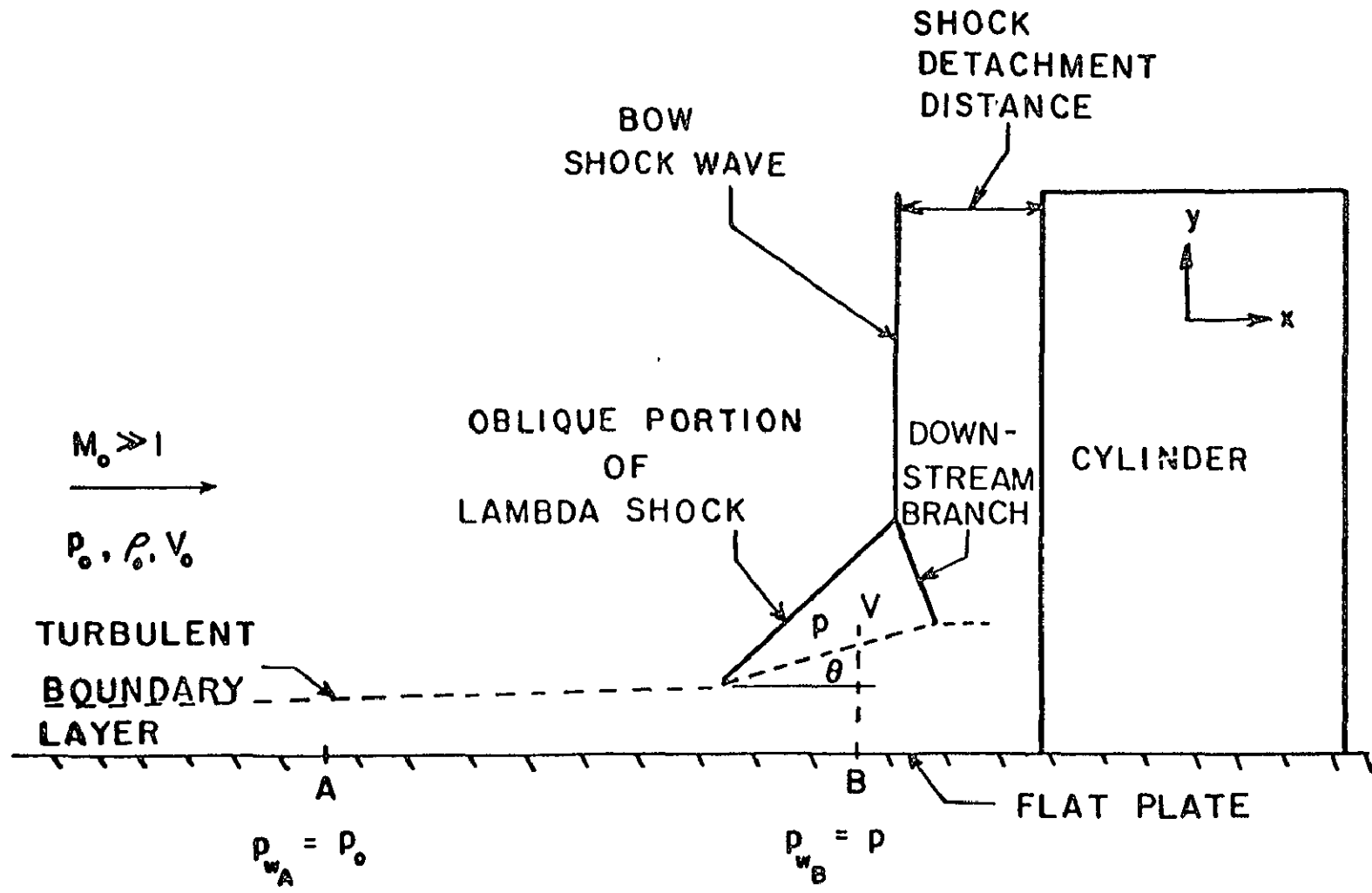


FIGURE 50. SHOCK INTERACTION WITH TURBULENT BOUNDARY LAYER

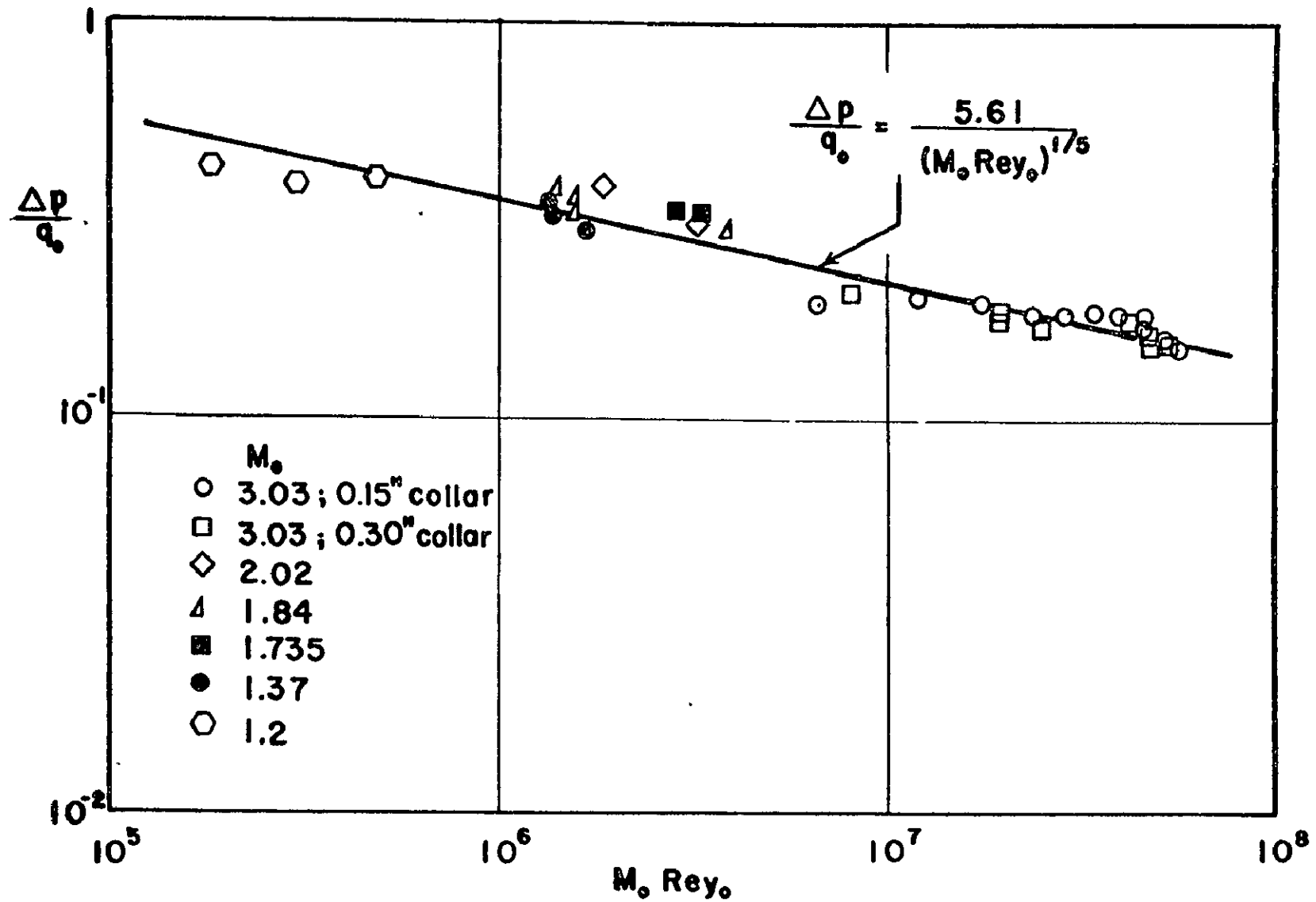


FIGURE 51. PRESSURE RISE VERSUS MACH NUMBER — REYNOLDS NUMBER PRODUCT FOR LAMBDA-FOOTED SHOCK

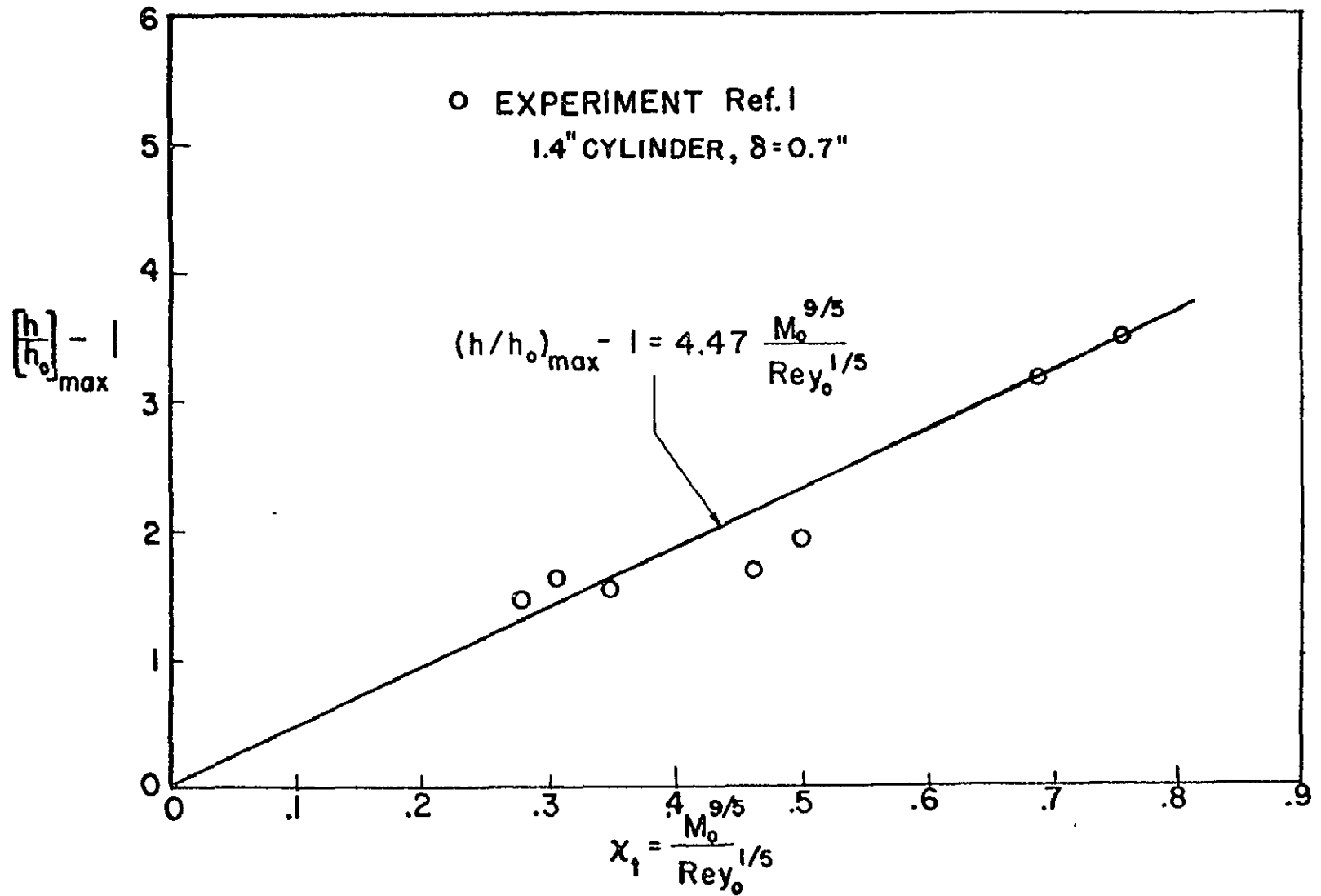


FIGURE 52. MAXIMUM HEATING RATE AS A FUNCTION OF  $\chi_T$

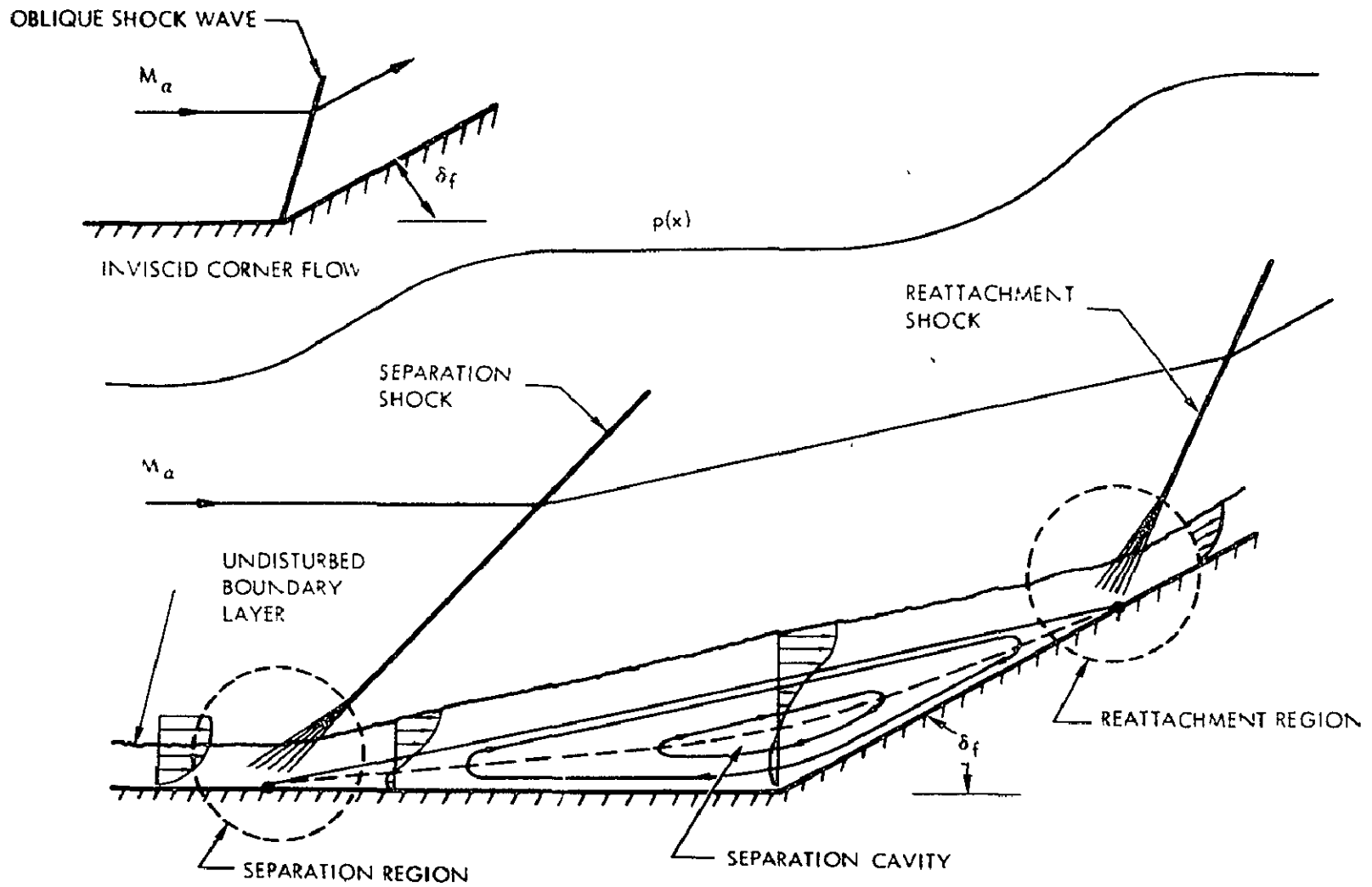


FIGURE 53. FLOW SEPARATION IN VISCOUS CORNER FLOW

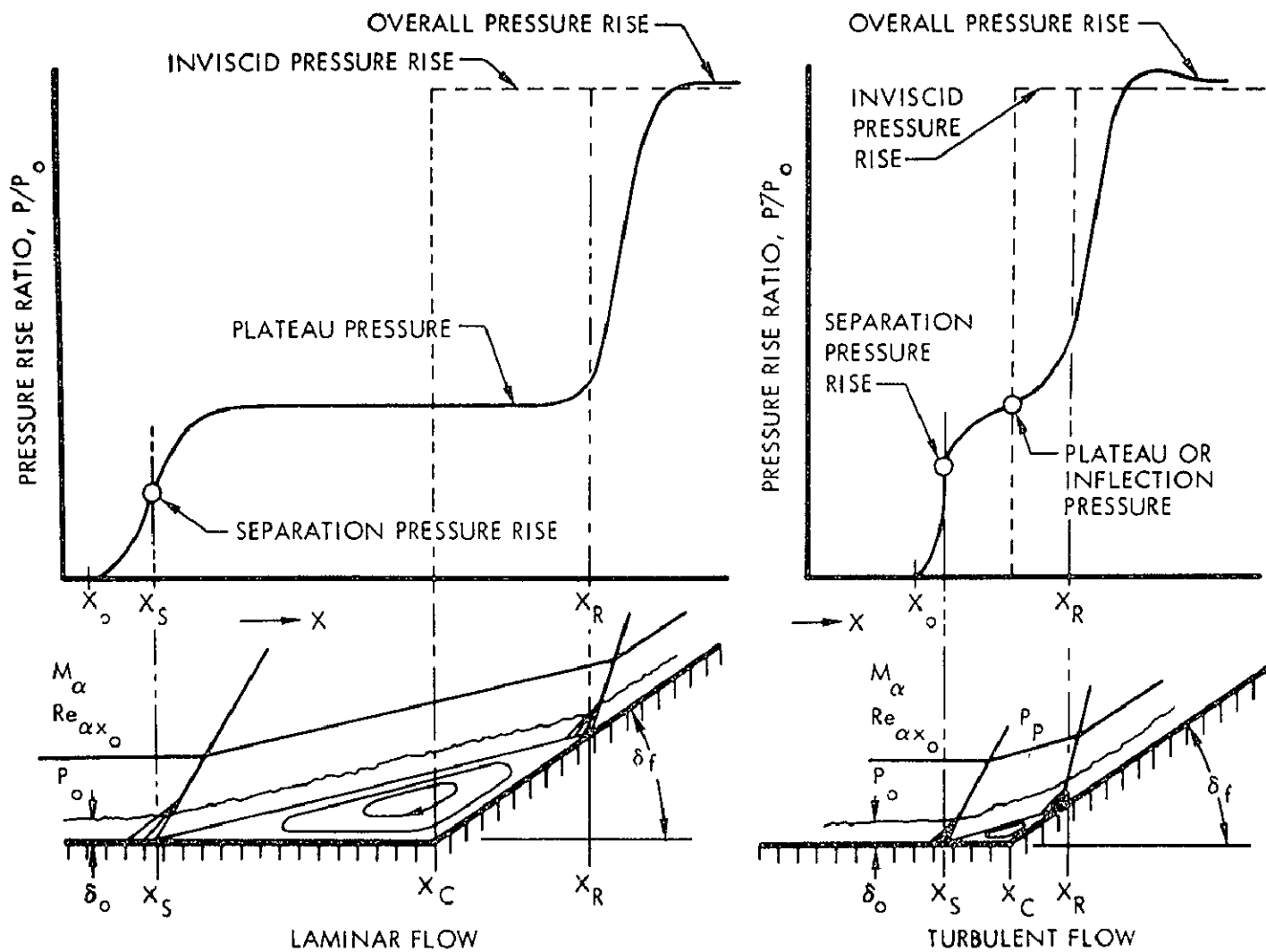


FIGURE 54. PRESSURE DISTRIBUTION IN LAMINAR AND TURBULENT SEPARATED FLOW

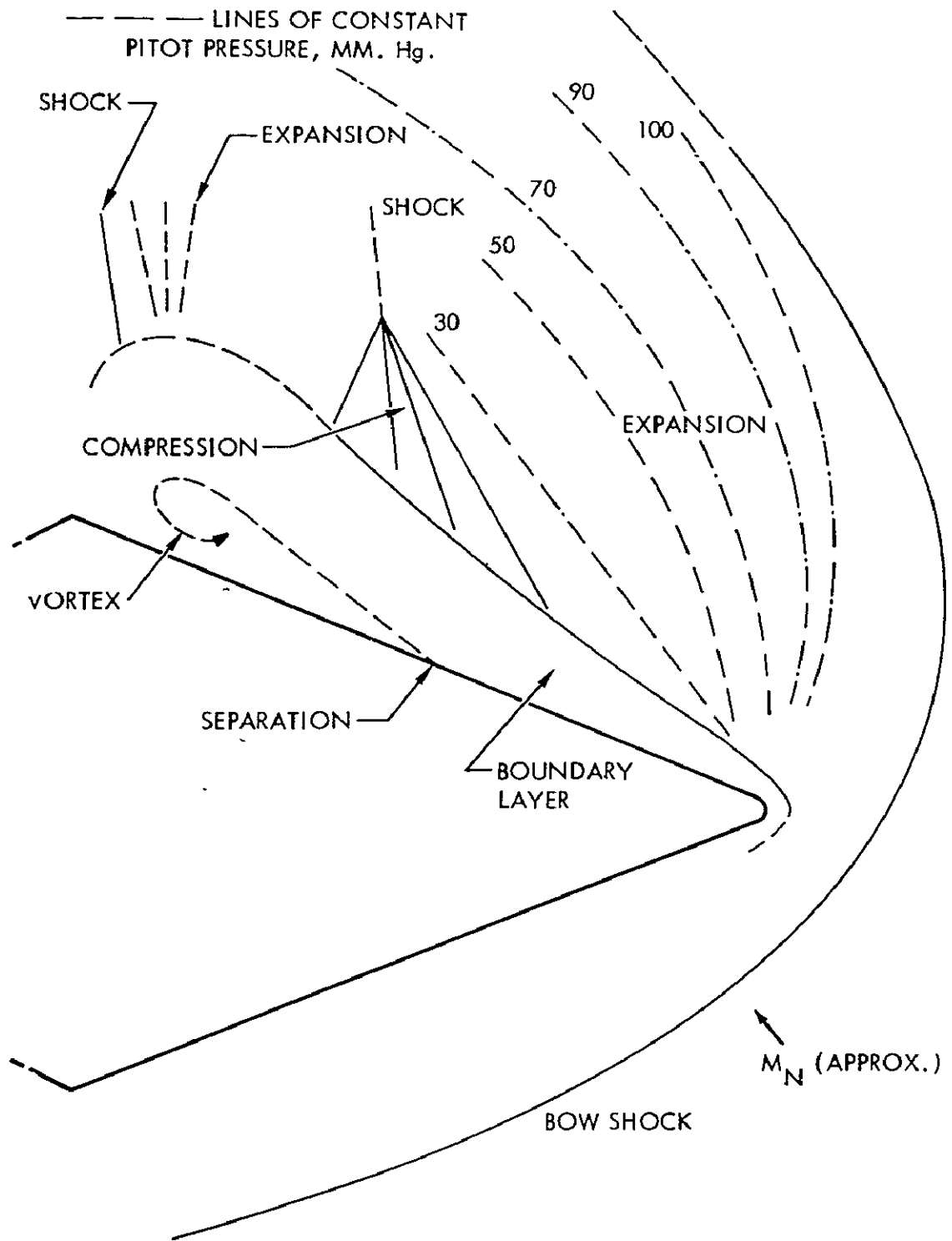


FIGURE 55. SPANWISE CROSS-SECTION OF FLOW AROUND DELTA WING  
 AT  $\alpha = 17.6^\circ$

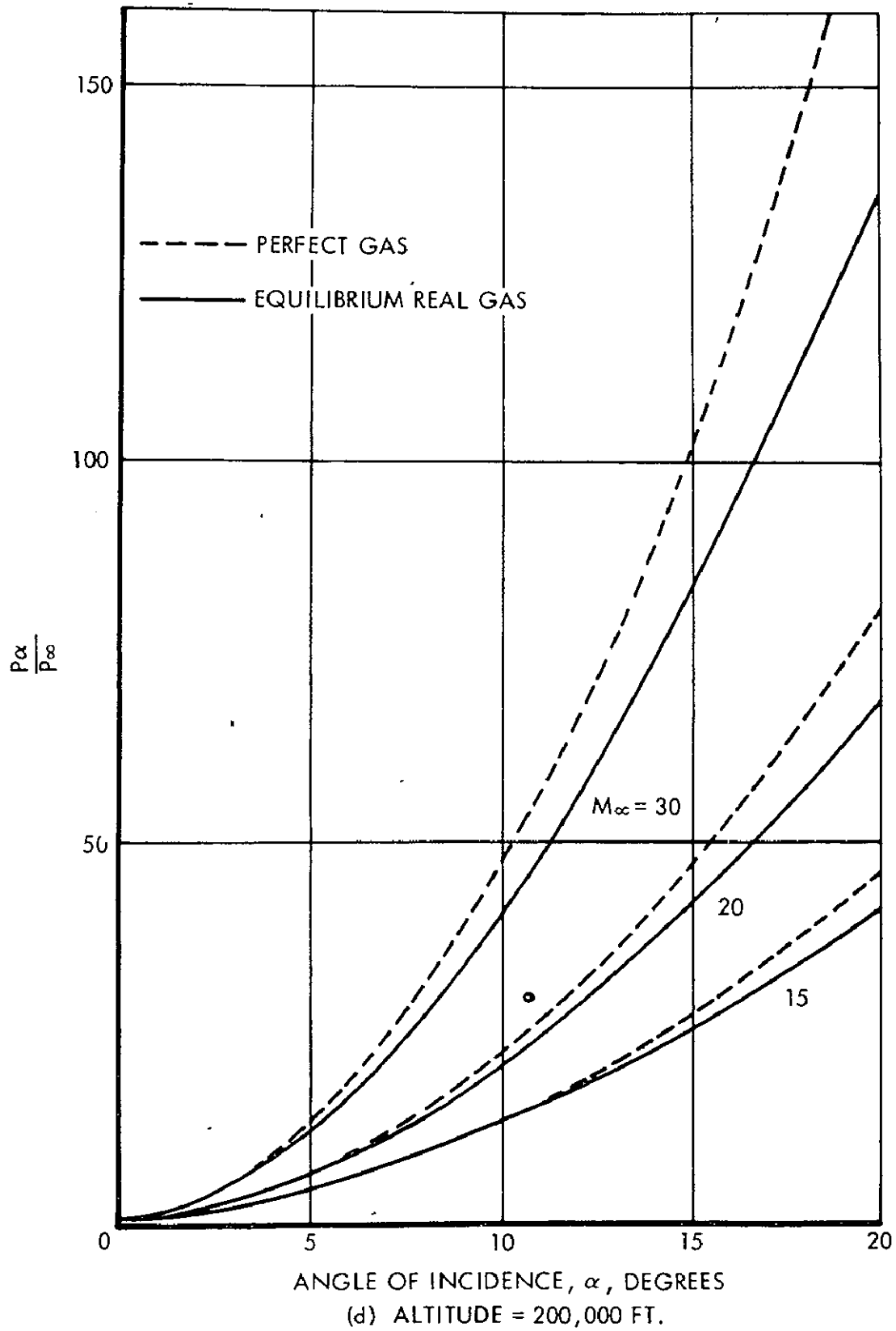


FIGURE 56. OBLIQUE SHOCK PRESSURE RATIO INCLUDING REAL GAS EFFECTS

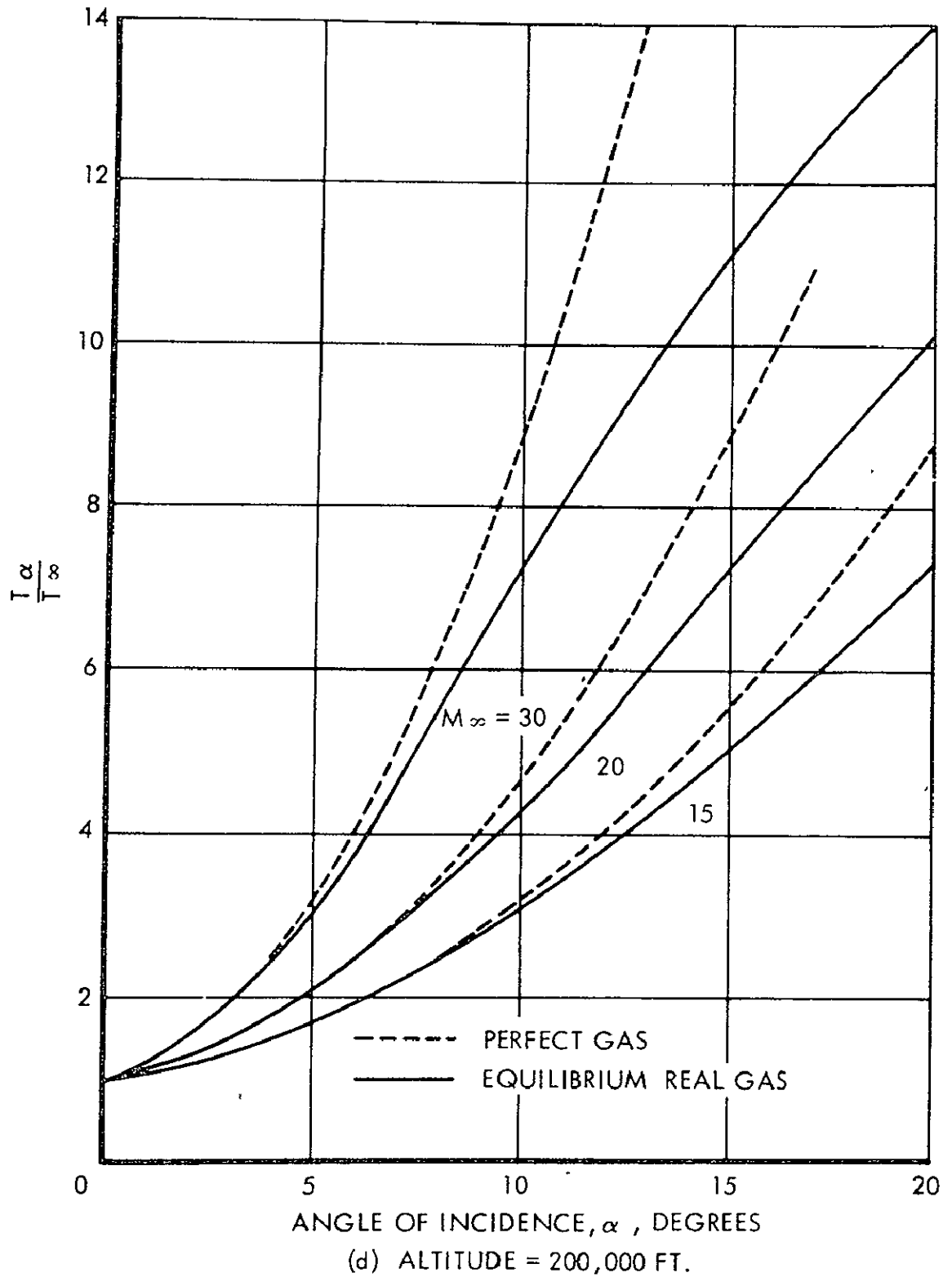


FIGURE 57. OBLIQUE SHOCK TEMPERATURE RATIO INCLUDING REAL GAS EFFECTS

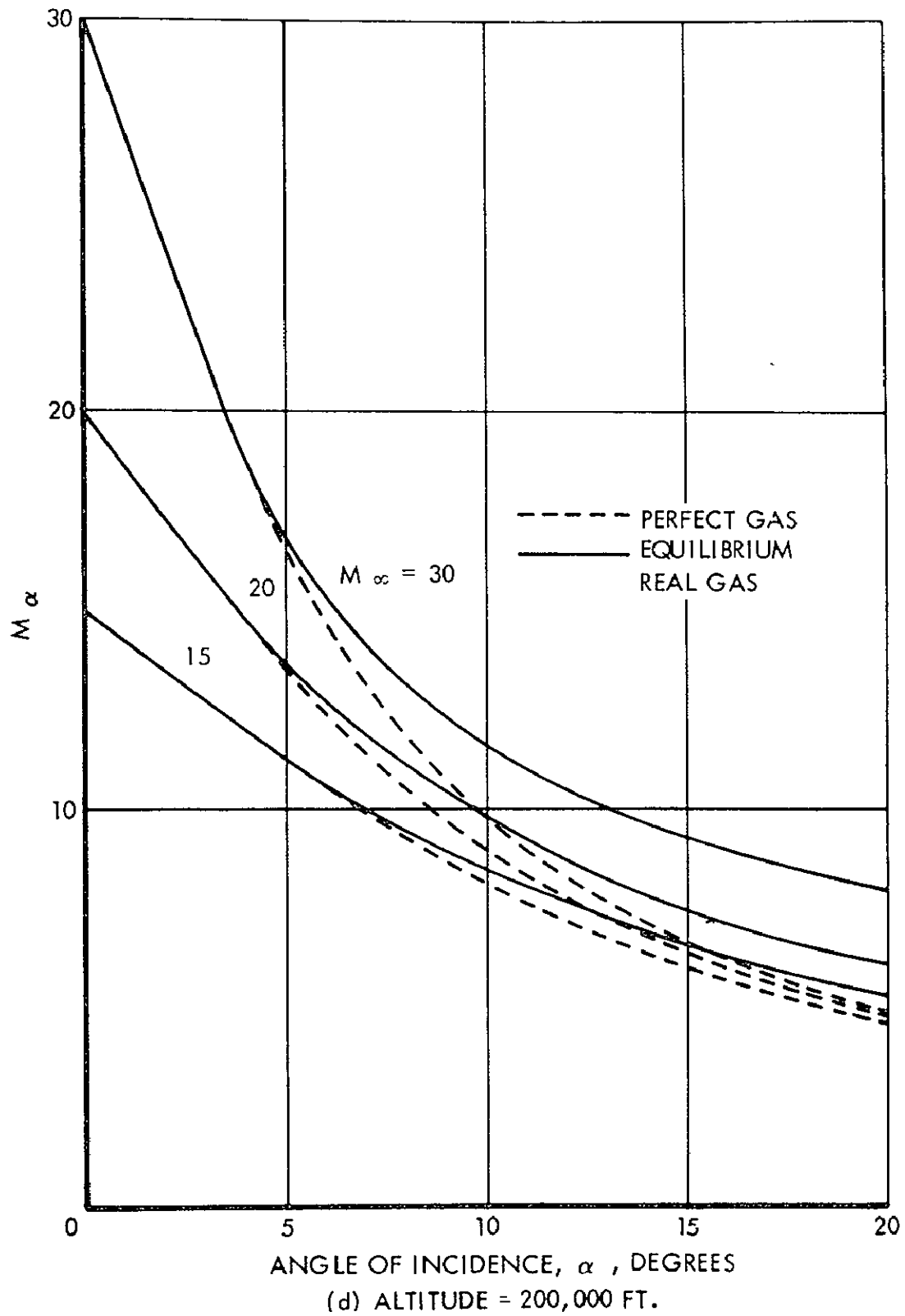


FIGURE 58. MACH NUMBER BEHIND AN OBLIQUE SHOCK INCLUDING REAL GAS EFFECTS

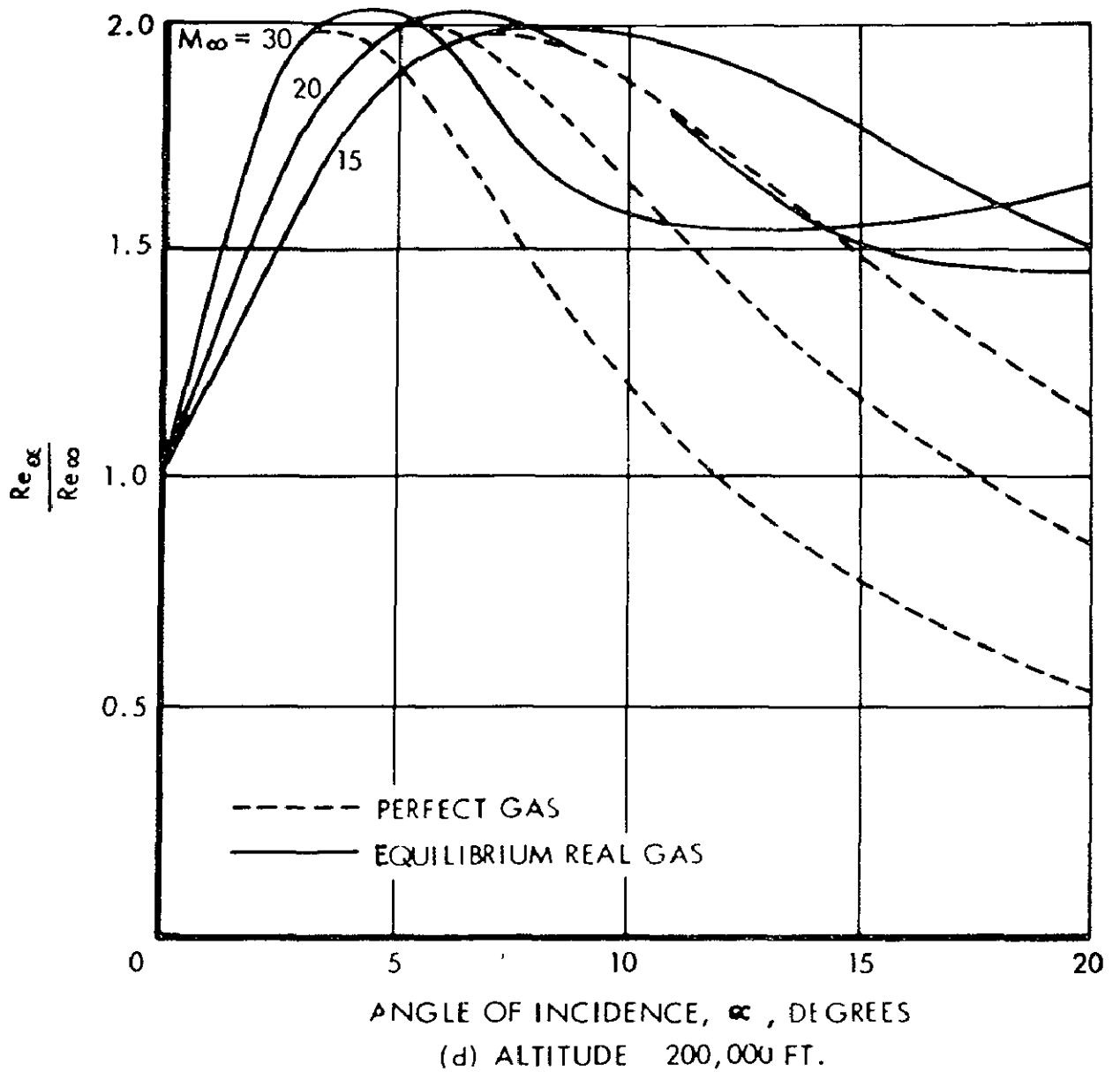


FIGURE 59. OBLIQUE SHOCK REYNOLDS NUMBER RATIO INCLUDING REAL GAS EFFECTS

## REFERENCES

1. Phillips, Dennis: Thermal Ionization Behind Strong Shock Waves in Argon. Unpublished M.S. Thesis, North Carolina State University (under the direction of R. W. Truitt), May 1966.
2. Truitt, R. W. : Hypersonic Aerodynamics, Ronald Press Co., New York, 1959.
3. Parker, John L., Jr.: The Equilibrium Flow of a Multi-Ionized Gas. Unpublished M.S. Thesis, North Carolina State University (under the direction of R. W. Truitt), May 1966.
4. Lighthill, M. J. · Dynamics of a Dissociating Gas, Part I, Equilibrium Flow. J. Fluid Mech., 2, 1, Jan. 1957.
5. Bray, K. N. C.: Departure from Dissociation Equilibrium in a Hypersonic Nozzle ARC 19, 983, March 1958.
6. Freeman, N. C.: Nonequilibrium Flow of an Ideal Dissociating Gas J Fluid Mech. 4, 4, Aug. 1958.
7. Lick, W.: Inviscid Flow Around a Blunt Body of a Reacting Mixture of Gases. Parts A and B. AFOSR TN 58-22, May 1968, and TN 58-1124, Dec. 1958.
8. Barrett, R. F.: A Study of the Laminar Boundary Layer Flow of a Reacting Gas. Unpublished Ph.D Thesis, North Carolina State University (under the direction of R. W. Truitt), 1965.
9. Truitt, R. W. · Fundamentals of Aerodynamic Heating. Ronald Press Co., New York, 1960.
10. Truitt, R. W : Hypersonic Turbulent Boundary-Layer Interference Heat Transfer in Vicinity of Protuberances. AIAA J., 1965, p. 1754.
11. Bertram, M. H. and Cook, B. S · The Correlation of Oblique Shock Parameters for Ratios of Specific Heats from 1 to 5/3 with Application to Real Gas Flows. NASA TR R-171, Dec. 1963.

## REFERENCES (Concluded)

12. Huber, P. W.: Hypersonic Shock-Heated Flow Parameters for Velocities to 46,000 Feet Per Second and Altitudes to 323,000 Feet. NASA TR R-163, Dec. 1963.

# THERMOPHYSICS RESEARCH

By

Gerhard B. Heller  
George C. Marshall Space Flight Center  
Huntsville, Alabama

N70 - 18690

## Introduction

Thermophysics research at Marshall Space Flight Center is concerned with the thermal space environment and its effect on space vehicles. Space craft are in radiative equilibrium with their environment, the main factors being solar radiation, the planetary albedo, the planetary infrared radiation, and aerodynamic heating only during the final phases of a decaying orbit. The following paragraphs deal with various aspects of thermophysics research.

The emissivities of various surfaces of space vehicles are essential to control the radiative exchange with the environment of celestial bodies like sun, planets, or moon.

Theoretical studies enable us to establish mathematical models and to develop computer programs for thermal design and for environmental effects, to other aspects of thermophysics.

Research in radiative and conductive physics is an experimental program carried out to solve such problems as modes of heat transfer in underdense materials, interfacial conductance between materials in space and others.

Thermal control has become a vital design area for all space vehicles. My division has been fully responsible for the thermal control of Explorers I through V, VII through XI, upper stages of the Saturn I flights, SA-4 and SA-5, and for the Pegasus satellites I, II, III. All of our research finds application in the thermal control of such spacecraft and contributes in general to the advancement of technology in this vital area of space exploration. The area includes such problems as the determination of launch windows, the selection

of thermal control coatings inside and on the outer skin of spacecraft and computer programs to predict temperatures for the total lifetime of the satellite in space.

The effects of the space environment on thermal coatings proved to be a very interesting research area with many problems still unsolved today. Even if we have found a good thermal design, if we have verified it in thermal-vacuum tests, and have predicted the changes of temperature in space due to orbital precessions, earth motion with respect to the sun, etc., we have to ascertain that the initial values of material emissivities do not change in space. We found that this is not possible. Even the most stable coatings and paints that we developed undergo considerable changes. The research emphasized two aspects: (1) to understand the basic degradation mechanisms, and (2) to make the changes due to the space environment predictable, such that it can be taken into consideration by the thermal design engineer.

An important aspect of direct involvement in the thermal control of spacecraft is the feedback of knowledge from the actual performance of the spacecraft in orbit. The evaluation of temperature measurements helps to learn how good the design approach was, how close the predicted temperature fluctuations are matched by the actual values. However, it proved to be very difficult to pinpoint the reasons for deviations, because more than 20 variable parameters are involved. We, therefore, initiated the development of a flight experiment of "thermal environment sensors." Various versions of the experiment were flown on the early Explorers, on the Saturn upper stages and on all three Pegasus satellites. Results from these experiments contributed to explain discrepancies between lab experiments and actual exposure to the space environment.

Because of the great demands for better knowledge about emittances and reflectances of solid matter for space application, new and advanced methods for laboratory measurements had to be developed. These include IR spectroradiometers, hohlraum reflectometers, calorimeters, in situ irradiation with UV and simulated solar wind and simultaneous measurement of the optical characteristics, bidirectional devices which allow to have goniometric variations of the incident and reflected beams.

Table IX gives a summary of the "work areas" in thermophysics research which are pursued by the Space Thermophysics Division. More details will be given in subsequent chapters. Activities in the "work areas" cover a wide range from basic research to the application for MSFC mainline space flight projects. The area of space flight experiments has been an

especially rewarding effort, because of the stimulus on our laboratory research, our theoretical studies, and its direct tie-in with the scientific payloads. The continuous participation in the Marshall mainstream efforts and the application of our research to space flight projects has proven to be rewarding in a dual sense: (1) the contribution to the MSFC projects makes our work an integral part of these projects, and provides an excellent training for our physicists and engineers, and (2) the experience gained allows us to plan future research and the selection of scientific areas with potential for contributions to the space flight effort.

TABLE IX. THERMOPHYSICS DIVISION WORK AREAS (Space Sciences Laboratory, MSFC)

PROGRAMS	ACTIVITIES
<u>Thermal Similitude</u>	Mathematical studies of new approaches to thermal model testing
<u>Theoretical Studies of Lunar Thermophysics</u>	Theory of electromagnetic waves interacting with the lunar surface, phase relationships and amplitudes of lunar subsurface heat waves Evaluation of IR and thermal mm wave measurements of the moon
<u>Electromagnetic Radiation Physics</u>	Especially IR and far IR IR of the moon
<u>Thermophysical Properties of Underdense Materials</u>	Thermal, electrical and acoustic contact resistance between particles Reduced gravity environments Conductive and radiative physics
<u>Lunar Geological and Geophysical Studies</u>	Mechanical forces between particles of simulated lunar materials Lunar drill studies
<u>Emissivity Physics</u>	Advanced measuring techniques of surface optical properties Effects of micrometeoroids UV and solar wind effects



## Thermal Similitude

The thermal vacuum testing of space hardware requires larger and larger chambers as the sizes of spacecraft increase. It is, therefore, of considerable interest to establish nondimensional modeling laws which allow to do some of the thermal testing with models of space hardware. During the past several years, research has at many places in the country unfortunately focussed on the question whether the models can replace the full scale tests. Some of the results seemed to disprove the usefulness of thermal models, however, their results are not conclusive. Research at the Space Sciences Laboratory was aimed at establishing dimensional parameters for model testing in a similar way as is done in wind tunnel tests for aerodynamic profiles. Just as the wind tunnel test does not replace the full scale test flight but helps the designer with vital knowledge about aerodynamic coefficients, thermal model testing can be expected to help in the early phase of the spacecraft design to establish the thermal design concept. A computer program was set up to find non-redundant and consistent sets of  $\pi$ -factors which are the nondimensional quantities.

For thermal modeling four  $\pi$  ratios and for time variable systems five  $\pi$  ratios have to be used. The computer program yielded a total of 57 different sets of such  $\pi$  ratios. The following equations show such a set of  $\pi$  ratios

$$\pi_1 = \frac{C_j T_k}{r A_j I_j t} \quad , \quad \pi_2 = \frac{C_{kj} t}{C_j} \quad , \quad \pi_3 = \frac{r A_j^3 I_j^3 R_{kj} t^4}{C_j^4}$$

$$\pi_4 = \frac{I_A}{r A_j} \quad , \quad \pi_5 = \frac{C_j T_j}{r A_j I_j t} \quad .$$

The symbols are defined as follows:

$$\begin{aligned} T_j &= \text{temperature of } j\text{th node, } [\Theta] \\ C_j &= \text{heat capacity of } j\text{th node, } [H\Theta^{-1}] \\ C_{kj} &= \text{over-all conduction coefficient between nodes } k \text{ and } j \\ & \quad [HT^{-1} \Theta^{-1}] \end{aligned}$$

- $R_{kj}$  = overall radiation coefficient for net radiative heat transfer from node k to j,  $[HT^{-1} \Theta^{-4}]$   
 $I_j$  = thermal input intensity on the jth node,  $[HT^{-1} L^{-2}]$   
 $I_{A_j}$  = area of jth node receiving thermal input,  $[L^2]$   
 $t$  = time,  $[T]$   
 $r_{A_j}$  = area of jth node radiating to space,  $[L^2]$   
 $T_k$  = temperature of kth node,  $[\Theta]$

The symbols for the dimensions are defined as follows:

- $\Theta$  = temperature in °K  
 $H$  = heat or energy in joule  
 $T$  = time in seconds  
 $L$  = length in meters

We assume  $\pi_s$  as a function of the other  $\pi$  ratios. That is,

$$\pi_s = f(\pi_1, \pi_2, \pi_3, \pi_4).$$

If we solve for  $T_j$  then,

$$T_j = \frac{r_{A_j} I_j t}{C_j} f \left( \frac{C_j T_k}{r_{A_j} I_j t}, \frac{C_{kj} t}{C_j}, \frac{r_{A_j}^3 I_j^3 R_{kj} t^4}{C_j^4}, \frac{I_{A_j}}{r_{A_j}} \right).$$

We have concentrated on transient thermal problems because of their importance for near earth orbits. The ingress into and egress out of the earth's shadow calls for model investigations of thermal transients. The theoretical studies were supplemented by experimental work on a set of models with well defined but simple geometries. Besides the largest model or "prototype" two scaled down models with linear scaling factors of 1 : 2 and 1 : 4 were used. Figure 60 shows the arrangement of a conical model. The top and bottom plates of the cone are connected by four rods which support an additional mass between them. The figure also explains the numbering system of the thermocouples. Figure 61 shows the cyclic response of the small top plate of the

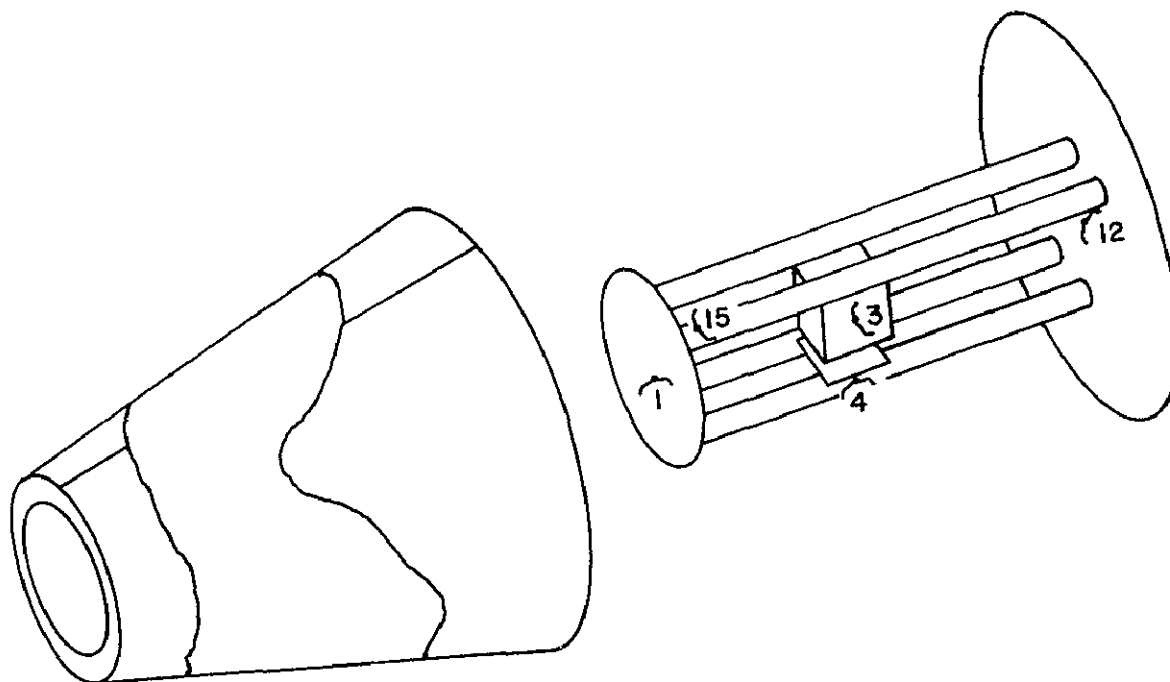


FIGURE 60. CONICAL MODEL USED IN THERMAL SIMILTUDE TESTS

cone frustum (thermocouple #1) due to the imposed heat indicated by the arrows in Figure 61. Figure 62 shows the thermal transients of the block supported between the four rods. A built-in heater is able to generate very steep temperature rises. The more graduate drop of temperatures is due to radiative and conductive heat transfer. The temperature curves of the prototype and the two scaled-down models follow the same pattern. The absolute match of the temperatures is not essential. However, the modeling laws should allow to predict the temperature transient for each, if the initial boundary conditions are given. The research has revealed that thermal models can be helpful to solve specific questions. Since the testing for full-size space vehicles in vacuum chanbers is quite extended in time and costly, not all necessary parameters and thermal transients can be tested. However, they can be tested in small models for a fraction of the cost and time, and as such supplement the full-scale tests.

## Theoretical Studies Of Lunar Thermophysics

Theoretical studies are carried out to establish a better understanding of the interaction of electromagnetic waves with the lunar surface. Such an understanding is necessary to determine the environmental criteria for lunar

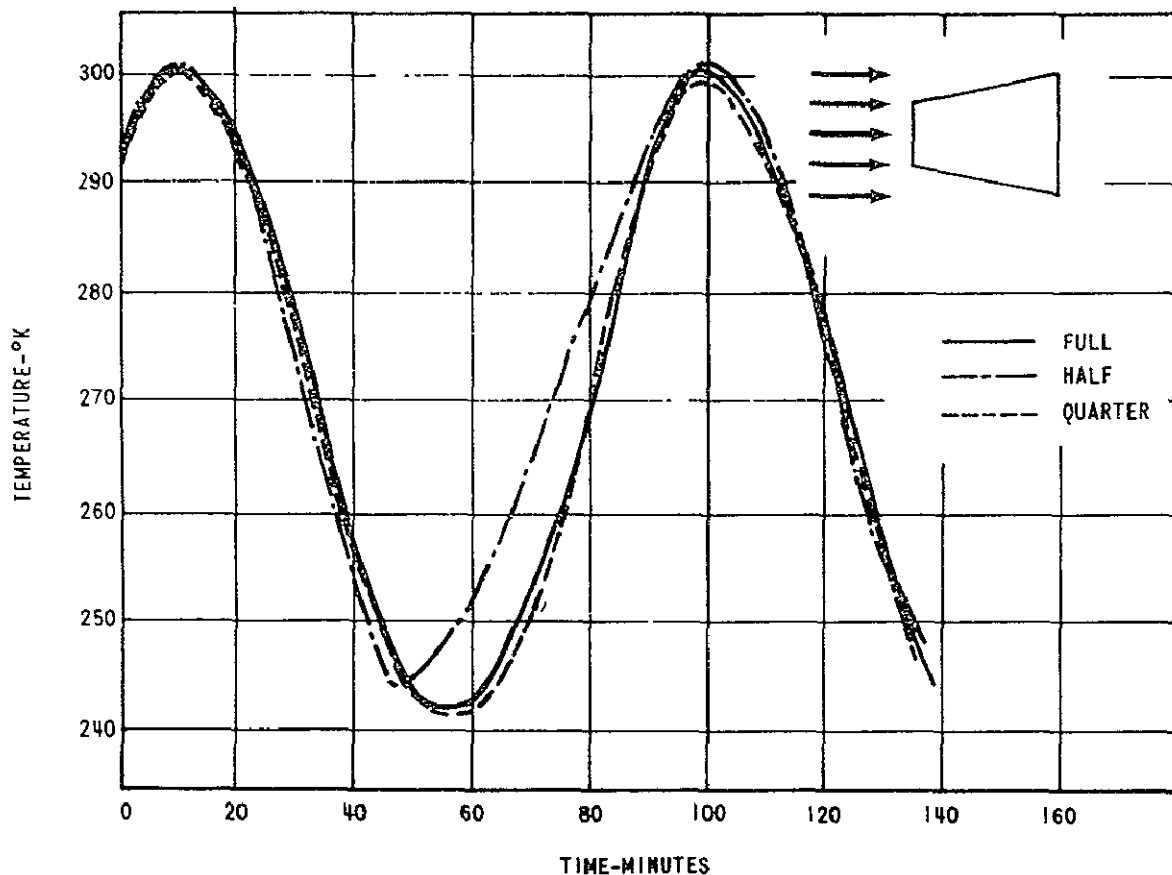


FIGURE 61 CONFIGURATION C - TRANSIENT THERMAL RESPONSE OF THERMOCOUPLE NO. 1

surface craft. The lunar surface has very unique properties which are quite different from those found for natural surfaces on the earth. One of the properties is the strong directivity of the backscattered solar radiation or photometric function. Figure 63 shows this function as derived by Hapke. It very closely approaches the reflected solar radiation for an average element on the lunar surface. It is a photograph of a three-dimensional model. The downward arrow is the direction of the sun's incoming radiation at an angle of  $30^\circ$  from the local vertical. The upward pointed arrow gives the local vertical. The intensity of the scattered or reflected radiation is depicted by the length of each point of the three-dimensional figure from the intersection of the sun vector with the local vertical in the center of the horizontal plane. Hapke's function is given by the equation also shown on Figure 63.

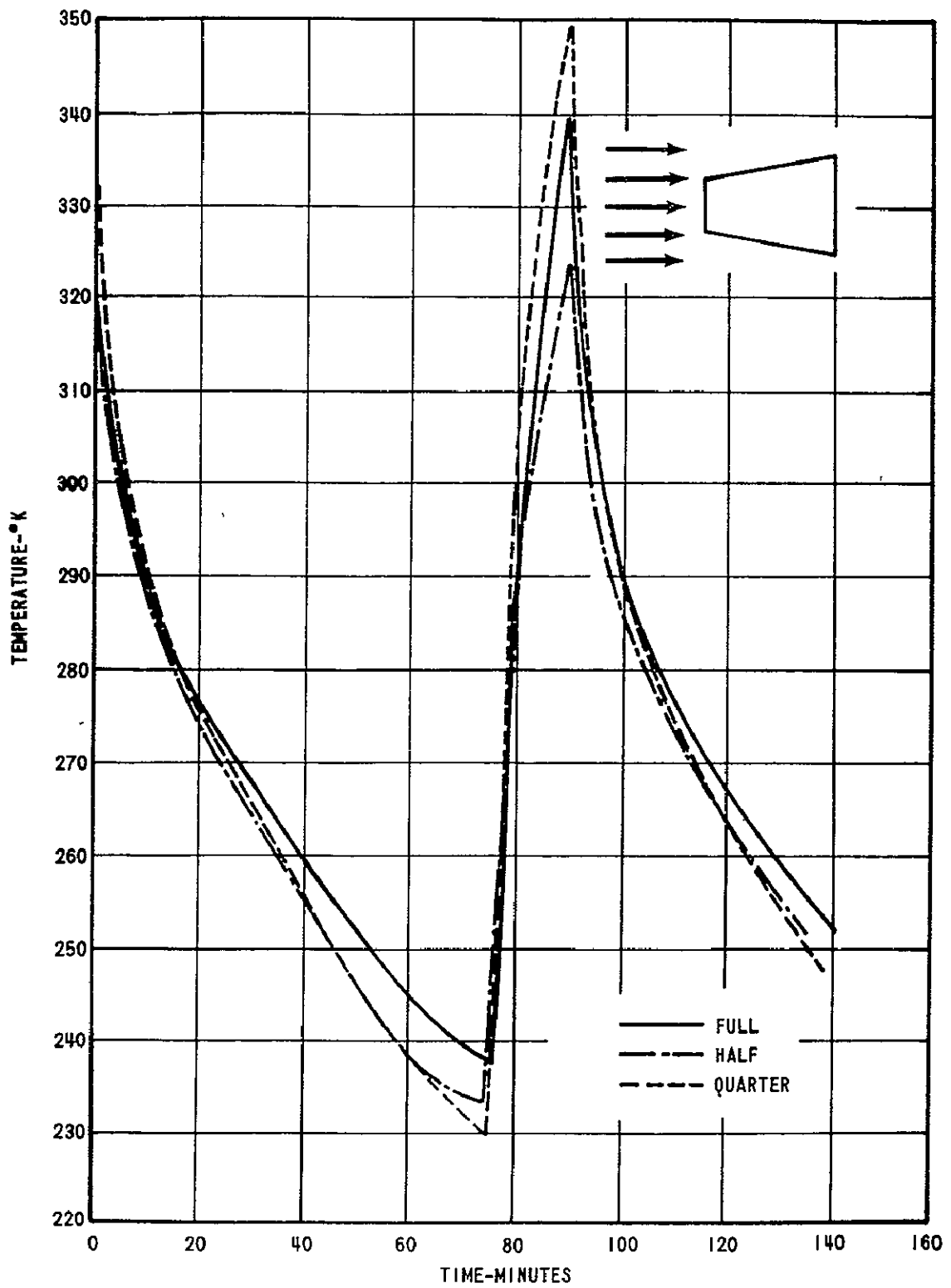


FIGURE 62. CONFIGURATION C - TRANSIENT THERMAL RESPONSE OF THERMOCOUPLE NO. 3

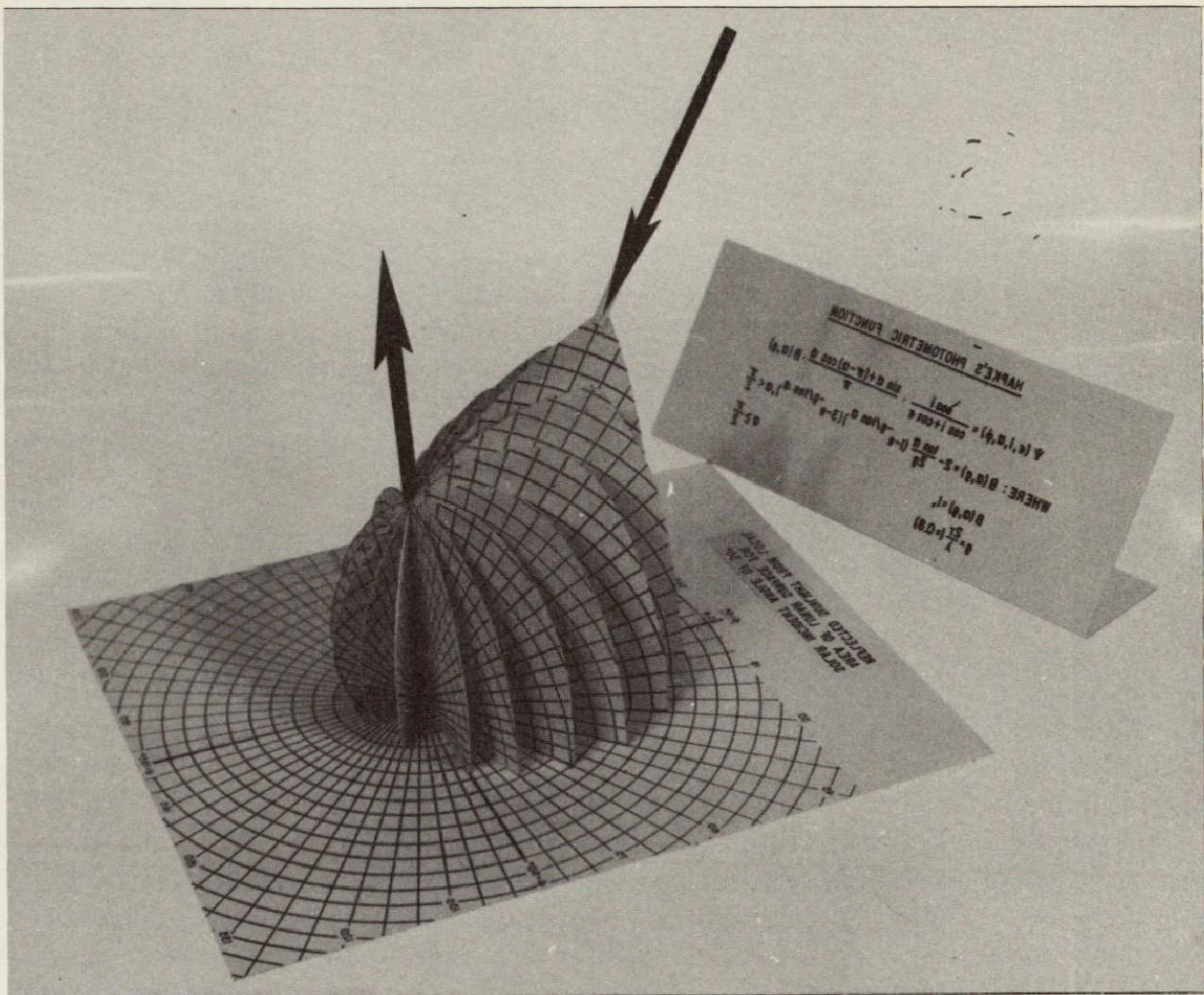


FIGURE 63. GEOMETRICAL REPRESENTATION OF THE HAPKE FUNCTION

$$\chi(\epsilon, i, \alpha, \phi) = \frac{\cos i}{\cos i + \cos \epsilon} \cdot \frac{\sin \alpha + (\pi - \alpha) \cos \alpha}{\pi}$$

$$B(\alpha, g)$$

Wherein

$$B(\alpha, g) = 2 - \frac{\tan \alpha}{2g} \left[ 1 - \exp\left(\frac{-g}{\tan \alpha}\right) \right] \left[ 3 - \exp\left(\frac{-g}{\tan \alpha}\right) \right]$$

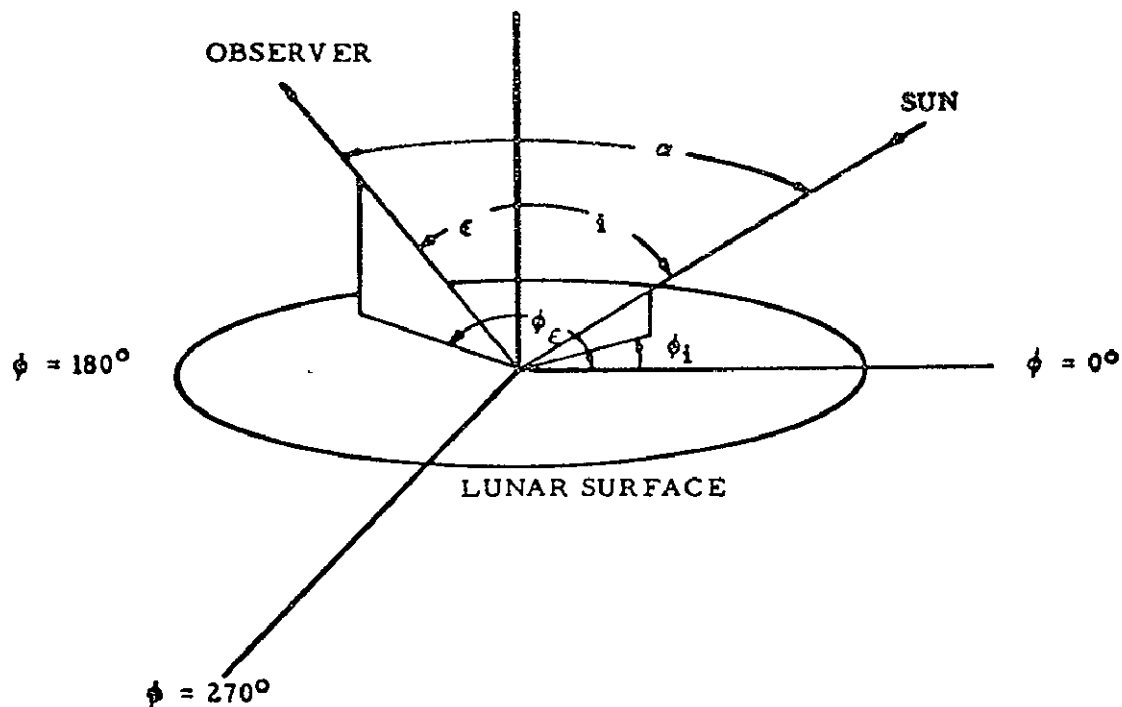
$$\text{for } \alpha < \frac{\pi}{2}$$

$$B(\alpha, g) = 1 \quad \text{for} \quad \alpha \geq \frac{\pi}{2}$$

$$g = \frac{2r}{\lambda}, \quad (= 0.8)$$

The angles in equation (1) are explained in Figure 64. The same figure shows an equation for the infrared emission flux (radiance) from a lunar surface element as a function of the sun elevation angle  $i$ , observer elevation angle  $\epsilon$  and the lunar phase angle  $\alpha$ . The angle  $\alpha^1$  is defined by the second equation as function of the known angles  $i$ ,  $\epsilon$ ,  $\phi_i$ ,  $\phi_\epsilon$ .  $A_1$ ,  $A_2$ ,  $A_3$  are empirically adjusted constants. The third equation of Figure 64 is the Stephan-Boltzmann equation which allows to compute radiance temperatures from the radiative Flux  $B$ , as can be seen from Figure 65. This radiance temperature is dependent on the angle of observation. It shows this temperature for an incidence angle  $i$  of  $30^\circ$  for an azimuth angle of the observer of zero, i. e., co-planar with the sun vector. The concept of a temperature which varies with the observation might be very disturbing. If we could assume that the temperature of the lunar surface spot is well defined and uniform, we could introduce such a temperature and compute the emittance which is variable with the viewing angle. However, this is not possible at the present time, because we still have some serious open questions which do not allow to define a constant temperature. One of the questions is whether the radiative behavior is due to the lunar structure on a microscale as inferred in the Ashley expression shown on Figure 64 or whether it is due to shadow effects in craters on a macroscopic scale. Another question is whether a meaningful lunar surface temperature can be defined, if we have a very underdense material on the surface with a temperature gradient of the order of  $100^\circ \text{K/cm}$ . Figure 66 shows the brightness or radiance temperatures as a function of the elevation angle of the observer with various sun angles as parameters. It can be seen that the brightness temperature peaks in all cases close to the direction of the sun angle. The theoretical curves are compared to measurements taken by various authors which are referenced on the graph.

Figure 67 shows a plot of the temperature of the full moon across the disk. Various sets of measurements are shown together with the Lambert distribution of temperature which should follow a  $\cos^{1/4}\theta$  relationship and the empirical relationship of a  $\cos^{1/6}\theta$  law established by Pettit and Nicholson. The deviation from Lambert's law has been explained that it is due to the surface roughness of the moon.



$$B(i, \epsilon, \alpha) = \frac{a_1 \cos i + a_2 \cos \alpha'}{1 + a_4 \sin \alpha' / \cos i} + \frac{a_3}{\pi} [(\pi - |\alpha|) \cos |\alpha| + \sin |\alpha|]$$

$$\alpha' = \frac{\pi}{2} \sqrt{\frac{i^2 + \epsilon^2 - 2i\epsilon \cos(\phi_i - \phi_\epsilon)}{\pi^2 + \frac{4i^2\epsilon^2}{4\pi^2} - 2i\epsilon \cos(\phi_i - \phi_\epsilon)}}$$

$$T^4 = \frac{\pi B(i, \epsilon, \alpha)}{\sigma}$$

FIGURE 64 ANGULAR EXPRESSIONS USED IN THE HAPKE FUNCTION

The problem of the variation of lunar surface temperatures during a lunation is important for the planning of lunar explorations. A computer program has been developed to compute temperatures using the thermal parameter  $(k\rho c)^{-1/2}$ . Figure 68 shows the result of such computations for the landing site of surveyor I. Also included in the graph are curves based on measurements by various investigators. The measurements from Surveyor show strong deviations. This has not been explained yet. It is quite possible

that the strong angular dependence and the above mentioned problems in connection with the definition of lunar temperature have a bearing on this discrepancy between measurements and our understanding of the moon expressed in the computed curves. It is at this moment not possible to match the computed curves by simply varying the values of the thermophysical parameters.

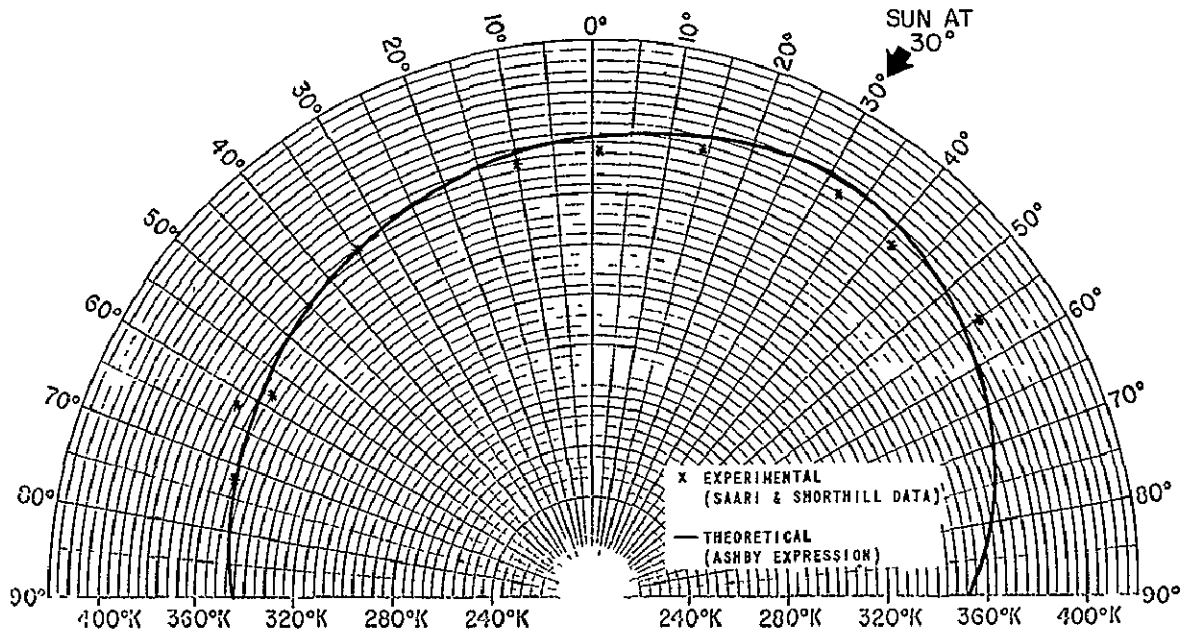


FIGURE 65. LUNAR BRIGHTNESS TEMPERATURE AS FUNCTION OF THE ANGLE OF OBSERVATION FOR SOLAR INCIDENCE OF 30°

## Electromagnetic Radiation Physics

The theoretical studies described previously are closely related to the experimental results obtained from ground based measurements made by various observatories. We recognized early that simultaneously with a theoretical effort we had to simulate the conditions in the laboratory, and to make additional observations of lunar IR radiation with ground based telescopes. Our Electromagnetic Radiation Laboratory covers a broad spectrum from solar radiation to the thermal infrared (IR) through the far IR extending all the way to the mm wave region. The instrumentation includes various IR methods such

as IR radiometry, grating, and filter spectrometers, Michelson interferometry, and IR imagery. Another area of instrumentation is that of IR detectors. Our investigations cover a wide variety of quantum and bolometer detectors which are needed for the various spectral bands of IR. An example is the gallium doped germanium bolometer detector which is suitable for the far IR from wave numbers of 200 to  $5\text{ cm}^{-1}$ . I would like to show some examples of the instrumentation. Figure 69 shows the schematic of an IR radiometer which uses an IR filter with a band width from  $10.2$  to  $12\mu\text{m}$ . Figure 70 shows this radiometer mounted on a Cassegrainian telescope. The research program is carried out in connection with extraterrestrial resources to determine the IR and thermal properties of lunar and planetary soil and minerals. Figure 71 shows an IR scan over the crater Tycho during the penumbral phase of the lunar eclipse of April 12, 1968. Such rayed craters as Tycho are showing as hot areas against a cooler surrounding shortly after

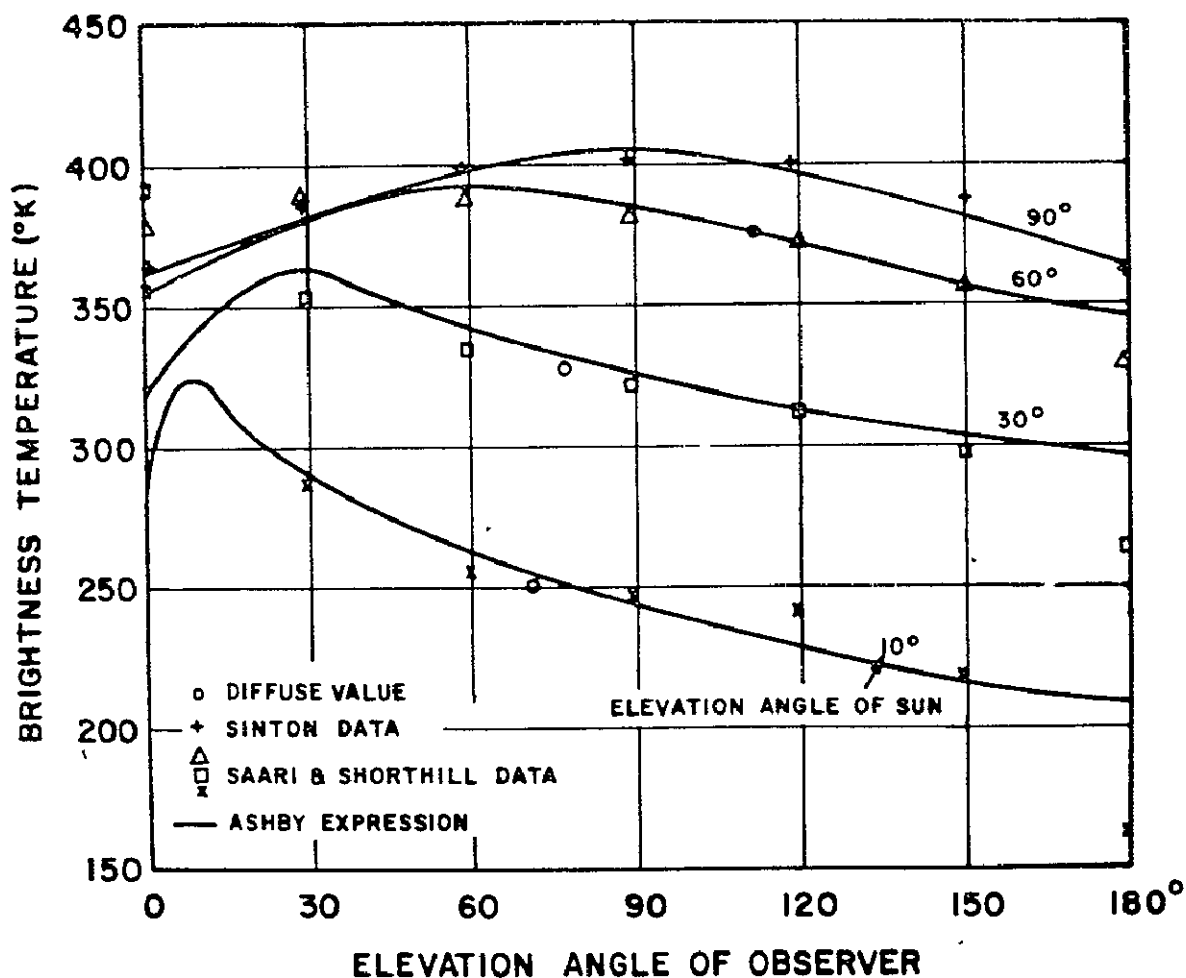


FIGURE 66. BRIGHTNESS TEMPERATURE VERSUS OBSERVER ELEVATION ANGLE

sunset during a normal lunation cycle, but even more pronounced during an eclipse. Figure 72 shows a schematic

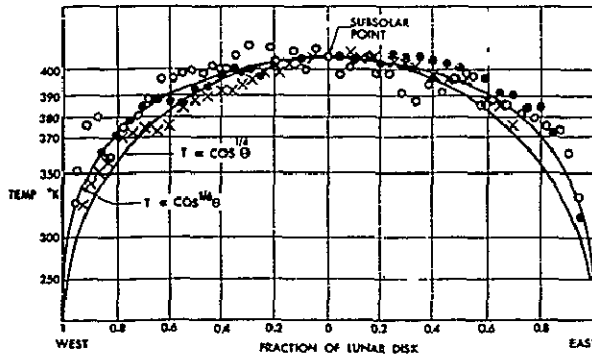


FIGURE 67. DISTRIBUTION OF PLANETARY HEAT ACROSS THE DISK OF THE FULL MOON

of a Michelson interferometer covering the spectral range up to 2000  $\mu\text{m}$ . The advantage of this instrument is in its integration times shorter than any other instrument in order to obtain a complete spectrum. In grating instruments most of the energy is eliminated except for one spectral line or band, whereas the interferometer allows to handle the complete spectrum simultaneously. Figure 73 shows a UBV photometer which is used for color photometry of stars. The letters U, B, and V stand respectively for the ultraviolet, blue, and visible filters, whose spectral characteristics are shown in Figure 74 together with those of other filters extending into the IR. The scientific project is concerned with the measure-

ment of binary stars and the analysis of their orbital elements. The UBV data will be supplemented by a photometer which operates in the various IR bands shown in Figure 74. This is specifically important for cases where the comparison star is a late type star with a low temperature which corresponds to a blackbody maximum in the IR. Figure 75 shows some results obtained at the University of Pennsylvania with IR photometry. It can be seen that the secondary minimum of the eclipsing binary almost disappears in the noise for visible light, but is quite pronounced in the IR.

Figure 65 discussed previously has been obtained by ground-based measurements. Similar results were obtained by goniometric IR measurements in the Electromagnetic Physics Lab. Figure 76 shows the experimental instrument in the laboratory used for these measurements.

## Thermophysical Properties Of Underdense Materials And Interface Conductance

Two problems connected with space vehicle projects at MSFC made the investigation of underdense materials attractive: Insulating powders which could accomplish required reduction of heat transfer under difficult geometrical

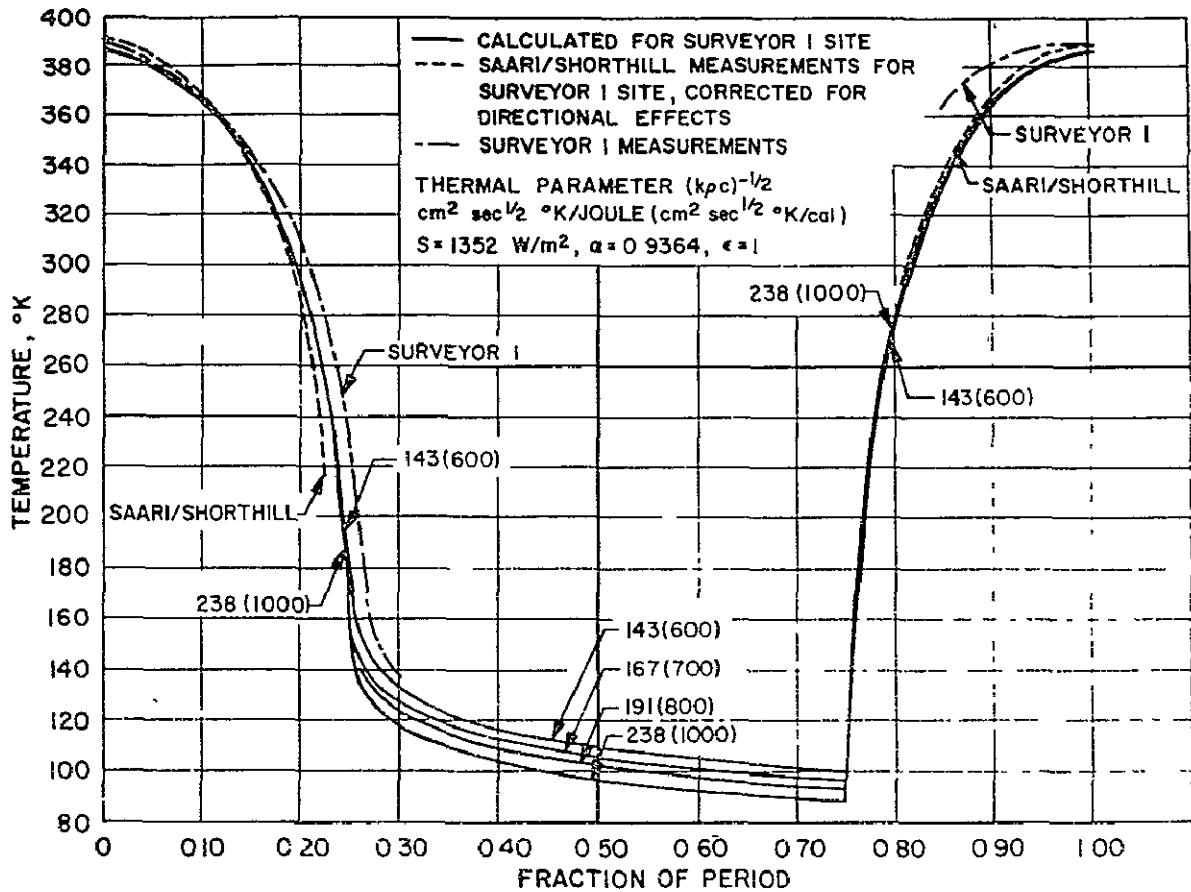


FIGURE 68. CALCULATED AND MEASURED TEMPERATURES FOR SURVEYOR I SITE

situations and the investigation of the top layer of the lunar surface. The properties of insulating powders have to be known under zero-g conditions, whereas lunar conditions correspond to 1/6-g. Our studies started initially with the problems of insulation materials for thermal design application. However, with the initiation of the lunar exploration by Ranger, Surveyor, and especially project Apollo the thermophysical properties of the moon took higher priority. Another aspect was that our thermal design studies showed that the insulation properties could be achieved by well known means other than powdered insulation materials. In connection with the lunar exploration it seemed desirable to simulate expected lunar surface materials in the laboratory and study the possible effects of reduced gravity by analytical means. The thermophysical properties of the moon are needed for correlation with the mechanical properties of the soil and also for correlation with the radiative characteristics of the moon in the IR and in thermal mm waves, which already has been discussed. Our research concentrates on the study of the heat transfer

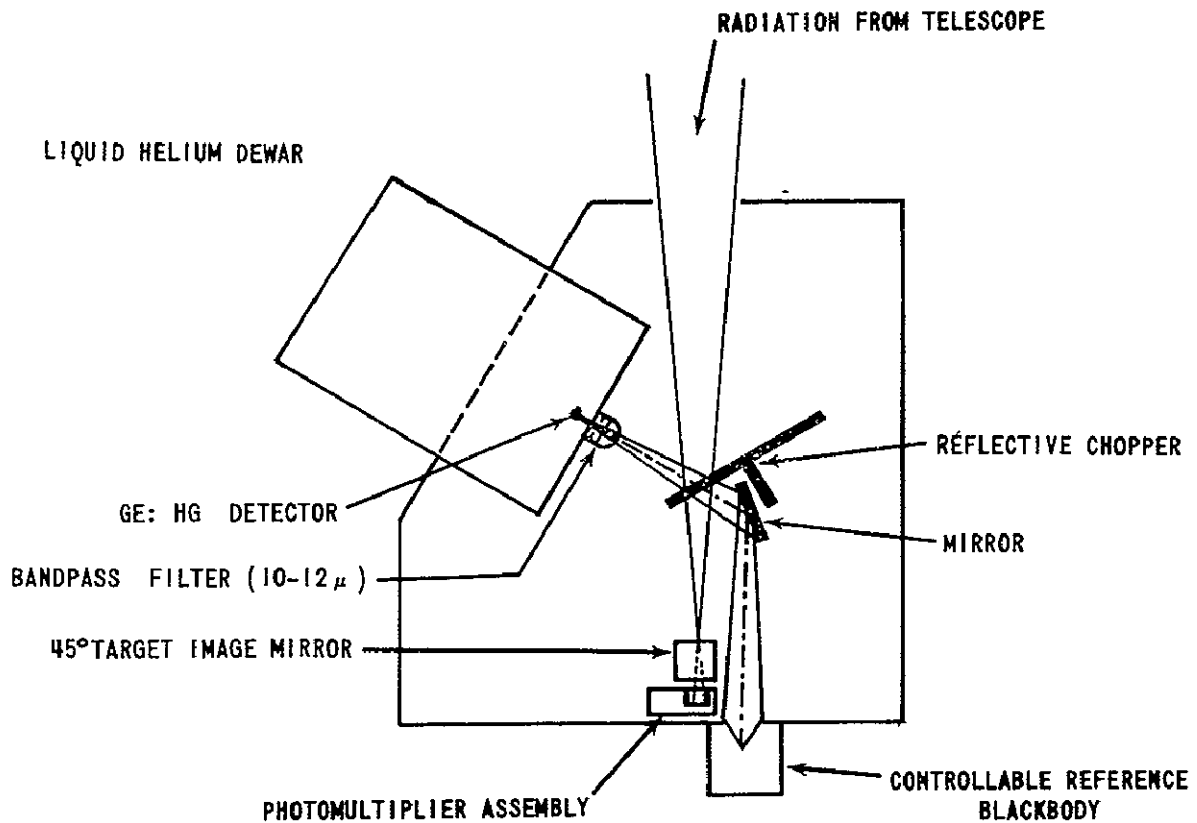


FIGURE 69. INFRARED RADIOMETER

modes, on their temperature dependence, on the influence of vacuum grain size, type of material and density. Figure 77 shows the dependence of the heat transfer on the density. At high densities the conductive transfer is dominant, it decreases with decreasing density. For highly underdense materials the conductive term is nearly negligible, but the radiative transfer is high. In between is a minimum. Present thinking about the lunar surface is that a thin layer on the top is highly underdense and that the packing density increases with depth. This is due to the "gardening effect" of the continuous impact of meteoroids and micrometeoroids. After one or several meters the density approaches that of solid rock. Research in this area is carried out in our Conductive and Radiative Physics Lab.

Another research activity conducted in this laboratory is in connection with the interface resistance between metallic surfaces under the hard vacuum conditions of space. The so-called metallic contact between two planar, well polished surfaces is in reality due to the airfilm between both surfaces. If this film is removed, the heat transfer depends on the conduction through a

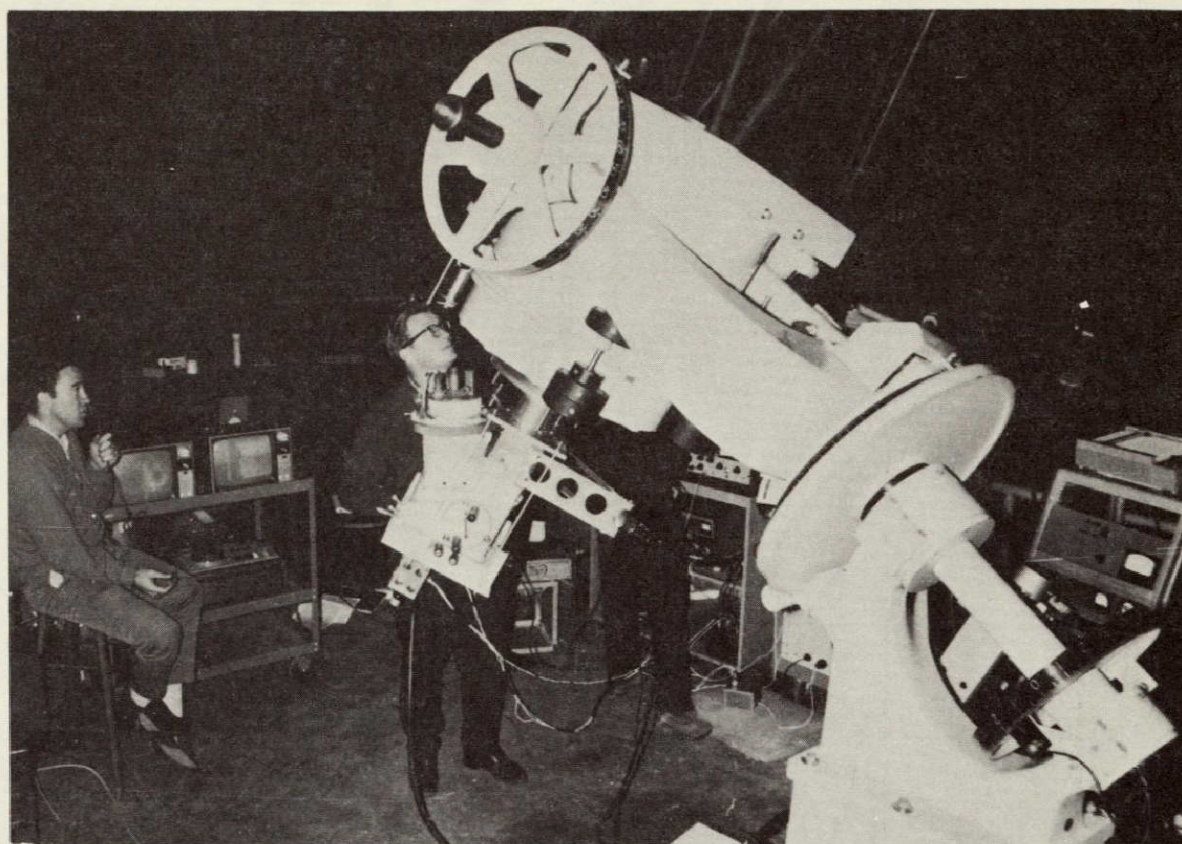


FIGURE 70. LUNAR IR EMISSION DATA ACQUISITION USING AN IR RADIOMETER ON UNIVERSITY OF GEORGIA 24" CASSEGRANIAN TELESCOPE

few actual grain to grain contacts and on radiative transfer which is low for polished metals. The interface resistance could become a real problem for metal to metal contacts which have to carry a heat load in space. Figure 78 shows some results of heat transfer of an interface as a function of the pressure applied. The research is presently concentrated on a better theoretical understanding of the surface physics problems involved.

## Lunar Geological And Geophysical Studies

Project Apollo has the purpose to land two astronauts on the moon and to bring them back safely. The problems connected with the landing require a knowledge of the mechanical properties of the lunar surface and the geological features and composition of the moon. A laboratory for geological

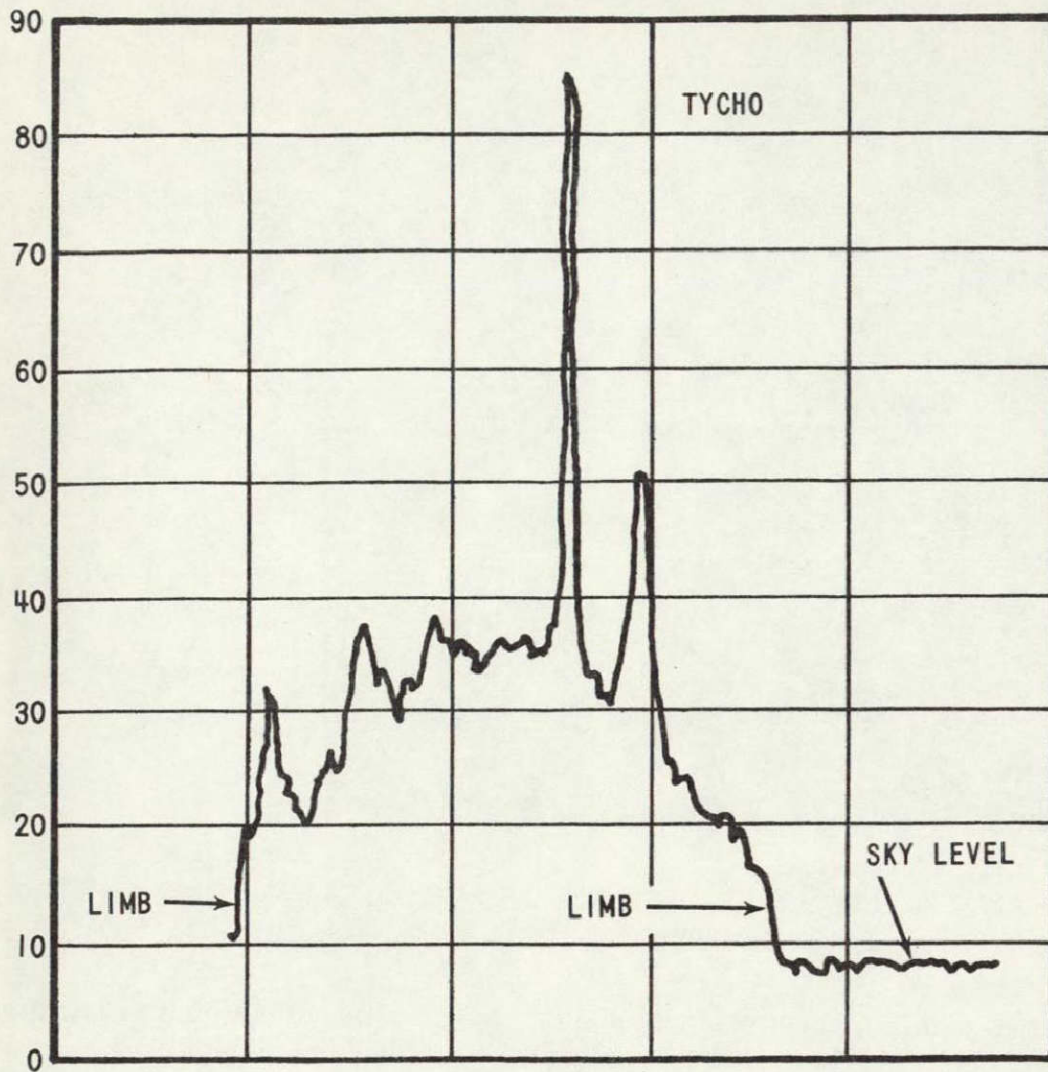


FIGURE 71. INFRARED SCAN ACROSS ENTIRE LUNAR DISK DURING UMBRAL PHASE OF ECLIPSE

and geophysical studies was set up for such studies. Figure 79 shows an ultraclean vacuum chamber which can be evacuated to  $10^{-12}$  torr. It provides for effective outgassing of simulated lunar surface material by tumbling of a drum. The vacuum was maintained at  $10^{-10}$  torr even during such an outgassing experiment. The materials were recommended by Dr. E. Schoemaker of the U. S. Geological Survey and other geologists who study lunar properties such as finely ground powders of basalt, pumice, rhyolite, etc. The results were very interesting. Basalt powder starts to adhere to the steel wall of the chamber and the grains to each other shortly after the outgassing is started.

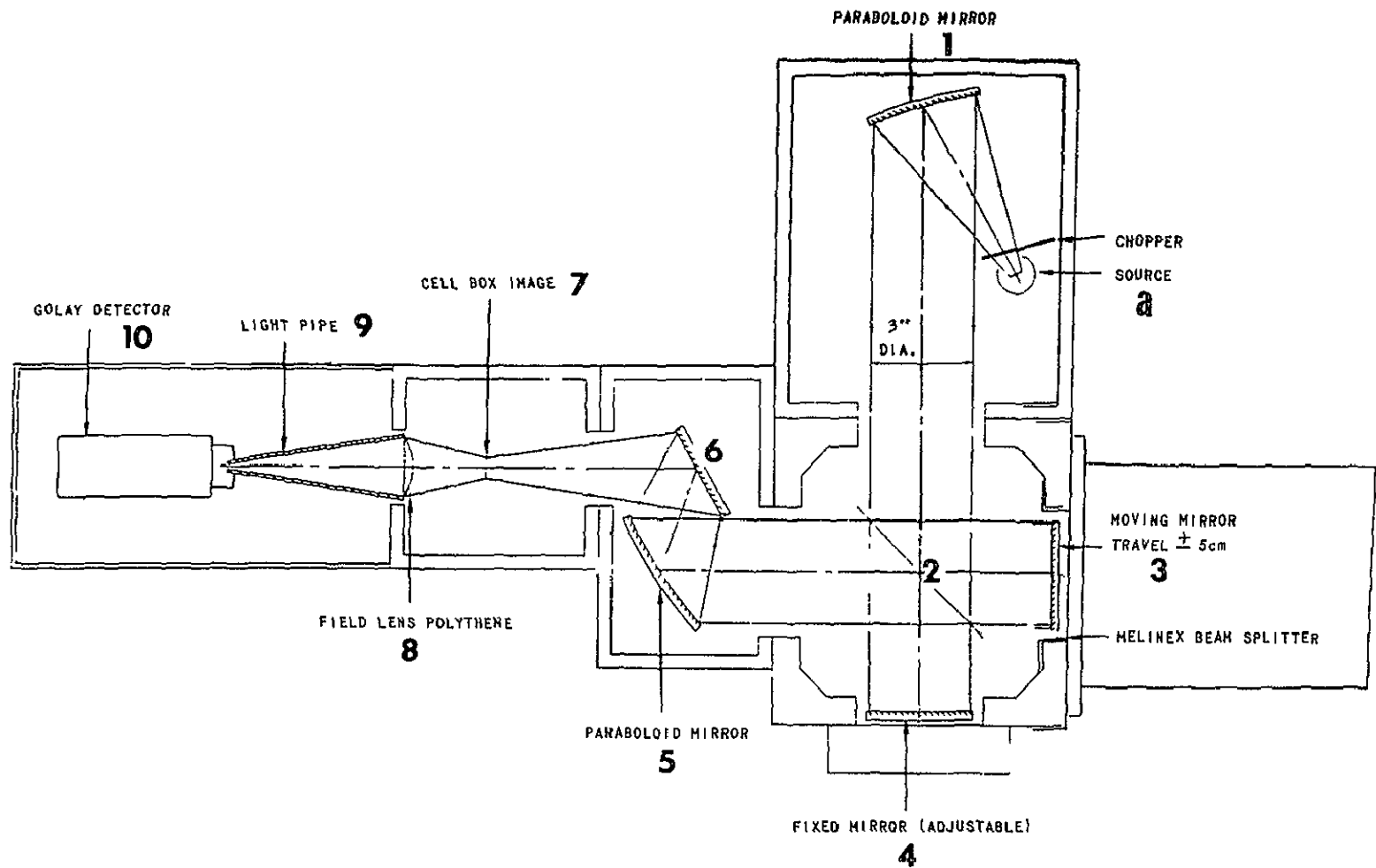


FIGURE 72 MICHELSON INTERFEROMETER

The *JA* photometer. In this diagram the numbered parts are as follows: 1 = the field lens and focal-plane diaphragm; 2 = the chopper, 3 = the PbS photoconductive detector, and 4 = the rubber hose leading to the drying agent (for preventing water from entering the inner refrigerated space). The mirror for reflecting the light to the guiding eyepiece is seen above the chopper motor, the filters and cold-box window are seen in this order between the chopper and the field lens.

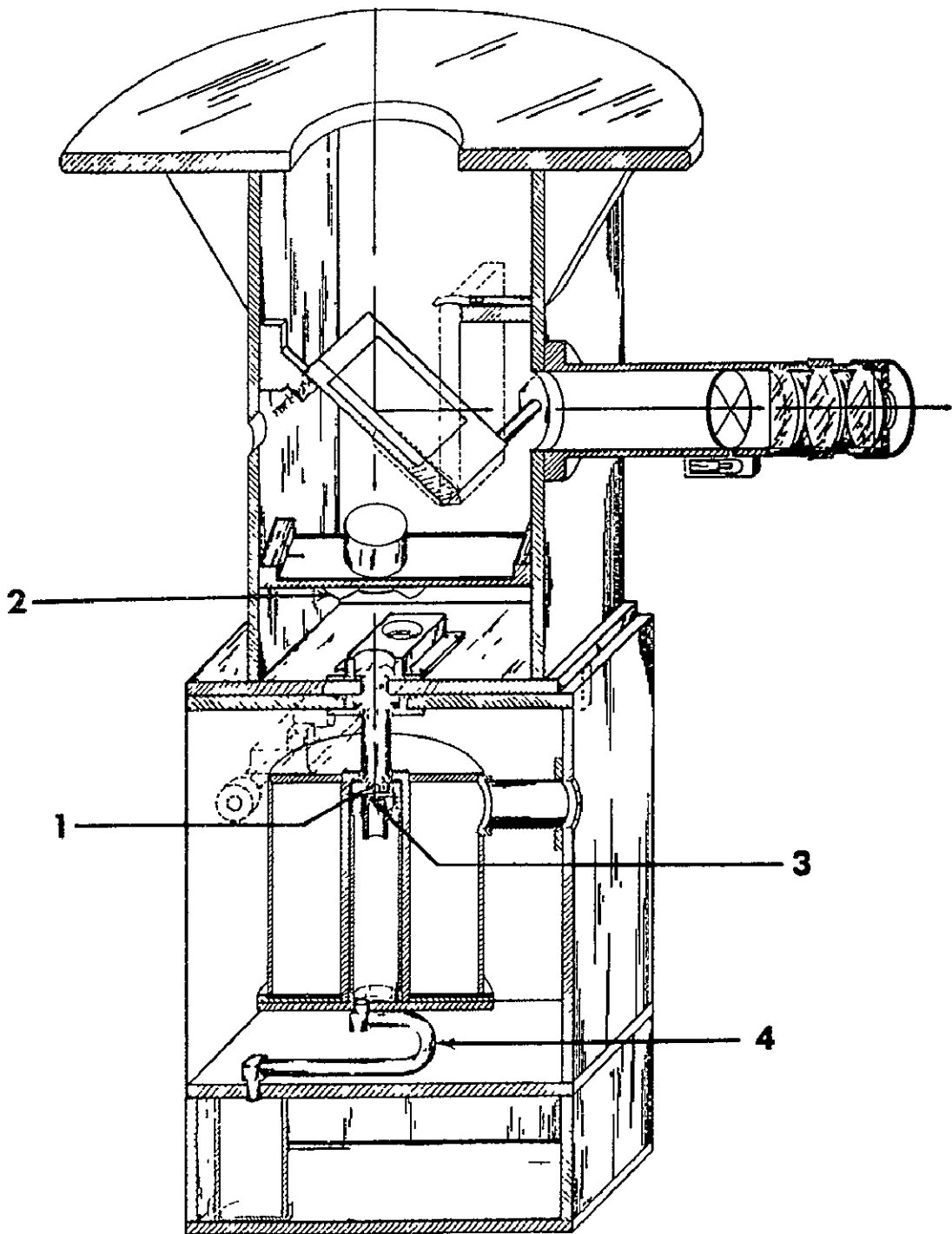


FIGURE 73 COMPLETELY DIGITIZED MULTI-COLOR PHOTOMETER

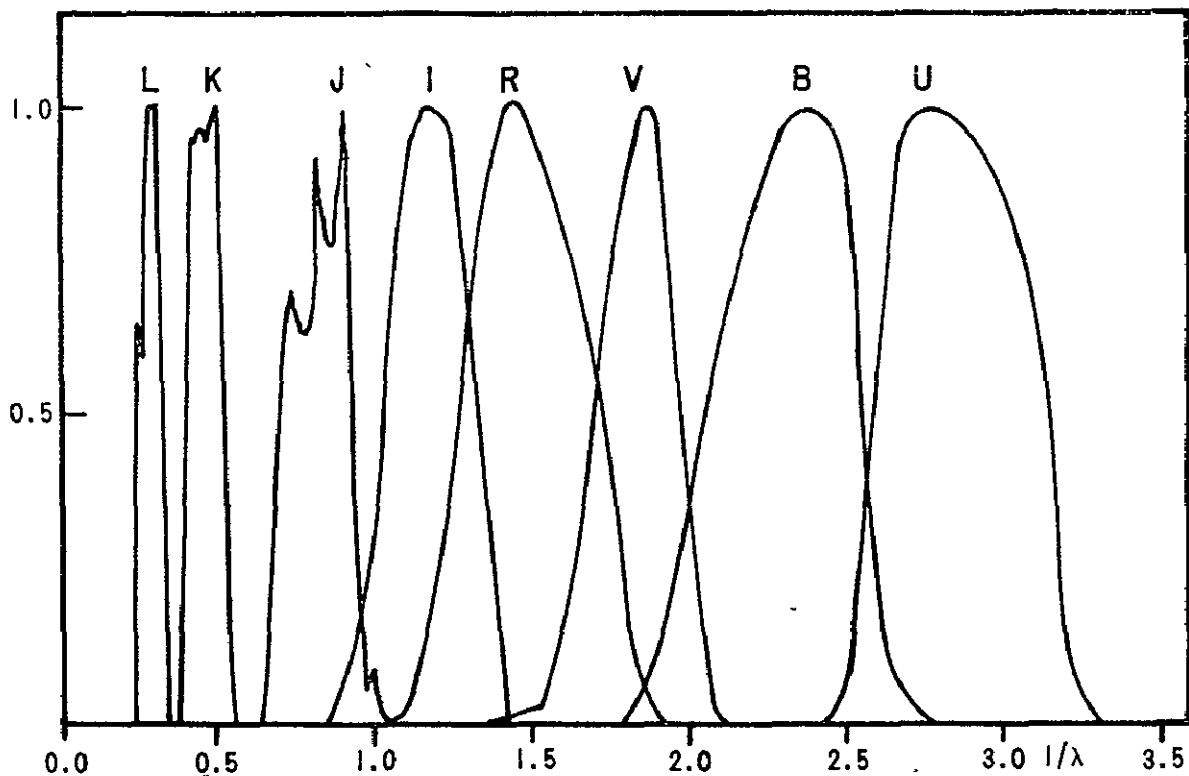


FIGURE 74. FILTER SPECTRAL BAND PASS AND LETTER DESIGNATION OF JOHNSON SYSTEM

After about 15 minutes, all of the powder adheres to the wall and does not drop anymore. This explains the consistency of lunar soil to behave somewhat like wet sand or the soil of a freshly plowed field. Since there is no amount of free water on the moon, the adhesion could not be explained in terms of capillary forces and adhesion of water to the soil grains. However, if the lubricating and separating surface layer of air is removed from silicate type minerals or from any other material, the van der Waals forces, chemical binding forces or electronic forces of metallic bonds become effective. It is this effect which makes the lunar "dust" behave more like "soil." Results found in our laboratories were continued by and are in agreement with the results of the recent Surveyor experiment of the Soil Mechanics Surface Sampler.

Another example of our research in this area is the analysis of simulated lunar materials by X-ray diffraction and Bragg crystal techniques. This area is quite promising to provide support for the X-ray solar astronomy projects for the Apollo Telescope Mount. Members of this Laboratory are the experiment scientist and alternate experiment scientist on S-054 which has Dr. R. Giacconi of the American Science and Engineering Corporation as Principle Investigator

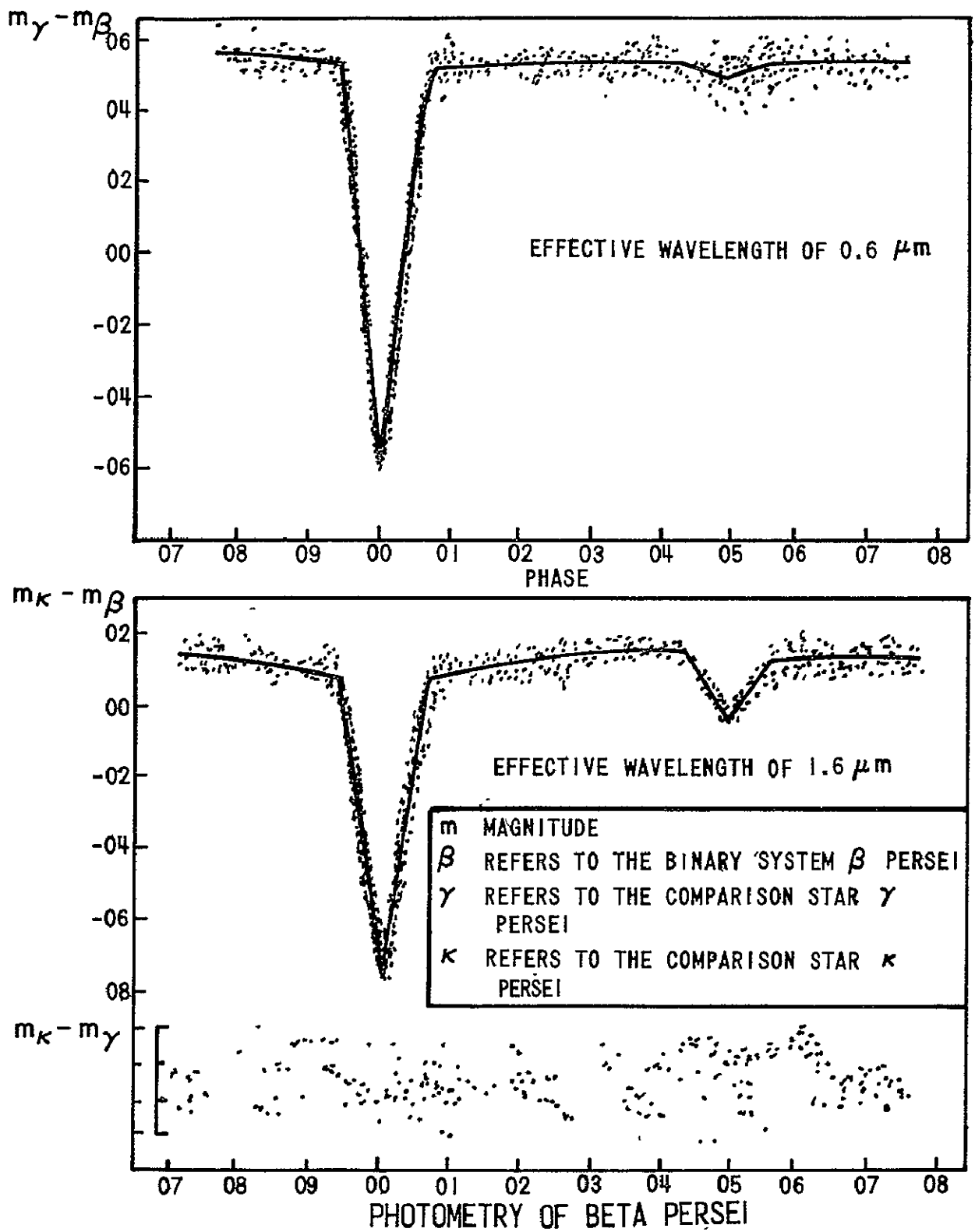


FIGURE 75. COMPARISON OF LIGHT CURVE OF  $\beta$  PERSEI AT ORANGE AND IR WAVELENGTH

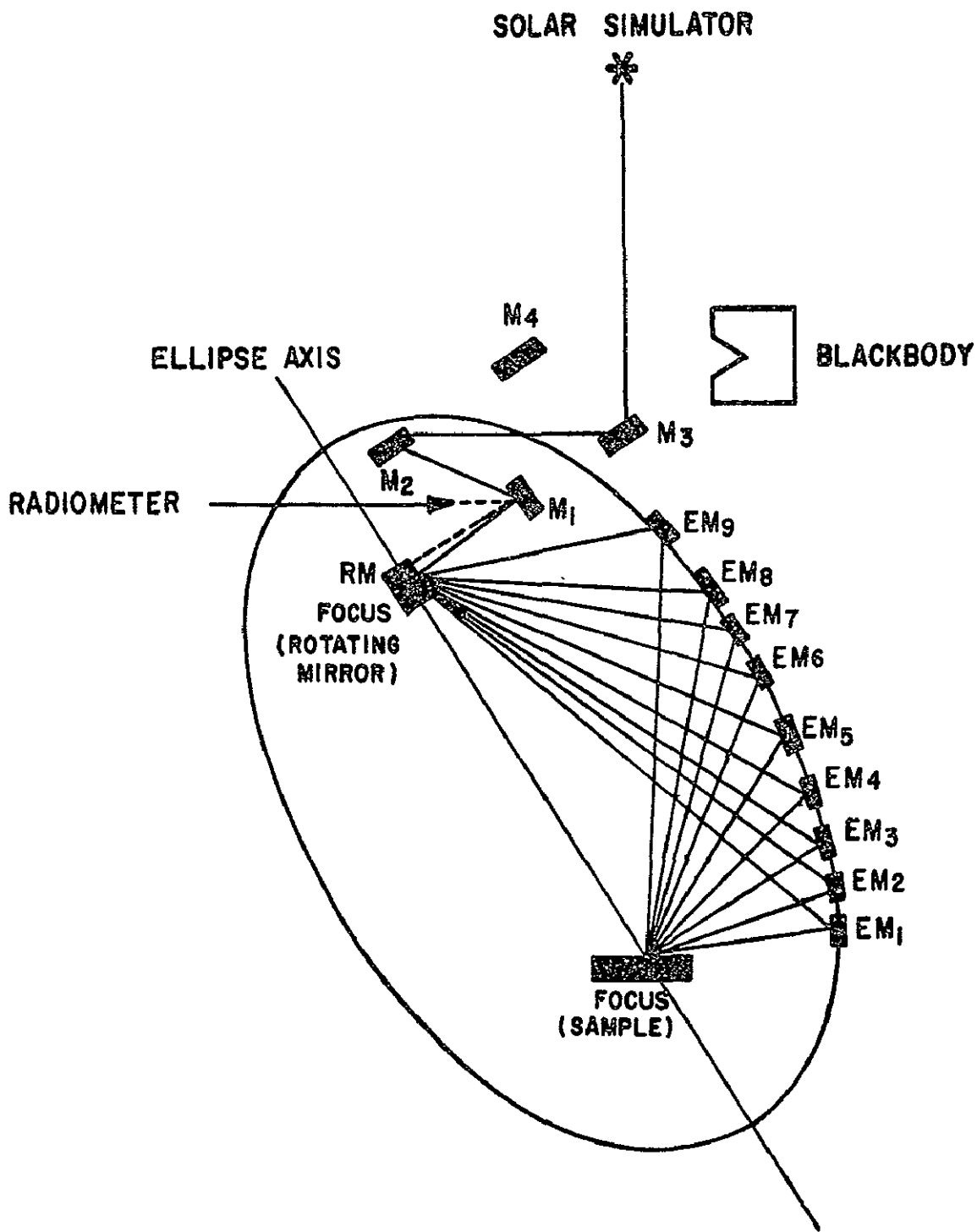


FIGURE 76. ANGULAR DEVICE USED FOR GONIOMETRIC IR STUDIES

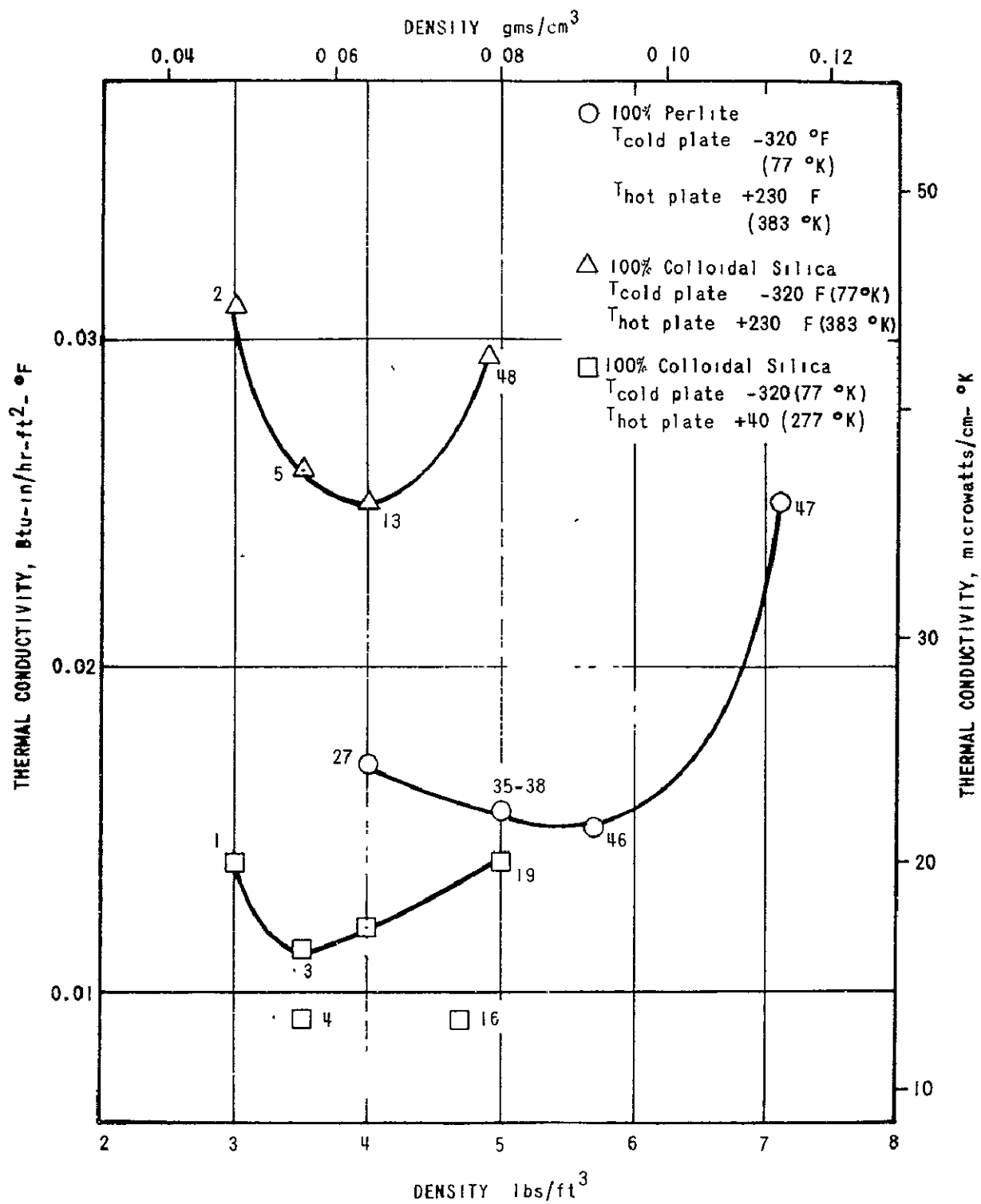


FIGURE 77. HEAT TRANSFER OF UNDERDENSE MATERIALS  
 VERSUS DENSITY

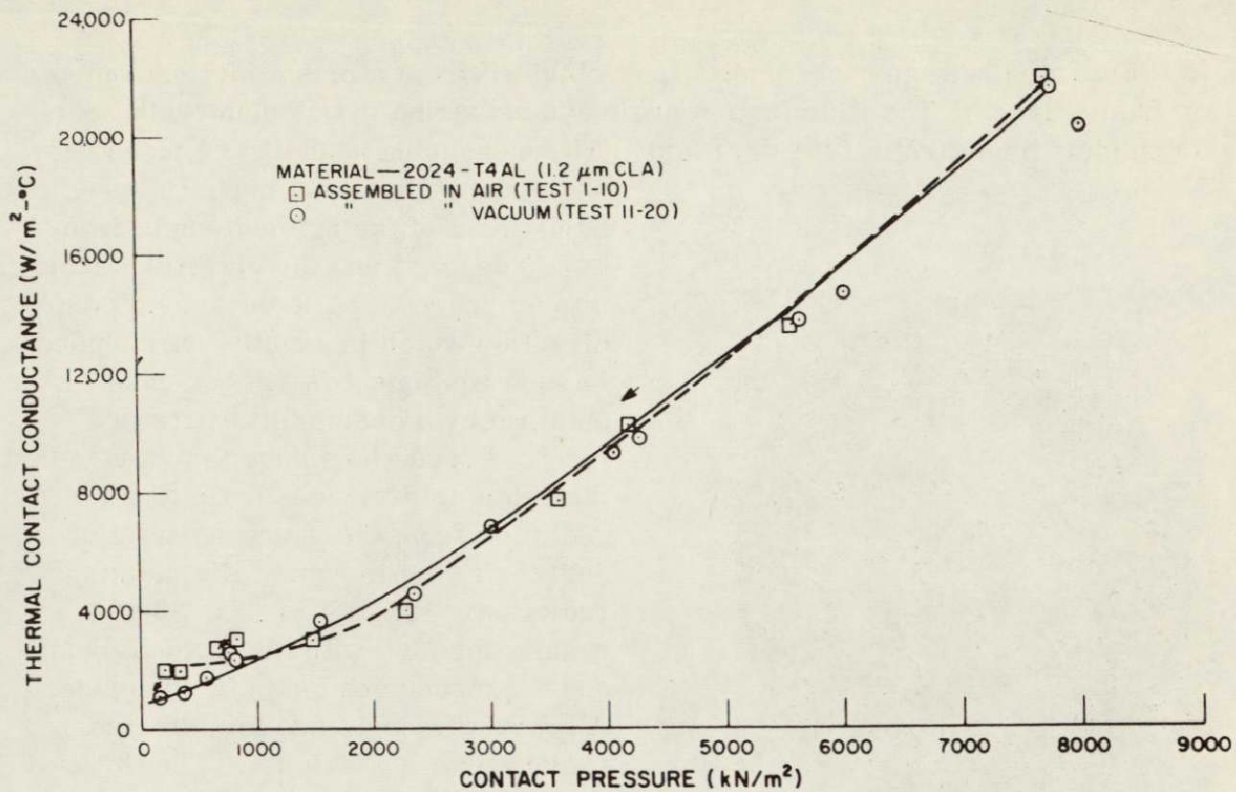


FIGURE 78. THERMAL CONTACT CONDUCTANCE OF Al AS A FUNCTION OF THE CONTACT PRESSURE

## Emissivity Physics

The selection of the emittances of outside surfaces of the spacecraft is a powerful method to control the onboard temperatures. The area of thermophysics obtained a considerable impetus because of this challenging task. In addition to the development of space-stable thermal control surfaces for a variety of different requirements, members of my division were involved in research in emissivity physics. New and advanced methods of laboratory apparatus were developed and our experimental facilities include a broad capability including hohlraum apparatus, radiative calorimeters, radiometers, and reflectometers covering ultra violet, visible and infrared radiation. This paper describes one of the devices, a bidirectional spectroreflectometer (Fig. 80). The arrows indicate the rotational degrees of freedom. The sample holder is mounted horizontal and allows investigation of any type of materials including powders such as underdense material simulating the top layer of the lunar soil. The sample can be rotated around its vertical axis and

is illuminated with monochromatic light obtained from a prism monochromator or from a laser. The illumination angle can be varied in one plane with nearly a complete hemicircle ( $\pm 90$  degrees). The measuring head can be placed

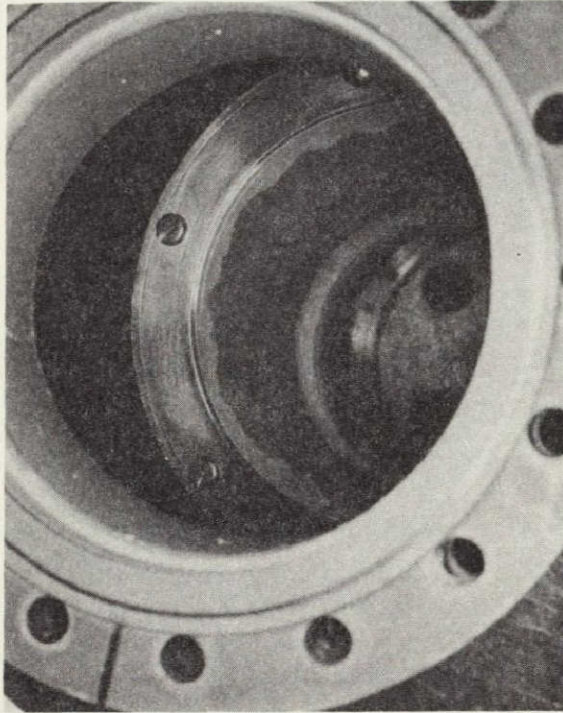


FIGURE 79. VACUUM CHAMBER USED IN STUDIES OF POSSIBLE LUNAR MATERIALS

anywhere within a hemisphere by adjustment of the azimuth angle from 0 to 360 degrees and the elevations from 0 to 90 degrees. The backscattering direction which is usually not included in such equipment is, in our case, obtained by a beamsplitter arrangement. Precautions have to be taken that the beam splitter does not pick up radiation from the surrounding at 90 degrees to the incoming illuminating radiation. Figures 81, 82, 83 give results for MgO with the incident beam and the measuring beam in one place. All measurements are for infrared radiation at  $\lambda = 2.0 \mu\text{m}$ . The three figures differ in the incidence angle, which is 0 degree in Figure 81, -30 degrees in Figure 82 and -60 degrees in Figure 83. Magnesium oxide is an especially interesting material because it is used as a standard and as diffusing surface material for integrating spheres. It can be seen that the reflection of MgO follows closely that of a Lambertian surface for all reflection angles with the exception of the backscattering angle.

Because it is difficult to measure at the backscattering angle, this effect had not been discovered. It is interesting to note that the curve ends in a sharp peak at the exact backscattering angle. This also resolves a problem in connection with the photometric function of the moon. Because the earth is in the way, the closest angles that can be measured are between 1.5 to 5 degrees before and after lunar eclipses. It was assumed by many investigators that the reflected light follows a shallow maximum and therefore the curves were rounded off at the backscattering point, instead of ending in a sharp point. This question has been resolved in favor of a sharp peak at a 0-degree angle between incident and measuring beam.

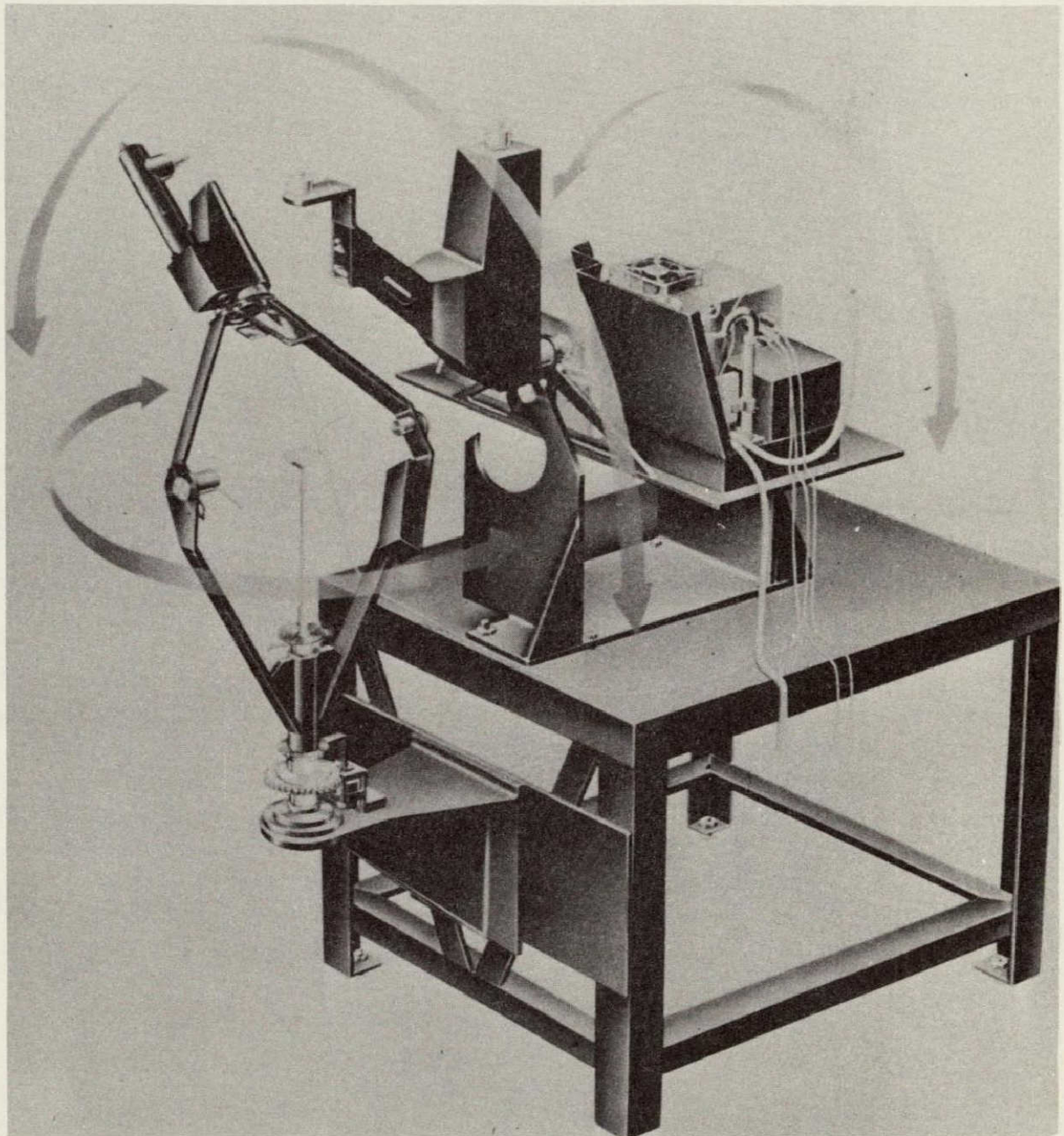


FIGURE 80. BIDIRECTIONAL SPECTROREFLECTOMETER

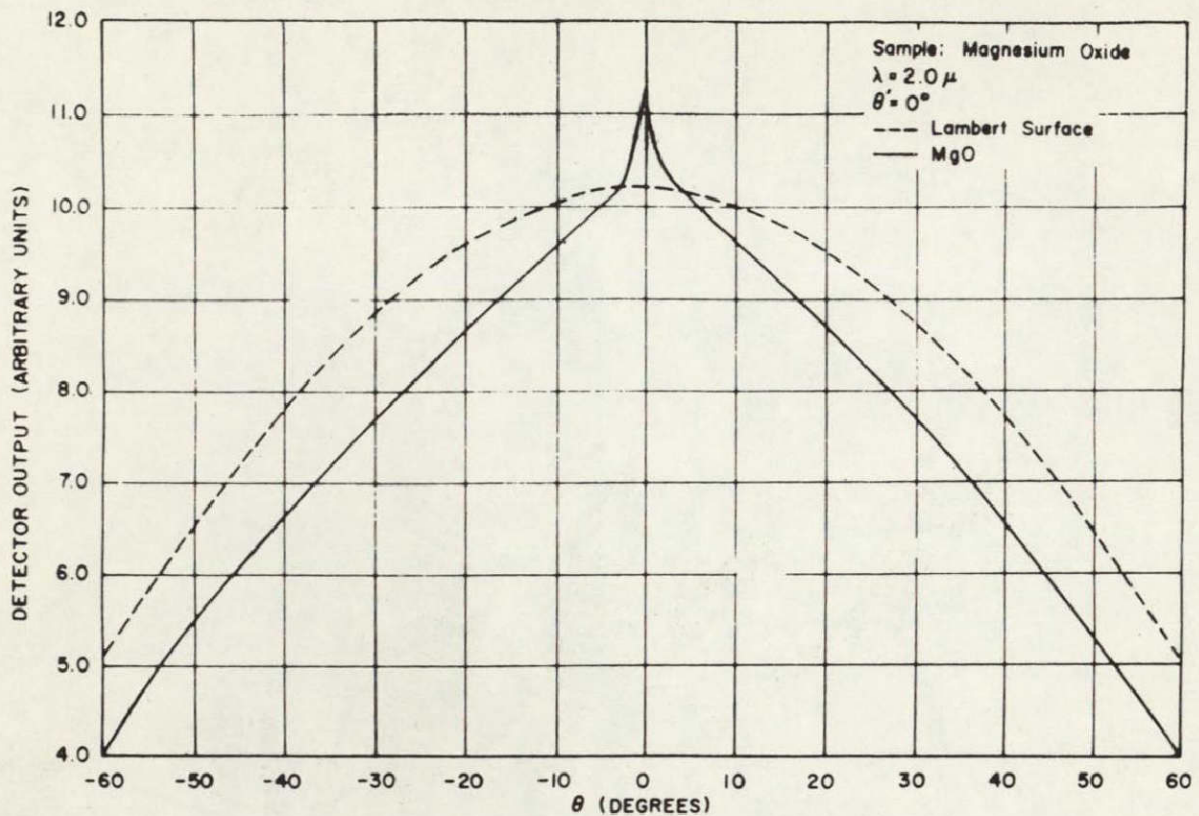


FIGURE 81. REFLECTANCE OF MgO VERSUS ANGLE FOR ILLUMINATION ANGLE = 0

Another example of the activity in emissivity physics may be given; the measuring of optical properties of thermal control coatings prior to and after exposure to ultraviolet irradiation. Figure 84 shows the spectral reflectance of a zinc oxide-silicone paint for the wavelength range from 0.3 to 2.4  $\mu\text{m}$ . Measuring points and curves are shown for initial conditions and for various time integrals of equivalent sun hours obtained by the irradiation of the sample with an A-H6 UV lamp. All curves show the absorption edge in the UV end of the spectrum due to the band gap of 3.2 eV of ZnO. The degradation by the UV irradiation is most pronounced in the red and IR end of the spectrum. The measurements were made with a spectroreflectometer.

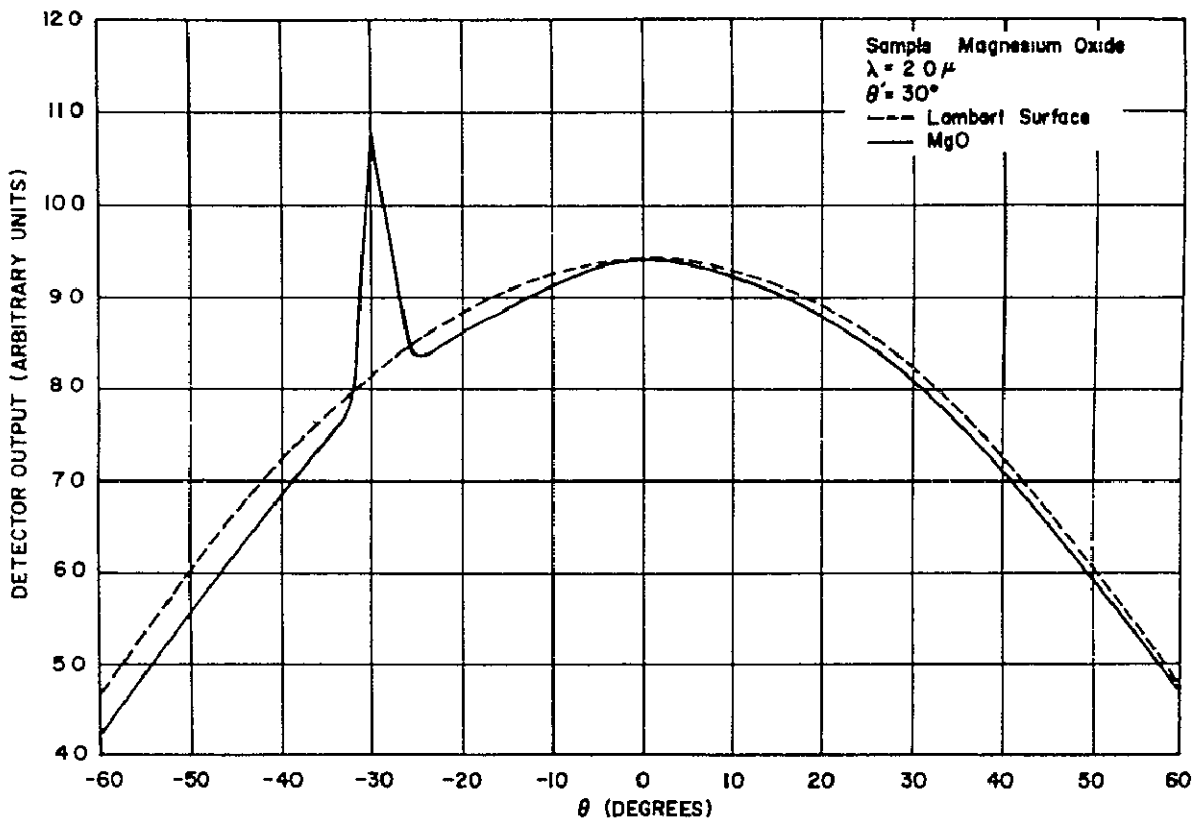


FIGURE 82. REFLECTANCE OF MgO VERSUS ANGLE FOR ILLUMINATION ANGLE =  $30^\circ$

## Solid State Physics And Ultraviolet Physics

Our concern with the space environmental effects on thermal control coatings necessitated an investigation of the basic mechanisms that underlie such effects as the degradation (yellowing) of "white" thermal control surfaces. During the development of the early Explorer satellite I had already a healthy respect for the environment. Very little was known at that time and surfaces, such as sandblasted metal and  $Al_2O_3$ , which were assumed to be very stable, were selected for the outside skin of Explorers I through XI. When satellites became larger and more sophisticated, new coatings were needed. Some of the most successful coatings developed by one of our contractors, the Research

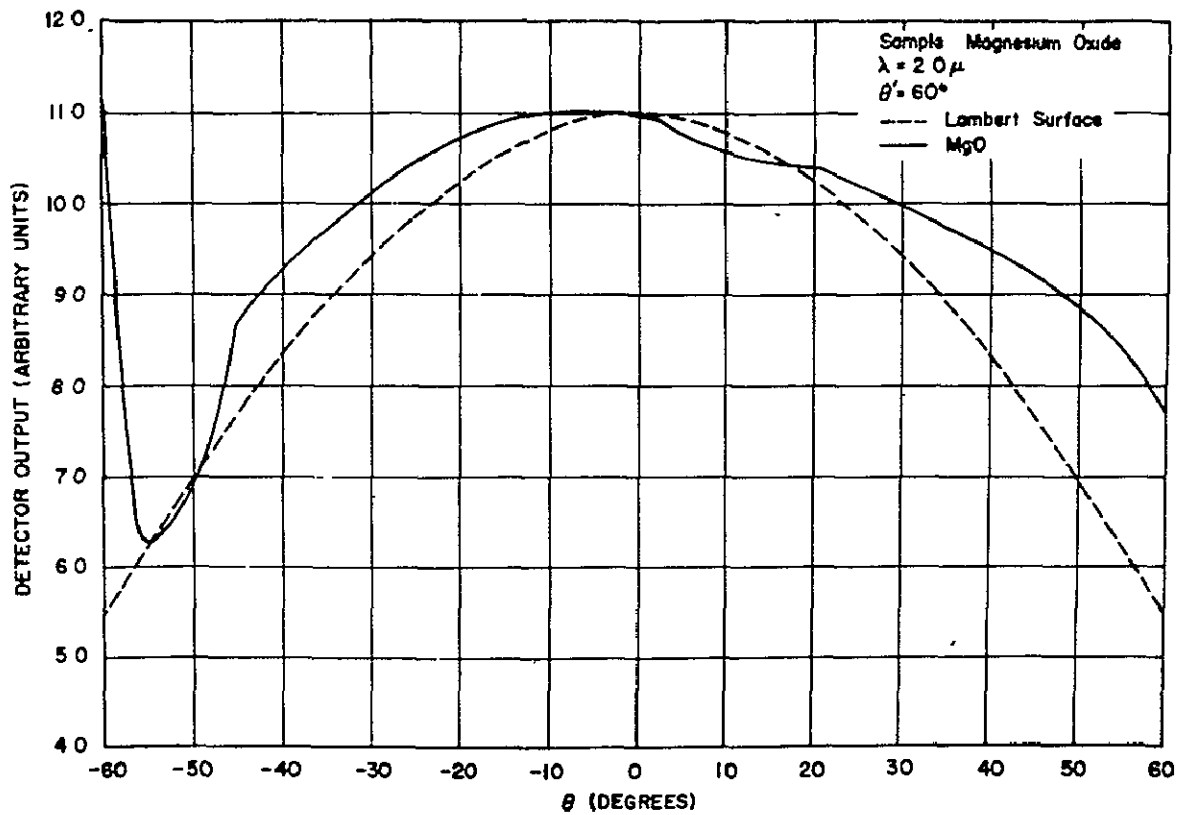


FIGURE 83. REFLECTANCE OF MgO VERSUS ANGLE FOR ILLUMINATION ANGLE =  $60^\circ$

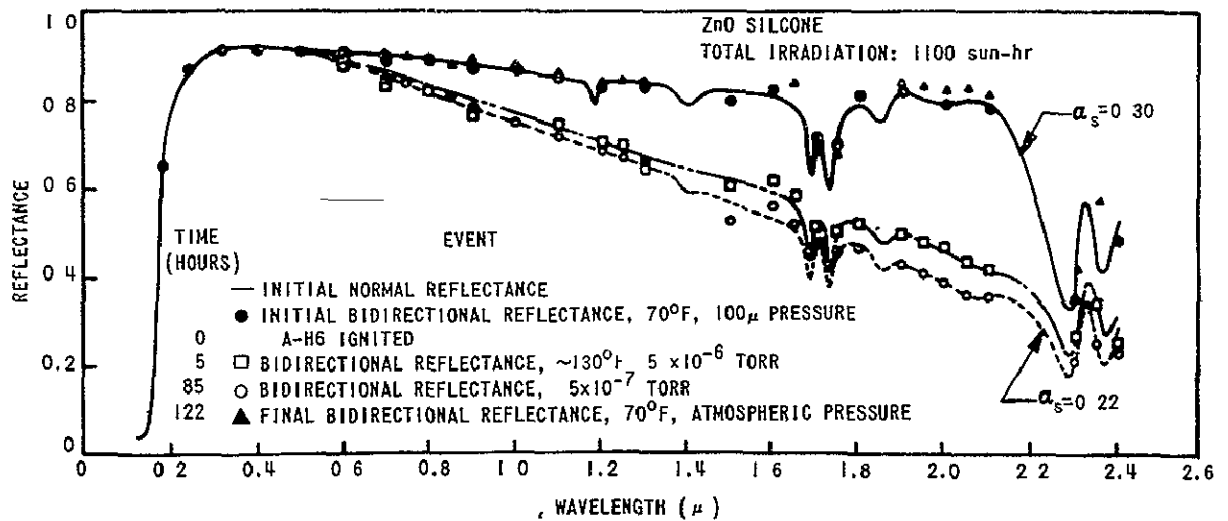


FIGURE 84. SPECTRAL REFLECTANCE STUDIES OF ZnO SILICONE PAINT

Institute of IIT, were S-13 (which has ZnO as pigment and a methylsilicone as binder), S-13 G (an improved version of S-13 and a silicate film on the ZnO grains), and Z-93 (which consists of SnO and silicates). Some essential requirements were easy applicability to large surfaces and to be as space stable as possible with respect to UV radiation, temperature, and vacuum. The stability with respect to solar wind becomes important for deep space probes or very eccentric satellites. In many cases coatings with best stability for UV radiation are still affected by solar wind and vice-versa. Actually, none of the coatings showed completely satisfactory behavior. The white S-13 paint on the S-IVB stage of the Pegasus satellite had an initial  $\alpha_s / \epsilon_{ir}$  value of 0.22 which increased during the launch trajectory and satellite injection into orbit to 0.51. This large increase caused the stage to have a much higher temperature than intended for the thermal control of the satellite.<sup>1</sup>

We have been instrumental in the formulation of many of the nation-wide research objectives and have contributed with original research in our laboratory. Some of the laboratory instruments used are shown in the following figures. Figures 85 and 86 show the 2 electron parametric resonance (EPR) apparatus operating in the X-band ( $8$  to  $12 \times 10^9$  Hz) and K-band ( $3.5 \times 10^{10}$  Hz). Both have a double cavity setup, one for comparison and one which can be irradiated with UV while the measurements are performed. Figure 87 shows some results obtained with the X-Band EPR. The frequencies are swept by varying the magnetic field H. The resonance is due to UV irradiation which generates unpaired electrons. Other instrumentation includes an apparatus for magnetic susceptibility, Hall effect equipment, UV irradiation apparatus for thermal control samples, solar wind simulator, thin film measurements, and photoconductance apparatus.

Another aspect of our activity is the definition of the UV radiation environment for space vehicles and the participation as experiment scientists in the implementation of present or future scientific experiments concerned with the measurements of solar UV and stellar UV. Figure 88 shows a UV spectrum of the sun compared to a spectrum measured by the Naval Research Laboratory (NRL) with the Zeta facility (Harwell). Figure 89 shows a spectrograph by the NRL which covers the spectral region from 500 to 1500 Å. A schematic of the S-083 B solar astronomy experiment of NRL on the Apollo Telescope Mount A(ATM-A), is shown in Figure 90. MSFC is responsible for

1. An overheating of the satellite and especially of the electronics canister was avoided because of an active louver control system which was introduced into the thermal control concept as insurance against such unforeseen occurrences.

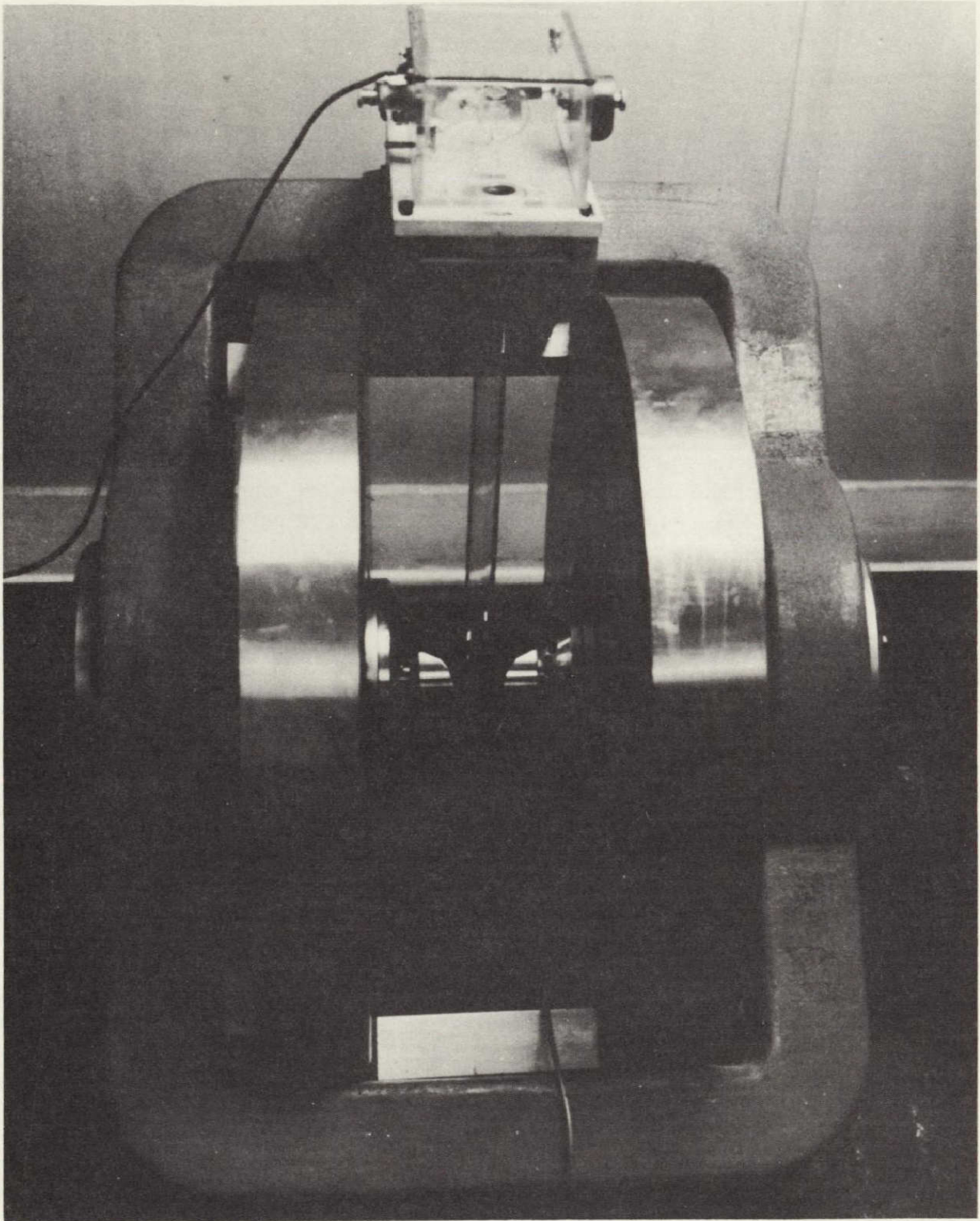


FIGURE 85. CLOSE-UP OF MAGNETS OF ELECTRON SPIN  
RESONANCE EQUIPMENT

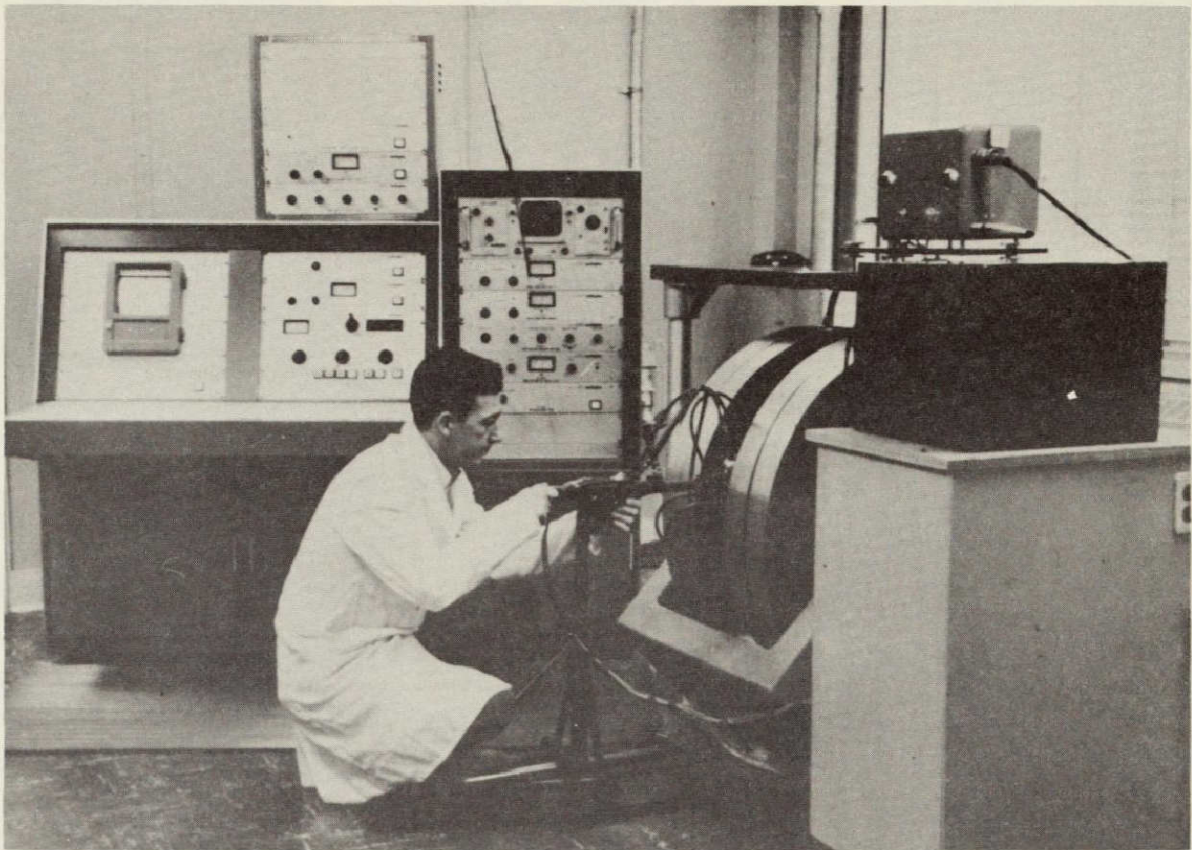


FIGURE 86. ELECTRON SPIN RESONANCE DATA-ACQUISITION EQUIPMENT OF SSL

the implementation of the ATM, the first manned astronomy project of the Apollo Applications Program. My division is responsible to furnish experiment scientists who work with the Principle Investigators (P.I.) of the NRL, Dewitt Purcell, and Richard Tousey. An experiment which is being prepared by another P.I. of the NRL is in the early stages of development. MSFC is presently studying this and many other experiments approved by the Astronomy Subcommittee of the Office of Space Sciences and Applications (OSSA). Figure 91 shows a schematic of the experiment. It is a double reflecting instrument planned for an astronomical sky survey in the far UV region from 900 to 1800Å. The low efficiency of the reflection grating and the primary mirror are compensated by the use of an image converter. The secondary mirror of the Cassegrain telescope is the photocathode. The electrons are accelerated by 20 kV and form an image on the film in the Cassegrainian focus with the help of a focussing magnet. Figure 92 shows a photograph of the assembled instrument. It was flown successfully in a rocket flight at White Sands Proving Ground, and has proven the principle of operation and furnished interesting far UV results of several stellar sources.

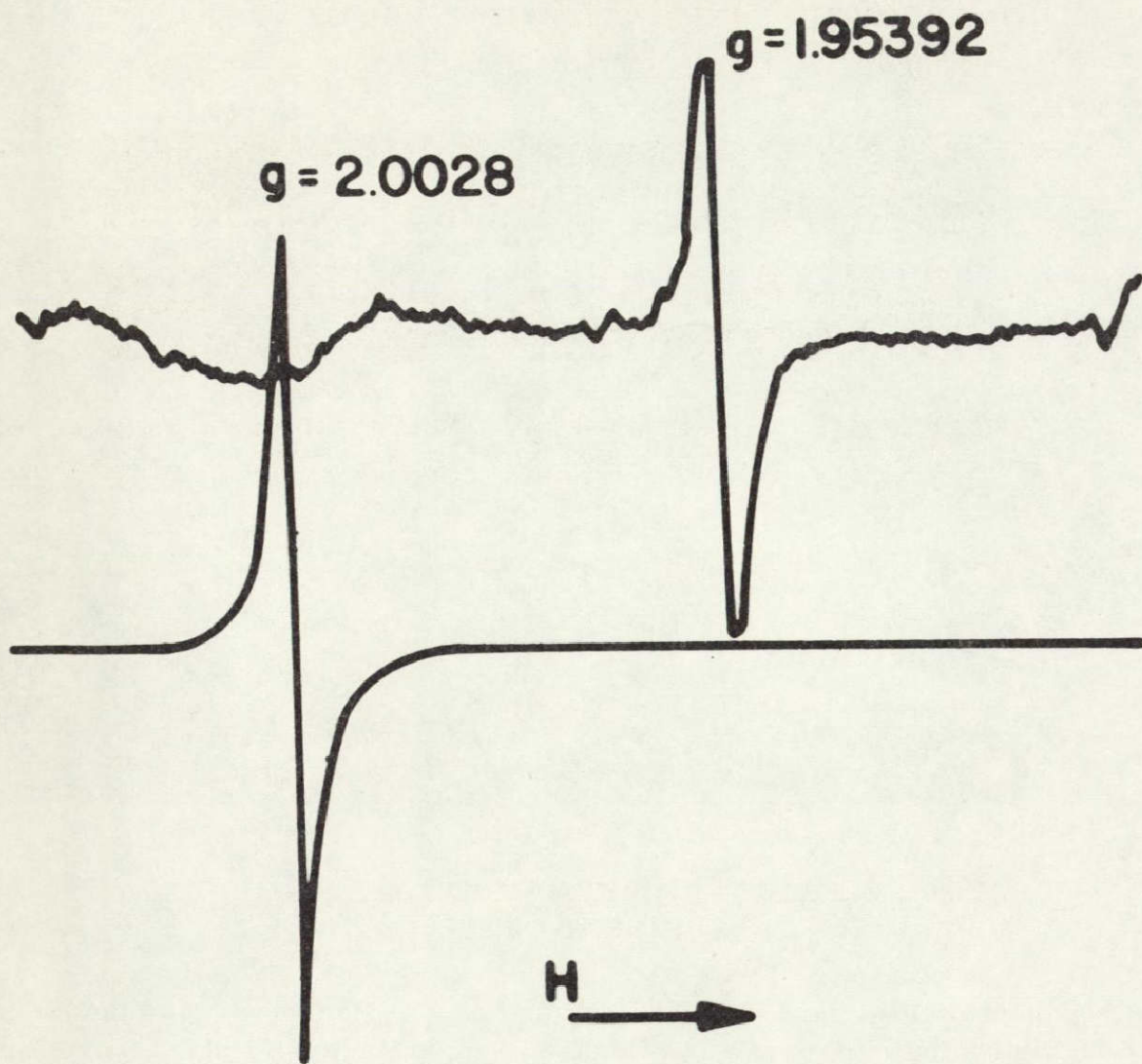


FIGURE 87. ELECTRON SPIN RESONANCE CURVE

### Thermal Space Environment

This research area covers one of the main assignments of the Space Thermophysics Division. The definition of the space environment is of importance to all spacecraft and affects their design and operation. The simulation of the thermal environment in the laboratory and the study of thermal control will also be described in this connection.

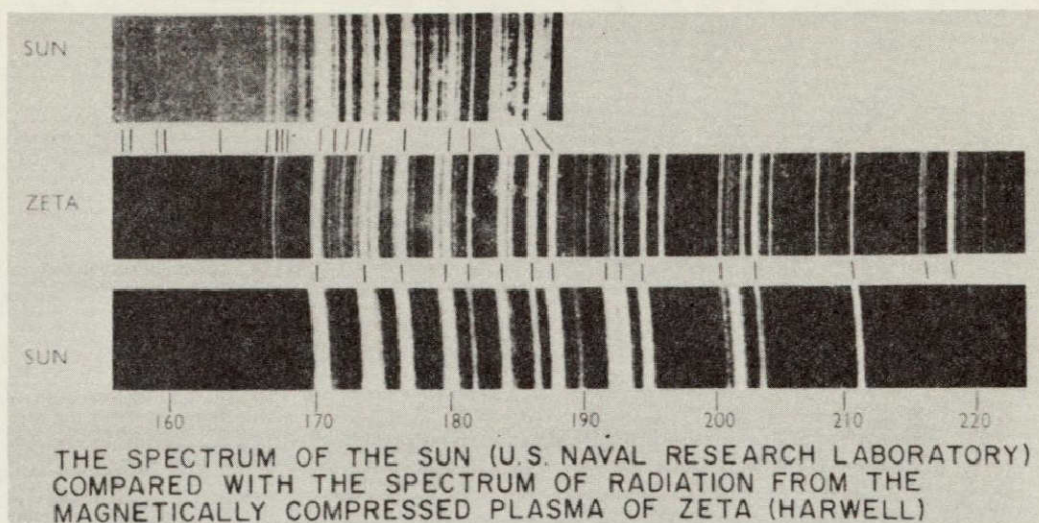
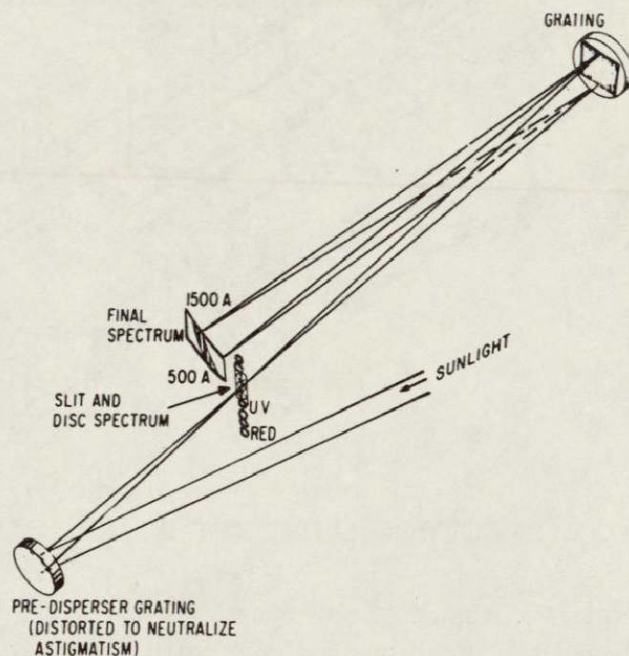


FIGURE 88. XUV SPECTRUM OF THE SUN FROM 160 TO 220 Å



THE DOUBLE-DISPERSION SPECTROGRAPH OF DETWILER, GARRET, PURCELL, AND TOUSEY (1961), FIRST FLOWN ON APRIL 19, 1960.

FIGURE 89. DOUBLE DISPERSION SPECTROGRAPH OF NRL

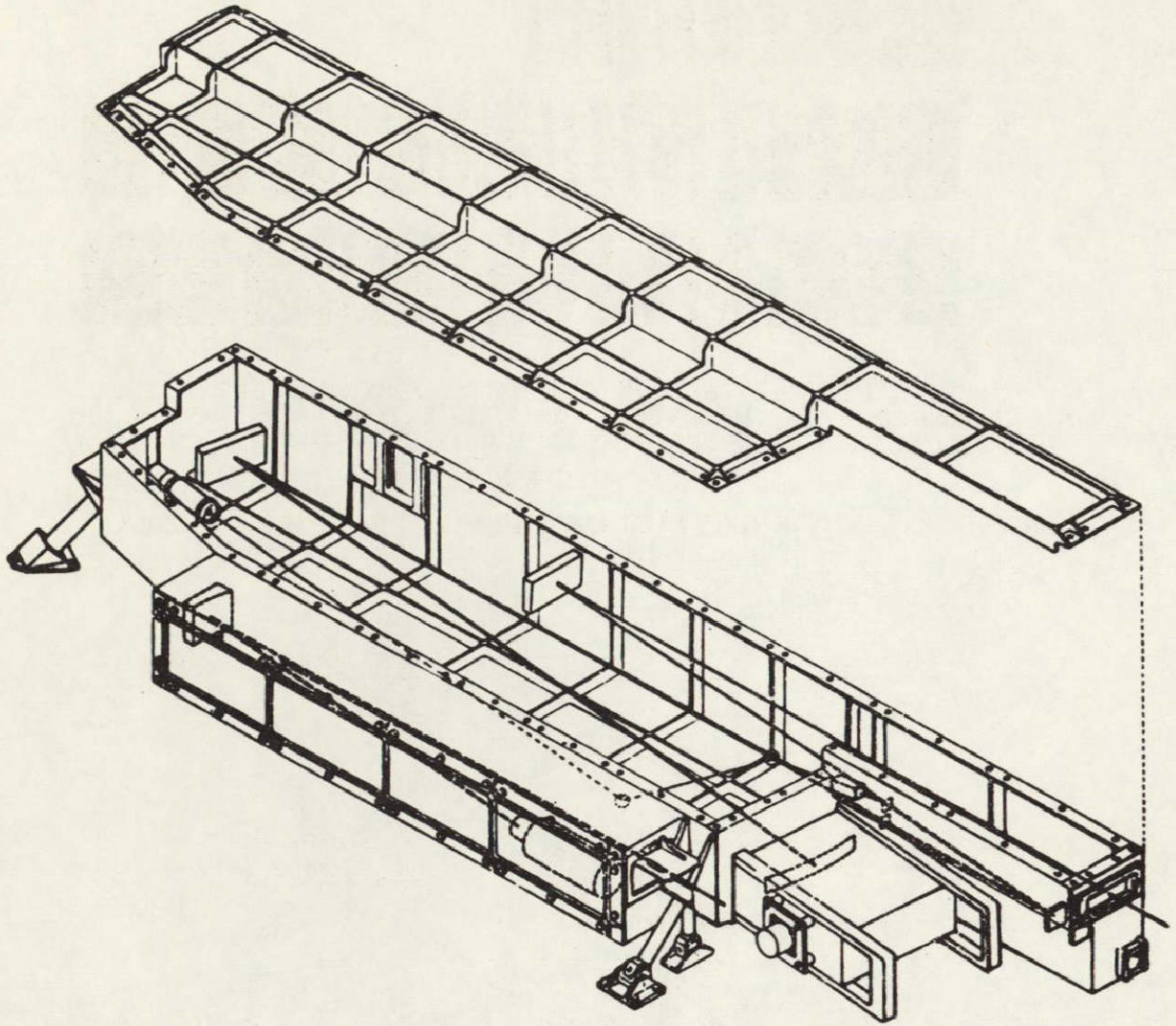


FIGURE 90. XUV SPECTROGRAPH, NRL ATM EXPERIMENT B

Figure 93 shows the result of computations of Rayleigh scattering in the earth's atmosphere, and the irradiation of a satellite surface element by the earth albedo due to Rayleigh scattering. The figure shows that the spectrum of the scattered sunlight differs from the solar spectrum. It is interesting to note that the spectral albedo radiation depends on the inclination of the satellite surface to the sun vector and to the radius vector to the earth. Figure 94 shows a radiometer for solar, albedo, and earth IR radiation. This concept has been studied as possible contender for a flight instrument. The solar constant has, to date, only been determined by extrapolation of ground

## SCHMIDT IMAGE CONVERTER STELLAR SPECTROGRAPH

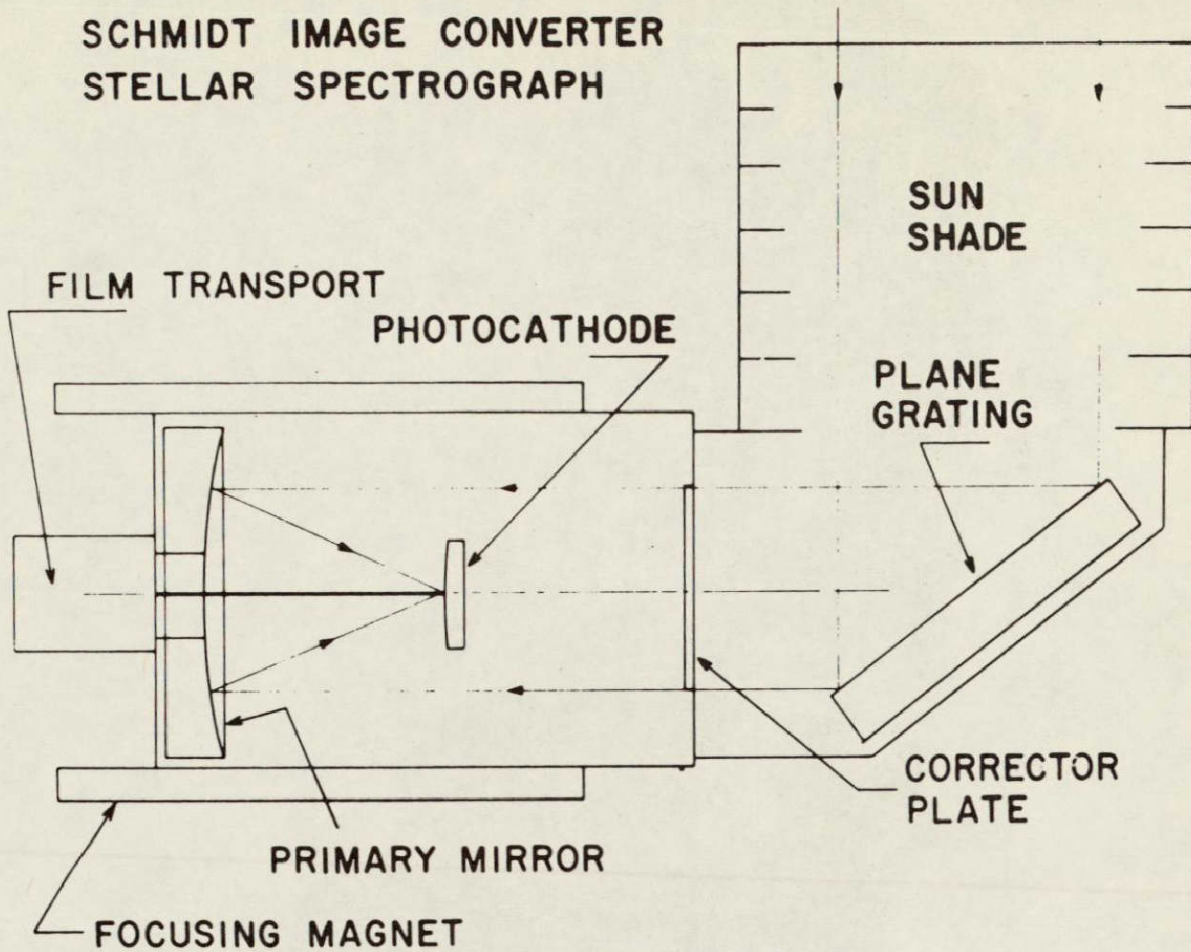


FIGURE 91. SCHMIDT IMAGE CONVERTER STELLAR SPECTROGRAPH OF NRL

measurements to space. The specific device shown here will not be selected; however, it shows some of the basic features of such radiometers: a black body cavity, insulation from the housing, thermal guards, and the possibility to heat with measured amounts of electric energy. One of the requirements for solar radiometers is a controlled attitude. Its control does not have to be very tight; however, the attitude has to be known to an accuracy of at least a degree. This allows, together with the ephemeris of the satellite orbit, to compute separately the solar constant, albedo, and IR radiation.

Figure 95 shows a solar simulator. Its cylindrical vacuum chamber can be evacuated to  $10^{-9}$  torr and the walls can be cooled to liquid nitrogen temperature. An Aerospace Controls Corporation xenon-type solar lamp allows simulation between 0.5 and 2 solar constants. The solar simulator is used for

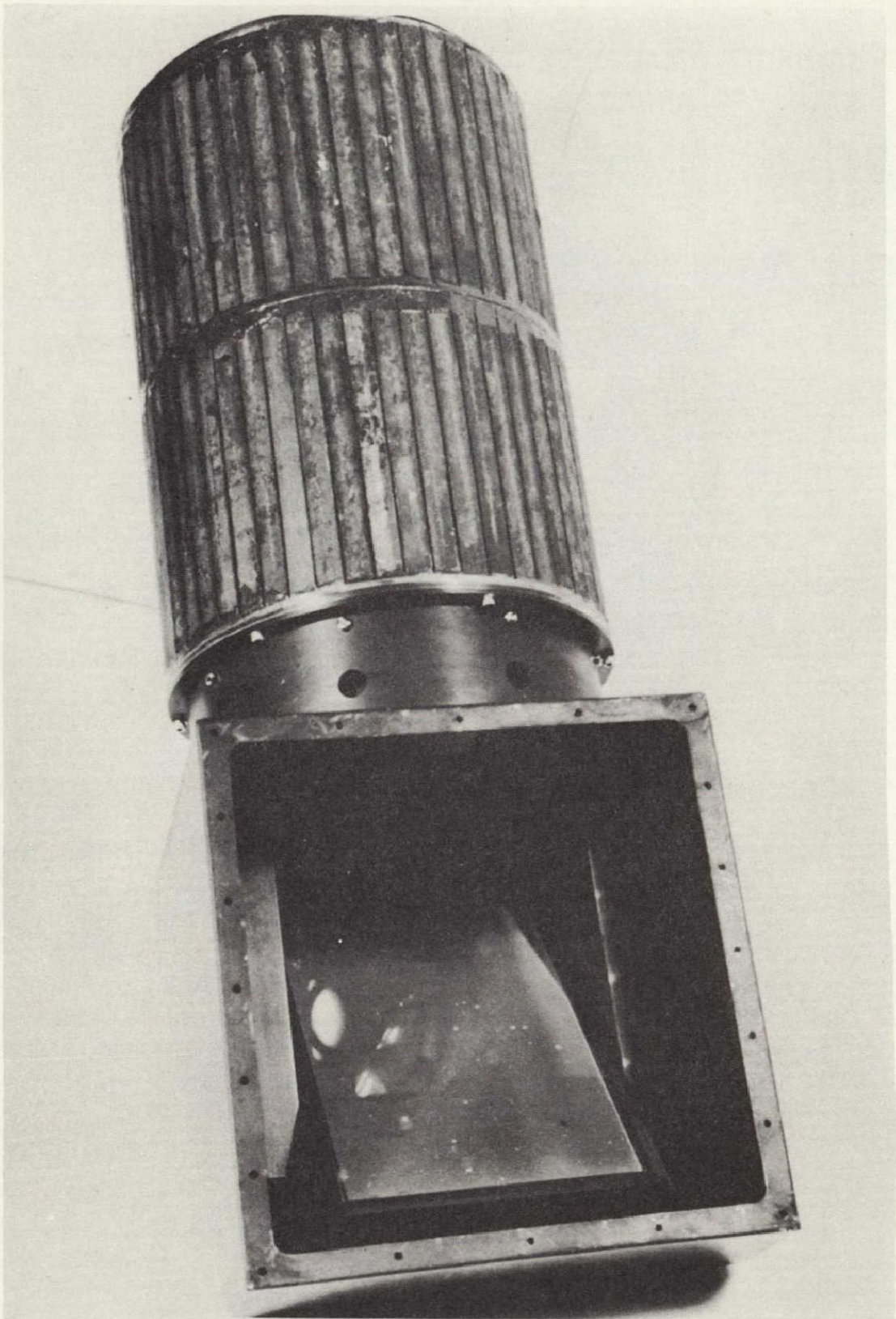


FIGURE 92. FLIGHT PACKAGE OF SCHMIDT SPECTROGRAPH (NRL)

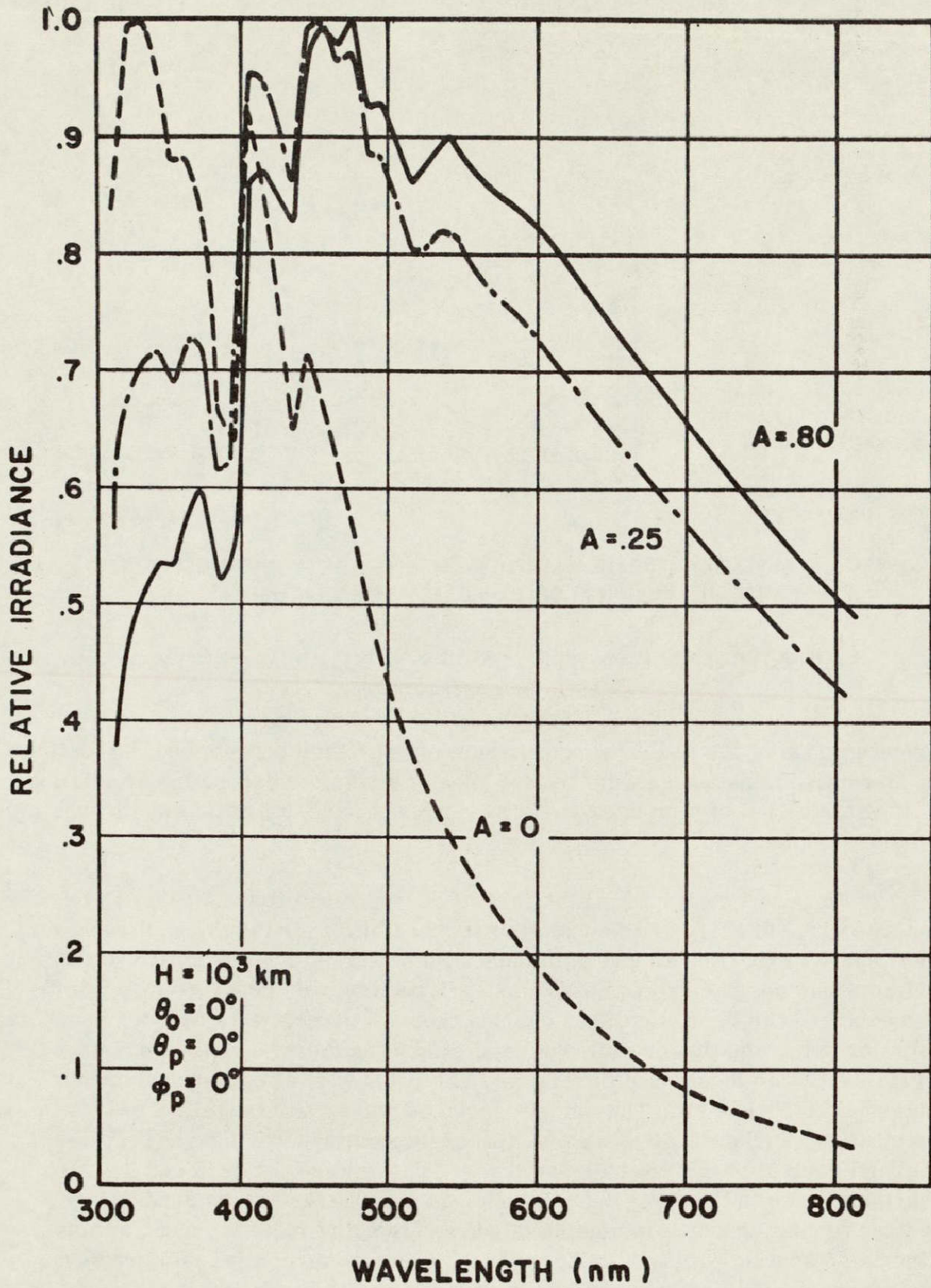
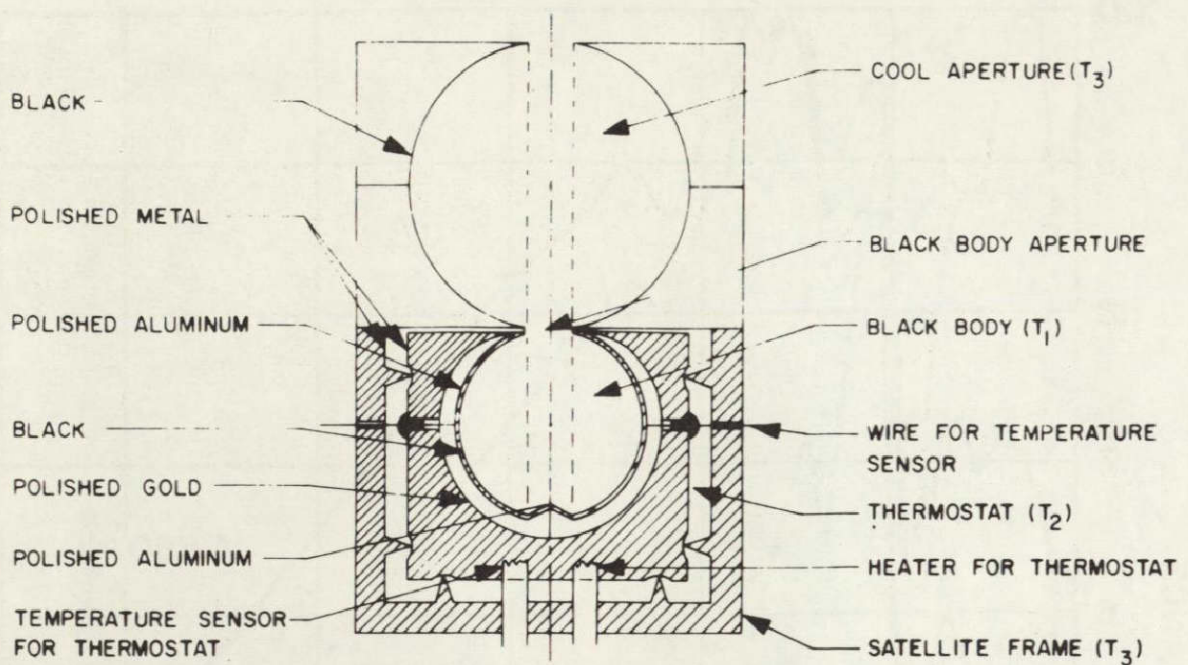


FIGURE 93. RAYLEIGH SCATTERING IN THE EARTH'S ATMOSPHERE



DETECTOR ASSEMBLY. THE BLACKBODY IS IMBEDDED IN A THERMOSTAT SET TO THE MIDRANGE OF EXPECTED TEMPERATURES

FIGURE 94. RADIOMETER USED FOR SOLAR ALBEDO AND EARTH RADIATION

investigations of the radiative equilibrium of space components and the testing of thermal shields such as the frontal area of a solar telescope for simulation of the irradiation of simulated lunar materials through a lunation or through a lunar eclipse.

Figure 96 shows one of the three Pegasus satellites. All three were launched in 1966. My division had the responsibility for the thermal control of the Pegasus experiments and of the electronics canister. In addition to the primary engineering experiments about micrometeoroid penetration frequencies, the three satellites carried thermal experiments with four sensors each for determination of environmental effects on thermal control surfaces (Fig. 97). The location of the thermal environmental effects experiment is indicated on Figure 96. The sample surfaces varied from satellite to satellite and included, in all cases, two of the coatings which were used for thermal control of the Pegasus satellites. These were the S-13 and the Alodine thermal control surfaces. S-13, which was used on the Saturn S-IVB stage, is a white coating which is highly reflective for solar radiation and contains a zinc oxide coating with a silicone binder. The Alodine coating is a greenish electro-deposited coating used on the wings of the Pegasus.

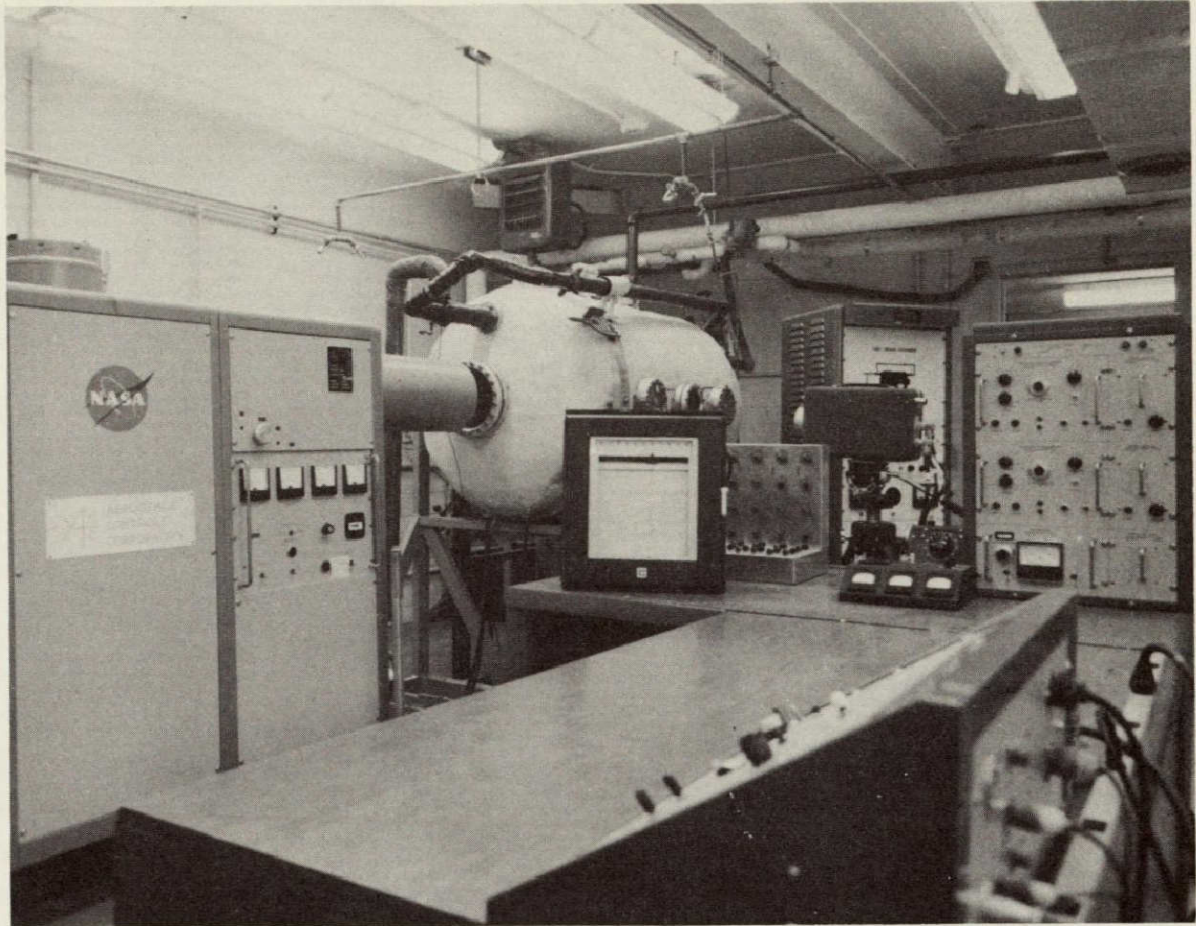


FIGURE 95. SOLAR SIMULATOR AT SSL

A new concept of preflight measurements of satellite thermal control coatings was introduced with the Pegasus satellites. The time interval between the application and vacuum testing of thermal control coatings and the actual launching is usually 4 to 6 months but may extend to more than a year. No provisions are made to reconfirm or test the accuracy of the emittance values of the satellite thermal control surfaces. For the Pegasus satellites we introduced a portable device which allows measurement, under "field conditions," of the solar reflectance or the IR emittance with two different measuring heads. Figure 98 shows the solar reflectometer head being used on flight hardware. Measurements with the portable instruments were made on the Pegasus satellite at various sites such as MSFC, Fairchild, the satellite prime contractor, and finally in the hangar and on the launching pad up to two days prior to the launch at the Kennedy Space Center. The status of all thermal

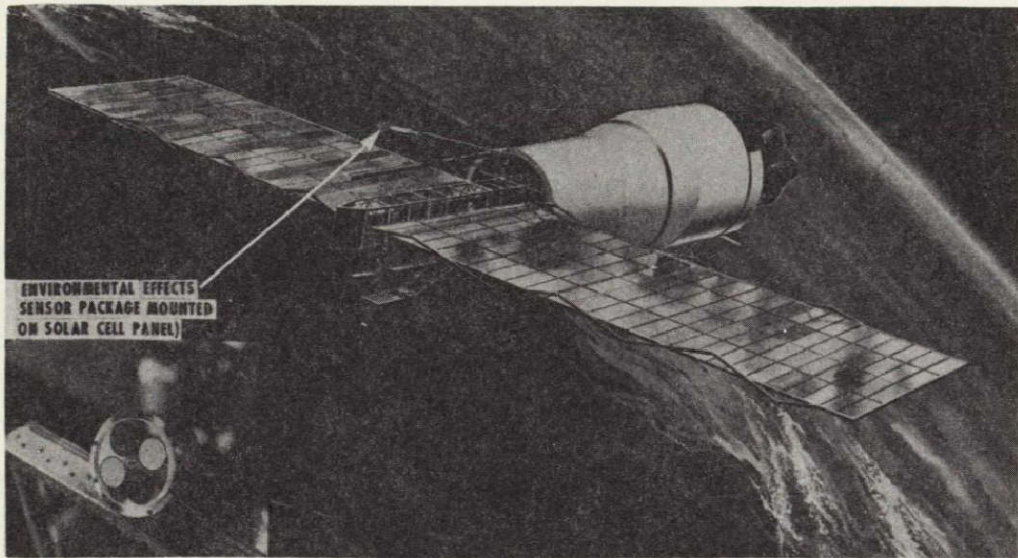


FIGURE 96. PEGASUS SATELLITE

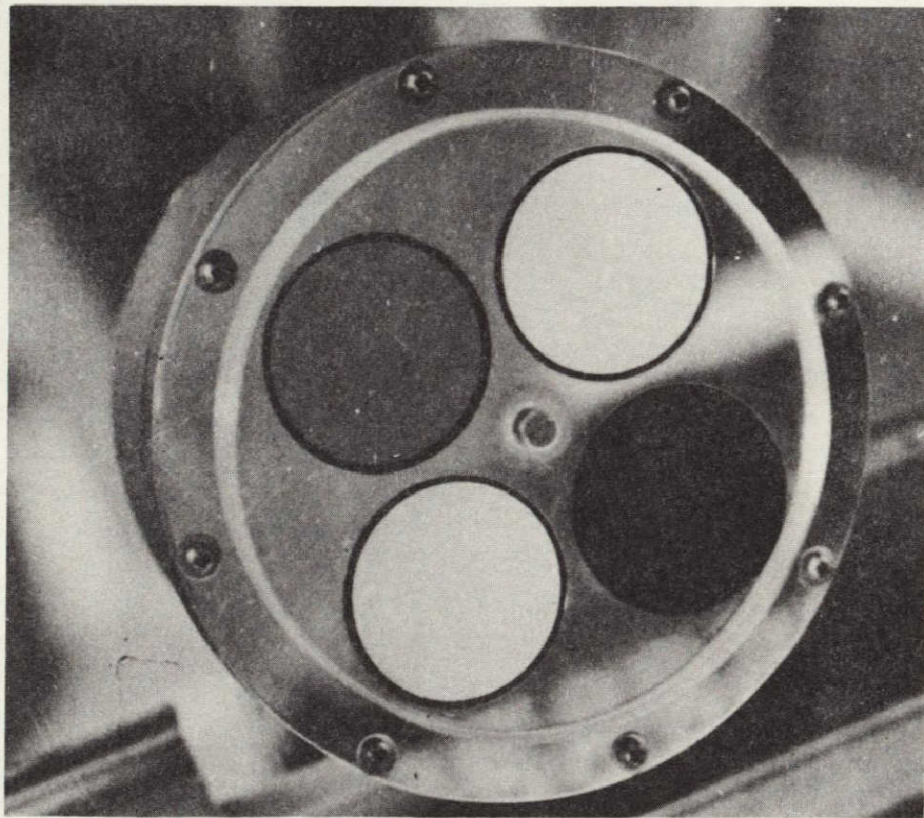


FIGURE 97. THERMAL ENVIRONMENT SENSORS FLOWN ON PEGASUS

control coatings prior to satellite launching could thus be ascertained, and this information was used for comparison to on-board measurements of the degradation by the space environment. We know from this that the initial rapid decrease of solar reflectance is a true space effect or atmospheric environment effect during launch.

A promising approach for the thermal control of easily overheated components of experiments on a boom-like magnetometer is the use of fusible materials. Requirements are a high heat of fusion and a minimum amount of supercooling effects for the fusing material. Figure 99 shows a flight experiment which was assigned the NASA Headquarters nomenclature Number T005. It is a schematic of the adiabatic test model of the heat of fusion radiator. The fusion material is embedded between the meshes of a honeycomb system for increased heat conduction. Figure 100 shows several temperature-time curves for different rates of heating per unit area. The main advantage of the heat-of-fusion principle is that it can be used in addition to other passive or active thermal control concepts, and that it reduces the extremes in temperatures. For this reason it is considered in the lunar module of the Apollo project to reduce the temperature extreme of a component (on an antenna). Another part of the heat of fusion experiment is to measure and observe the phase change of materials under a zero-g environment. This experiment will be separated and carried under a separate experiment number as a manned flight experiment, whereas the radiator portion could be flown as unmanned or manned experiment. Figure 101 shows the result of a study which included the possible incorporation of the above phase-change experiment in the Apollo command module. Figure 102 shows a photo of the phase change observation unit of this experiment which has been built under a contract to Northrop. In connection with this experiment and in support of it, research is carried out in our laboratories. The experimental studies include crystal growth, parameter studies of various modes of convection, temperature gradients, drop tests to simulate zero gravity, differential calorimeter measurements, interface between solid and liquid. The emphasis in these experiments is to arrive at an understanding of the basic mechanisms involved in crystal growing and the solid-liquid interface under one-g and zero-g conditions.

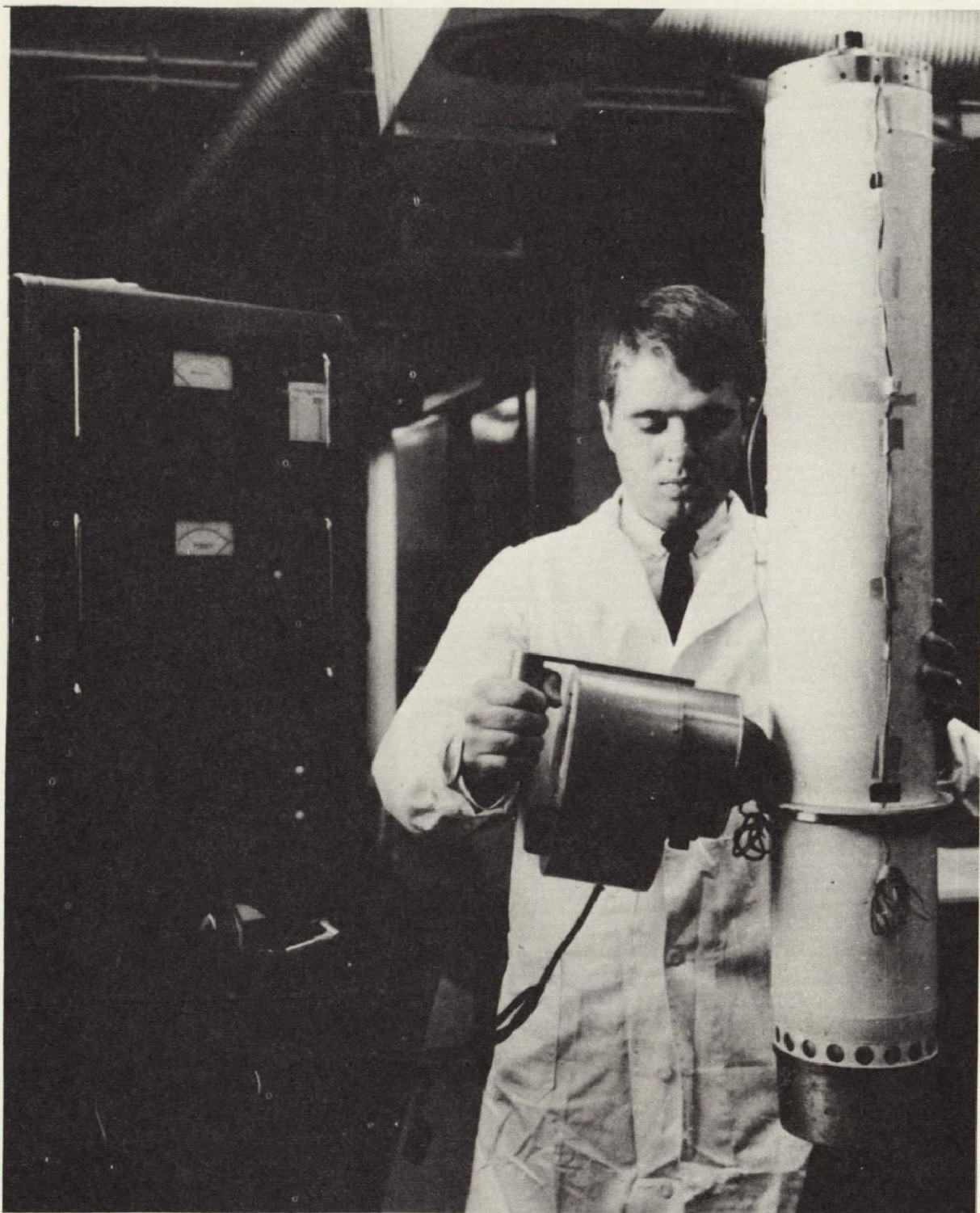


FIGURE 98. PORTABLE SOLAR REFLECTOMETER

# HEAT OF FUSION RADIATOR ADIABATIC TEST MODEL

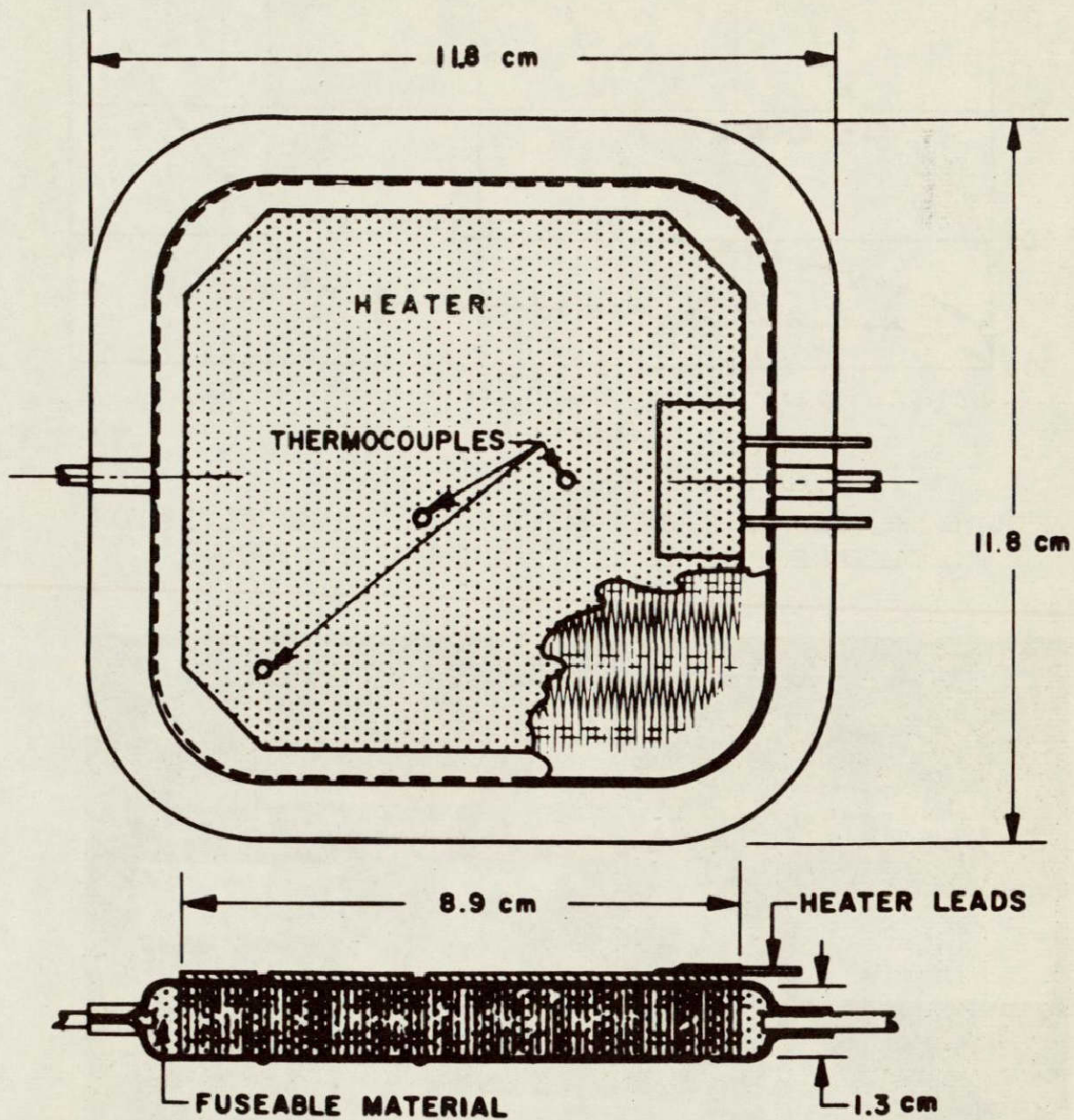


FIGURE 99. FLIGHT EXPERIMENT FOR MEASURING HEAT OF FUSION

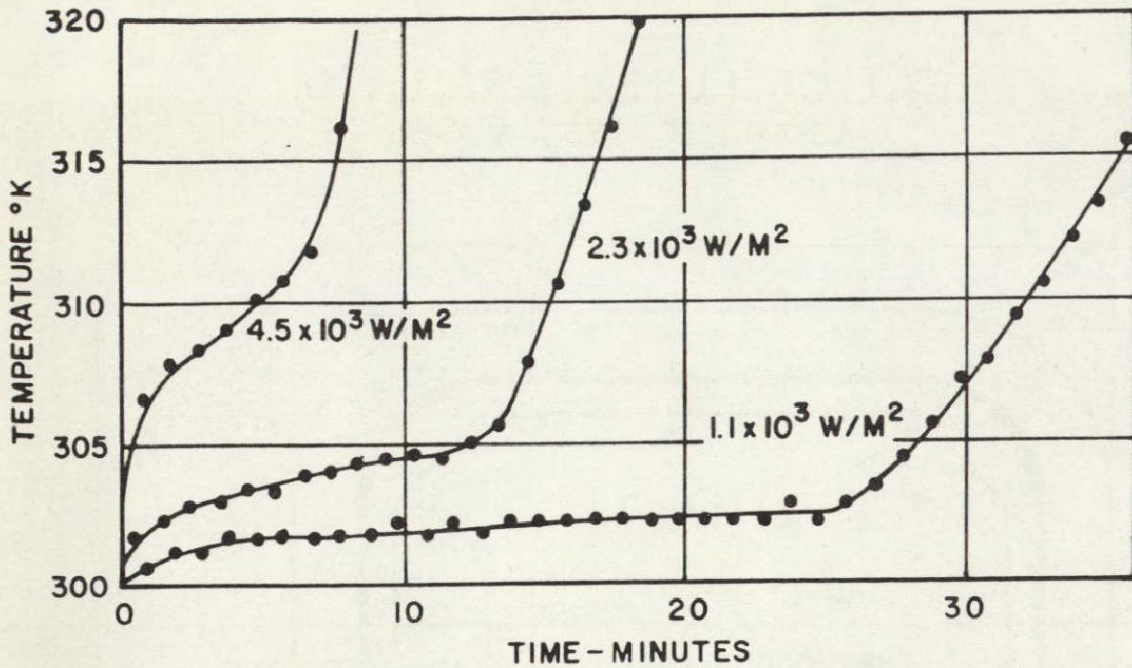


FIGURE 100. LAB TESTS OF TEMPERATURE - TIME CURVES FOR DIFFERENT RATES OF HEATING PER UNIT AREA

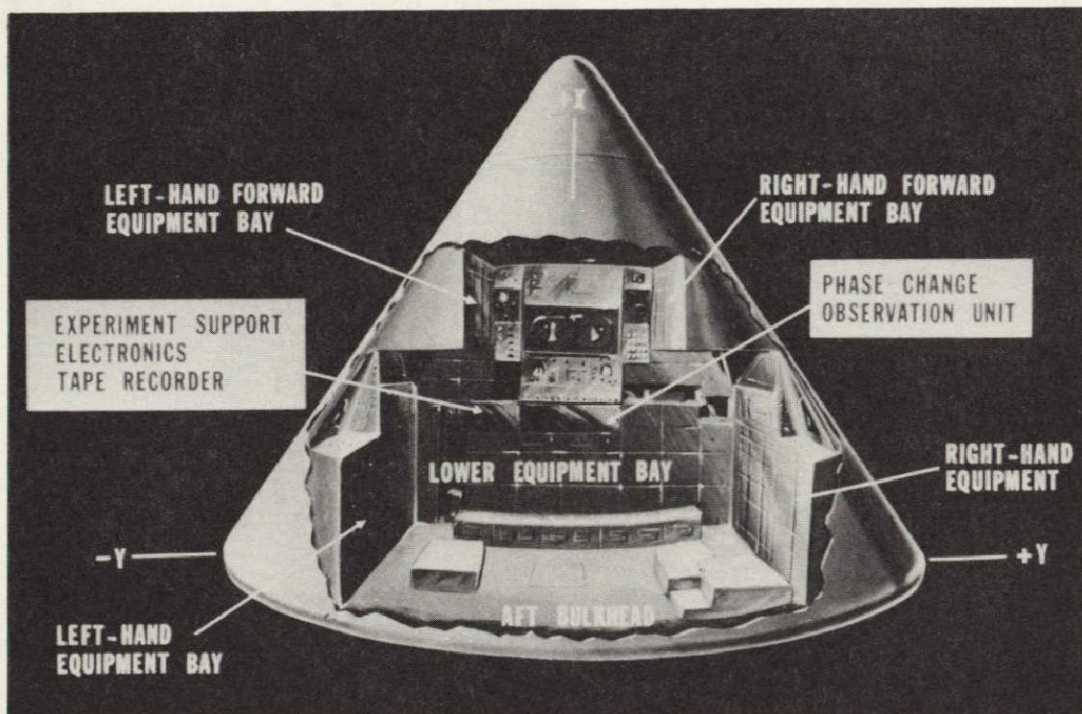


FIGURE 101. AAP FLIGHT EXPERIMENT T-005 - APOLLO CREW COMPARTMENT

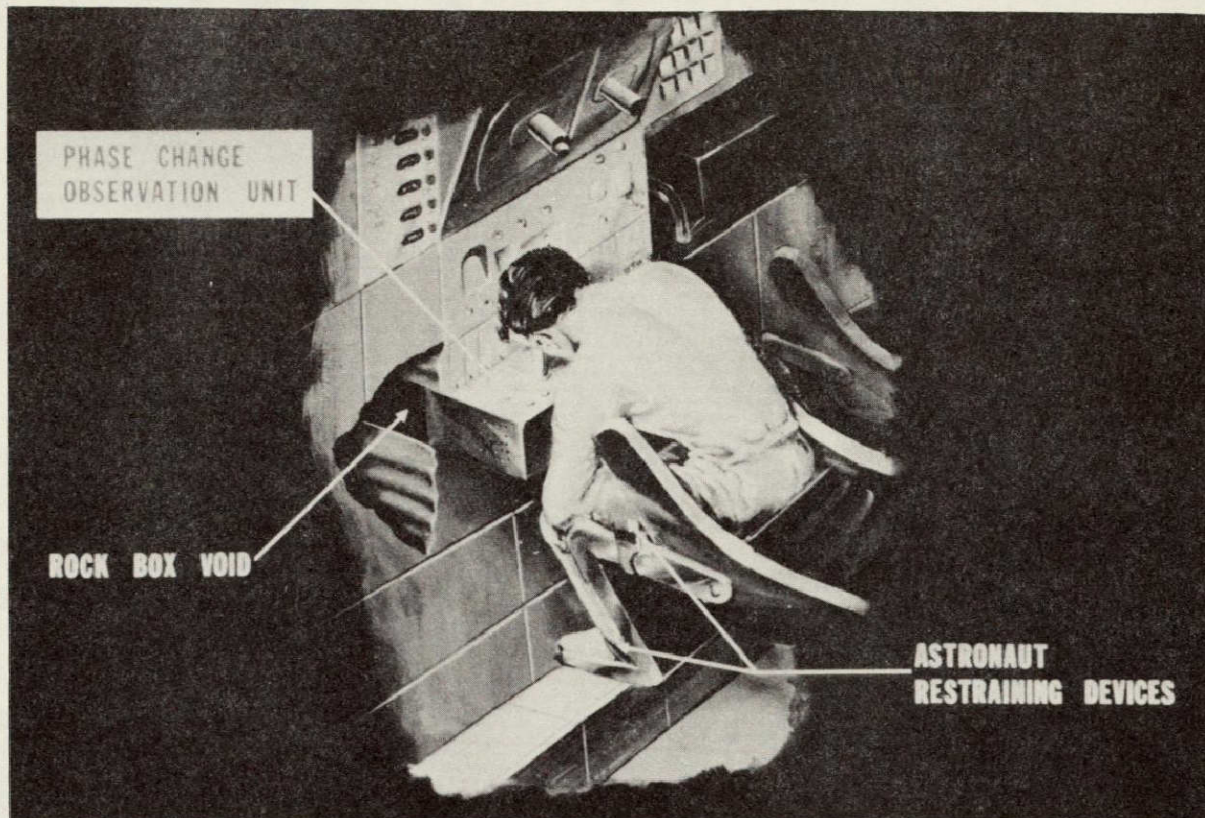


FIGURE 102. AAP FLIGHT EXPERIMENT T-005 — OBSERVATION UNIT

ABSTRACTS OF PROGRESS REPORTS

# BUOYANCY EFFECTS ON THERMAL BURNOUT IN VERTICAL CHANNELS<sup>1</sup>

By

W. R. Gambill  
Oak Ridge National Laboratory

## Abstract

The effect of buoyant forces on burnout heat flux, which can be significant in low-velocity downflow systems, has been generally neglected. We are investigating the subject phenomenon in three related areas: (1) burnout of vertical channels blocked at the base and open at the top to a liquid supply, (2) burnout of vertical channels cooled by a low-velocity downflow of water, and (3) flow reversal or inversion phenomena in the HFIR (High Flux Isotope Reactor) geometry.

In the blocked-base case, the hypothesis that the critical heat flux corresponds to that flux producing sufficient vapor to cause a transition from countercurrent liquid-vapor flow to cocurrent upward flow (flooding) has been successful. For a series of 56 tests conducted with round and square electrically heated tubes at pressures near atmospheric and with upper pool subcoolings of 0 to 142° F, the quantitative expression of this hypothesis may be written as follows:

$$(\phi_c)_{\min} = \frac{\lambda D_e^{3/2} [\rho_v g(\rho_l - \rho_v)]^{1/2}}{3L[1 + (\rho_v/\rho_l)^{1/4}]^2}$$

in which  $\phi_c$  is the critical heat flux,  $\lambda$  is the latent heat of vaporization,  $D_e$  is the equivalent diameter of the channel,  $\rho_l$  and  $\rho_v$  are liquid and vapor

---

1. Research sponsored by the U. S. Atomic Energy Commission under contract with the Union Carbide Corporation.

densities, respectively;  $g$  is the gravitational acceleration; and  $L$  is the heated length.

Low-velocity downflow tests conducted at atmospheric pressure with water have shown that the difference between upflow and downflow burnout fluxes increases monotonically with decreasing coolant velocity for velocities less than  $\sim 1$  meter/sec, and that upflow fluxes may be as much as  $\sim 7$ -fold larger than those observed with downflow under conditions otherwise the same. It has been postulated, but not yet demonstrated, that the minimum critical heat flux in a buoyant system will occur with a net liquid downflow just equal to the gravitational rise velocity of bubbles in the channel, in which case the net body force on such bubbles is zero.

If the downflow rate in a heated channel is reduced sufficiently, a flow reversal or inversion will ultimately occur if the geometry provides a parallel flow path. In tests of the HFIR geometry, it was found that the downflow velocity just preceding reversal to free upflow could be characterized by the ratio of channel-average Grashof to von Kármán moduli (a grouping also useful in correlating the results of the low-velocity-downflow burnout experiments).

## ULTRAVIOLET RADIATION DAMAGE

By

M. L. McDaniel  
Brown Engineering Company, Inc.

### Abstract

The effectiveness of thermal environment design, as applied to thermal coatings presently employed on this nation's space vehicles, depends upon the reliability of the optical constants of the material comprising this coating. Zinc oxide, exhibiting the most useful solar absorptance to emittance ratio, is presently employed as the thermal coating pigment. However, the experience with this material has been that under the conditions of solar irradiation in vacuum, the solar absorptance coefficient is not constant, faulting the thermal design. In the present work, the degrading conditions of radiation in space have been simulated in an effort to determine the mechanism whereby the thermal-optical qualities of this material are compromised.

# PROBLEM AREAS IN THE COMPOSITIONAL ANALYSIS OF THE LUNAR SURFACE BASED ON MEASUREMENTS OF FAR-INFRARED SPECTRAL EMISSION OBTAINED BY REMOTE SENSING

By

J. M. Scarborough  
Brown Engineering Company, Inc

## Abstract

Problems confronting the analyst of far-infrared radiant emission from the lunar surface are enumerated and discussed. Two simple mathematical models incorporating salient features of the radiating process are described. One model simulates the radiating properties of a surface composed of monolithic grains much larger than the wavelengths of the radiation. The other simulates a surface composed of very small particles agglomerated into larger clumps which are arranged in an open structure of extreme roughness on a scale large compared to the wavelength.

# THE EFFECT OF CRATERS ON LUNAR THERMAL RADIATION

By

---  
J. P. Doty  
Brown Engineering Company, Inc.

## Abstract

A mathematical model of the lunar surface has been constructed to explain the directionality of the lunar thermal radiation. For this purpose a

surface with hemispherical craters has been assumed. A perturbation on the radiation intensity, caused by these craters, is added to Lambert's radiation cosine law. The resulting equation is shown to agree with experimental data very well. Through the use of this equation, the local crater density is calculated from a general crater distribution of  $N = N_0 r^{-3}$  where  $r$  is the radius of the crater

## THERMALLY STRATIFIED SHEAR FLOWS

By

Hsing Chuang  
University of Louisville

### Abstract

The mean velocity distribution in the inner or wall region outside of the viscous sublayer of a shear flow is always assumed to be logarithmic if the flow field is neutral, but it is approximately expressed as a log-plus-linear profile if the flow field is thermally stratified. The extent of deviation from the logarithmic profile depends largely on the temperature gradient across the region. This is quite understandable from the turbulent momentum transfer mechanism.

In heat transfer computation, it is still a practice to use a logarithmic velocity distribution in a neutral flow for the deduction of the turbulent Prandtl number. However, both the laboratory and field data indicate that the coefficient of the logarithmic term,  $u_*^*/k$ , is a function of a thermal stability parameter, Richardson number.

# FREE CONVECTION HEAT TRANSFER TO AIR BETWEEN NARROW VERTICAL CHANNELS

By

K. G. Soderstrom and Carlos Reoyo-Sánchez  
University of Puerto Rico

## Abstract

An experimental model of adjacent fuel plates of the Puerto Rico Nuclear Center Reactor was built using the same size plates and spacing as those in the Puerto Rico Nuclear Center Reactor. Data have been taken of several variables to determine the convection coefficient between the plates and the air between the plates in free convection. The results will be used to calculate the temperature rise of the fuel plates of the reactor in the case of a sudden loss of water under reactor operation at various power levels.

# THE LAMINAR BOUNDARY LAYER WITH HYDROGEN INJECTION INCLUDING DIFFUSION DUE TO THERMAL AND CONCENTRATION GRADIENTS

By

W.-S. Lanier and F. Shahrokhi  
The University of Tennessee Space Institute

## Abstract

When analytical solutions to the problem of hydrogen injection into a laminar boundary layer are sought, many of the simplifications which characterize boundary layer investigations are no longer valid. In the present work, hydrogen is injected through a porous wall into a boundary layer

composed of nitrogen and oxygen. It is assumed that equilibrium chemistry as idealized by the flame sheet model will prevail. Further it is assumed that a single combustion product, water, results from the combustion of hydrogen and oxygen. The nitrogen present is taken to be an inert species. Because of the molecular weights involved, multi-component diffusion must be employed instead of the usual Fick's law. Also, there will be an extreme temperature gradient which disallows dropping the thermal diffusion term from the diffusion velocity equation. In most investigations this term is dropped at the expense of accuracy and generality due to the difficulty involved with evaluating the thermal diffusion coefficient.

By assuming a rigid sphere molecular model, the thermal diffusion coefficients have been evaluated through the use of Sonine expansion coefficients. The results for the diffusion coefficients have been specialized to the problem at hand but may be easily modified to yield results for an "n" component flow field.

## TWO-PHASE FLOW DURING THE FORCED CONVECTION ELECTROLYSIS OF WATER<sup>1</sup>

By

J. E. Funk and J. F. Thorpe  
University of Kentucky

### Abstract

Recent interest in the water electrolysis process for life support systems and commercial plants for producing hydrogen and oxygen has created a need for information about the two-phase flow which occurs during water electrolysis.

This progress report will describe an experimental apparatus which will be used to determine the two-phase pressure drop and void fraction.

---

1. This research is being supported by the National Science Foundation under Grant NSF GK-775.

distribution during the forced convection electrolysis of an aqueous potassium hydroxide electrolyte using stainless steel electrodes at atmospheric pressure. The data will be compared with the homogeneous and Martinelli-Nelson models of two-phase flow.

The design and construction of the first electrolysis cell and recirculation loop has been completed. Preliminary data have been obtained and will be presented, along with a brief description of the planned experimental program.

## DIRECTIONAL DIMENSIONAL ANALYSIS

By

Dr. R. L. Young

### Abstract

Directional (or vector) dimensional analysis is shown to yield more information than that obtained from the conventional dimensional analysis. Applications of this method to fluid mechanics and heat transfer problems are described and discussed.

## DETERMINATION OF THE MOON'S TEMPERATURE AND THERMAL PROPERTIES FROM MICROWAVE STUDIES

By

J. D. Eggert  
Brown Engineering Company, Inc

### Abstract

The methods of calibrating microwave receivers for lunar studies are described. The most consistent and significant experimental results are

presented and the importance of this data in drawing conclusions about the lunar thermal environment is discussed. Relating the microwave measurements to the depth dependence of the Moon's temperature is a central problem in this study. The possibility of analytically solving this problem is considered.

## THE EFFECT OF VIBRATION ON CONVECTIVE HEAT TRANSFER IN ENCLOSURES

By

E. H. Bishop, C. J. Bell, and C. T. Carley  
Mississippi State University

### Abstract

This research task includes both analytical and experimental efforts directed at determining the effect of vibration on convective heat transfer in enclosures. Published results of the effect of vibration on convective heat transfer are apparently limited to cylinders, planes, etc., submerged in an infinite fluid. No previous work has been done for a fluid confined in an enclosure.

A mathematical model has been evolved which yields a computer solution for velocity and temperature fields. An experimental test cell has been constructed for rectangular enclosures and is currently undergoing "shade-down" tests on a 2000-pound-force, university-owned, electromagnetic vibration system.

A third portion of the total research effort is directed toward determining the effect of intense vibration on fluid properties, especially in the cryogenic region.

The objective of this research is to determine the effect of vibration on heat transfer in various geometrical enclosures and to develop a predictive ability, for design purposes, for any effects found

# REPORT ON STUDIES OF TRANSIENTS IN COMPOSITE SYSTEMS WITH SURFACES OF CONTACT

By

Harold A. Blum  
SMU Institute of Technology

## Abstract

The major concern of investigators who have been dealing with heat transfer across surfaces in contact has been with the determination and prediction of the contact coefficient of heat transfer. Most of these studies have been carried out under steady state conditions.

We have been concerned with the heat transfer across surfaces in contact in composite systems but under transient conditions. In one situation we started with a one-dimensional system consisting of a sink, a source, and two metallic cylinders in contact. The system, initially at a uniform temperature, was suddenly exposed at one end to the source temperature. In this case, the contact conductance coefficient was essentially constant. In another situation starting with the system just described but initially with a steady state temperature distribution, the contact conductance coefficient was suddenly increased by a rapid change of the contact pressure. In a third case the contact conductance coefficient was changed by suddenly allowing air to enter the space which was previously evacuated.

Both numerical and analytical solutions of the applicable differential equations for the three cases have been verified by experiments so that given the properties of the metals and the contact conductance coefficients, the temperature-time response to either changes in environmental temperature or contact conductance coefficient changes can be predicted accurately enough for most engineering purposes. The complete description of this study can be found in the dissertation of C. J. Moore, Jr. (SMU, April 1967). Some aspects of thermal inertia which were predicted by the theory also showed up experimentally.

The situation in which one or more heat sources will be placed on a common sink with surfaces in contact has also been considered in our study. In this case one would be concerned with the temperature-time response of such systems and with the area of thermal influence (that is, the area beyond the source in which thermal effects of the source are sensed by the sink). For this purpose a numerical solution was developed (two dimensions) for a block placed upon a plate. This solution has been checked by (1) developing a steady state solution and observing the match between the transient and steady state solutions as the time becomes large and (2) by adjusting the geometry of the system for the two dimensional solution in such a way that we could compare it with the one dimensional case. This has been done successfully and some runs (computer) have been obtained.

During the course of this study a passive thermal control device was conceived and constructed which made use of a changing contact surface as the means for heat transfer control at a given temperature level.

This study has been supported by a grant from the National Aeronautics and Space Administration (NsG711/44-007-004).

## EXPERIMENTAL DETERMINATION OF THE CONSTANT IN THE CORRELATION FOR NATURAL CONVECTION FROM A HORIZONTAL FLAT PLATE

By

Walter Frost and Kenneth L. Anderson  
The University of Tennessee Space Institute

---

### Abstract

An investigation has been initiated to ascertain the correct value of the constant,  $C$ , which appears in the correlation for heat transfer by turbulent natural convection to a liquid from a horizontal heated flat plate. The standard equation given in heat transfer texts [1, 2, 3, 4] is

$$N_{Nu} = C (N_{PR} N_{GR})^{1/3}$$

where  $C$  is assigned a value between 0.13 and 0.17. Recent pool boiling heat transfer experiments, [5, 6, 7] however, show the value of the constant as being on the order of 0.30; a factor of 2.5 difference. A closer examination of the true value of  $C$  is thus needed.

Preliminary data taken from a  $5 \times 4\frac{1}{2}$  in electrically resistance heated plate contained in a  $6 \times 12 \times 12$  in glass container gives 0.28 for  $C$ . Further experiments with different sizes plates and with different fluids are planned. Heater plate size variation will discern the length-width ratio necessary for true simulation of an infinite heating surface. The use of dissimilar fluids will establish if physical properties of the fluid effect the constant. It is hoped that this study will assist in illuminating the reasons underlying the reported disagreement in  $C$ .

1. Hsu, S. T.: Engineering Heat Transfer. D. Van Nostrand Company, Inc., New Jersey, 1963.
2. Eckert, E. R. G. and Drake, R. M., Jr.: Heat and Mass Transfer. McGraw-Hill Company, Inc., New York, 1959.
3. Jakob, M.: Heat Transfer. Vol. 1, John Wiley and Sons, Inc., London, 1949.
4. Kreith, F.: Principles of Heat Transfer. International Textbook Co., Pennsylvania, 1958.
5. Zuber, N.: Nucleate Boiling: The Region of Isolated Bubbles and the Similarity with Natural Convection. International Journal of Heat and Mass Transfer. Vol. 6, 1963, p. 53.
6. Bushell, A. L.: Comments on Nucleate Boiling Heat Transfer Correlations and Suggestions for Evaluating the Number of Boiling Sites. Royal Aircraft Establishment, England, Technical Note No. Mechanical Engineering 391, 1963.
7. Calculated by the present authors from the data given in:  
Westwater, J. W. and Kirby, D. B., AIChE paper 14, Sixth National Heat Transfer Conference, Boston, August, 1963.

# BI-DIRECTIONAL THERMAL AND SPECTRAL INVESTIGATIONS OF POSTULATED LUNAR MATERIALS

By

C. D. Cochran  
George C. Marshall Space Flight Center

## Abstract

The thermal properties of the lunar surface have been measured from earth with infrared instruments using an astronomical telescope. From these studies, the lunar surface was found to have directional properties and to be nonspectral in the infrared portion of the spectrum. This progress report presents the results of laboratory experiments with postulated lunar materials to study the effect on bidirectional properties of reflectance and emittance, particle sizes and mixing of rocks and minerals.

# UNSTABLE NATURAL CONVECTION FLOW IN HORIZONTAL CYLINDRICAL ANNULI

By

E. H. Bishop, C. T. Carley, and R. E. Powe  
Mississippi State University

## Abstract

This progress report describes some of the results of an experimental investigation of the natural convection of air in horizontal cylindrical annuli. Specifically, it deals with an unstable oscillatory flow condition recently observed by the authors.

The flow oscillation is described in terms of dimensionless parameters containing the amplitude, period, and wavelength of the oscillations. Empirical equations are given which predict the variation of these parameters with annulus pressure, Grashof number, and diameter ratio. An equation which gives the incipient Grashof number is also presented.

Work is continuing in this area in an attempt to categorize completely natural convection flows in cylindrical annuli in terms of the various dimensionless parameters pertinent to flows of this type. The present effort is directed toward determining the role of the radius of curvature of the cylinders on the flow characteristics.

## STUDIES OF SOLAR RADIATION

By

Glenn E Daniels  
George C Marshall Space Flight Center

### Abstract

The Terrestrial Environment Branch, Aero-Astrodynamics Laboratory has a special interest in solar radiation at the earth's surface. This is to define solar radiation such that it can be used to determine thermal loads on the space vehicle on the launch pad and on the components at times when exposed to the sun in fabrication, testing, and transportation

In the document, "Terrestrial Environment (Climatic) Criteria Guidelines for Use in Space Vehicle Development," the spectral distribution of solar radiation is presented for an extreme value of 1142 watts per square meter. The total spectral values versus time of day are also given for the extreme and the 95 percentile probability level. These data were based on a detail analysis of data from two solar radiation stations: Apalachicola, Florida, and Santa Monica, California.

Future studies are planned to evaluate the diffuse sky radiation for extreme values obtained on clear days and for overcast conditions.

# ENERGY TRANSFER THROUGH EVACUATED NONMETALIC MATERIALS

By

D. W. Tarbell  
Brown Engineering Company, Inc.

## Abstract

An equation for the apparent thermal conductivity of a quasi-transparent medium due to the transfer of energy by radiation has been applied to the case of a medium composed of tiny glass spheres in a highly evacuated environment. A tentative conclusion is that for spheres with a maximum diameter of 800 microns, this contribution should be important at temperatures higher than 200°K.

## APPENDIXES

APPENDIX A  
ORGANIZING COMMITTEE

H. L. Atkins  
George C. Marshall Space Flight Center

Herbert W. Hoffman  
Oak Ridge National Laboratory

J. Edward Sunderland  
North Carolina State University

Gerald E. Tanger  
Auburn University

Reginald I. Vachon  
Auburn University

Robert L. Young  
University of Tennessee Space Institute

## APPENDIX B PROGRAM

Monday, May 8, 1967

9:00 AM - Welcome: R. W. Cook, R&D Operations, MSFC

### SPECIAL LECTURES

9:15 AM - R. B. Bird, University of Wisconsin, "Rheology"

10:30 AM - R. E. Sonntag, University of Michigan  
"Low Temperature Thermodynamics--Hydrogen-Helium  
Systems"

11:45 AM - Lunch

### PROGRESS REPORTS

1:00 PM - W. R. Gambill, Oak Ridge National Laboratory  
"Buoyancy Effects on Thermal Burnout in Vertical Channels"

1:15 PM - L. McDaniel, Brown Engineering  
"Ultraviolet Radiation Damage"

1:30 PM - H. W. Hoffman, Oak Ridge National Laboratory  
"Incipient and Stable Boiling Superheat for Potassium  
Boiling on a Surface Containing Reentrant Cavities"

1:45 PM - J. M. Scarborough, Brown Engineering  
"Problem Areas in the Compositional Analysis of the  
Lunar Surface Based on Measurements of Far-Infrared  
Spectral Emission Obtained by Remote Sensing"

2:00 PM - J. P. Doty, Brown Engineering  
"The Effect of Craters on Lunar Thermal Radiation"

2:15 PM - H. Chuang, University of Louisville  
"Thermally Stratified Shear Flows"

- 2:30 PM - Coffee
- 2:45 PM - K. G. Soderstrom, University of Puerto Rico  
 "Free Convection Heat Transfer To Air Between  
 Narrow Vertical Channels"
- 3:00 PM - W. S. Lanier and F. Shahrokhi, University of Tennessee Space  
 Institute  
 "The Laminar Boundary Layer with Hydrogen Injection  
 Including Diffusion Due to Thermal and Concentration  
 Gradients"
- 3:15 PM - J. E. Funk, University of Kentucky  
 "Two-Phase Flow During the Forced Convection Electrolysis  
 of Water"
- 3:30 PM - R. L. Young, University of Tennessee Space Institute  
 "Directional Dimensional Analysis"
- 3:45 PM - L. W. Crawford, Tennessee Technological University  
 "Fluid Dynamics of a Plane Turbulent Subsonic Air Jet  
 Impinging Normally on a Wall"
- 4:00 PM - J. Eggert, Brown Engineering  
 "Determination of the Moon's Temperature and Thermal  
 Properties from Microwave Studies"
- 4:15 PM - H. W. Butler, West Virginia University  
 "Variational Methods in Non-equilibrium Thermodynamics"
- 4:30 PM - E. H. Bishop, Mississippi State University  
 "Unstable Natural Convection Heat Transfer in Enclosures"
- 4:45 PM - Adjourn
- 6:30 PM - Reception
- 7:30 PM - Dinner

Tuesday, May 9, 1967

SPECIAL LECTURES

8:30 AM - R. W. Truitt, North Carolina State University  
"Some Aspects of Aerodynamic Heating"

9:45 AM - G. B. Heller, Marshall Space Flight Center  
"Thermophysics Research"

11:00 AM - Lunch

PROGRESS REPORTS

12:15 PM - H. A. Blum, Southern Methodist University  
"Report on Studies of Transients in Composite Systems  
With Surfaces of Contact"

12:30 PM - W. Frost and K. L. Anderson, University of Tennessee Space  
Institute  
"Experimental Determination of the Constant in the  
Correlation for Natural Convection from a Horizontal  
Flat Plate"

12:45 PM - C. D. Cochran, Marshall Space Flight Center  
"Bidirectional Thermal and Spectral Investigations of  
Postulated Lunar Materials"

1:00 PM - D. Irey, University of Florida  
"Errors in One Dimensional Fin Solution"

1:15 PM - C. J. Bell, Mississippi State University  
"The Effects of Vibrations on Natural Convection Heat  
Transfer in Enclosures"

1:30 PM - G. E. Daniels, Marshall Space Flight Center  
"Studies of Solar Radiation"

1:45 PM - D. W. Tarbell, Brown Engineering  
"Energy Transfer Through Evacuated Nonmetallic  
Materials"

2:00 PM - Coffee

GROUP DISCUSSIONS

2:15 PM - I Heat Transfer in Cryogenic Systems - Leader, W. R. Gambill, ORNL

2:15 PM - II Radiation Heat Transfer in Space - Leader, W. C. Snoddy, MSFC

2:15 PM - III Topic to be elected

3:00 PM - General Session: Discussion of Bylaws and Plans for Future Seminars

4:00 PM - Adjourn

# APPENDIX C

## BY-LAWS OF THE

### SOUTHEASTERN SEMINAR OF THERMAL SCIENCES

#### ARTICLE 1. Name

This organization shall be known as the SOUTHEASTERN SEMINAR ON THERMAL SCIENCES, hereinafter referred to as the "Seminar." The Seminar, following the adoption of these By-Laws, shall be denoted as the Fourth Southeastern Seminar on Thermal Sciences, and subsequent conferences shall be numbered in sequential order. Three seminars having been conducted on a "de facto" basis establishes the aforementioned numbering.

#### ARTICLE 2. Purpose

The purpose of the Seminar is to stimulate interest in Thermal Sciences in the Southeastern area by providing an outlet for technical paper on the results of scientific and engineering research of both applied and theoretical nature and by encouraging informal exchange of ideas in the field on Thermal Science. The Seminar will embrace heat transfer, mass transfer, thermodynamics, energy conversion, and fluid mechanics.

To this end it will arrange for technical sessions of the Seminar to be held at approximately two-year intervals or until a change in interval is voted by the Policy Committee of the Seminar. The sessions will be held on even numbered years unless a change is voted by the Policy Committee. It will also arrange for the publication of the proceedings of the technical sessions and possibly of other scientific research reports.

#### ARTICLE 3. Membership

All interested colleges, universities, and industrial organizations in the Southeastern Area of the United States may be members of the Conference. The Southeastern Area of the United States as used here includes Louisiana, Arkansas, Kentucky, West Virginia, Virginia and all states to the east and south thereof and the Commonwealth of Puerto Rico. An organization desiring membership in the Seminar shall so state, in writing, to the Executive

Chairman. Upon receipt of a letter of recognition from the Executive Committee, the petitioner becomes a member when: (a) a designated representative from the organization is appointed to the Policy Committee, and (b) the Executive Committee is notified of the appointment.

#### ARTICLE 4. Executive Committee

A. Composition. The Executive Committee is an appointed body and consists of three or four members. There are an executive chairman, an executive vice-chairman, and a secretary-treasurer

B. Duties. The executive chairman has full responsibility for the Seminar. The Executive Committee is the overall governing body for the current technical session of the Seminar and for conducting the business of the Conference in the interim between seminar sessions. The Executive Chairman is the chairman of the Policy Committee. The secretary-treasurer is responsible for collecting and organizing records of executive committee actions and correspondence, for passing them on to his successor, and for occasionally making permanent disposition of old correspondence, and shall be accountable and responsible for all collected funds.

C. Appointment of Executive Committee Members. The executive vice-chairman is appointed by the host organization for the next succeeding technical session and becomes executive chairman for that session. The remaining members of the Executive Committee are appointed by the host organization for the current technical session of the Seminar. The current technical session is defined as the session for which the newly appointed officers are responsible.

D. Assumption of Office. The newly appointed Executive Committee takes office at the conclusion of the Business Meeting, as defined in Article 6D, following the Seminar Session.

#### ARTICLE 5. Policy Committee

A. Composition. The Policy Committee consists of one designated representative from each member organization in the Southeastern area and the executive chairman of the Seminar. The remaining members of the Executive Committee and the immediate past Executive Committee shall be ex-officio members of the Policy Committee

B. Duties. The Policy Committee is responsible for the organization and locations of all Seminar Sessions. The members are responsible for soliciting papers from their respective organizations. Amendments to or changes in the by-laws can be made only by the Policy Committee. The secretary-treasurer shall keep a continuing record of its actions and correspondence.

At least three months prior to each Business Meeting the Executive Chairman shall request, in writing, the name of the representative to the Policy Committee from each member organization.

#### ARTICLE 6. Conference Sessions

A. Selection of Sites for Seminar Sessions. Before a Seminar session, an institution desiring to be host to a Conference session should communicate with the Executive Committee. The Executive Committee may also solicit invitations from prospective host institutions. The Executive Chairman shall inform the Policy Committee of the Seminar of all invitations received, and may recommend acceptance. The decision to accept is, however, made by majority vote of Policy Committee members present at the Business Meeting.

If no invitations have been received, prior to the Business Meeting, for sponsoring the session following the next session, the new Executive Committee shall solicit invitations and a special Policy Committee meeting shall be called to make the decision as to where that seminar session will be held. If, at the Business Meeting, no site is available for the next session, the Seminar is automatically dissolved.

B. Responsibility for Planning Next Seminar. The actual planning of the next Seminar session will be done by officials or faculty members at the host institution, which is also financially responsible for all arrangements. The host institution is responsible for the formation of an editorial committee, which may include persons from other institutions, to select contributed papers and invited papers for the Seminar sessions.

The Policy Committee may provide financial assistance to the next host institution, either by an outright grant or by a guarantee of a certain number of paid registrants or both, if the Seminar has funds available for this purpose.

C. Publication of the Proceedings of the Technical Sessions of the Seminar. The host organization has full responsibility for publishing the

proceedings of the technical sessions for which it is responsible. The purpose of publication and the guiding principle in the choice of publication arrangements is the widest possible circulation of the papers presented at the Seminar session.

D. Business Meeting of the Seminar. In conjunction with each regular session of the Seminar, a Business Meeting shall be held. The attendance at this meeting shall be limited to members of the Policy Committee, and non-participating guests as approved by the Charman. The agenda shall include:

1. Report on business transacted since the last Business Meeting, including a Financial Statement. These may be duplicated and distributed in advance of the Business Meeting and need not be read in full at the meeting.
2. Selection of sites for future Seminar Sessions.
3. Announcement of secretary and executive vice-chairman of Executive Committee by the appropriate organizations.
4. Other business presented by Policy Committee members.

An opportunity for Committee members to introduce new business shall also be provided.

If procedural questions arise, Roberts Rules of Order shall apply, unless the rules are changed by a majority vote of the Committee members present at the Business Meeting.

Interim business may be transacted according to the second procedure for amendments as given by Article 7 of these by-laws.

#### ARTICLE 7. Amendments

Two alternative procedures are available for amending these by-laws:

First Procedure: Proposed amendments to these by-laws shall be made by Policy Committee members only, and shall be submitted in writing to the Executive Chairman at least three days before the beginning of the session, and copies distributed on the first day of the session to all Policy Committee members present. Additional copies of the proposed amendments shall be available at the Business Meeting.

Amendments so proposed may be adopted by an affirmative vote of two-thirds of the Policy Committee members present and voting at the Business Meeting.

Second Procedure: The Executive Committee may propose amendments between sessions by mail ballot sent to all Policy Committee members. At least thirty days shall be allowed for replies to reach the Executive Committee, and at least 50% of the ballots must be returned. Under these conditions the amendment may be adopted by an affirmative vote of two-thirds of the ballots returned

Approved at Third Annual SESTS  
Huntsville, Alabama  
May 9, 1967

## APPENDIX D ATTENDEES

Huntsville, Alabama  
May 8-9, 1967

Anderson, Kenneth L  
University of Tennessee Space  
Institute  
Tullahoma, Tennessee 37388

Arendale, W. F.  
University of Alabama  
Huntsville Campus  
P. O. Box 1247  
Huntsville, Alabama 38507

Atkins, Harry L.  
Space Sciences Lab, R-RP-T  
NASA, Marshall Space Flight Center  
Huntsville, Alabama 35812

Bell, Charles J.  
Mississippi State University  
State College, Mississippi 39762

Bird, Byron R.  
University of Wisconsin  
Madison, Wisconsin 53706

Bishop, Eugene H  
Mississippi State University  
State College, Mississippi 39762

Blum, Harold A.  
Southern Methodist University  
Dallas, Texas 75222

Caiola, N. J.  
IBM Corporation  
P. O. Box 1250  
Huntsville, Alabama 35807

Cochran, Charles D.  
Space Sciences Lab, R-RP-T  
NASA, Marshall Space Flight Center  
Huntsville, Alabama 35812

Chung, Hsing  
University of Louisville  
Louisville, Kentucky 40208

Crawford, Lloyd  
Tennessee Technological University  
Cookeville, Tennessee 38501

Daniels, Glenn E  
R-AERO-YT, Bldg 4200  
NASA, Marshall Space Flight Center  
Huntsville, Alabama 35812

Doty, J. P.  
Brown Engineering Company  
300 Sparkman Drive  
Huntsville, Alabama 35805

Edwards, John A  
North Carolina State University  
Raleigh, North Carolina 27607

Eggert, John  
Brown Engineering Company  
300 Sparkman Drive  
Huntsville, Alabama 35805

Elrod, Alvon C.  
Clemson University  
Clemson, South Carolina 29631

Foster, Howard J.  
Alabama A & M College  
P. O. Box 288  
Normal, Alabama 35762

Frost, Walter  
University of Tennessee Space  
Institute  
Tullahoma, Tennessee 37388

Funk, James E.  
University of Kentucky  
Lexington, Kentucky 40506

Gambill, W. R.  
ORNL, P. O. Box Y  
Oak Ridge, Tennessee 37830

Heller, Gerhard B.  
Space Sciences Lab, R-RP-DIR  
NASA, Marshall Space Flight Center  
Huntsville, Alabama 35812

Hoffman, Herbert  
Reactor Division, ORNL  
Oak Ridge, Tennessee 37830

Holstead, Robert D.  
Louisiana Polytechnic Institute  
Ruston, Louisiana 71270

Klopfenstein, A. G.  
IBM Corporation  
P. O. Box 1250  
Huntsville, Alabama 35807

Kuenzel, H.  
University of Alabama  
P. O. Box 1974  
University, Alabama  
Lanier, W. S.  
University of Tennessee Space  
Institute  
Tullahoma, Tennessee 37388

McDaniels, L.  
Brown Engineering Company  
300 Sparkman Drive  
Huntsville, Alabama 35805

Moore, Clifford J.  
North Carolina State University  
Raleigh, North Carolina 27607

Phillips, R. V.  
IBM Corporation  
P. O. Box 1250  
Huntsville, Alabama 35807

Rust, James H.  
University of Virginia  
School of Engineering & Appl. Sci.  
Charlottesville, Virginia 22903

Scarborough, J. M.  
Brown Engineering Company  
300 Sparkman Drive  
Huntsville, Alabama 35805

Shahrokhi, F.  
University of Tennessee Space  
Institute  
Tullahoma, Tennessee 37388

Snyder, William T.  
University of Tennessee Space  
Institute  
Tullahoma, Tennessee 37388

Soderstrom, Kenneth G.  
University of Puerto Rico  
Mayaguez, Puerto Rico 00708

Sonntag, R. E  
University of Michigan  
Ann Arbor, Michigan 48104

Somogyi, Dezso  
Sperry Rand Corporation  
716 Arcadia Circle, NW  
Huntsville, Alabama 35806

Sunderland, J. Edward  
Georgia Institute of Technology  
Atlanta, Georgia 30332

Tarbell, D. W.  
Brown Engineering Company  
300 Sparkman Drive  
Huntsville, Alabama 35805

Thorpe, James F.  
University of Kentucky  
Lexington, Kentucky 40506

Truitt, R. W.  
North Carolina State University  
Raleigh, North Carolina 27607

Vachon, Reginald I.  
Auburn University  
Auburn, Alabama 36830

Young, Robert L.  
University of Tennessee Space  
Institute  
Tullahoma, Tennessee 37388

Jerry Dunn  
Auburn University  
Auburn, Alabama 36830

Gerald Lowery  
Auburn University  
Auburn, Alabama 36830

Glen Maples  
Auburn University  
Auburn, Alabama 36830

Gordon Nix  
Auburn University  
Auburn, Alabama 36830

Dick Irely  
University of Florida  
Gainesville, Florida 32601

H. W. Butler  
University of West Virginia  
Morgantown, W. Virginia 26506

Roger Jump  
R-AERO-X  
NASA, Marshall Space Flight Center  
Huntsville, Alabama 35812

Brian Price  
R-P&VE-AVB, Bldg 4202  
NASA, Marshall Space Flight Center  
Huntsville, Alabama 35812

APPROVAL

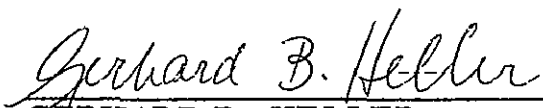
PROCEEDINGS OF THE  
THIRD SOUTHEASTERN SEMINAR  
ON THERMAL SCIENCES

H. L. Atkins

R. I. Vachon

The information in this report has been reviewed for security classification. Review of any information concerning Department of Defense or Atomic Energy Commission programs has been made by the MSFC Security Classification Officer. This report, in its entirety, has been determined to be unclassified.

This document has also been reviewed and approved for technical accuracy.

  
\_\_\_\_\_  
GERHARD B. HELLER  
Director, Space Sciences Laboratory

# DISTRIBUTION

## INTERNAL

### DIR

Mr. Shepherd

### AS-D

Dr. Stuhlinger  
Dr. Bucher

### AST-W

Mr. Mohlere

### DEP-T

### PM-PR-M

### A&TS-MS-H

### A&TS-MS-IL(8)

### A&TS-MS-IP(2)

### A&TS-MS-T(6)

### A&TS-PAT

Mr. Wofford

### S&E-ASTN-DIR

### S&E-ASTN-AVB

Mr. Brian Price

### S&E-ASTR-DIR

### S&E-AERO-DIR

### S&E-AERO-YT

Mr. Glenn Daniels

### S&E-AERO-X

Mr. Roger Jump

### S&E-ME-DIR

### S&E-QUAL-DIR

### S&E-SSL-DIR

Mr. Heller  
Mr. Hembree

### S&E-SSL-X

Dr. Weber  
Mr. Weathers  
Dr. Dozier  
Dr. Decher

### S&E-SSL-C

Mr. Mathis  
Reserve (25)

### S&E-SSL-T

Mr. Snoddy

### S&E-SSL-TE

Mr. Miller  
Mr. Atkins (15)

### S&E-SSL-TR

Mr. Arnett

### S&E-SSL-TT

Mr. Jones

## EXTERNAL

Kenneth L. Anderson  
University of Tennessee Space  
Institute  
Tullahoma, Tennessee 37388

W. F. Arendale  
University of Alabama  
Huntsville Campus  
P. O. Box 1247  
Huntsville, Alabama 35807

Charles J. Bell  
Mississippi State University  
State College, Mississippi 39762

Byron R. Bird  
University of Wisconsin  
Madison, Wisconsin 53706

Eugene H. Bishop  
Mississippi State University  
State College, Mississippi 39762

Harold A. Blum  
Southern Methodist University  
Dallas, Texas 75222

N. J. Caiola  
IBM Corporation  
Huntsville, Alabama 35807

Hsing Chung  
University of Louisville  
Louisville, Kentucky 40208

Lloyd Crawford  
Tennessee Technological University  
Cookeville, Tennessee 38501

A. G. Klopfenstein  
IBM Corporation  
P. O. Box 1250  
Huntsville, Alabama 35807

H. Kuenzel  
University of Alabama  
P. O. Box 1974  
University, Alabama 35486

J. P. Doty  
Brown Engineering Company  
300 Sparkman Drive  
Huntsville, Alabama 35805

John A. Edwards  
North Carolina State University  
Raleigh, North Carolina 27607

John Eggert  
Brown Engineering Company  
300 Sparkman Drive  
Huntsville, Alabama 35805

Alvon B. Elrod  
Clemson University  
Clemson, South Carolina 29631

Howard J. Foster  
Alabama A&M College  
P. O. Box 288  
Normal, Alabama 35762

Walter Frost  
University of Tennessee Space  
Institute  
Tullahoma, Tennessee 37388

James E. Funk  
University of Kentucky  
Lexington, Kentucky 40506

W. R. Gambill  
ORNL, P. O. Box Y  
Oak Ridge, Tennessee 37830

Herbert Hoffman  
Reactor Division, ORNL  
Oak Ridge, Tennessee 37830

Robert D. Holstead  
Louisiana Polytechnic Institute  
Ruston, Louisiana 71270

W. S. Lanier  
University of Tennessee Space  
Institute  
Tullahoma, Tennessee 37388

L. McDaniels  
Brown Engineering Company  
300 Sparkman Drive  
Huntsville, Alabama 35805

Clifford J. Moore  
North Carolina State University  
Raleigh, North Carolina 27607

R. V. Phillips  
IBM Corporation  
P. O. Box 1250  
Huntsville, Alabama 35807

James H. Rust  
University of Virginia  
School of Engineering & Applied  
Sciences  
Charlottesville, Virginia 22903

J. M. Scarborough  
Brown Engineering Company  
300 Sparkman Drive  
Huntsville, Alabama 35805

F. Shahrokhi  
University of Tennessee Space  
Institute  
Tullahoma, Tennessee 37388

William T. Snyder  
University of Tennessee Space  
Institute  
Tullahoma, Tennessee 37388

Kenneth G. Soderstrom  
University of Puerto Rico  
Mayaguez, Puerto Rico 00708

R. E. Sonntag  
University of Michigan  
Ann Arbor, Michigan 48104

Dezso Somogyi  
Sperry Rand Corporation  
716 Arcadia Circle, NW  
Huntsville, Alabama 35806

J. Edward Sunderland  
Georgia Institute of Technology  
Atlanta, Georgia 30332

D. W. Tarbell  
Brown Engineering Company  
300 Sparkman Drive  
Huntsville, Alabama 35805

James F. Thorpe  
University of Kentucky  
Lexington, Kentucky 40506

R. W. Truitt  
North Carolina State University  
Raleigh, North Carolina 27607

Reginald I. Vachon (15)  
Auburn University  
Auburn, Alabama 35830

Robert L. Young  
University of Tennessee Space  
Institute  
Tullahoma, Tennessee 37388

Jerry Dunn  
Auburn University  
Auburn, Alabama 35830

Glen Maples  
Auburn University  
Auburn, Alabama 35830

Gordon Nix  
Auburn University  
Auburn, Alabama 35830

Dick Irey  
University of Florida  
Gainesville, Florida 32601

H.W. Butler  
University of West Virginia  
Morgantown, West Virginia 26506

Scientific and Technical Information (2)  
Facility  
P.O. Box 33  
College Park, Maryland 20740  
Attn: NASA Representative (S-AK/RKT)